The University of Nottingham
UNITED KINGDOM · CHINA · MALAYSIA

Yue, Peng (2016) A MICRO MECHANICAL STUDY OF CRITICAL STATE SOIL MECHANICS USING DEM. PhD thesis, University of Nottingham.

Access from the University of Nottingham repository:
http://eprints.nottingham.ac.uk/38060/1/Yue%20_correction%20PDF.pdf

Copyright and reuse:

The Nottingham ePrints service makes this work by researchers of the University of Nottingham available open access under the following conditions.

This article is made available under the University of Nottingham End User licence and may be reused according to the conditions of the licence. For more details see: http://eprints.nottingham.ac.uk/end_user_agreement.pdf

For more information, please contact eprints@nottingham.ac.uk



A MICRO MECHANICAL STUDY OF CRITICAL STATE SOIL MECHANICS USING DEM

By
Yue Peng
BEng, MSc

A Thesis submitted to The University of Nottingham

for the degree of Doctor of Philosophy

July, 2016

Abstract

One of the greatest breakthroughs in soil mechanics was the development of Critical State Soil Mechanics (CSSM) in the 1950s and 1960s and the derivation of a continuum elasto-plastic constitutive model, namely Cam clay, which was the foundation for other continuum models for clays, and much later for sands. However, as yet there has been no micro mechanical analysis which explains the existence of such continuum models; such a micro perspective must take into account the discontinuous nature of soil. Without such insight, the engineer cannot understand which micro parameters affect soil behaviour.

This work uses the discrete element method (DEM) to model a silica sand as a sample of discrete particles, with properties which have been calibrated against experimental data in previous work, to build up a micro mechanical picture of the behaviour of sand under different loading conditions. The simplest of loading conditions is the one-dimensional or oedometer test and has been modelled to check whether this agrees with previously published research. The simulated sample has then been subjected to isotropic compression to establish a normal compression line in log voids ratio – log stress space, and which turns out to be parallel to the one-dimensional normal compression line, in agreement with CSSM. The evolution of the isotropic normal compression line is due to local shear stresses within the sample, and the origin of the existence of both lines lies in the evolution of a fractal distribution of particles with a fractal dimension of 2.5. The effect of boundary particles has then been minimised by choosing an appropriate aspect ratio and a smaller number of particles in the sample

to give a computational time which is acceptable for subsequent shearing to critical states.

Isotropically normally compressed samples have been unloaded to different stress levels and sheared to critical states. A unique critical state line (CSL) exists at high stress levels, which is parallel to the normal compression lines, in agreement with CSSM. At low stress levels, the CSL is not linear and is non-unique; that is to say it is a function of preconsolidation pressure because the fractal distribution of sizes has not fully evolved. Samples sheared on the dense side of critical dilate and have a peak strength whilst loose samples exhibit ductile contraction, in agreement with CSSM. At a critical state, the work shows that crushing continues in the formation of 'fines', small particles with smaller than 0.1mm dimensions, which plays no part in the mechanical behaviour, which is reflected in the average mechanical co-ordination number and which means that plastic hardening can be assumed to have ceased at a critical state.

For the isotropically overconsolidated samples sheared to critical states, a number of different definitions of yield have been used to establish a yield surface in stress space. The work shows that a previously published yield surface for sand (Yu, 1998; McDowell, 2002) gives a good representation of the behaviour, and it has therefore been shown that the sample of discrete particles has been shown to give rise to observed continuum behaviour. The work is, to the author's knowledge, the first that has shown a DEM soil to show many of the desirable features of sand, in that the sample qualitatively gives normal compression lines and a CSL of the correct slope, which obeys CSSM and which gives a Cam Clay type yield surface in stress space.

The work means that the established model can be used in the study of other micro mechanics problems such as particle shape and time effects and the application of DEM to boundary value problems directly.

Acknowledgement

The author would like to express her sincerest gratitude to her supervisors, Professor Glenn McDowell, Professor Hai-Sui Yu and Dr Charlie Heron, for their guidance, understanding, patience and encouragement during her PhD study. Their great supervision, endless help and constant passion on geotechnical research has shaped the author's view on research and future career. Their attitudes towards work and life will also lead the author in the future.

The author also acknowledges the University of Nottingham for the financial support from the `Dean of Engineering Research Scholarship for International Excellence' to carry out this research project in the Nottingham Centre for Geomechanics (NCG).

Sincere thanks also goes to the author's internal, Dr. Alec Marshall, for his academic comments in the past years of study.

Appropriation goes to all the members in NCG, especially Dr John de Bono and Dr Huiqi li, for their friendship, encouragement and help; Miss Qiong Xiao and Miss Jingyi Shen for their accompany and love. It's them who make the author's life in Nottingham full of happiness.

Finally, the author thanks her beloved parents for their endless understanding, support and help.

Abstract ..... **I**
Acknowledgement ..... **IV**
List of Figures ..... **VIII**
List of Tables ..... **XIV**
Nomenclature ..... **XV**
Chapter 1 Introduction **1**
1.1 Background and problem definition 1
1.2 Aims and objectives 2
1.3 Thesis outline 3
Chapter 2 Literature Review **5**
2.1 Introduction 5
2.2 Critical state soil mechanics 6
2.2.1 Fundamental tests to investigate soil behaviour 6
2.2.2 The concept of Critical States 10
2.2.3 Basic ingredients of soil constitutive models 12
2.2.4 Cam-Clay and Modified Cam-Clay 15
2.2.5 Unified State Parameter Model 24
2.2.6 Critical State Model for sands 26
2.3 Particle fracture in soil mechanics 30
2.3.1 The role of particle fracture in CSSM 30
2.3.2 Tensile strength of a particle 32
2.3.3 The distribution of single particle tensile strength 35
2.3.4 Hardening law 38
2.4 Discrete element method (DEM) 43
2.4.1 General description of DEM 44
2.4.2 Particle flow code 44
2.4.3 Contact models 49
2.4.4 Servo-control 52
2.5 Applications of Discrete Element Method (DEM) 53
2.5.1 DEM modelling single particle breakage 53
2.5.2 DEM investigation of critical state 68
2.6 Summary 86

Chapter 3 Methodology 88
3.1 Introduction 88
3.2 General descriptions 88
3.3 Simulation of a single crushable silica sand particle 90
3.4 Sample generation 94
3.5 Loading procedure 96
3.5.1 Loading method: stress control & strain control 96
3.5.2 1-D and isotropic compressions 97
3.5.3 Triaxial shear test 99
3.6 Measurement 101
3.6.1 Stress measurement 101
3.6.2 Strain measurement 102
3.7 Conclusions 103
Chapter 4 Discrete Element Modelling of 1-D and Isotropic Normal Compression 105
4.1 Introduction 105
4.2 Comparison between isotropic and 1-D normal compression 107
4.3 Comparison of the influence of aspect ratio 115
4.4 1-D and isotropic normal compression results for triaxial sample 118
4.5 Conclusions 122
Chapter 5 Triaxial Shear and Critical States 126
5.1 Introduction 126
5.2 Preparation of over-consolidated samples 128
5.3 Macro observations during shearing to critical state 130
5.3.1 Stress path effects 130
5.3.2 The influence of p_0' 142
5.4 Micro behaviour of sample during shearing 153
5.4.1 The evolution of the total number of spheres when shearing to critical state 153
5.4.2 The evolution of average coordination number during shearing 158

5.5 Conclusions 166

Chapter 6 CSL and Yield Surface 169

6.1 Introduction 169

6.2 Definition of yielding and yield point 170

6.2.1 Definition of yielding 170

6.2.2 Methods of choosing yield point 171

6.3 Data smoothing function 179

6.3.1 Direct smoothing 180

6.3.2 Smoothing according to an exponential function 183

6.4 Yield points and yield surface 185

6.4.1 Yield points 185

6.4.2 Yield surfaces 192

6.5 Conclusions 198

Chapter 7 Conclusions and Recommendations for Future Work ..201

7.1 Conclusions 201

7.1.1 1-D and isotropic normal compressions 201

7.1.2 Triaxial shear and critical states of the simulated sand 202

7.1.3 Yield criterion and yield surface of the simulated sand 204

7.2 Recommendations for future work 206

7.2.1 Better geometry of grains 206

7.2.2 Reducing boundary effect 206

7.2.3 Using a flexible membrane instead of stiff confining walls 207

7.2.4 Constant volume shearing 207

7.2.5 Investigating the behaviour of crushable soil at low stress level. 208

References 209

Appendix A 218

Appendix B 235

Appendix C 236

Appendix D 237

Appendix E 244

List of Figures

Figure 2.1 The Oedometer apparatus (Craig, 1997) 7
Figure 2.2 Schematic plot of 1-D and isotropic normal compression lines 8
Figure 2.3 Conventional triaxial apparatus (following Atkinson, 2007) 9
Figure 2.4 Stress on a triaxial sample (following Atkinson, 2007) 9
Figure 2.5 The concept of critical states: (a) in $q - p'$ space; (b) in $v - \ln p'$ space 12
Figure 2.6 Schematic plots of plastic potential surface and plastic strain increment 15
Figure 2.7 Yield locus and stress-strain lines in e-ln p' scale of the Original Cam-clay model (following Schofield and Wroth, 1968) 19
Figure 2.8 $p - q - e$ plots of the Original Cam-Clay Model (following Schofield and Wroth, 1968) 20
Figure 2.9 Cam-clay stress-strain response of heavily-overconsolidated soils during conventional drained triaxial shear (following Schofield and Wroth, 1968) 21
Figure 2.10 Yield locus of modified Cam-clay model (following Roscoe and Burland, 1968) 23
Figure 2.11 Modified Cam-clay stress-strain response of heavily over-consolidated soils during conventional drained triaxial shear (following Roscoe and Burland, 1968) 23
Figure 2.12 Schematic of state parameter and spacing ratio (Yu, 1998) 25
Figure 2.13 Family of yield loci: (a) for various values of a (N=M) (McDowell, 2002); (b) for various values of r and n (Yu, 1998) 28
Figure 2.14 Modified definition of Hardin's breakage index Br(Einav, 2007) 32
Figure 2.15 Particle tensile strength test set-up (Lee, 1992) 33
Figure 2.16 Typical plot of force against deformation for a typical particle (Lee, 1992) 34
Figure 2.17 Results of mean tensile strength for single particle crushing tests (Lee, 1992) .. 35
Figure 2.18 Cumulative distribution functions for various Weibull distributions, with a characteristic value $X_0 = 1$, showing the influence of the Weibull modulus (de Bono, 2013) 36
Figure 2.19 37% strength σ_0 as a function of particle size (McDowell and Amon, 2000) 38
Figure 2.20 Particle size distributions for various crushed materials, showing consistent fractal dimensions of 2.5 (Turcotte, 1986) 39
Figure 2.21 Compression behaviour for silica sand plotted on log e-log σ_v' axes (McDowell, 2005) 43
Figure 2.22 Calculation cycle in PFC^{3D} (Itasca, 2008) 45

Figure 2.23 Two fragmented samples using different fracture modes (a) fracture mode (1); (b) fracture mode (Astrom and Herramann, 1998) 55
Figure 2.24 Identification of hydrostatic state and deviatoric state (Tsoungui *et al.*, 1999).. 56
Figure 2.25 Fracture mode in 2D scale (Tsoungui *et al.*, 1999) 56
Figure 2.26 Idealization of induced tensile stress (Lobo-Guerrero *et al.*, 2005) 57
Figure 2.27 Three alternative breakage configurations, showing the random rotation followed by expansion of the new particles (Ben-Nun and Einav, 2010)..... 58
Figure 2.28 Final particle size distribution by number in log-log scale with a slope giving a fractal dimension of 1.16 (Ben-Nun and Einav, 2010) 59
Figure 2.29 Final topology of crushed 2D sample, showing self-similarity across scales (Ben-Nun and Einav, 2010) 59
Figure 2.30 Three fragment functions (a) splitting into two fragments (b) splitting into three fragments (c) splitting into four fragments (McDowell and de Bono, 2013) 62
Figure 2.31 Crushing test on agglomerate (Robertson, 2000). 64
Figure 2.32 Typical result of a crushing test on an agglomerate (Robertson, 2000). 64
Figure 2.33 Weibull probability plot for (a) 0.5mm (b) 1mm agglomerates (McDowell and Harireche, 2002a)..... 65
Figure 2.34 (a) Orientation of HCP agglomerate under diametral compression; (b) Orientation of HCP agglomerate in x–z plane; (c) Distribution of contacts for a rotation angle of 0° in the x–y plane; (d) Distribution of contacts for a rotation angle of 90° in the x-y plane (Li *et al.*, 2013)..... 66
Figure 2.35 (a) particle assembly after initial generation but before rearrangement; (b) contact-force distribution after step 2; (c) floating particles (with less than three contacts) and contacts after step 4; (d) Bonds added after step 4 (Potyondy and Cundall , 2004)..... 67
Figure 2.36 The location of the new ball to occupy the tetrahedral space between four existing micro-spheres forming the agglomerate packing (Li, 2013) 68
Figure 2.37 3-D sample consisting of a group of agglomerates (Cheng *et al*., 2003) 69
Figure 2.38 A single yield surface obtained from 'change of slope': (a) curves of deviator stress against deviator strain; (b) curves of voids ratio against mean effective stress; (c) yield points in *q-p'* space (Cheng *et al.*, 2004)..... 70
Figure 2.39 Multiple yield surfaces in relation to particle breakage: (a) continuous breakage; (b) quantity and shape of pbb surfaces (Cheng *et al*., 2004)..... 73
Figure 2.40 Comparison of stress-dilatancy of Zone H and Rowe's theory: stress-dilatancy in Zone H; (b) Rowe's theory (Cheng *et al*., 2004)..... 74
Figure 2.41 Critical state lines observed for soils: (a) different stress history; (b) different

stress path(Cheng and Bolton, 2005) 76
Figure 2.42 Deviator stress against pressure at final states, *i.e.* 60% deviator strain (Cheng and Bolton, 2005)..... 77
Figure 2.43 Variation of specific volume with mean stress under different stress paths for isotropically rebounded assembly of granular materials for different initial conditions (Sithram and Vinod, 2008). 78
Figure 2.44 Critical state line for samples with different stress path (Sitharam and Vinod, 2008) 78
Figure 2.45 Numerical sample: (a) before compression; (b) after 100 MPa (McDowell and de Bono, 2013)..... 79
Figure 2.46 Evolving particle size distribution for simulation of silica sand (McDowell and de Bono, 2013)..... 80
Figure 2.47 One-dimensional compression plot for simulation of silica sand (McDowell and de Bono, 2013)..... 80
Figure 2.48 One-dimensional compression plots for: (a) various particle strengths q_0; (b) vertical stress σ normalised by particle strength q_0 (McDowell and de Bono, 2013) 81
Figure 2.49 Effect of comminution limit on compression plot (McDowell and de Bono, 2013) 82
Figure 2.50 Effects of different grading on compression plot (McDowell and de Bono, 2013) 82
Figure 2.51 Effects of Weibull modulus on one-dimensional compression plots (McDowell and de Bono, 2013) 83
Figure 2.52 Effects of breakage mechanisms on (a) one-dimensional compression plots ; (b) final particle size distribution (McDowell and de Bono, 2013)..... 84
Figure 2.53 Evolving particle size distribution from simulation of silica sand plotted on double logarithmic axes (McDowell and de Bono, 2013) 85
Figure 2.54 Fractal dimension as a function of stress (McDowell and de Bono, 2013) 85
Figure 3.1 Logic of simulation of fundamental tests in this investigation..... 90
Figure 3.2 Simple particle splitting mechanism (McDowell and de Bono, 2013)..... 93
Figure 3.3 The initial monodisperse oedometer and triaxial samples..... 96
Figure 3.4 Logic of loading procedure for normal compression 99
Figure 3.5 Logic of loading procedure in triaxial test..... 101
Figure 4.1 Normal compression plots for oedometer sample 108
Figure 4.2 Evolving particle size distribution of oedometer sample: (a) traditional plot by mass grading curve and (b) fractal plot of number of particles on a log scale..... 109

Figure 4.3 Evolving fractal dimension of oedometer sample under isotropic normal compression 110
Figure 4.4 Schematic diagram on log-log axes, showing the two set of data points (ABC and DEF) at which the particle size distributions are compared 111
Figure 4.5 Evolving particle size distributions for points A, B and C: (a) percentage by mass of particles finer than size d against size d on the traditional linear-log scale and (b) percentage by number of particles greater than size d against size d on log-log axes. 113
Figure 4.6 Evolving particle size distributions for points D, E and F: (a)percentage by mass of particles finer than size *d* against size *d* on the traditional linear-log scale and (b) percentage by number of particles greater than size *d* against size *d* on log–log axes 114
Figure 4.7 Distribution of octahedral shear stress q for the particles: (a) at points A and B; (b) at points D and E 115
Figure 4.8 One-dimensional normal compression plots for samples with different aspect ratio 118
Figure 4.9 Contact force distribution of one-dimensional compression at p'=8 MPa: (a) triaxial sample, maximum contact force 1.916×102N; (b) oedometer sample, maximum contact force 2.239×102N. 118
Figure 4.10 Evolving K_0 for triaxial sample during 1-D normal compression 119
Figure 4.11 One-dimensional and isotropic compression behaviour of the triaxial sample 120
Figure 4.12 Comparison of contact force distribution under 1-D and isotropic compressions at the same stress level, p'=11 MPa: (a) triaxial sample; (b) oedometer sample. 121
Figure 4.13 Evolving particle size distribution for triaxial sample: (a) by mass of particles smaller; (b) by number of particles larger. 122
Figure 5.1 Normal compression lines and critical state line (Wood, 1990) 126
Figure 5.2 Unloading line of samples with 17 MPa and 20 MPa 129
Figure 5.3 Stress-strain and volume plots for samples under conventional shearing 131
Figure 5.4 Stress-strain plots with fitted curve for triaxial shear at constant confining stress and a preconsolidation stress of 20 MPa 133
Figure 5.5 Samples at critical state at same axial strain of 20%: (a) constant confining stress of 2 MPa; (b) constant confining stress of 10 MPa. 137
Figure 5.6 Samples after deleting inactive spheres: (a) constant confining stress of 2 MPa; (b) constant confining stress of 10 MPa 137
Figure 5.7 Stress-strain and volume plots for samples under constant p' shearing with p_0'=20 MPa and different mean effective stresses 139
Figure 5.8 Stress-strain plots for triaxial shear with fitted curve at constant p' and a

preconsolidation stress of 20 MPa. 140
Figure 5.9 Critical states for samples with p_0'=20 MPa 142
Figure 5.10 Stress-strain and volume plots for samples under conventional shearing with p_0'=17 MPa and different confining pressures..... 144
Figure 5.11 Stress-strain and volume plots for samples under constant-p' shearing with p_0'=17 MPa and different mean effective stresses 145
Figure 5.12 Stress-strain plots with fitted curve for triaxial shear at constant confining stress and a preconsolidation stress of 17 MPa. 146
Figure 5.13 Stress-strain plots with fitted curve for triaxial shear at constant-p' and a preconsolidation stress of 17 MPa 147
Figure 5.14 Comparisons of constant p' tests for two different samples at mean effective stress equal to 10 MPa 150
Figure 5.15 Critical state line for samples with different pre-consolidation pressures. 152
Figure 5.16 The evolution of total number of spheres as the axial strain increases for samples with p_0'=20 MPa : (a) constant-p' stress path; (b) conventional constant confining pressure stress path 155
Figure 5.17 The evolution of total number of spheres as the axial strain increases for samples with p_0'=17 MPa: (a) constant-p' stress path; (b) conventional constant confining pressure stress path. 156
Figure 5.18 The evolution of the total number of spheres during conventional shear with the confining pressure of 8 MPa 157
Figure 5.19 PSD and mechanical PSD at critical state. 158
Figure 5.20 Evolution of average coordination number of samples with p_0'=20 MPa: (a) constant-p' stress path; (b) conventional constant confining pressure stress path 160
Figure 5.21 Evolution of average coordination number of samples with p_0'=17 MPa: (a) constant-p' stress path; (b) conventional constant confining pressure stress path 161
Figure 5.22 Evolution of average mechanical coordination number of samples with p_0'=20 MPa: (a) constant-p' stress path; (b) conventional constant confining pressure stress path 162
Figure 5.23 Evolution of averagemechanical coordination number of samples with p_0'=17 MPa : (a) constant-p' stress path; (b) conventional constant confining pressure stress path 163
Figure 5.24 Evolution of mechanical average coordination number during triaxial shearing 164
Figure 5.25 Evolution of coordination number with deviatoric stress response during shearing (Fonseca et al. 2013)..... 165
Figure 5.26 Vertical section of different samples at critical state: (a) constant confining

stress of 2 MPa; (b) constant confining stress of 10 MPa; (c) enlarged view of the blue area in (b) 166
Figure 6.1 Identification of Zone I, II and III in normalised stress space (Jardine, 1992) ... 171
Figure 6.2 Yield points on the stress-strain plots using intersection method (Yasufuku *et al.*, 1991) 172
Figure 6.3 Yield points according to the intersection method (Cheng, 2004) 173
Figure 6.4 Schematic plot of the modified intersection method of choosing yield point 175
Figure 6.5 Schematic plot of the maximum curvature on a curve 176
Figure 6.6 Schematic plot of peak and critical strength and associated dilation 178
Figure 6.7 Schematic plots of the stiffness degradation method 179
Figure 6.8 The smoothed $q - \varepsilon_a$curve of triaxial shear test of samples at constant-p' and 17 MPa preconsolidation pressure 181
Figure 6.9 The smoothed $q - \varepsilon_a$ curves of triaxial shear tests of samples at constant confining stress and 17 MPa preconsolidation pressure. 181
Figure 6.10 The smoothed $q - \varepsilon_a$curves of triaxial shear tests of samples at constant-p' and 20 MPa preconsolidation pressure 182
Figure 6.11The smoothed $q - \varepsilon_a$ curves of triaxial shear tests of samples at constant confining stress and 20 MPa preconsolidation pressure 182
Figure 6.12 Yield points according to different methods for the 17 MPa samples under constant-p' triaxial shearing 188
Figure 6.13 Yield points according to different methods for the 17 MPa samples under constant confining stress triaxial shearing 189
Figure 6.14 Yield points according to different methods for the 20 MPa samples under constant-p' triaxial shearing 190
Figure 6.15 Yield points according to different methods for the 20 MPa samples under constant confining stress triaxial shearing 191
Figure 6.16 Yield surfaces according to different methods of choosing yield point: 195
Figure 6.17 Schematic plot of the location of the highest point on yield surface and the direction of the plastic strain increment vector: (a) highest point coincides with the intersection of CSL and yield surface; (b) peak stress and critical state do not coincide 198
Figure 7.1 Schematic plot of the studied region A and to be studied region B..... 208

List of Tables

Table 3-1 Physical parameters of a simulated sand particle 91
Table 3-2 Initial parameters of oedometer and triaxial samples 96
Table 3-3 Loading parameters for triaxial shear tests 100
Table 4-1 Details of two groups of points chosen to compare the particle size distribution 111

Nomenclature

Roman Symbols

V_i^s	shear component of the contact velocity
$\ddot{x}_\iota$	acceleration of particle
A_1, B_1, a_1	artificial constants in exponential equations
A_2, B_2, a_2	artificial constants in exponential equations
B_r	relative breakage parameter
F_f	diametral fracture force
F_i	contact force vector
K_0	lateral earth coefficient
K^n	normal stiffness
K^s	shear stiffness at the contact
M_i	resultant moment acting on particles
N_c	number of contacts
N_{cy}	number of cycles
P_s	survival probability
S_m	surface area per unit mass of solids
S_p	proportion of particles on the surface
U^n	overlapping of the two particles
V_s	volume of solids,
W^p	plastic work
g_i	body force acceleration vector
k_n , k_s	normal and shear stiffness
l_r	aspect ratio
n_i	unit normal vector
n_{oc}	over-consolidation ratio
p_0	pre-consolidation pressure
q_0	particle strength
r^*	spacing ratio

w_h	horizontal displacement in direct shearing
A	area of the wall
D	fractal dimension
E	surface energy
G	elastic shear modulus
G_a	target state parameter
I	moment of inertia of a particle
M	critical state dissipation constant
N	stress ratio corresponding to the peak value of q
Q	plastic potential surface
R	radius of a spherical particle
S	surface area of particles
T	real period of time
V	volume of the particle
X	random variable
a	artificial coefficient
d	diameter of the grain
$d\varepsilon_{ij}^{e}$	elastic strain increment
$d\varepsilon_{ij}^{p}$	plastic strain increment
dW	work increment done by the active stress along its direction
b	the rate of the changing of strength against size
e	the volume of voids divided by the volume of solids
f	yield surface
m	Weibull modulus
n	stress-state coefficient
p'	mean effective stress
q	deviator stress
r	characteristic linear dimension
u	vertical displacement in direct shearing
$tdel$	critical time step of PFC

Greek Symbols

$\dot{\omega}_\iota$	angular acceleration of a particle
$\varepsilon_1, \varepsilon_a$	axial strain
ε_q	deviator strain
ε_r	radial strain
ε_v	volume strain
ξ_R	reference state parameter
τ_r	constant such that$u = 0$ when $w_h = 0$
σ_0	37% survival strength
σ_c	cell pressure
σ_1'	major principle stress
σ_2'	intermediate principle stress
σ_3'	minor principle stress
σ_f	tensile stress at failure
σ_r	confining stress of the confining wall
σ_v'	applied macroscopic vertical stress
Δt	length of each time-step in real
α	relaxation factor
ε	strain on the stress direction
η	stress ratio q/p'
κ	slope of the elastic rebounding line
λ	slope of the normal compression line
μ	friction coefficient
υ	Poisson's ratio
ν	soil specific volume
τ	shear stress in direct shearing
ξ	state parameter
σ	active stress
ϕ	friction angle
ϕ_{mob}	mobilised friction angle
ψ_{max}	dilation angle

Abbreviations

pbb	percentage of broken bonds
BCC	body centred cubic
BPM	bonded particle model
CASM	clay and sand model
CD	consolidated drained test
CSL	critical state line
CSSM	critical state soil mechanics
DEM	discrete element method
DRP	dense random packing
FCC	face centred cubic
HCP	hexagonal close packing
NCL	normal compression line
PBM	population balance model
PSD	particle size distribution
UD	consolidated undrained test
UU	unconsolidated undrained test

Chapter 1 Introduction

1.1 Background and problem definition

In the late 1950s and 1960s, researchers from Cambridge University (Parry, 1956; Roscoe *et al.*, 1958; Schofield and Wroth, 1968) developed the concept of the 'Critical State'. By taking the critical state as a reference state, the framework of Critical State Soil Mechanics (CSSM) has been established. Constitutive models (Roscoe *et al.*, 1958; Schofield and Wroth, 1968; Yu, 1998) have been proposed contributing to the development of the CSSM during the past half century. The Cam clay model and modified Cam-clay (MCC) model, both of which predict the behaviour of clay satisfactorily are the most famous and widely applied constitutive models. However, Cam clay and MCC are not particularly suitable for application of a discontinuous assembly of particles, such as sands.

Discrete element modelling (DEM), developed by Cundall (1971) is a powerful numerical simulation method that focusses on interaction between individual particles and models granular material as discrete elements. Therefore, DEM is an efficient method to investigate the behaviour of sand because of the discontinuous nature of sand. It has many advantages when investigating granular issues: it can store the initial data to reproduce the exact same sample and control the initial state, so that different parameters can be given to the same sample again and again. In addition, large strain levels can be achieved, which can be limited in lab tests. Many studies on sands have utilised DEM (eg. Robertson, 2000; McDowell and Harireche, 2002; Cheng *et al.*, 2004). Findings in DEM research have resulted in more and more attention to the

research by Rowe (1962), who looked into the interaction between single particles and successfully linked it to the macro behaviour of sands, a decade earlier than Cundall (1971) and around the same time as the development of the continuum Cam clay models.

Considering Rowe's stress-dilatancy rule, Yu (1998) proposed a unified constitutive model for both clay and sand (CASM), based on a large number of macroscopic testing results. Also, McDowell (2002) proposed a state boundary surface (SBS) for sands which, despite taking a different approach, ultimately is the same as CASM. However, McDowell's model is based on the microscopic crushing and size effect of single particles, proposed by Lee (1992). Given the widely observed particle crushing and the discontinuous nature of sand, it is therefore supposed that by properly defining the microscopic crushing of a single particle the macroscopic behaviour of sands within the critical state soil mechanics frame work, such as CASM, can be produced using DEM. Furthermore, if DEM can generate the constitutive model, then with increased computational power, boundary value problems could be solved using DEM directly. In that way, there is no need to obtain parameters from tests to solve boundary value problems according to constitutive models using FEM. Since this study focuses on the discontinuity and the crushable nature of soils, taking silica sand as a typical case in point, the term 'crushable soil' refers to the simulated silica sand in this project.

1.2 Aims and objectives

The aim of this project is to use DEM to study the constitutive behaviour of crushable soil and provide micro mechanical insight into the origins of critical states and elasto-plastic behaviour.

In order to achieve the presented aim, the objectives of the study are:

- To simulate particle crushing using an appropriate breakage mechanism.
- To simulate one-dimensional (1-D) normal compression and generate a normal compression line (NCL) and compare with previous work by McDowell and de Bono (2013).
- To simulate isotropic normal compression and generate a normal compression line and compare with the 1-D NCL.
- To simulate isotopic unloading of the isotropically normal consolidated sample to prepare samples for subsequent triaxial shear tests.
- To simulate triaxial shear tests of the prepared overconsolidated samples to critical states to examine the sample behaviour during shearing and establish the critical state line.
- To determine the yield point from stress-strain triaxial shear tests thus permitting the presentation of a yield surface.
- To conduct comparisons of the obtained yield surface with the theoretical predicted yield surface according to CASM (Yu, 1998) and McDowell (2002) yield surface.

1.3 Thesis outline

The chapters of the thesis are organised in seven parts as listed below:

- Chapter 1 gives a general description of the background of this study and explains the aims and objectives. The outline of the thesis is also introduced.

- Chapter 2 presents a literature review of the project. The concept of a critical state and different constitutive models within the CSSM framework are introduced. The size effect and hardening law are introduced. The DEM method, together with the software (PFC3D), are discussed. Bonding particle model (BPM) and population balance model (PBM), models of simulating particle crushing, are introduced. DEM applications to investigate the critical state behaviour of sands are also reviewed.
- Chapter 3 describes the logic and the simulation method in this study.
- Chapter 4 presents the results from the one-dimensional and isotropic normal compression. Normal compression lines and particle size distributions together with the local distributions of deviator stress are presented.
- Chapter 5 shows the results from the triaxial shear tests. The influence of stress path and preconsolidation pressure are compared. In addition, the critical state line is obtained. Macroscopic stress-strain behaviour during shearing is discussed and linked to micro mechanical observations.
- Chapter 6 shows data processing methods to obtain a yield surface. MATLAB data smoothing methods are applied to produce smooth stress-strain curves to choose yield points. Five methods of choosing yield points are compared and the yield surfaces according to different yield point choosing methods are presented. Given the established yield surface and the critical state line, the flow rule of the simulated sand is discussed briefly.
- Chapter 7 gives a conclusion of the thesis and presents the potential for future work.

Chapter 2 Literature Review

2.1 Introduction

This chapter first gives an introduction of the development of critical state soil mechanics (CSSM), followed by the basic theories of particle fracture. The third section introduces discrete element method (DEM) and the basic theory and calculation procedures of the commercial software PFC^{3D}. Finally, relevant DEM applications in the literature are critically reviewed.

The starting point is the definition of a critical state in soil mechanics, followed by the introduction of the basic ingredients of soil constitutive models. The 'Original' and Modified Cam-clay models are described. There follows an introduction of a more advanced unified state parameter model, the CASM model (Yu, 1998), which can interpret the behaviour of clay and sand using the same model. A further critical state model for sands is also reviewed.

Following the introduction of some basic constitutive models, the role that particle fracture plays in basic soil mechanics is introduced. A hardening law based on particle breakage is then presented. The role of tensile strength in particle fracture is explained, followed by the statistical distribution of tensile strengths. How the size effect on particle strength relates to the hardening of crushable soils will then be reviewed.

DEM applications relevant to this project will be examined, with particular emphasis on the two most popular breakage models: the population balance model (PBM) and the bonded particle ('agglomerate') model (BPM). The last section of this review examines historical DEM investigations on critical state behaviour of soil.

2.2 Critical state soil mechanics

2.2.1 Fundamental tests to investigate soil behaviour

Normal compression

Normal compression is probably the most fundamental and most simple while also being an effective method to investigate the stress-strain behaviour of soil. The oedometer test is used to investigate the stress-strain behaviour of clay or silt in one-dimensional vertical compression or swelling. Figure 2.1 shows the schematic of the oedometer apparatus. The disc shape specimen is held within the rigid metal ring between the upper porous stone, which applies compression, and bottom stone which supports the sample. The fixed metal cylinder ensures the radial strains are zero. The dimension of the sample is usually 75 mm diameter and 14-20 mm thick. Because of wall friction, the stresses on the top of the sample and the base of the sample are not the same; hence the aspect ratio of the oedometer sample is selected to reduce the effect of side friction. The test involves applying increments of vertical static load to the sample and recording the corresponding settlement. The vertical stress, σ_1, is applied and measured directly. The horizontal confining stress, σ_3, cannot be measured in an oedoemter; in order to do this a triaxial test is performed in which the horizontal stress required to maintain zero lateral strain, is measured. The mean effective stress, p', is then calculated, using

$$p' = (\sigma_1' + \sigma_2' + \sigma_3')/3 \qquad (2\text{-}1)$$

where $\sigma_2' = \sigma_3'$ in the triaxial apparatus.

The voids ratio, e, can also be measured. The one-dimensional (1-D) normal compression line (NCL), which is conventionally assumed to be linear in $e - \log p'$ space, can be drawn. Since the deviator stress, q,

$$q = \sigma_1' - \sigma_3' \tag{2-2}$$

is not zero in 1-D normal compression, the 1-D normal compression is effectively a shear test. In order to investigate the stress strain behaviour of soils without shearing, isotropic normal compression is usually conducted and the triaxial apparatus (introduced later) is used. During isotropic normal compression, stresses in three directions are kept equal, *i.e.* $\sigma_1' = \sigma_2' = \sigma_3'$. Under anisotropic compression, there are different combinations of isotropic stress, p' and deviatoric stress, q, that will cause yield and hence plastic deformation. The resulting compression line lies below the isotropic normal compression line in *e*-log *p'* space, which is also true for the one-dimensional normal compression line in $e - \log p'$ space also obeys this rule as is shown in Figure 2.2. The critical state line (CSL) which can be obtained from triaxial shear tests is also shown in the figure. Different triaxial shear tests and the method to obtain the CSL will be described shortly.

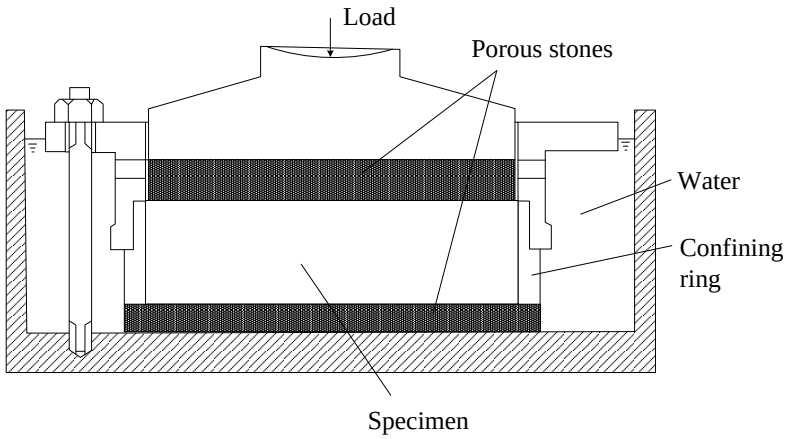

Figure 2.1 The Oedometer apparatus (Craig, 1997)

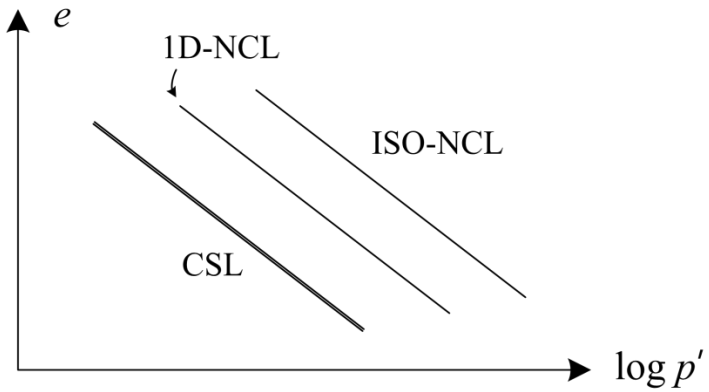

Figure 2.2 Schematic plot of 1-D and isotropic normal compression lines

Triaxial tests

The triaxial apparatus is the most common and widely used apparatus to conduct isotropic consolidation, unloading and shearing to critical states, when the stress does not change with the increasing strain. The conventional apparatus and test procedures were described in detail by Bishop and Henkel (1962). The basic features of the conventional triaxial tests are shown in Figure 2.3. The soil sample is a cylinder with height of about twice the diameter (to reduce end effects); the most commonly used diameters of the triaxial sample are 38 mm and 100 mm. The soil sample is enclosed in a thin rubber sleeve sealed to the top platen and to the base pedestal by rubber rings and contained in a water-filled cell with the water applied cell pressure σ_c. The applied stress on the soil sample in a triaxial apparatus is shown in Figure 2.4 (Atkinson, 2007). The stress of the sample is composed of the cell pressure, σ_c, and an extra stress applied through the top plate, calculated as the applied force, F_a, over the area of the top plate (the deviatoric stress).

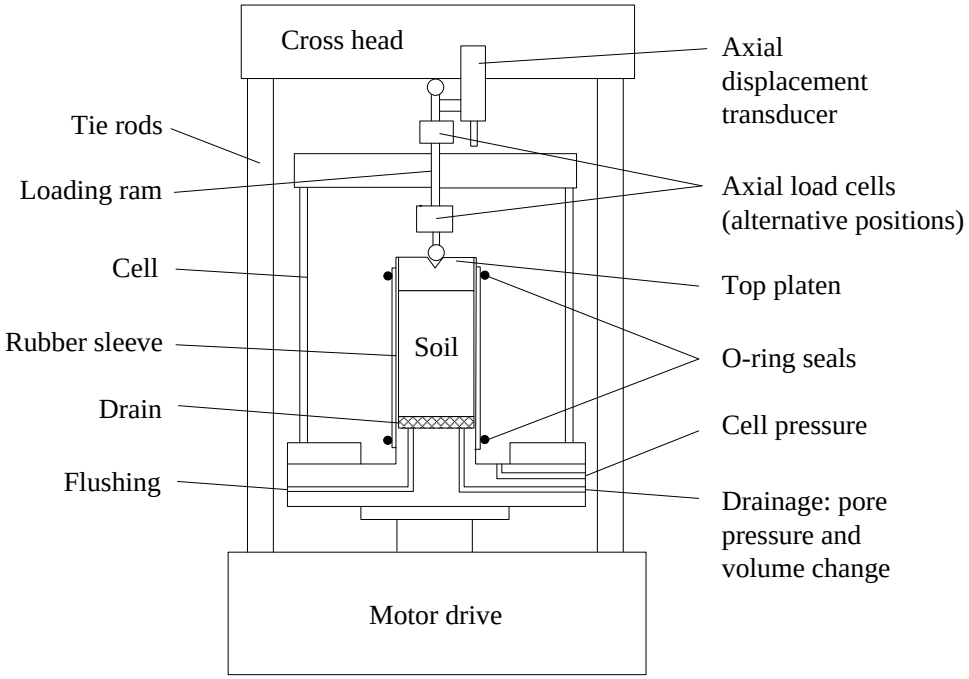

Figure 2.3 Conventional triaxial apparatus (following Atkinson, 2007)

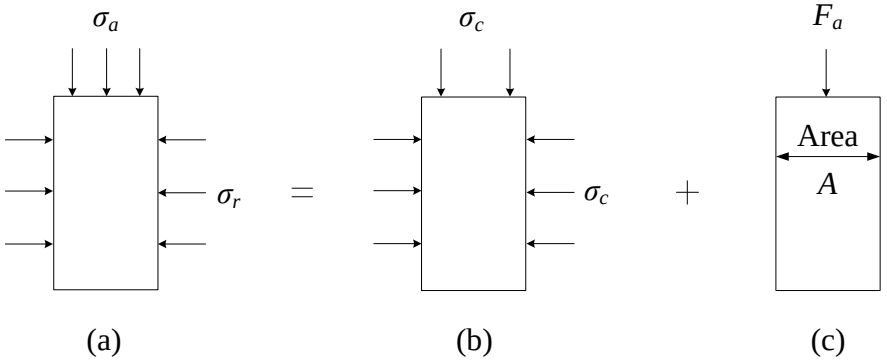

Figure 2.4 Stress on a triaxial sample (following Atkinson, 2007)

Soil samples can be sheared to failure and the critical state can be achieved during triaxial shear tests. Four kinds of triaxial tests have been widely applied: the consolidated drained (CD) test, during which the soil sample is consolidated and sheared in compression slowly to allow pore pressures built up by the shearing to dissipate; the consolidated undrained (CU) test, in which the soil sample is consolidated and sheared but not allowed to drain, while the sample is assumed to be fully saturated and the shear characteristics are measured under undrained conditions; the unconsolidated undrained (UU) test, during which the loads are applied quickly

and the sample is compressed under a constant strain rate while not allowed to consolidate; and a true triaxial test, which is conducted using different apparatus from the other three tests. In a true triaxial test the sample is loaded under a three-axis triaxial testing system and the stresses are controlled independently in three perpendicular directions.

After the triaxial shearing, a soil sample will reach a state, during which the deviator stress, q, and the mean effective stress, p', and the volume strain, ε_v, (or pore pressure u in an undrained test) won't change with the applied axial strain, ε_a. The state is then called a critical state which represents large shear deformations of the soil. The critical state line is a set of the critical states of a soil under different stress conditions and is conventionally assumed to be linear in $e - \log p'$ space and parallel with the normal compression lines, as is shown in Figure 2.2. The line also exists in the q-p' plane and usually has a constant slope representing a constant ultimate angle of shearing resistance.

2.2.2 The Concept of Critical States

Within the concepts of traditional continuum mechanics, many realistic soil models have been developed to analyse geotechnical problems. The classical plasticity theory of geomaterials is based on elastic-perfectly plastic models, which have been based on metal plasticity. The Tresca model (Tresca, 1864) and von Mises model (von Mises, 1913) are well known plasticity theories for metals and for fully saturated cohesive soils under undrained conditions. Due to the fact that yielding is mean effective pressure dependent for cohesive-frictional geomaterials, the Mohr-Coulomb model

(Coulomb, 1773) and Drucker-Prager model (Drucker and Prager, 1952) have been widely used for describing general behaviour of granular soils.

However, perfect plasticity with an assumption of constant strength during the loading/unloading process is not adequate for soil modelling, when considering the strong influence of plastic deformation and loading history on the strength of the soil. Given the strong influence, it is suggested herein that soil be treated as a work-hardening material which may reach the perfectly plastic state (Drucker *et al.*, 1957). Among the work-hardening models in soil mechanics, models based on the critical state concept developed at the University of Cambridge are most widely used, as described by Wroth (1973).

The concept of critical states has been adopted for the development of soil constitutive models since the 1950's, proposed independently by Parry (1956) and Roscoe *et al.* (1958). At a critical state, soil continually deforms to large deviator strain ε_q at constant effective stresses q and p' and constant volume or voids ratio e (or pore pressure in undrained tests). In critical state soil mechanics (CSSM) the critical state voids ratio, e, uniquely determines both the deviator stress, q, and the mean effective stress, p'; the critical state line ('CSL') is unique for a given soil regardless of stress paths (Schofield and Wroth, 1968), which is fully defined as:

$$q = Mp' \tag{2-3}$$

$$v = \Gamma - \lambda \ln p' \tag{2-4}$$

where

- q and p' are the shear and mean effective stresses;

- v is soil specific volume;
- M, λ and Γ represent basic soil-material properties

Figure 2.5 (b) shows that the $e - \ln p'$ space can be divided into two regions by the critical state line. The 'dry' side, also known as dense side, denotes the space below the CSL; the 'wet' side, also known as loose side, denotes the space above the CSL. These terms refer to states denser and loose, respectively, than critical at the same mean effective stress.

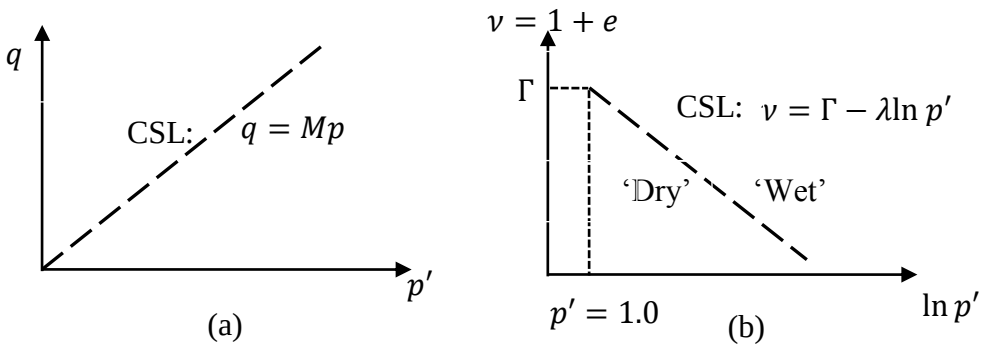

Figure 2.5 The concept of critical states: (a) in $q - p'$ space; (b) in $v - lnp'$ space

Due to the assumption of constant volume and effective stress at the critical state, both elastic and plastic volumetric strain increments are zero and the uniqueness of the critical state line contributes to formulating a strain hardening/softening plasticity model (Yu, 1998). Additionally, the concept of critical states was generally confirmed by experimental data for many types of soil and granular materials over the last fifty years, as pointed out by Yu (2006).

2.2.3 Basic ingredients of soil constitutive models

Despite the difference between constitutive models of soils, four major ingredients need to be discussed and defined in all the models: an elastic law that describes the behaviour before yielding and during unloading-reloading; a yield criterion that

defines the limits of the elastic deformations; a flow rule that defines the directions of the plastic strain increments; and a hardening rule that defines the magnitudes of the plastic deformations and the change in size of the yield surface.

In order to discuss the above ingredients, several basic concepts need to be clarified.

Work equation

The increment of total work done by a deformable material during a strain increment can be written as:

$$dW = \sigma d\varepsilon \tag{2-5}$$

where

- σ is the active stress;
- $d\varepsilon$ is the strain in the stress direction;
- dW is the work increment done by the active stress along its direction.

Soil is said to yield when it undergoes plastic deformation. The deformation behaviour of soil is divided into elastic and plastic regions by a yield surface in stress space. Deformations within the yield surface are elastic; deformations outside yield surface are plastic. The yield surface defines the limit of the elasticity of the soil. The total work can also be treated as the sum of elastic work done by elastic strain and plastic work done by the irrecoverable plastic strain, as shown below:

$$dW = \sigma(d\varepsilon^e + d\varepsilon^p) = \sigma d\varepsilon^e + \sigma d\varepsilon^p = dW^e + dW^p \tag{2-6}$$

where

- $d\varepsilon^e$ is the elastic strain increment;
- $d\varepsilon^p$ is the plastic strain increment;
- dW^e is the elastic work increment;
- dW^p is the plastic work increment.

Hardening behaviour

Soils exhibit hardening behaviour beyond yield. During loading, when soil starts to yield, it undergoes plastic deformation. The yield surface of the soil will expand in size if the yielding is stable, from the initial surface to subsequent larger surfaces. This means that the stress path will always be on the new, expanded yield surface with associated plastic deformation. Therefore, the soil hardens during successive and continuous states of stable yielding.

Yield surface

Loading from one plastic state will lead to another adjacent plastic state. However, for a certain plastic state, the work done along the single yield surface should be zero. The plastic work done by the mean effective stress (Eq. 2-1) and the deviator stress (Eq. 2-2) increments should be zero along the yield surface. So that

$$\delta W^P = \delta q \cdot \delta \varepsilon_q^P + \delta p' \cdot \delta \varepsilon_v^P = 0 \tag{2-7}$$

where

- δq is the deviatoric stress increment;
- $\delta \varepsilon_q^P$ is the plastic shear strain increment;
- $\delta p'$ is the mean effective stress increment;

- $\delta\varepsilon_v^P$ is the plastic volumetric strain increment.

Eq. 2-7 is essentially the Normality Rule, which is now described.

Flow rule

As was described by Wood (1990), the plastic potential surface, Q, in the $q - p'$ stress space gives the direction of plastic strain increment, $d\varepsilon^p$. The direction of $d\varepsilon^p$ is orthogonal to the plastic potential, by definition – see Figure 2.6. The associative flow rule is followed when the shape of the plastic potential surface Q is the same as the shape of the yield surface f. The non-associative flow rule is followed when $Q \neq f$. For soils, the yield surface f and the plastic potential surface Q are often different and the plastic strain increment is not always normal to the yield surface. However, for simplicity of application, many soil models still use the associative flow rule to define the directions of the plastic strain increments.

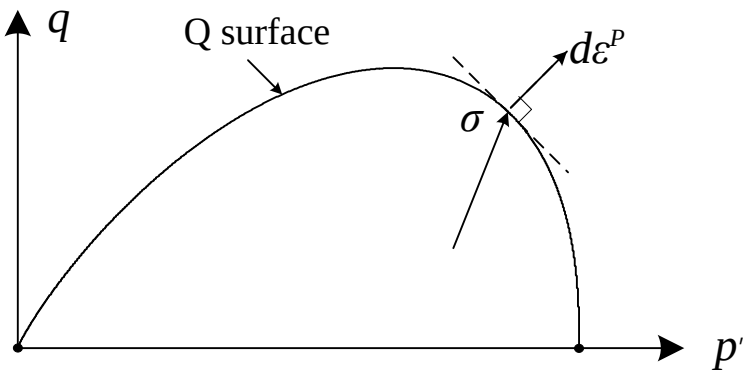

Figure 2.6 Schematic plot of plastic potential surface and plastic strain increment (following Wood, 1990)

2.2.4 Cam-Clay and Modified Cam-Clay

Original Cam-clay model

The Original Cam-clay model (OCC), developed by Roscoe and Schofield (1963) and Schofield and Wroth (1968), is one of the earliest and the most commonly used elastic-

plastic critical state models that gives a good description of soil behaviour. Two basic assumptions for the Original Cam-clay model are listed as below:

(1) the elastic deviatoric strain increment is ignored ($d\varepsilon_q^e = 0$);

(2) the associative flow rule is followed ($Q = f$).

The work done can be written as the sum of elastic and plastic work.

$$dW = d\mathrm{W}^{\mathrm{e}} + d\mathrm{W}^{\mathrm{p}} = pd\varepsilon_{\mathrm{v}}^{\mathrm{e}} + qd\varepsilon_{\mathrm{q}}^{\mathrm{e}} + pd\varepsilon_{\mathrm{v}}^{\mathrm{p}} + qd\varepsilon_{\mathrm{q}}^{\mathrm{p}} \tag{2-8}$$

where

- ε_v^e is the elastic volume strain;
- ε_v^p is the plastic volume strain;
- ε_q^e is the elastic deviator strain;
- ε_q^p is the plastic deviator strain.

in which, the plastic part can be rewritten as a dissipation function :

$$dW^p = p'd\varepsilon_{\mathrm{v}}^{\mathrm{p}} + qd\varepsilon_{\mathrm{q}}^{\mathrm{p}} = Mp'd\varepsilon_q^p \tag{2-9}$$

which can be rewritten as

$$\frac{d\varepsilon_v^p}{d\varepsilon_q^p} = M - \frac{q}{p'} \tag{2-10}$$

Considering the associated flow rule,

$$\frac{d\varepsilon_v^p}{d\varepsilon_q^p} = -\frac{dq}{dp'} \tag{2-11}$$

where the stress ratio q/p' is usually replaced with η. At a critical state, soil deforms with constant volume and effective stresses, such that, $d\varepsilon_v^p = dq = 0$ and $M = q/p'$ at critical state. Eq. 2-11 can also be written in the form

$$\mathrm{d}\eta + M\frac{\mathrm{d}p'}{p'} = 0 \tag{2-12}$$

By integrating the above equation:

$$\eta + M\ln p' + c = 0 \tag{2-13}$$

where c is a constant. So that the yield function of the OCC model is given as:

$$f = \frac{q}{p'M} + \ln\frac{p'}{{p_0}'} = 0 \tag{2-14}$$

where

- M is a material constant;
- p' and q are the stress components;
- ${p_0}'$ is the value at the non-zero intersection of the yield locus with the p' axis at $q = 0$.

Figure 2.7 (a) presents the yield surface of the OCC model. The quantity, p_0, which is known as the pre-consolidation pressure, has a unique value at any yield locus and defines the size of the yield locus. The mean effective stress at the intersection point of the CSL and the yield surface is ${p_c}'$. A fan shape with a vertex point of yield locus at $p' = {p_0}'$ can be observed. This is because the yield locus also exists in triaxial extension, while the slope of the yield locus for consolidation and extension are

different at $p' = {p_0}'$, and this provides the vertex. This means that the slope of the yield locus of the OCC model is not defined at $p' = {p_0}'$.

Figure 2.7 (b) shows the isotropic normal compression line and the critical state line. The value of ${p_0}'$ is the mean effective stress that corresponds to the intersection of the normal compression line and the rebounding line, *i.e.* the unload-reload line. The value of ${p_c}'$ is the mean effective stress that corresponds to the intersection of the unloading line and the CSL. The slope of the normal compression line is λ and the slope of the elastic rebounding line is κ. The total change in the voids ratio, Δe, during normal compression can be divided into two parts: the elastic part, Δe^e, which can be recovered during unloading, and the plastic part, Δe^p, which is non-recoverable.

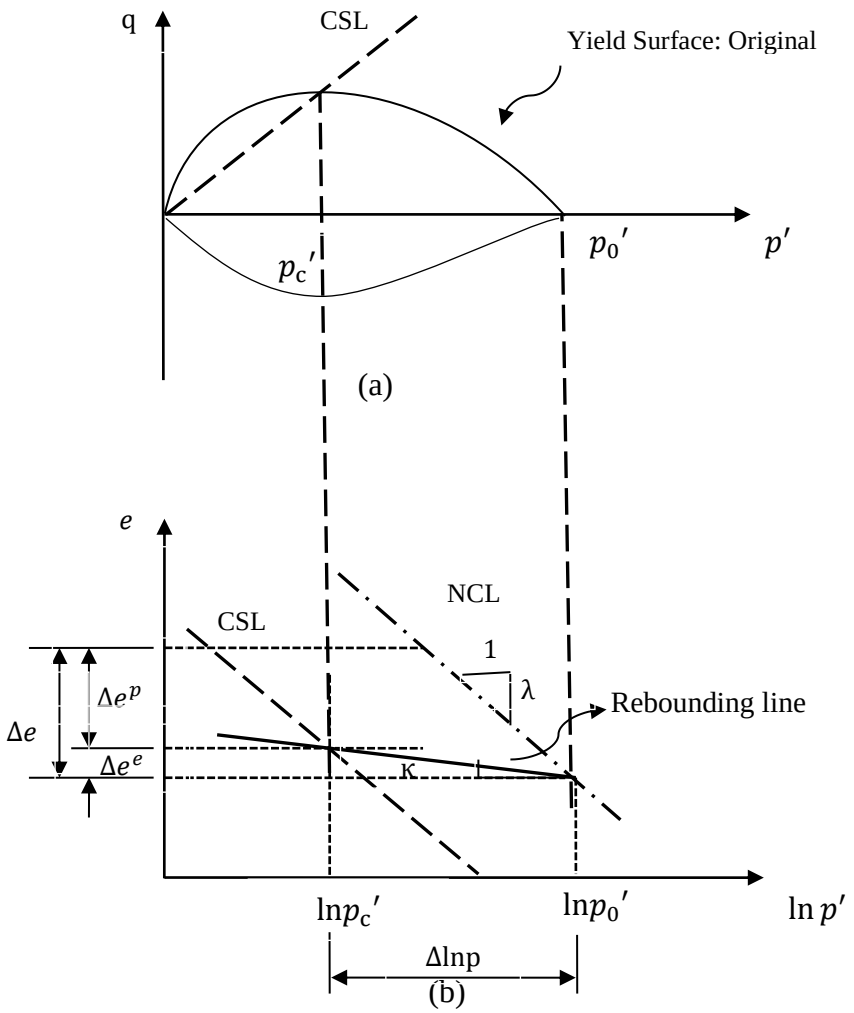

Figure 2.7 Yield locus and stress-strain lines in e-ln p' scale of the Original Cam-clay model (following Schofield and Wroth, 1968)

Figure 2.8 (a) gives the combined normal compression line, critical state line and yield surface of the OCC model in 3D. Figure 2.8 (b) gives the projection of elements in (a) on to $q - p'$ space. Figure 2.8 (c) gives the projection on to $e - p'$ space. It can be seen from the figure that the CSL is the line going through the highest points of the yield loci in this three-dimensional space; the unloading-reloading line is the projection of yield locus on to the $e - p'$ plane; the yield locus enlarges as the pre-consolidation pressure, p_0, increases to higher values.

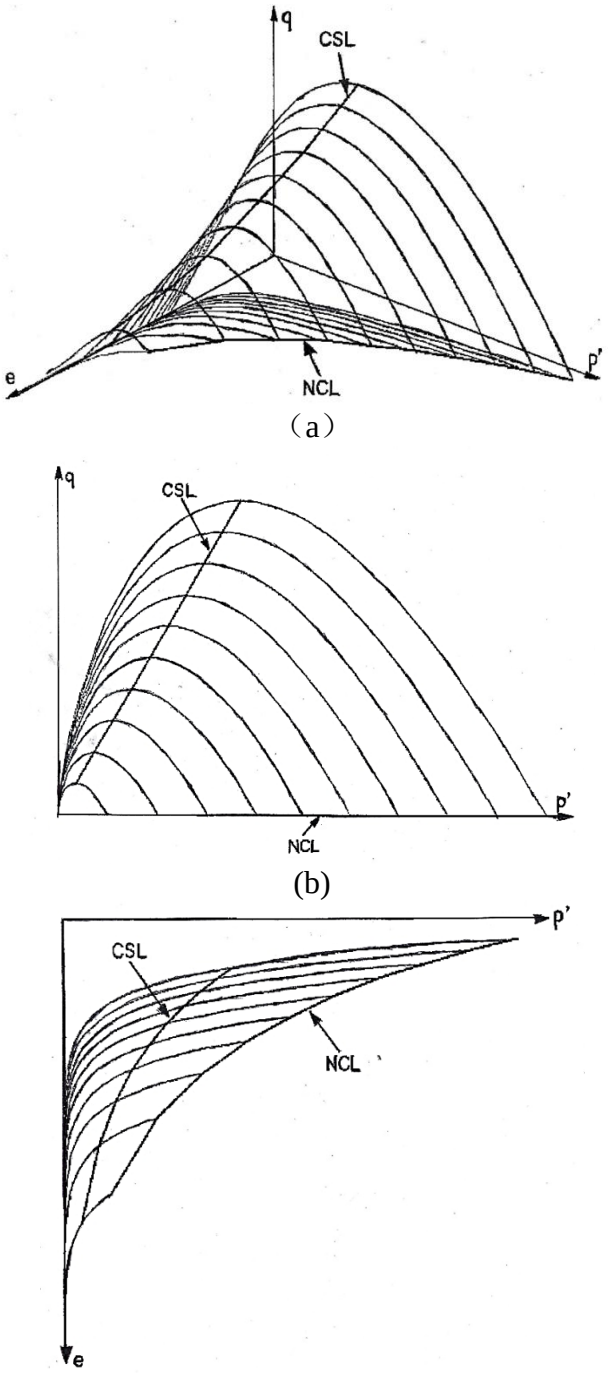

Figure 2.8 $p-q-e$ plots of the Original Cam-Clay Model

(following Schofield and Wroth, 1968)

Figure 2.9 shows the Original Cam-clay theoretical stress-strain behaviour of soil during a conventional drained triaxial test on a dense soil. The loading starts from the initial point D and the yield point E is reached without any elastic deviatoric strain.

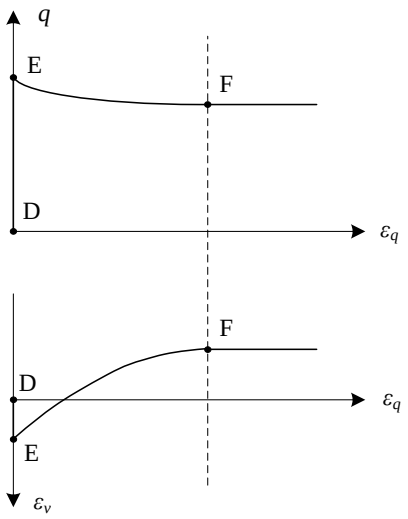

Figure 2.9 Cam-clay stress-strain response of heavily-overconsolidated soils during conventional drained triaxial shear (following Schofield and Wroth, 1968)

Modified Cam-clay model

As has already been described, the Original Cam-clay model has some shortcomings:

- Discontinuity of the yield locus: the slope of the yield loci at (p_0', q) has two values, as is shown in Figure 2.7 (a). This means that even for an associative flow rule, the strain increment vector is undefined.

- Assuming the elastic deviatoric strain to be zero: the basic assumption is unreal when $G \to \infty$ and Poisson ratio $\upsilon \to -1$.

- The OCC model is limited to triaxial loading conditions.

The Modified Cam-clay (MCC) model, developed by Roscoe and Burland (1968), modifies the yield function of the Original Cam-clay model, takes the elastic deviatoric

strain into consideration and application of the model is extended to the general stress strain space.

The plastic part of the work equation for the MCC model is:

$$dW^{\mathrm{p}} = p'd\varepsilon_{\mathrm{v}}^{\mathrm{p}} + qd\varepsilon_{\mathrm{q}}^{\mathrm{p}} = \mathrm{p}'\sqrt{(d\varepsilon_{\mathrm{v}}^{\mathrm{p}})^2 + (\mathrm{M}d\varepsilon_{\mathrm{q}}^{\mathrm{p}})^2} \tag{2-15}$$

This is re-written as a stress-dilatancy rule and considering the associated flow rule gives:

$$\frac{d\varepsilon_{\mathrm{v}}^{\mathrm{p}}}{d\varepsilon_{\mathrm{q}}^{\mathrm{p}}} = \frac{M^2 - \eta^2}{2\eta} = -\frac{dq}{dp'} \tag{2-16}$$

so that:

$$\frac{M^2 - \eta^2}{2\eta} = -\eta - p'\frac{d\eta}{dp'} \tag{2-17}$$

Hence the yield function can be derived by integrating Eq. 2-17

$$f = M^2p'^2 - M^2{p_0}'p' + q^2 = 0 \tag{2-18}$$

It can be seen from Figure 2.10 that the yield locus of the MCC model is an ellipse, which guarantees the consistency (single tangential line slope) of the yield surface at $p' = {p_0}'$. The yield function of the MCC getting rid of the vertex solves a numerical problem when applying finite element method. Figure 2.11 shows the modified stress-strain behaviour of heavily over-consolidated Cam-clay soils under drained triaxial shear. Comparing with the response shown in Figure 2.9, the MCC model gives a more realistic prediction of soil behaviour, since the elastic deviatoric strain is also

considered. In addition, OCC overestimates peak strength considerably, compared to MCC.

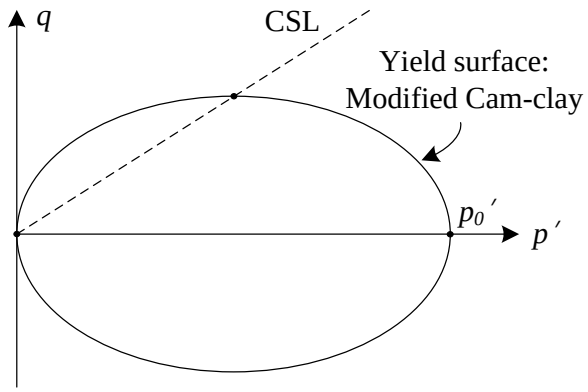

Figure 2.10 Yield locus of modified Cam-clay model (following Roscoe and Burland, 1968)

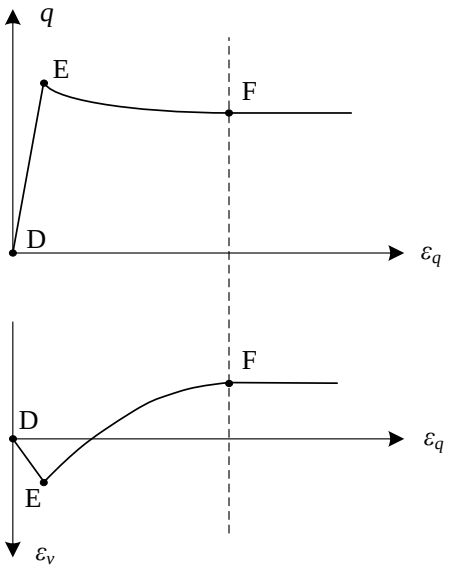

Figure 2.11 Modified Cam-clay stress-strain response of heavily over-consolidated soils during conventional drained triaxial shear (following Roscoe and Burland, 1968)

As the most widely used critical state models, the Original and modified Cam-clay models have been proven to have the ability to predict the behaviour of normally and lightly over-consolidated clay, which means $p_0'/p' < p_0'/p_c'$ for a soil with over-

consolidation history. However, it should also be noted that these two models are developed based on assumptions of isotropy, time-independence, the normality condition (also known as associated flow rule) and volumetric hardening. Comparing with experimental data, it was found that the models are poor at predicting the response of heavily overconsolidated clay and granular materials (e.g. sand), which is due to the shape of the yield surface adopted and the principle of normality (Wood, 1990).

2.2.5 Unified State Parameter Model

Been and Jefferies (1985) proposed a state parameter ξ to define the difference of specific volume between the current and critical states at the same mean effective stress (Figure 2.12):

$$\xi = v + \lambda \ln p' - \Gamma \tag{2-19}$$

The state parameter has shown its ability to describe the behaviour of granular material over a wide range of stresses and densities (Been and Jefferies, 1985; Sladen *et al.*, 1985; Sladen and Oswell, 1989). The state parameter was also successfully applied to determine the soil responses for both clay and sand (Yu, 1998).

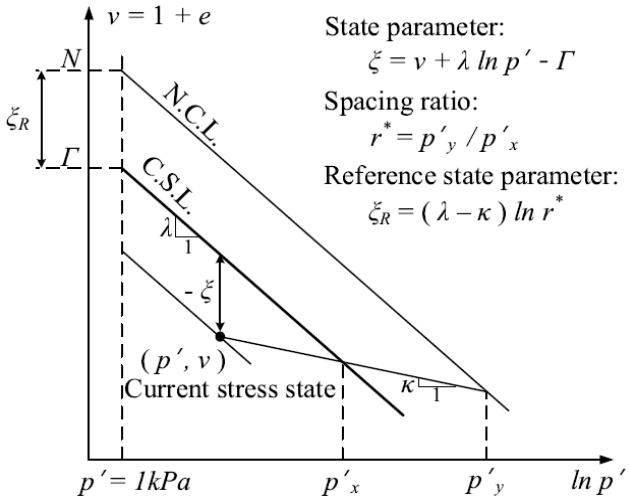

Figure 2.12 Schematic of state parameter and spacing ratio (Yu, 1998)

A unified state parameter model for clay and sand, which is referred to as 'Clay and Sand Model' (CASM), was proposed by Yu (1998), taking the state parameter described above into consideration. CASM is a simple constitutive model with two additional material constants introduced to the standard Cam-clay model, such that the overall behaviour of clay and sand can be satisfactorily modelled under both drained and undrained loading conditions.

The equation of the state boundary surface (yield surface) of CASM can be written with p_0', p' and the spacing ratio, r^*, which relates to the horizontal distance between the NCL and the intersection of the unloading line and the CSL (see Figure 2.12)

$$\eta = M \times \left[ln\left(\frac{p_0'}{p}\right) / \ln r^* \right]^{1/n} \tag{2-20}$$

where n is the 'stress-state coefficient', which is a new material constant that defines the shape of the yield surface. The value of n usually ranges between 1.0 ~ 5.0.

The plastic potential in CASM is defined on the basis of Rowe's stress-dilatancy relation (Rowe, 1962), as expressed by:

$$\frac{\delta\varepsilon_p^p}{\delta\varepsilon_q^p} = \frac{9\ (M-\eta)}{9+3\ M-2\ M\eta} \tag{2-21}$$

which has been widely accepted with great success in describing the deformation of granular material. The plastic potential can then be obtained by the integration of the stress-dilatancy relation, and the plastic flow rule is shown to be non-associated.

The original Cam-clay yield surface is a special case of the CASM yield locus, and the modified Cam clay yield surface can also be approximated by CASM (Yu, 1998). Comparing with experimental data, CASM showed its ability to capture the overall behaviour of clay and sand observed under both drained and undrained loading conditions, and thus represents a very useful extension of Cam clay. The proposed CASM yield surface is later proved to be the same as the yield locus for sand proposed by McDowell (2002).

2.2.6 Critical State Model for Sands

McDowell and Bolton (1998) proposed a clastic hardening law, which will be described in detail in Section 2.3, such that the fractal crushing (described later), of particles gives rise to the normal compression line and the hardening of the yield surface for sands.

A work equation was proposed by McDowell and Bolton (1998) to describe the energy of aggregates dissipated

$$q\delta\varepsilon_q^p + p'\delta\varepsilon_v^p = M\,p'\,\delta\varepsilon_q^p + \frac{EdS}{V_s(1+e)} \tag{2-22}$$

where

- S is the total surface area of particles,
- V_s is the volume of solids,
- E is the surface energy

For one-dimensional compression, Eq. 2-22 can be rewritten as:

$$\sigma_v{}' \frac{\mathrm{d}e}{1+e} = -\frac{E\mathrm{d}S}{(1-\mu)V_s(1+e)} \tag{2-23}$$

where

- $\sigma_v{}'$ is the applied macroscopic vertical stress,
- μ is a friction coefficient that represents the proportion of plastic work dissipated in friction.

McDowell (2000) proposed a new family of yield loci of sands by mathematically rewriting the work equations proposed by McDowell and Bolton (1998). McDowell (2000) assumed the proportion of energy dissipated in fracture and friction is a function of stress ratio, $F(\eta)$, then Eq. 2-22 can be written as:

$$\frac{EdS}{V_s(1+e)} = M\ p'\ \delta\varepsilon_q^p[F(\eta)] \tag{2-24}$$

So that, by interpreting the energy dissipated in fracture with the energy dissipated in friction, Eq. 2-24 can be rewritten as a stress-dilatancy rule form:

$$\eta + \frac{d\varepsilon_v}{d\varepsilon_q} = M[1+F(\eta)] \tag{2-25}$$

McDowell (2000) proposed a simple function of $F(\eta)$, containing an artificial parameter a, as shown in Eq. 2-26, which suits the two limit cases: for isotropic case, $\eta = 0,\ \mathrm{d}\varepsilon_q = 0,\ \mathrm{F}(0) = \infty$; for critical state case, $\eta = M,\ \mathrm{d}\varepsilon_v = 0,\ \mathrm{F}(M) = 0$.

$$F(\eta) = \frac{M^a - \eta^a}{\eta^a} \tag{2-26}$$

Hence, the stress dilatancy rule is given as:

$$\frac{d\varepsilon_v}{d\varepsilon_q} = \frac{M^{a+1} - \eta^{a+1}}{\eta^a} \tag{2-27}$$

and the whole family of yield loci can be derived by substituting Eq. 2-26 into Eq. 2-25:

$$\eta = M\,[(a+1)\,ln\,p_0'/p']^{\frac{1}{a+1}} \tag{2-28}$$

As is shown in **(a)**

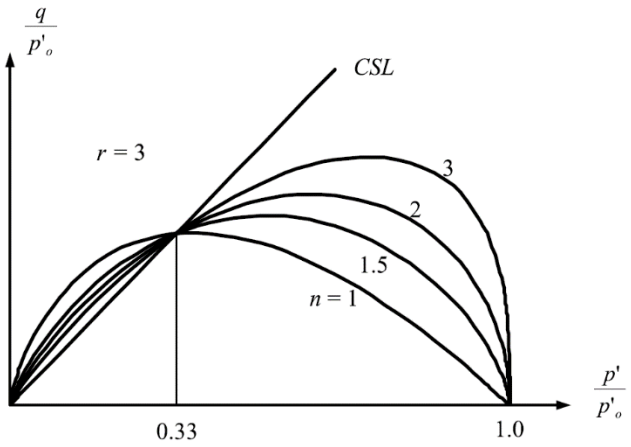

(b)

Figure 2.13, the proposed family of yield surfaces by McDowell (2000) is the same as the yield surfaces for the CASM model by Yu (1998). The shape of the yield surface changes with different values of *a*. When choosing the coefficient a to be 1, the theoretical yield surface coincides well with the experimental results by Murata *et al.* (1987).

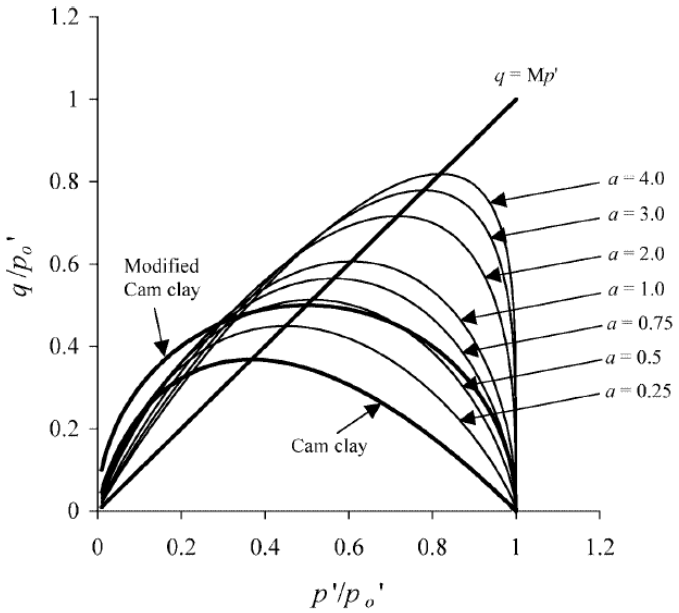

(a)

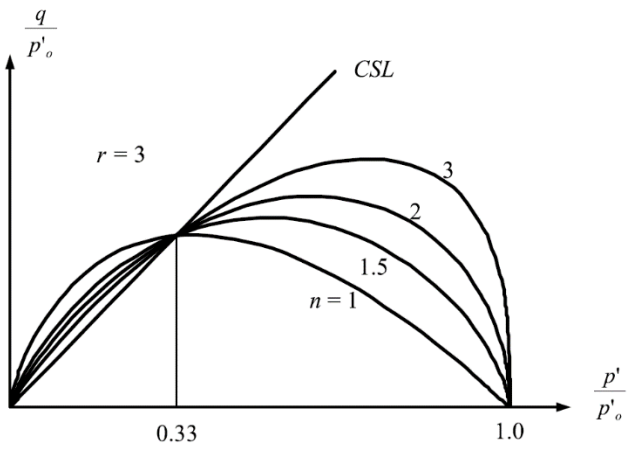

(b)

Figure 2.13 Family of yield loci: (a) for various values of *a* (*N*=*M*) (McDowell, 2002); (b) for various values of *r* and *n* (Yu, 1998)

McDowell (2002) further proposed the critical state model for sands following the non-associative flow rule. The yield surface equation was then given as

$$\eta = N\left[(a+1)\,ln\frac{p_0}{p}\right]^{\frac{1}{a+1}} \tag{2-29}$$

where N is stress ratio corresponding to the peak value of q on the yield locus (replacing the critical state dissipation constant, M). By adopting a non-associated flow rule, the equation for the plastic potential surface was given as:

$$\eta = M\left[(b+1)\,ln\frac{p'_p}{p'}\right]^{\frac{1}{b+1}} \tag{2-30}$$

where p'_p is the value of p' at $q = 0$ for the plastic potential through the current point on the yield surface. The simple non-associated flow rule makes it possible to model the undrained behaviour of sand on the dry and wet side of critical. More realistic behaviour can be obtained by incorporating kinematic hardening or bounding surface plasticity inside the state boundary surface.

2.3 Particle fracture in soil mechanics

2.3.1 The role of particle fracture in CSSM

Particle crushing or fragmentation, which alters the particle size distribution, has long been regarded as an important micro-mechanism that governs the stress-strain behaviour of granular materials. Particle crushing is widely observed in fundamental testing of soils. The crushing of a particle is influenced by several factors, such as stress state, particle shape, particle size, internal flaw size distribution and contacts with surrounding particles. Much research has been carried out to investigate the role of particle crushing during both isotropic compression and shearing of soils.

Hagerty *et al.* (1993) examined the influence of particle crushing in one-dimensional compression tests. The yielding in one-dimensional compression was found to coincide with the onset of crushing. The location of the yield stress was found to be affected by the angularity of particles, in that large particles, being more susceptible to crushing, showed a lower yield stress.

The influence of particle crushing on the yield stress in normal compression was also studied by Nakata *et al.* (2001a). They reported that the initial particle size distribution was observed to influence the curvature of the yield region of the one-dimensional (1-D) normal compression line (NCL) in $e - \log \sigma_v'$ space: distinct yielding was observed for uniformly graded sand; more gradually evolved yielding was observed for well-graded sand. They also found that large particles tend to undergo surface grinding while small particles tend to undergo major splitting. The phenomenon could be explained by McDowell *et al.*'s (1996) theory that particles with more contacts with

surrounding particles, *i.e.* particles with high coordination numbers (number of contacts), have higher survival probability compared with particles with fewer contact numbers, since the induced tensile stress in a particle diminishes as a result of the compressive stress generated due to an increased interaction between constituent particles. Later work by Nakata *et al.* (2001b) revealed that the yield stress increased with reducing median particle size, due to the size effect on the average strength of single particles, which was proposed by Lee (1992) and explained by McDowell (1998), that small particles tend to contain fewer and smaller internal flaws than large particles and hence exhibit a higher tensile strength in general when compared with larger particles.

High stress drained triaxial tests were also carried out (Yamamuro and Lade, 1996) to investigate the role of particle crushing. To quantify the amount of particle breakage, Hardin's (1985) relative breakage parameter, B_r, was taken as a measurement, which reflected the change of PSD curve before and after shearing. Einav (2007) further proposed a modified definition of Hardin's breakage index, B_r, see Figure 2.14. He showed that Br increases with increasing mean effective stress at failure. The increase of failure mean effective stress was also observed to be associated with the increase of the volumetric strain and axial strain. The observation could be explained that high effective stress, which leads to a stress state that exceeds the strength of a particle, tends to cause more crushing than low effective stress. Hardin (1985) proposed that the sharp rise in strains is caused by a marked increase in particle crushing.

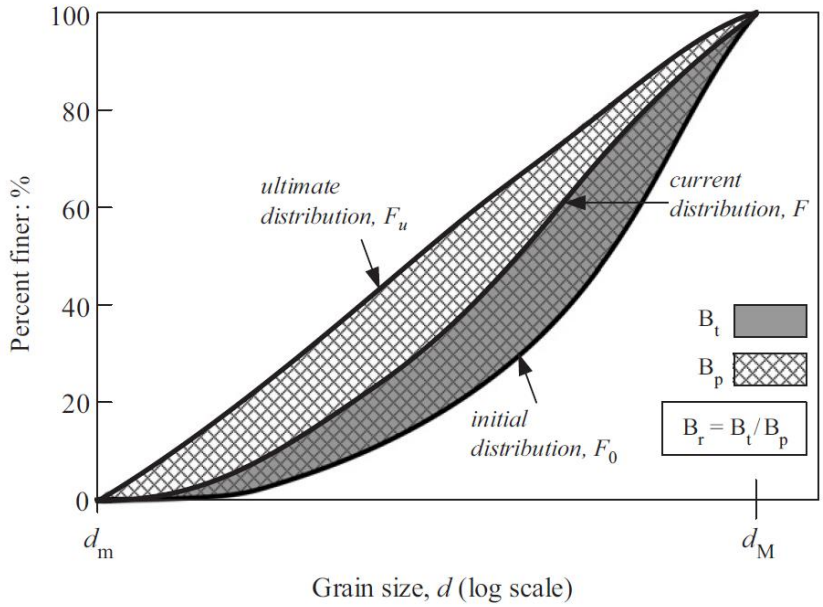

Figure 2.14 Modified definition of Hardin's breakage index B_r(Einav, 2007)

Due to the importance and common occurrence of particle crushing, much research has been carried out in order to investigate the crushability of granular materials. A review of this research will be given in this section from three aspects:

- How does single particle crushing occur?
- What is the distribution of the strengths and how is it measured?
- Why does the crushing of particles give rise to the normal compression line?

2.3.2 Tensile strength of a particle

The failure of a spherical particle under diametral compression is widely accepted as a tensile failure (McDowell and Bolton, 1998). Jaeger (1967) first proposed that the tensile strength of grains could be measured following the Brazilian test method, by diametrically compressing individual grains between flat platens. The tensile strength of the particles was given by:

$$\sigma_f = F_f / d^2 \qquad (2\text{-}31)$$

where

- σ_f is the tensile stress at failure;
- F_f is the diametral fracture force applied;
- d is the diameter of the grain at failure.

Lee (1992) investigated a series of different sand particles for a range of particle sizes using the same method described above. As is shown in Figure 2.15 the sand particles were diametrically compressed between flat platens. Lee (1992) also gave an intuitive insight into the development of the crushing by plotting force against deformation as shown in Figure 2.16.

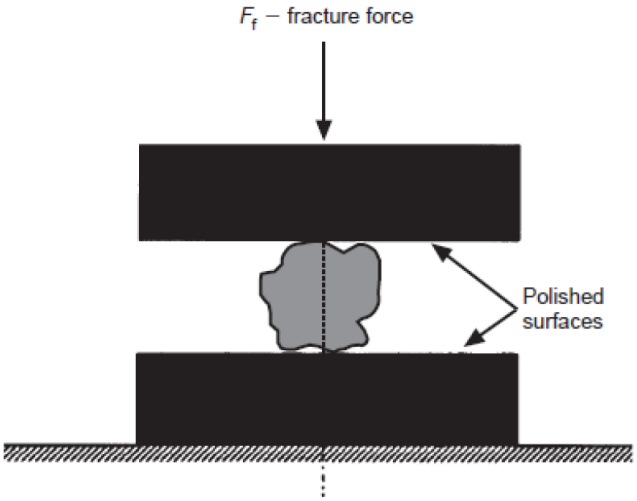

Figure 2.15 Particle tensile strength test set-up (Lee, 1992)

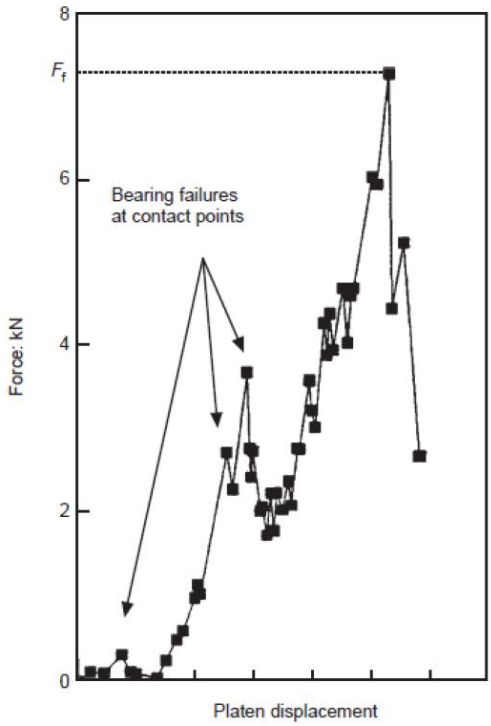

Figure 2.16 Typical plot of force against deformation for a typical particle (Lee, 1992)

The initial peaks, as can be observed in the plot, imply the bearing failures at contact points corresponding to breakage of asperities and rounding of the particles. The maximum peak is taken to correspond to the major fracture of the particle along the loading axis. The tensile strengths of different particles were then calculated according to Eq. 2-30 and Eq. 2-31, taking the maximum peak load as F_f. Figure 2.17 shows the calculated tensile strength against the average particle size.

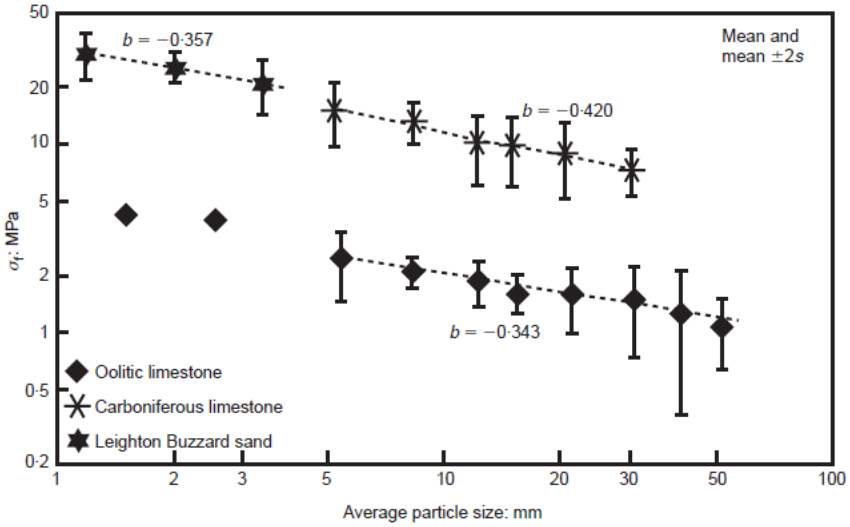

Figure 2.17 Results of mean tensile strength for single particle crushing tests (Lee, 1992)

It was found that strength was a function of size according to:

$$\sigma_f \propto d^b \tag{2-32}$$

where b defines the rate at which average strength increases with decreasing size.

2.3.3 The distribution of single particle tensile strength

Weibull (1951) statistics have been widely applied to analyse the breakage of brittle materials. The simplicity of Weibull statistics lies in its conformance to a 'weakest link' model for which the failure of one element in a larger block of interconnected identical elements results in the failure of the entire block.

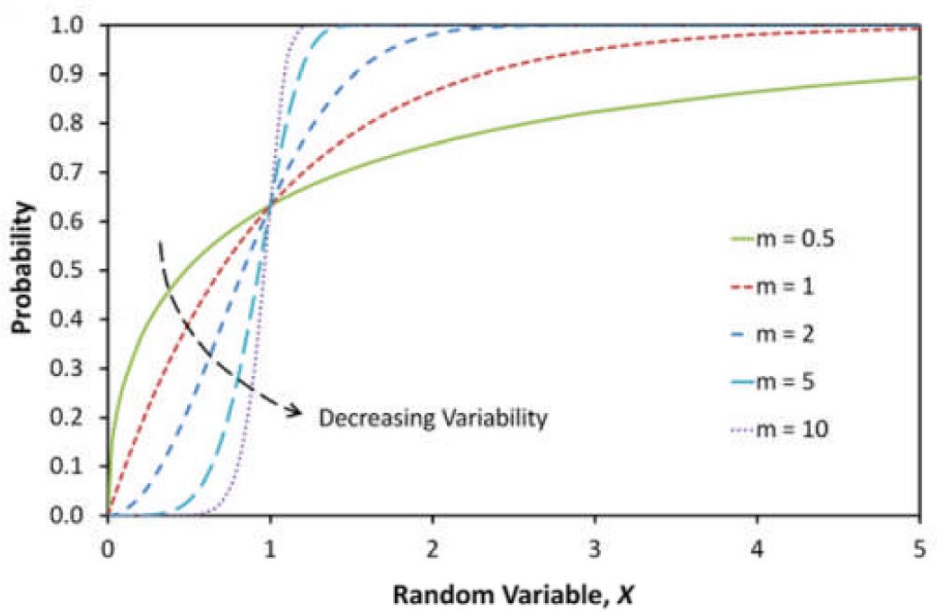

Figure 2.18 Cumulative distribution functions for various Weibull distributions, with a characteristic value $X_0 = 1$, showing the influence of the Weibull modulus (de Bono, 2013)

The Weibull distribution is usually governed by two parameters: the Weibull modulus, m, which defines the shape of the probability distribution; and a characteristic value of the distribution such that 37% of random variables are greater, which defines the scale. McDowell and Bolton (1998) first related the size effect (Lee, 1992) to the Weibull statistics and showed the effect of increasing the Weibull modulus for a random variable X in cumulative distributions with constant scale, discussed by de Bono *et al.* (2013) and shown in Figure 2.18.

McDowell and Amon (2000) further widened the application of Weibull statistics to the fracture of soil grains. As is stated by Weibull (1951), for a volume V, under an applied tensile stress σ, the survival probability $P_s(V)$ of the block is given by:

$$P_s(V) = exp[-\frac{V}{V_0}(\frac{\sigma}{\sigma_0})^m] \tag{2-33}$$

where V_0 is a reference volume of material such that

$$P_s(V_0) = \exp[-\left(\frac{\sigma}{\sigma_0}\right)^m] \tag{2-34}$$

where

- σ_0 is the value of stress to cause the crushing of 63% of the volume of V_0 solids
- m is the Weibull modulus that decreases with increasing variability in strength

Hence it can be derived from Eq. 2-34 that:

$$P_s(d) = \exp[-(\frac{d}{d_0})^3(\frac{\sigma}{\sigma_0})^m] \tag{2-35}$$

According to Eq. 2-33, for a particle with volume V_1 under tension, when the particles are geometrically similar, the 37% survival strength σ_1 could be derived as:

$$\sigma_1 = \sigma_0 \left(\frac{V_0}{V_1}\right)^{1/m} \tag{2-36}$$

Eq. 2-35 and Eq. 2-36 show that the 37% survival strength of a particle is a function of particle size. It could be derived from Eq. 2-36 that

$$\sigma_0 \propto d^{-3/m} \Leftrightarrow d \propto (\sigma_0)^{-m/3} \tag{2-37}$$

which is equivalent to Eq. 2-32, when $P_s(d)$ is limited to a certain value of 37%, and σ_0 is the value of F/d^2 at which 37% of the tested particles of size $d_0$survive, m is the Weibull modulus. Eq. 2-35 could also be rewritten in logarithmic form:

$$\ln\left[\ln\left(\frac{1}{P_s(d)}\right)\right] = m \ln\left(\frac{\sigma}{\sigma_0}\right) \tag{2-38}$$

The Weibull modulus m could then be determined from the slope of the line when $\ln\left[\ln\left(\frac{1}{P_s(d)}\right)\right]$ is plotted against $\ln\left(\frac{\sigma}{\sigma_0}\right)$.

Single particle crushing tests carried out by McDowell and Amon (2000) showed a successful application of Weibull statistics. Geometrically similar grains were categorized by size. Grain particles were directly compressed between two flat platens, following Lee (1992). As was found by Lee (1992), McDowell and Amon (2000) also

noticed fracture of small asperities before final particle splitting. However, for the majority of cases they studied, failure was found to correspond with catastrophic splitting of the grain and peak force. Thus, they defined particle failure as the catastrophic splitting of the grain, and failure force as the maximum force recorded before the particle diameter became less than half of its original diameter.

Particle strengths for the tested samples were then calculated, according to Eq. 2-31. The Weibull modulus was determined according to Eq. 2-38. The particle strength from laboratory tests was then compared with the predicted strength assuming the tensile strength follows a Weibull distribution. Figure 2.19 showed that the tensile strength could be characterised by the 37% strength, σ_0.

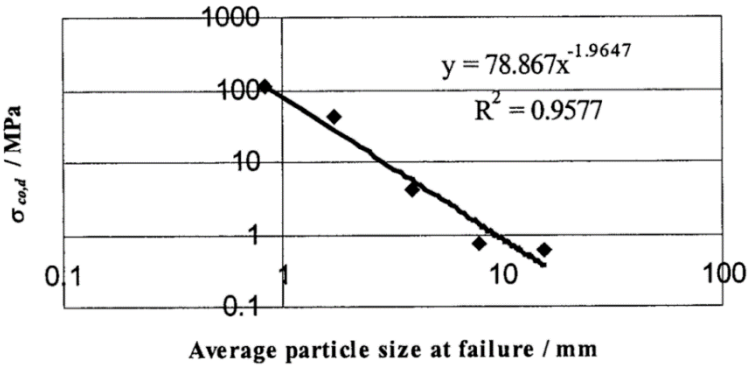

Figure 2.19 37% strength σ_0 as a function of particle size (McDowell and Amon, 2000)

2.3.4 Hardening law

The emergence of fractal size distributions resulting from fragmentation was studied by Turcotte (1986). The fractal size distribution is a power law limited by the largest and smallest particle sizes. For a certain fractal distribution, the number N of particles could be expressed by a characteristic linear dimension, r, following Eq. 2-39:

$$N \propto r^{-D} \tag{2-39}$$

where D is the fractal dimension.

For the number of particles, N, of size L, larger than d, Eq. 2-39 could be rewritten as:

$$N(L > d) \propto d^{-D} \tag{2-40}$$

Hence, the size distribution would be linear when plotted with two logarithmic axes, and the fractal dimension D would be the slope of the plot.

As has been pointed out by many researchers, brittle materials tend to evolve towards a final fractal dimension between 2 and 3, typically 2.5, under pure crushing (Turcotte, 1986; Sammis *et al*., 1987; Palmer and Sanderson, 1991; Steacy and Sammis, 1991; McDowell and Daniel, 2001). Figure 2.20 (Turcotte, 1986) gave the particle size distributions for different brittle materials and shows that the fractal dimensions of different materials share the consistent value of 2.5.

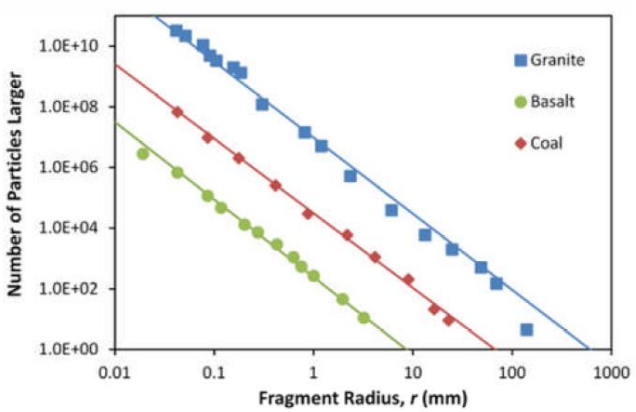

Figure 2.20 Particle size distributions for various crushed materials, showing consistent fractal dimensions of 2.5 (Turcotte, 1986)

McDowell *et al*. (1996) also investigated the splitting of grains, in which the probability of fracture is a function of applied stress, particle size and co-ordination number. For a given stress state, large particles are more susceptible to crushing than small particles, because internal flaws of the structure increase in size and number as the particle size increases and hence weaken the particle, while particles with low coordination number are more likely to crush than those with high coordination number. When the effect of co-ordination number was the dominant factor rather than

the particle size in determining the fracture probability of a particle, a fractal distribution with realistic fractal dimension could be achieved. However, if the particle size dominates the probability of fracture of a particle, large particles, which are weaker than small particles, would always crush until a uniform matrix of fine particles is achieved, which is not realistic, when compared with available laboratory data. It is therefore suggested that the coordination number dominates over the size effect on particle survival probability. McDowell *et al*. (1996) proposed that the smallest particles continue to fracture and fill in the voids as the macroscopic stress increases, which makes the system statistically stronger- the soil 'hardens' and can sustain a higher stress because of the generation of new statistically stronger and smaller particles which fill voids. Even if a large particle did break, then there is no large void for it to fill in; the small particles are what are important in this hardening mechanism. McDowell and Bolton (1998) further investigated micromechanical behaviour of crushable soils. They found that it is the fracture of the smallest particles that result in a limited fractal geometry which gives an insight into the existence of linear normal compression lines in e-log p' space, which is regarded as the 'clastic hardening' law.

For granular materials subjected to one-dimensional compression, it is usual to plot voids ratio e against the logarithm of vertical effective stress σ_v'. A linear normal compression line develops beyond yield (the region of maximum curvature). Butterfield (1979) suggested an alternative compression law for clay in which the normal compression line is linear in $\log v - \log \sigma_v'$ space (where v is specific volume). However, the normal compression line cannot remain linear at high stress levels. Pestana and Whittle (1995) suggested a linear limiting compression curve in

$\log e - \log \sigma_v'$ space. Typical values for the slope of this curve are around 0.4-0.5 for sands (Pestana and Whittle, 1995). McDowell (2005) justified the $\log e - \log \sigma_v'$ space based on fractal crushing and particle kinematics, and suggested -0.5 to be the slope of the NCL in $\log e - \log \sigma_v'$ space with Weibull modulus $m = 3$, giving a size effect in Eq. 2-37 of b=1.

Usually, for granular materials subjected to one-dimensional normal compression, the particle size distribution evolves towards a fractal distribution with a fractal dimension of 2.5 (Palmer and Sanderson, 1991; Turcotte, 1986; Joer *et al*., 1999). Hence, the number of particles $N(L \geq d_s)$ greater than or equal to a size d_s is given as:

$$N(L \geq d_s) \propto d_s^{-2.5} \tag{2-41}$$

Following the recursive method,

$$N(L \geq d_{s-1}) \propto d_{s-1}^{-2.5} \tag{2-42}$$

Hence the number of smallest particles could be expressed as:

$$N(L = d_s) \propto d_s^{-2.5} \tag{2-43}$$

Given the volume of particle being proportional to d_s^3, the volume of the smallest particles could be given as:

$$V(L = d_s) = N(L = d_s) \times d_s^3 \propto d_s^{1/2} \tag{2-44}$$

As was shown in Eq. 2-37, the 37% survival strength of a particle is proportional to the particle size. McDowell (2002) found the Weibull modulus *m* for silica sand should be approximately 3, so that the size effect on the average strength could be given as:

$$\sigma_0 \propto d^{-3/m} \propto d^{-1} \tag{2-45}$$

By assuming the macroscopic stress level to be proportional to the microscopic average strength of the smallest particles, the relationship between the volume of smallest particles and the macroscopic stress level could be derived as:

$$V(L = d_s) \propto d^{\frac{1}{2}} \propto (\sigma^{-1})^{1/2} = \sigma^{-1/2} \tag{2-46}$$

Assuming void space to be proportional to the total volume of all the smallest particles once a fractal distribution emerges (McDowell, 2005), then the voids ratio e satisfies the relationship

$$e \propto \sigma^{-1/2} \tag{2-47}$$

so that the slope of the normal compression curve in $\log e - \log \sigma'$ space is -0.5, which is in agreement with the experimental normal compression locus curve when plotted on double logarithmic axes, as shown in Figure 2.21.

For more general cases the relationship between the voids ratio and the stress can be derived as:

$$e \propto V(L = d_s) \propto d^{(3-D)} \propto (\sigma^{-m/3})^{(3-D)} = \sigma^{\frac{m(D-3)}{3}} \tag{2-48}$$

where the Weibull modulus m and the fractal dimension D are material constants. Hence, the slope of the normal compression line can be defined by $\frac{m(D-3)}{3}$.

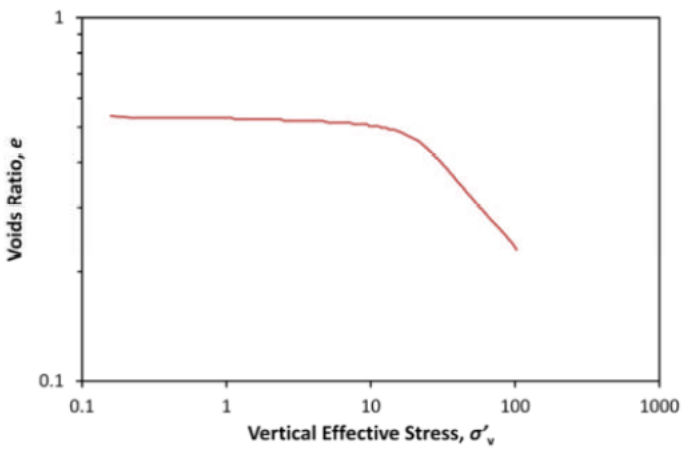

Figure 2.21 Compression behaviour for silica sand plotted on log *e*-log σ_v' axes (McDowell, 2005)

2.4 Discrete element method (DEM)

The importance of the micro-scale interaction between particles has been described in the previous section that: the crushing of single particles and the size effect of particle strength will finally result in the hardening of the soil. Studies regarding the micro-mechanics of soil is therefore of great importance. During lab tests, X-ray micro-computed tomography (micro-CT) is usually used to obtain the micro-structure of a soil sample in full 3-D space. With the application of X-ray micro-CT, the micro structure of soils has been studied (Fonseca *et al*. 2013; Fonseca *et al*. 2014; Paniagua *et al*. 2015). However, in lab tests, it is hard to obtain exactly the same micro-structure for every initial sample and perform a series of different tests based on the same initial sample with the same initial conditions. This issue can be solved in discrete element modelling. The initial conditions of samples are easy to control; different tests on the same sample can be simulated again and again. The discrete element method (DEM) which will be applied in this project will be introduced in this section.

.

2.4.1 General description of DEM

The Discrete Element Method (DEM) is a numerical method developed by Cundall (1971) for the analysis of rock mechanics problems. It models granular materials as assemblies of discrete elements. The method was applied to soils by Cundall and Strack (1979). DEM uses an explicit numerical scheme to model the interaction of the particles contact by contact and the motion of the particles particle by particle. The method is based on the idea that the time-step is small enough that disturbances cannot propagate from any particle other than its immediate neighbours, so that the forces acting on each particle are generated from the interaction with directly contiguous particles. The velocities and accelerations are assumed to be constant within each time step.

The calculations performed in the DEM alternate between the application of Newton's second law to the particles and a force-displacement law at the contacts. Newton's second law is integrated to give velocities and displacements and hence new contact forces and new accelerations via a time-stepping scheme.

2.4.2 Particle flow code

PFC^{3D} is a commercial software developed by Itasca (2008). It models the movement and interaction of stressed assemblies of arbitrarily-shaped particles using DEM.

Walls and balls are the only basic elements in *PFC*^{3D}with walls to apply velocity boundary conditions for assemblies of balls during compaction and confinement. Balls and walls interact with each other at contact points where forces arise. Basic assumptions of *PFC*^{3D} are as follows:

- particles are treated as rigid bodies;
- the soft-contact is employed, so that the rigid particles are allowed to overlap one another at contact points;
- contacts occur at points;
- the force-displacement law controls the magnitude of the overlap that relates to the contact force;
- bonds can exist at contacts between particles;
- all particles are spherical, while a clump consists of a set of overlapping spheres.

The calculation cycle in *PFC*^{3D} is a time-stepping algorithm. The repeated application of the law of motion and the force-displacement law is shown in Figure 2.22.

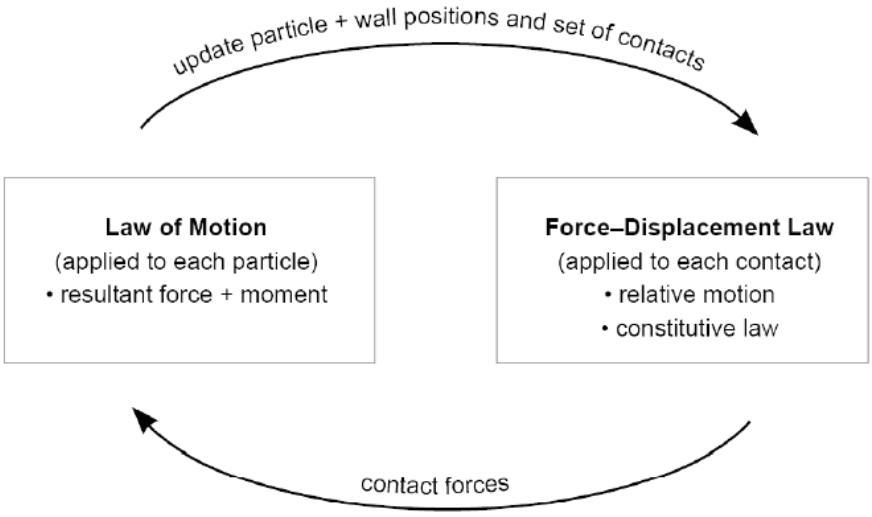

Figure 2.22 Calculation cycle in *PFC*^{3D} (Itasca, 2008)

Force-displacement Law

The force-displacement law is applied to each contact to calculate the contact forces that generated from the relative motion between the two particles at the contact (Itasca, 2008). The contact force vector F_i consists of normal and shear components

$$F_i = F_i^n + F_i^s \tag{2-49}$$

where

- F_i^n stands for normal component
- F_i^s stands for shear component.

The normal contact force is calculated as the force generated perpendicular to the contact plane that the two particles overlap each other.

$$F_i = K^n U^n n_i \tag{2-50}$$

where

- K^n is the normal stiffness,
- U^n is the overlapping of the two particles
- n_i is the unit normal vector.

For ball-to-ball contact, the normal vector lies along the line between the ball centres; for ball-to-wall contact, the normal vector lies along the line defining the shortest distance between the ball centre and the wall.

The shear contact force is calculated from the force-increment vector. The total shear contact force is set to zero when the contact is initially formed. An increment of elastic shear force is added to the total shear contact force at each subsequent relative shear displacement increment.

$$\Delta F_i^s = -K^s V_i^s \Delta t \tag{2-51}$$

where

- K^s is the shear stiffness at the contact
- V_i^s is the shear component of the contact velocity
- Δt is the length of each time-step in real.

Hence, the integrated shear contact force in total is:

$$F_i^s = \{F_i^s\}^{old} + \Delta F_i^s \tag{2-52}$$

Law of motion

In *PFC*^{3D}, the force and moment vectors of the particle determine its motion. The force equation is given as

$$F_i = m(\ddot{x}_i - g_i) \tag{2-53}$$

where

- F_i means the sum of all external forces acting on the particle;
- $m$means the mass of the particle;
- $\ddot{x}_i$means the acceleration of particle;
- g_i means the body force acceleration vector.

The moment equation is given as:

$$M_i = I\dot{\omega}_i = \left(\frac{2}{5}mR^2\right)\dot{\omega}_i \tag{2-54}$$

where

- M_i means the resultant moment acting on particles;
- I means the moment of inertia of a particle;
- $\dot{\omega}_i$means the angular acceleration of a particle;

- R means the radius of a spherical particle with uniformly distributed density

The given equations of motion, Eq. 2-53 and Eq. 2-54, are integrated using the centred finite-difference procedure involving a time-step, Δt. Then incremental velocity $\dot{x}_i$ and angular velocity ω_i are calculated at the mid-intervals of $t \pm \Delta t/2$. The accelerations of velocity and angular velocity are given as:

$$\ddot{x}_i^{(t)} = \frac{1}{\Delta t}\left(\dot{x}^{(t+\Delta t/2)} - \dot{x}^{(t-\Delta t/2)}\right) \tag{2-55}$$

$$\dot{\omega}_i^{(t)} = \frac{1}{\Delta t}\left(\dot{\omega}^{(t+\Delta t/2)} - \dot{\omega}^{(t-\Delta t/2)}\right) \tag{2-56}$$

Substituting equations into Eq. 2-53 and Eq. 2-54, taking the velocity at the mid-interval to be the average velocity of each time increment

$$\dot{x}_i^{(t+\Delta t/2)} = \dot{x}_i^{(t-\Delta t/2)} + \left(\frac{F_i^t}{m} + g_i\right)\Delta t \tag{2-57}$$

$$\dot{\omega}_i^{(t+\Delta t/2)} = \dot{\omega}_i^{(t-\Delta t/2)} + \left(\frac{M_i^t}{I}\right)\Delta t \tag{2-58}$$

Hence, the updated position of the particle could be derived as:

$$x_i^{(t+\Delta t)} = x_i^{(t)} + \dot{x}_i^{(t+\Delta t/2)}\Delta t \tag{2-59}$$

And the rotation of the particle updated as:

$$\omega_i^{(t+\Delta t)} = \omega_i^{(t)} + \dot{\omega}_i^{(t+\Delta t/2)}\Delta t \tag{2-60}$$

2.4.3 Contact models

The overall constitutive behaviour of a material is simulated in *PFC*^{3D} by associating a simple constitutive model with each contact. The constitutive model acting at a particular contact consists of three parts: a stiffness model, a slip model and a bonding model. Since the slip model and bonding model are not applied in this study, only the contact stiffness model will be described in detail in the following sections.

Linear contact model

The linear model provides force-displacement behaviour, an optional contact-bond behaviour and constant stiffness. A parallel-bond component can be added to a contact with the linear contact model. The contact stiffness is defined by the normal and shear stiffness, k_n and k_s, of the two contacting entities (ball-to-ball or ball-to-wall). These parameters are specified using the 'PROPERTY' command. The contact stiffness for the linear contact model is computed assuming that the stiffness of the two contacting entities act in series. The contact normal secant stiffness is given by

$$K^n = \frac{k_n^{[A]} k_n^{[B]}}{k_n^{[A]} + k_n^{[B]}} \tag{2-61}$$

$$K^s = \frac{k_s^{[A]} k_s^{[B]}}{k_s^{[A]} + k_s^{[B]}} \tag{2-62}$$

where the superscripts [A] and [B] denote the two entities in contact.

Hertz contact model

The Hertz-Mindlin contact model is a nonlinear contact formulation based on an approximation of the theory of Mindlin and Deresiewicz (1953) and described in

Cundall (1988). The sliding behaviour and stiffness at the contact point are evaluated by calculating the overlap and normal force between the two entities.The Hertz contact model is strictly applicable only to the case of spheres in contact, and does not reproduce the continuous nonlinearity in shear.

The model is defined by the following two parameters: shear modulus G [stress] and Poisson's ratio υ [dimensionless] of the two contacting balls, hence, the contact normal secant stiffness and shear tangent stiffness are given by

$$K^n = \left(\frac{2\langle G\rangle\sqrt{2\tilde{R}}}{3(1-\langle \nu\rangle)}\right)\sqrt{U^n} \tag{2-63}$$

$$k^n \equiv \frac{dF^n}{dU^n} = \frac{3}{2}K^n \tag{2-64}$$

$$k^s = \left(\frac{2\left(3\tilde{R}\langle G\rangle^2(1-\langle \nu\rangle)\right)^{1/3}}{2-\langle \nu\rangle}\right)|F_i^n|^{1/3} \tag{2-65}$$

where, for ball to ball contact

$$\tilde{R} = \frac{R^{[A]}R^{[B]}}{R^{[A]}+R^{[B]}} \tag{2-66}$$

$$\langle G\rangle = \frac{1}{2}\left(G^{[A]} + G^{[B]}\right) \tag{2-67}$$

$$\langle \upsilon\rangle = \frac{1}{2}\left(\upsilon^{[A]} + \upsilon^{[B]}\right) \tag{2-68}$$

and for ball to wall contact

$$\tilde{R} = R^{[ball]} \tag{2-69}$$

$$\langle G\rangle = G^{[ball]} \tag{2-70}$$

$$\langle \upsilon \rangle = \upsilon^{[ball]} \tag{2-71}$$

where

- G is the elastic shear modulus;
- υ is Poisson's ratio;
- R is sphere radius;
- the superscripts [A] and [B] denote the two spheres in contact.

The Hertz-Mindlin contact model cannot be used between two balls that are joined by a contact bond, because the model is not defined for spheres that are in tension.

Parallel bond model

Since the parallel bond is widely applied in DEM simulations, a brief introduction of the parallel bond is given as below. A parallel bond works as a disc of elastic glue lying on the contact plane. Both forces and moments between particles can be transmitted with parallel bond, while contact bonds can only transmit forces acting at the contact point. Relative motion at the contact causes a force and a moment to develop within the parallel bond as a result of the stiffness of the parallel bond. The bond fails when the stress in any part of the bond exceeds the limit of the bond strength. It should be noted that the parallel bond cannot work together with the Hertz contact model on the same contact point, however can work together with the linear contact model. Full details are given by Itasca (2008).

2.4.4 Servo-control

In *PFC*^{3D} calculations, the force and displacement of the entities influence each other. In order to maintain the loading stress of the test in a predetermined stress path, such as the normal compression test and triaxial test, the servo-control mechanism is implemented. The servo-control in *PFC*^{3D} is a function to achieve the stress state of the test throughout the simulation. The velocities of walls are adjusted in every calculation cycle using the servo-control function to reduce the deviation between the target stress and the measured stress. The calculation of the servo-control is given as

$$\dot{u}^{(w)} = G_a\left(\sigma^{measured} - \sigma^{required}\right) = G_a\Delta\sigma \tag{2-72}$$

where G_a is the target state parameter. The maximum increment on wall force generated from wall displacement in each time-step is calculated as

$$\Delta F^{(w)} = {k_n}^{(w)} N_c \dot{\mu}^w \Delta t \tag{2-73}$$

where

- N_c is the number of contacts on the wall
- k_n is the average stiffness of the contacts.

The wall stress increment generated in each time-step, Δt, can be derived as

$$\Delta\sigma^{(w)} = \frac{{k_n}^{(w)} N_c \dot{\mu}^w \Delta t}{A} \tag{2-74}$$

where A is the area of the wall.

To maintain the stress path and keep the deviation of stress within the target limit, a relaxation factor, α, is introduced such that

$$\left|\Delta\sigma^{(w)}\right| < \alpha|\Delta\sigma| \tag{2-75}$$

Substituting equation Eq. 2-74 into Eq. 2-75

$$\frac{k_n{}^{(w)} N_c \dot{\mu}^w \Delta t}{A} < \alpha |\Delta \sigma| \tag{2-76}$$

Substituting equation Eq. 2-76 into Eq. 2-72

$$G_a = \frac{\alpha A}{k_n{}^{(w)} N_c \Delta t} \tag{2-77}$$

where G_a is the gain parameter described previously in Eq. 2-72. The servo is therefore a feedback method that adjusts wall velocities to achieve a target wall stress.

2.5 Applications of Discrete Element Method (DEM)

2.5.1 DEM modelling single particle breakage

Soil strength and dilatancy were related to stress level and density according to Bolton (1986), who also suggested a possible link between grain crushing and the dilatational component of the angle of internal friction. However, it is difficult to quantify the influence of soil crushability on the plastic behaviour of soil, due to the limitation in the interpretation of the macro-mechanical behaviour of soil in lab tests using micro-scale parameters. With the development of the discrete element method (DEM), new approaches were launched to investigate the plasticity of soils and sands, taking crushability into consideration.

The crushing of particles is usually realized in DEM by two alternative methods: the population balance model (PBM) proposed by Herbst *et al.* (2003) and bonded particle model (BPM) proposed by Potyondy and Cundall (2004). The former replaces crushed particles with a number of new smaller fragments and the latter bonds a number of spheres together with finite bond strengths.

Population balance model (PBM)

This approach initially involves two functions: (1) a selection function used to determine which particles should break; (2) a breakage function used to determine the size distribution and packing of the fragments. However, various breakage criteria and fragment functions were employed by previous researchers and there is no agreement in the literature about which selection function or breakage criteria should be used in DEM.

As far as the author knows, the earliest attempt to model particle crushing using PBM was by Astrom and Herramann (1998) in 2D. They tried two alternative selection functions based on different breakage criteria: (a) the limit of confining pressure of the particle: the particle will crush when the pressure is larger than the predetermined limit; (b) the value of the largest compressive force acting on the particle: the particle will crush when the largest force exceeds the predetermined limit. For the breakage functions, they also investigated two different mechanisms:

(1) Simple splitting into two equal fragments. The use of this fragment distribution function can avoid the appearance of a huge number of particles but it induces large and unrealisable local pressures.
(2) Twelve fragments of three different sizes are placed into the area of the broken grain and the rest of the mass in placed just outside the 'pockets' between the surrounding grains. This mechanism keeps the induced local pressure within a reasonable threshold but increases the number of particles dramatically.

Figure 2.23 shows different fragmentation results of two samples starting from the same initial packing (the same number of particles and the same initial particle size

distribution). Figure 2.23 (a) shows that the fracture mechanism (1) leads to more crushing of large particles and a more continuous particle size distribution. Figure 2.23 (b) shows that the fracture mechanism (2) leads to a faster radius decrease, hence newly generated small fragments quickly surrounding large particles and providing better protection, resulting in more survival of large particles.

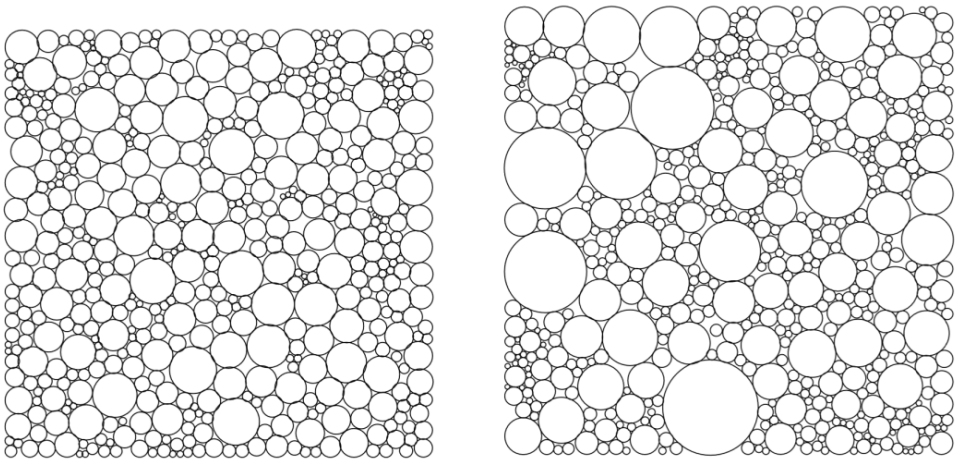

(a) (b)

Figure 2.23 Two fragmented samples using different fracture modes (a) fracture mode (1); (b) fracture mode (Astrom and Herramann, 1998)

Tsoungui *et al*. (1999) investigated the effect of the hydrostatic state and deviatoric state in terms of the selection function. Figure 2.24 shows the identification of the two simplified stress states. The hydrostatic one reduced the probability of particle breakage; the latter one increased the probability of particle breakage. The same was revealed in the lab experiment that fragmentation was initially observed in particles close to boundaries (particles with fewer contacts and coordination numbers) and followed by particles within the central area of the sample (particles with more contacts). As for the breakage function, they introduced the direction of the crack, which lay along the line between the maximum contact forces, and applied fracture mechanism (2) which has been described above (Astrom and Herrmann, 1998). Figure 2.25 shows the fracture mechanism applied in their research.

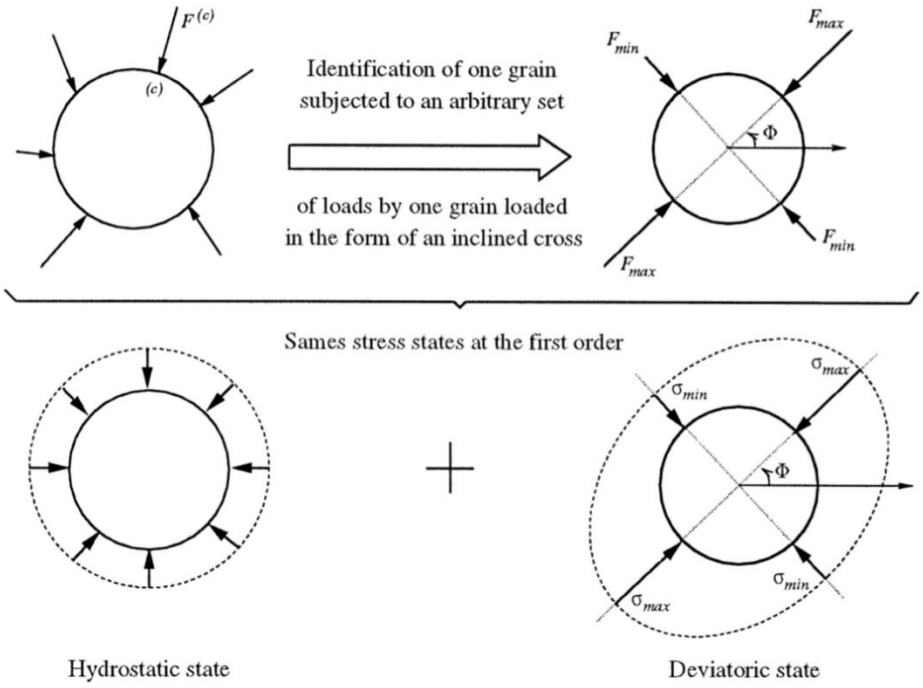

Figure 2.24 Identification of hydrostatic state and deviatoric state (Tsoungui *et al.*, 1999)

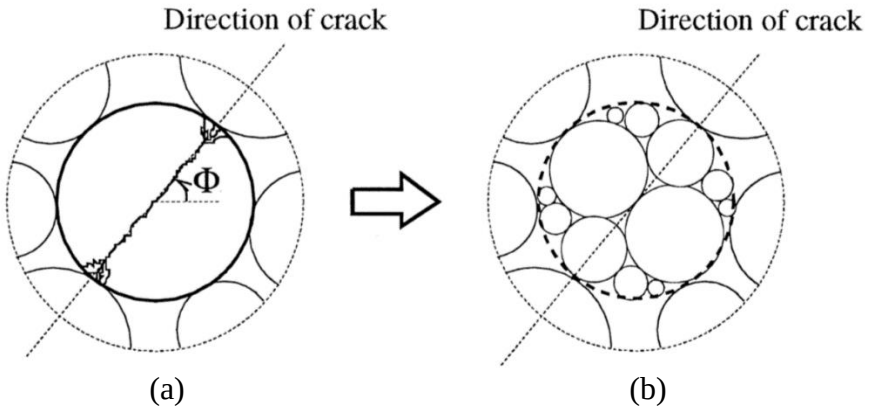

Figure 2.25 Fracture mode in 2D scale (Tsoungui *et al.*, 1999)

Lobo-Guerrero *et al*. (2005) proposed two more limitations on the selection function: (1) crushing only occurs in particles with coordination numbers smaller than or equal to 3 (particles with sufficient contact number are not easily crushed (Lade *et al*. 1996; Nakata *et al*. 2001a)); (2) size effect was introduced thereby giving smaller particles higher strengths than larger particles, Figure 2.26.

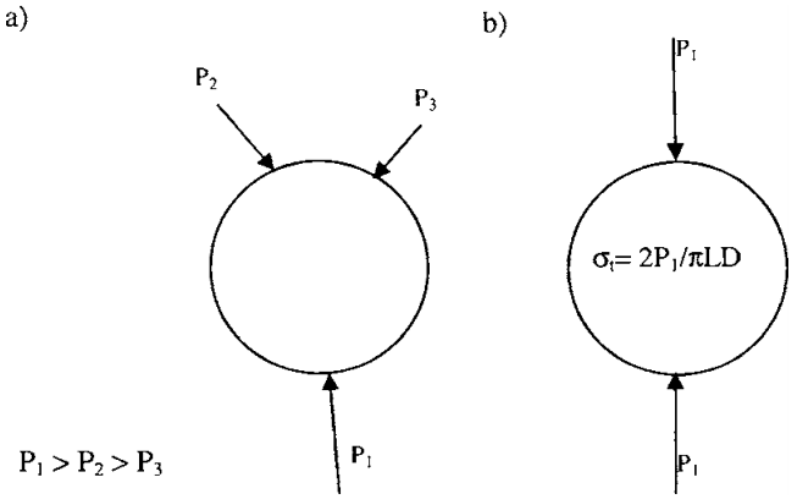

Figure 2.26 Idealization of induced tensile stress (Lobo-Guerrero *et al*., 2005)

Lobo-Guerrero *et al*. (2005) also analysed the evolution of a grain size distribution, and suggested the final emerged distribution was fractal in nature, although conservation of mass was not observed. The disappearance of fine particles would be expected to have an influence on the applicability of the crushing model to replicate the evolution of a physically realistic voids ratio.

Ben-Nun and Einav (2010) developed their own PBM. They described two criteria in terms of selection function, the first of which used a measure of shear stress obtained from the stress tensor for a particle, and the second of which allowed particles to break under hydrostatic stress. As for the breakage function, they proposed a fracture mechanism that replaced the parental broken particles with new smaller particles. Differing from other researchers, the newly generated particles are initially set to small sizes to avoid overlap and then expanded to maintain conservation of mass, hence, minimizing artificial pressure spikes from large particle overlap. In their second function, the new fragments were initially generated with a smaller size within the parental particle area; the packing of the fragments was then given a random rotation and expanded as a whole thereafter. Three types of packing of fragments were

investigated as is shown in Figure 2.27. A Weibull distribution of particle strengths and the size effect were also involved in their simulations. They found that an ultimate grain size distribution could be achieved independent of the initial porosity or initial grading and even fracture mechanism. The ultimate fractal dimension was calculated by plotting the particle size distribution using number of particles larger against the particle size on a log-log scale, so that the final slope of the particle size distribution line revealed the ultimate fractal dimension, as is shown in Figure 2.28. Self-similarity was also observed in different scales of the topology of the crushed sample, as is shown in Figure 2.29.

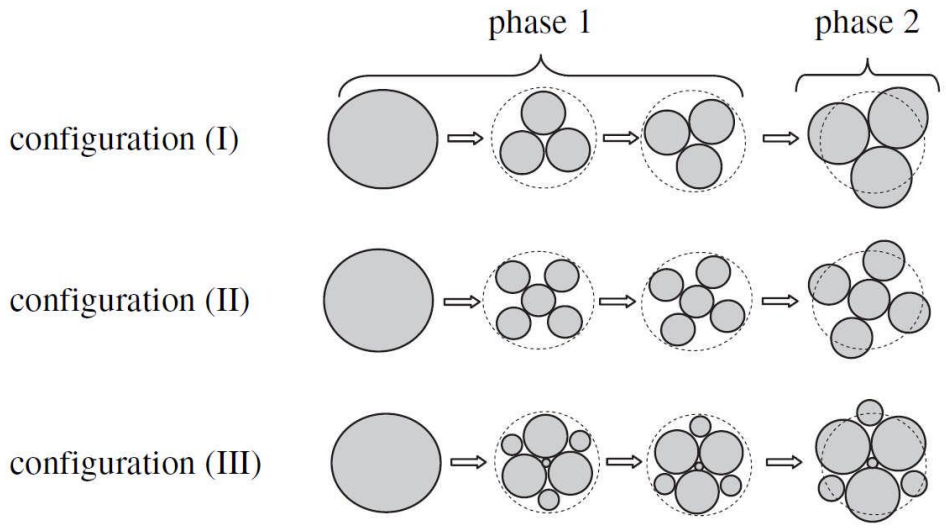

Figure 2.27 Three alternative breakage configurations, showing the random rotation followed by expansion of the new particles (Ben-Nun and Einav, 2010)

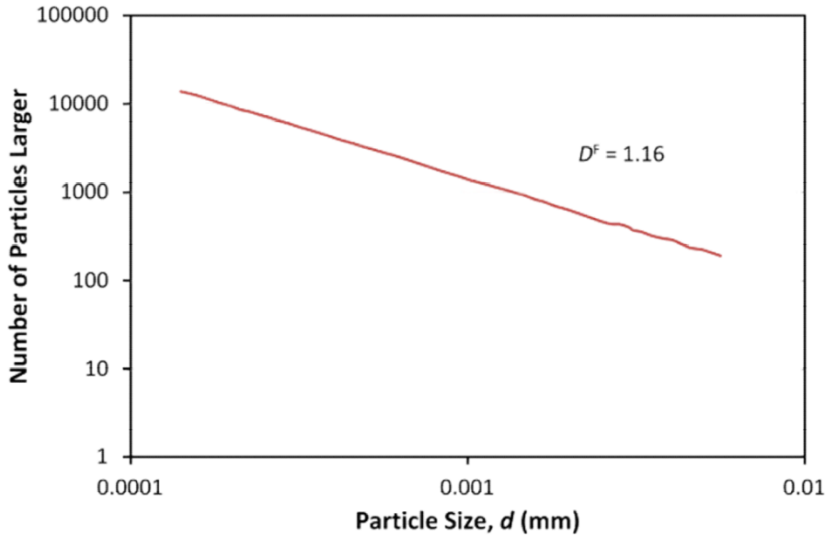

Figure 2.28 Final particle size distribution by number in log-log scale with a slope giving a fractal dimension of 1.16 (Ben-Nun and Einav, 2010)

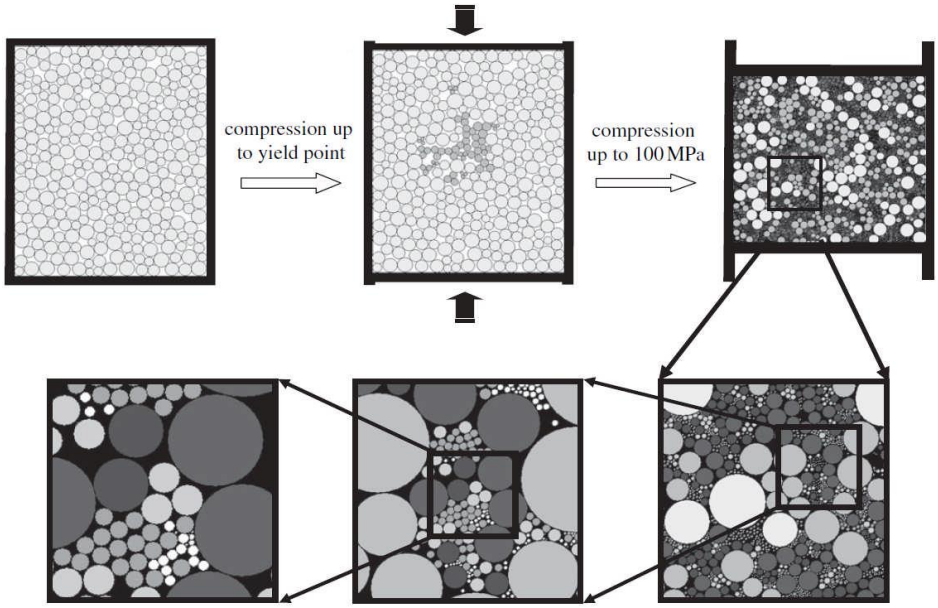

Figure 2.29 Final topology of crushed 2D sample, showing self-similarity across scales (Ben-Nun and Einav, 2010)

McDowell and de Bono (2013) further applied three dimensional PBM simulations of particle crushing. Initially uniformly distributed spherical particles and a simple breakage mechanism were introduced. In their approach, the selection function is governed by three factors: (1) the octahedral shear stress within the particle; (2) the size effect on the tensile strength of a particle, i.e. the strength is increasing with a

smaller particle (3) the Weibull distribution of particle strength, so that 37% of the particles with the same tensile strength will survive when the octahedral shear stress exceeds the predetermined tensile strength. The octahedral shear stress in 3D is derived from the principal stresses of the particle

$$q = \frac{1}{3}\sqrt{[(\sigma_1 - \sigma_2)^2 + (\sigma_2 - \sigma_3)^2 + (\sigma_3 - \sigma_1)^2]} \tag{2-78}$$

where σ_1,σ_2 and σ_3 are major, intermediate and minor principal stresses respectively. In this way the particle won't break when the principal stresses in three directions are equal, which is a hydrostatic stress state ($q = 0$). The average stress tensor calculated in *PFC*^{3D} is given as:

$$\sigma_{ij} = \frac{1}{V}\sum_{N_c}\left|x_i^{(c)} - x_i^{(p)}\right| n_i^{(c,p)} F_j^{(c)} \tag{2-79}$$

where

- V is the volume of the particle,
- N_c is the contact number of a particle,
- $x_i^{(c)}$ and $x_i^{(p)}$ are the locations of the contact and particle respectively,
- $n_i^{(c,p)}$ is the unit-normal vector directed from the centre of the particle to the location of the contact
- $F_j^{(c)}$ is the contact force (Itasca, 2008).

For the Brazilian test, i.e. diametrically compression test, the major principal stress is calculated :

$$\sigma_{11} = \frac{\frac{\pi}{6}1}{d^3} F \times \frac{d}{2} \times 2 = \frac{\pi}{6}\frac{F}{d^2} \tag{2-80}$$

Substituting Eq. 2-80 into Eq. 2-79, so that the octahedral stress in Brazilian test could be derived as:

$$q = \frac{\sqrt{2}}{3}\left(\frac{\pi}{6}\frac{F}{d^2}\right) = 0.9\frac{F}{d^2} \tag{2-81}$$

Hence the octahedral stress calculated in *PFC*^{3D} is related to the tensile strength of a particle in this way (McDowell and de Bono, 2013)

$$q = 0.9\frac{F}{d^2} = 0.9\sigma \tag{2-82}$$

Hence:

$$q_0 = 0.9\sigma_0 \tag{2-83}$$

Given the size effect of the particle strength $\sigma \propto d^b$, as has already been introduced previously in Section 2.3 (σ is the particle strength, d is the particle size, and b is the material constant), the tensile strength σ_0 could be replaced by the octahedral stress $q_0$when considering the Weibull distribution of particle strength in this way:

$$q_0 \propto d^{-3/m} \tag{2-84}$$

When determining the breakage function, three possible approaches were investigated by McDowell and De Bono (2013): splitting into two equal fragments, three fragments and four fragments respectively. Figure 2.30 shows the fragment functions. The breakage function here not only conserves mass but also ensures that the progeny fragments locate inside the boundary of the original particle. The drawback is that the generation of a large undesirable local pressure caused by the overlap of the fragments. In order to dissipate this artificially induced energy, a number of computational cycles equivalent to 0.003s is assigned to the system for particles to adjust positions and allow for energy dissipation. The interval of 0.003s can be modified; the interval should be large enough that the number of particles breaking will not change when increasing

the interval. The particle stress states are updated (for the whole sample) after the energy dissipation procedure.

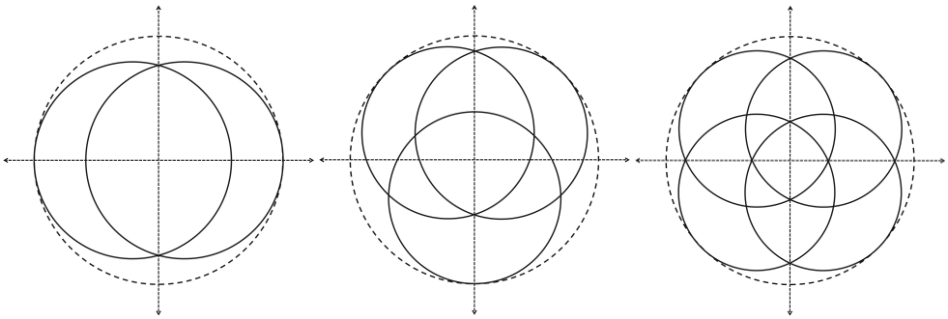

Figure 2.30 Three fragment functions (a) splitting into two fragments (b) splitting into three fragments (c) splitting into four fragments (McDowell and de Bono, 2013)

Bonded particle model (BPM)

In this approach, the particle is represented by an agglomerate which is a dense packing of spheres bonded at their contact points. When a desired load is applied, the macroscopic fractures are formed by the coalescence of broken bonds. The packing method of the spheres forming the agglomerate is important here as it directly determines the fabric structure of the agglomerates. There are mainly three algorithms used to generate agglomerates in the literature: Hexagonal closed packing (HCP) agglomerates (Robertson and Bolton, 2001; McDowell and Harireche, 2002a, 2002b; Cheng *et al.*, 2003; Lim *et al.*, 2004; Lim and McDowell, 2007), agglomerates generated by radius expansion method (Lubachevsky and Stillinger, 1990; Potyondy and Cundall, 2004; Cil and Alshibli, 2012) and dense random packing agglomerates (Li *et al.*, 2013; Schopfer *et al.*, 2009; Li *et al.*, 2014) .

Agglomerates of regular packing were initially used to represent soil grains. Robertson (2000) examined three types of regular packing: face centred cubic (FCC), body centred cubic (BCC), and hexagonal close packing (HCP). The results of HCP

agglomerates were found to be the most consistent packing in the simulations. Moreover, HCP provides the theoretically densest packing (a porosity of 0.26) for a particle modelled by bonding uniformly sized spheres. This density is achieved without requiring any particle overlap which would result in locked-in forces inside the agglomerate. Figure 2.31 shows an individual HCP agglomerate of 527 balls compressed diametrically between two platens (Robertson, 2000). The load was applied after randomly rotating the agglomerate. Figure 2.32 shows a typical result for this test, which shows a force-strain (displacement divided by the initial separation) curve, and the fractured agglomerate. The agglomerate appears to have well-defined peak strength due to the sudden failure of the agglomerate. However, it is observed that there is an initial gap before the force begins to rise steadily. Robertson (2000) explained this delay as being due to an unstable rotation of the particle. McDowell and Harireche (2002a) showed that by allowing the agglomerate to stabilize under the application of gravity, the force will increase from the beginning of the test because the agglomerate is in a stable position when load is applied. The use of frictionless walls in the tests by Robertson (2000) means that slip was allowed to occur at the ball to wall contact at all times. If the walls had been assigned a coefficient of friction, the force should increase slowly or erratically at the early stage of the test and rise rapidly prior to failure. Of course, in this case the failure mechanism and the peak strength obtained would both be different. Nevertheless, stabilizing the agglomerate under gravity is considered to be a more realistic approach (McDowell and Harireche, 2002a).

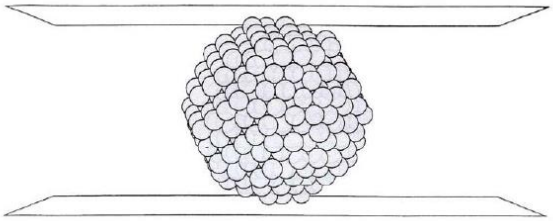

Figure 2.31 Crushing test on agglomerate (Robertson, 2000).

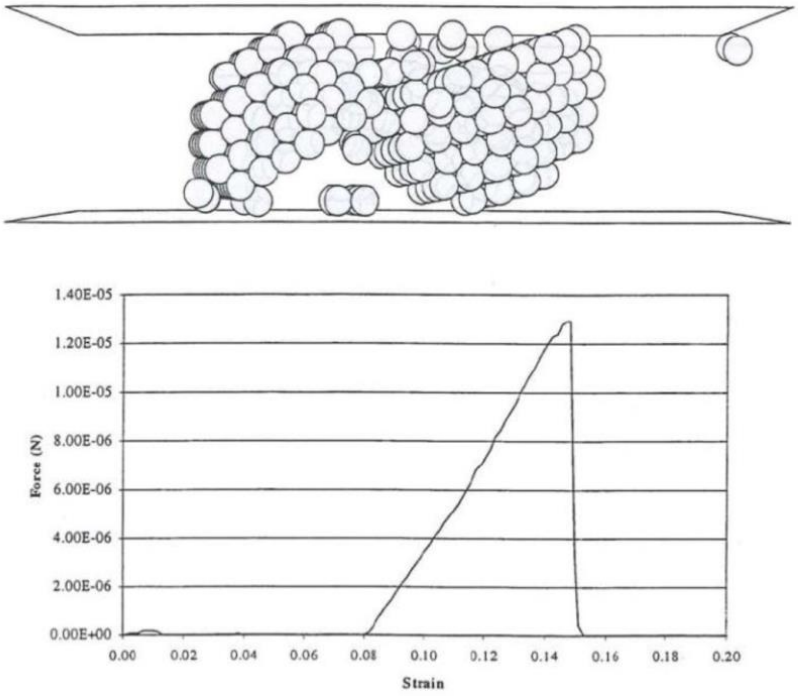

Figure 2.32 Typical result of a crushing test on an agglomerate (Robertson, 2000).

Robertson (2000) also showed that it is possible to produce a Weibull (1951) distribution of soil particle strengths by randomly removing some regularity in the HCP agglomerate to represent the various particle strengths for the particles of the same size. Three types of flaws were introduced by Robertson (2000): removing bonds, reducing some bond strengths and removing balls. It was found that the Weibull distribution of strengths was best reproduced by randomly removing balls in the agglomerate and the Weibull modulus depended on the range of the number of balls removed. The removed balls are therefore intended to simulate a 'flaw' in the material.

McDowell and Harireche (2002a) introduced further randomness to obtain the correct size effect of particle strengths for the HCP agglomerate, achieved by initially removing a certain percentage of balls in the agglomerate before removing a random percentage of balls. Figure 2.33 shows the Weibull distribution of strength tests for a crushing of the 0.5mm and 1mm diameter agglomerates which gives a correct size effect. In these tests, 30% of the balls were initially removed at random before a further random 0-25%. Lim and McDowell (2007) also pointed out that a minimum of around 500 balls in each agglomerate is necessary to give an approximately constant coordination number and the correct size effect; that is to say that the smallest fragment should contain no less than 500 balls if the correct size effect is to be modelled.

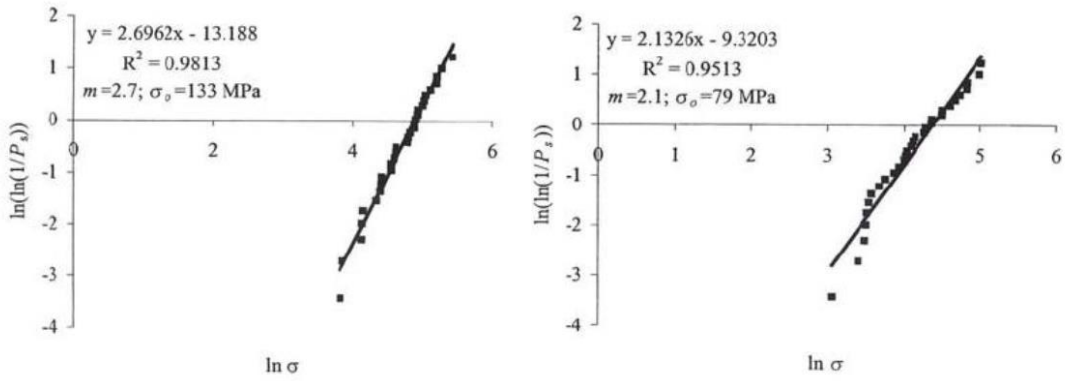

(a) (b)

Figure 2.33 Weibull probability plot for (a) 0.5mm (b) 1mm agglomerates (McDowell and Harireche, 2002a)

However, the HCP method produces a regular and anisotropic packing (Figure 2.34 a and b). If the HCP agglomerate is rotated through 90° in the x-y plane during diametral compression, the contact chains (the distribution of contact forces among the micro spheres in a particle) between two loading platens will change as shown in Figure 2.34 c and d. As the contact force chains will mirror the contact orientations, the contact force chains will also change. Li *et al*. (2013) showed that the maximum tensile

strength is nearly twice the minimum tensile strength for the same agglomerate under different loading directions.

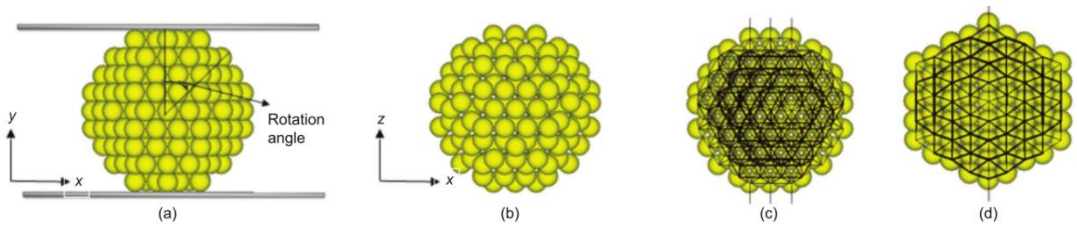

Figure 2.34 (a) Orientation of HCP agglomerate under diametral compression; (b) Orientation of HCP agglomerate in x–z plane; (c) Distribution of contacts for a rotation angle of 0° in the x–y plane; (d) Distribution of contacts for a rotation angle of 90° in the x-y plane (Li *et al.*, 2013).

The radius expansion method introduced by Lubachevsky and Stillinger (1990) and later modified by Potyondy and Cundall (2004) is another conventional method of forming a random packing agglomerate. This type of agglomerate is generated by a four step process. Figure 2.35 shows the procedure for a two dimensional model:

(a) Particles with radii chosen randomly from a uniform size distribution are randomly generated within a volume bound by planar, frictionless walls.

(b) The system is allowed to adjust by particle movement under zero friction.

(c) The radii of all spheres are then increased simultaneously until the system reaches a prescribed confining pressure.

(d) The radii of 'floating' spheres that have less than three contacts are iteratively increased to achieve at least four contacts.

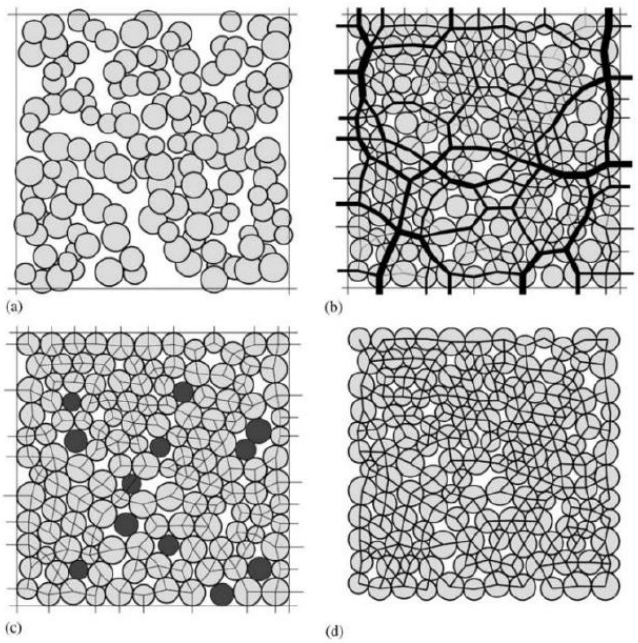

Figure 2.35 (a) particle assembly after initial generation but before rearrangement; (b) contact-force distribution after step 2; (c) floating particles (with less than three contacts) and contacts after step 4; (d) Bonds added after step 4 (Potyondy and Cundall , 2004).

This type of agglomerate has been used to investigate the behaviour of materials such as sand particles (Cil and Alshibli, 2012) and rocks (Potyondy and Cundall, 2004). Although this type of agglomerate is isotropic compared with the HCP agglomerate, it is too porous so that progressive fracture of small parts of the agglomerate can occur, which produces a significant load reduction and multiple peaks in some simulations (Cil and Alshibli, 2012), as opposed to well-defined bulk fracture into two or three fragments with a single peak in the load–deflection curve.

There is another type of agglomerate called the dense random packing (DRP) agglomerate which was firstly used by Schopfer *et al*.(2009) and later modified by Li *et al*. (2013), which is basically inserting smaller and smaller spheres into the smaller and smaller voids inside the agglomerate, Figure 2.36.

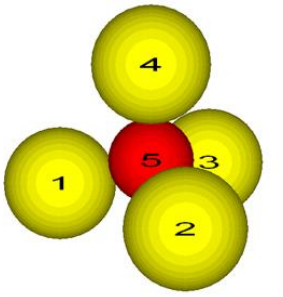

Figure 2.36 The location of the new ball to occupy the tetrahedral space between four existing micro-spheres forming the agglomerate packing (Li, 2013)

Thus the packing density could be governed by a size ratio (the ratio of largest diameter of micro sphere and the smallest inserted micro sphere). By the use the DRP agglomerate, Li *et al*. (2013) found that the packing density has a strong influence on particle tensile strength: a denser agglomerate results in a geometrically more isotropic alike particles and less statistical variation in strength for different DRP agglomerates. Li *et al*. (2013) also obtained the correct Weibull distribution and size effect by using a DRP of size ratio 4. This type of agglomerate provides not only a more isotropically distributed internal stress than other packing methodsbut also exhibits realistic fast bulk fracture. However, the limitation is that it needs too many spheres to represent a single particle which is very challenging in terms of computing time.

2.5.2 DEM investigation of critical state

The critical state behaviour of sands has been investigated using DEM methods, with and without particle crushing.

Cheng *et al.* (2003) used BPM, described in Section 2.5.1, to simulate particle crushing during both isotropic compression and shear. Hexagonal close packing was employed to avoid the initial overlap of spheres within the agglomerate. The internal flaws of soil particles were achieved by assigning 80% probability of existence to the spheres within the agglomerate; that is the 20% randomly distributed missing spheres

correspond to the internal flaws. Fracture occurs when the parallel bond breaks and the initial particle falls apart. Isotropic normal compression tests of soil samples, shown in Figure 2.37, with different loading speeds were simulated to find the maximum loading speed while still maintaining the quasi-steady state. Triaxial shear tests of the same sample following different stress paths were simulated, until the critical states were achieved.

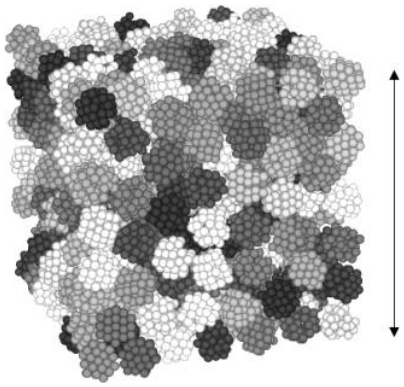

Figure 2.37 3-D sample consisting of a group of agglomerates (Cheng *et al*., 2003)

Cheng *et al*. (2004) further investigated the influence of particle breakage on the plastic deformation of soils. A yield point was taken as the change of the slope of macroscopic scale stress-strain plot. Two lines for the pre-yield and post-yield regions were drawn on the stress-strain plot and the point of intersection was taken as the yield point, as is shown in Figure 2.38 (a) and (b). However, the pre-yield fitted line shown in the left plot of Figure 2.38 (a) lies a little below the original curve, which may lead to an inaccurate estimation of the yield point. In other words, the method does appear to be rather subjective. A yield surface was drawn afterwards with those yield points, as shown in Figure 2.38 (c).

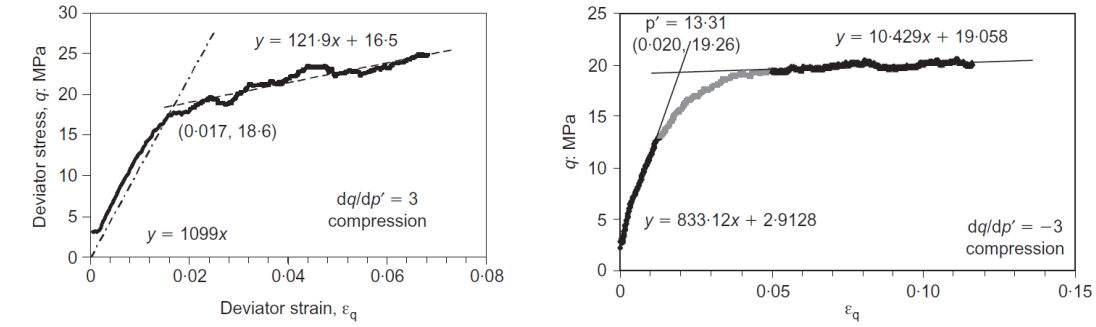

(a)

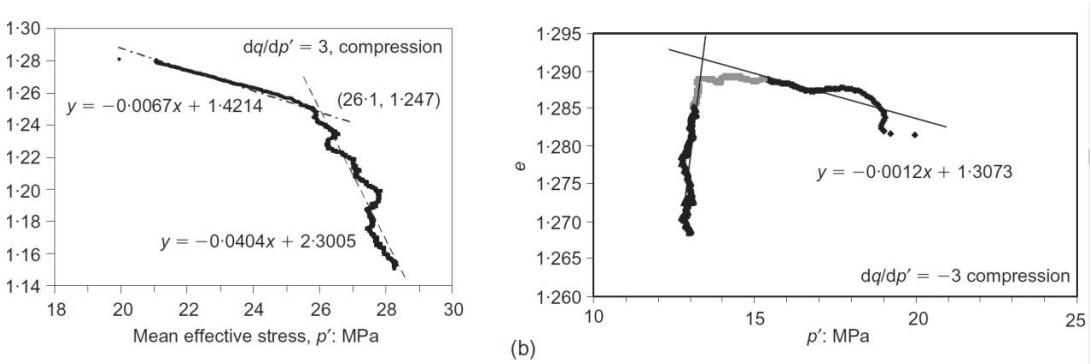

(b)

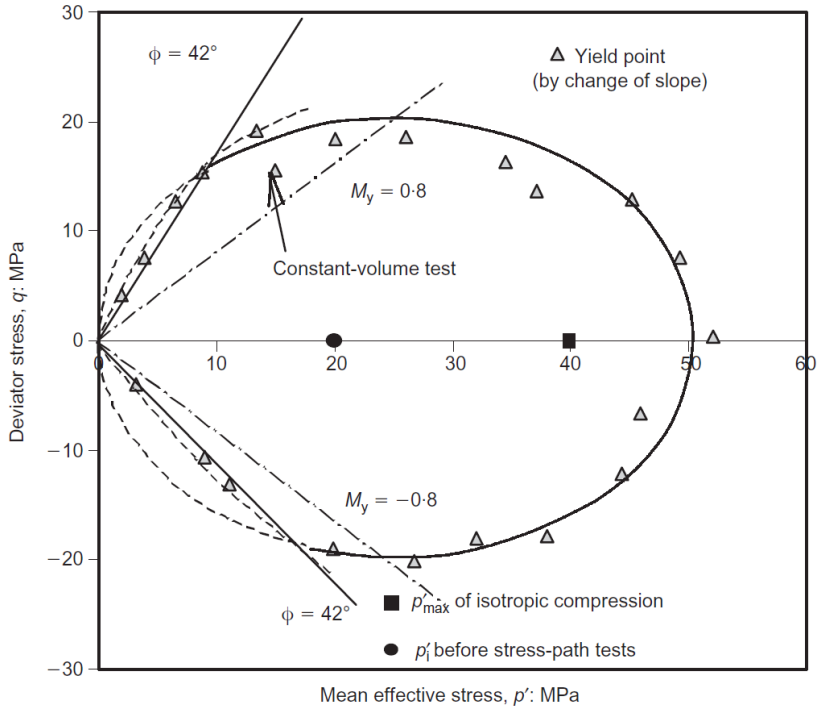

(c)

Figure 2.38 A single yield surface obtained from 'change of slope': (a) curves of deviator stress against deviator strain; (b) curves of voids ratio against mean effective stress; (c) yield points in *q*-*p'* space (Cheng *et al.*, 2004)

The derived critical stress ratio as shown in the figure is '$M_y = 0.8$' according to the modified Cam-clay model. However, a much higher stress ratio, which corresponded to a mobilized friction angle, $\phi = 42°$, was generated in their simulation. The mobilised friction angle, ϕ_{mob}, for sand is usually $25\,\eta$, so that the critical state friction angle is $25 \times M_y$ which is 20°. Hence, the maximum volumetric component of shearing resistance is:

$$\phi_{max} - \phi_{crit} = 42 - 20 = 22^{\circ} = \psi_{max} \tag{2-85}$$

which is too high to be reasonable under triaxial conditions according to Bolton (1986). Cheng *et al*. (2004) explained that the phenomenon may have resulted from the hardening during the unloading-reloading cycle. However, if it is agreed that the unloading-reloading inside the yield surface causes only the elastic deformation of soils, then plastic hardening should not occur during the elastic deformation (Wood, 1990).

During the stress path shear tests by Cheng *et al.* (2004), the amount of bond breakage was quantified by the percentage of broken bonds (pbb). The loading process stopped when the bond breakage exceeded 10% or the deviator strain exceeded 30%. The microscopic scale percentage of bond-breaking (pbb) was also taken as a parameter that could characterise the yield of the soil sample (Cheng *et al.*, 2004). Figure 2.39 (a) shows continuous change of pbb during different stress path tests. The pbb surface is shown in Figure 2.39 (b). Cheng *et al.* (2004) divided the behaviours of over-consolidated soils into two groups based on the over-consolidation ratio n_{oc} at yield where:

$$n_{oc} = p_0'/p' \tag{2-86}$$

In the lightly over-consolidated region (Zone L) $n_{oc} < 2$; and in the heavily over-consolidated region (Zone H) $n_{oc} > 2$ (Figure 2.40 (a)). They found that the modified cam clay model coincides well with the simulated results at Zone L. Each yield surface plotted in $q - p'$ space corresponds well with 'κ-line' in $e - \log p'$ space. The behaviour in Zone H agreed with Rowe's stress-dilatancy theory (1971), as is shown in Figure 2.40. Despite the difference in the behaviour between the two regions, particle crushing was proven to have an important influenceon the yielding behaviour.

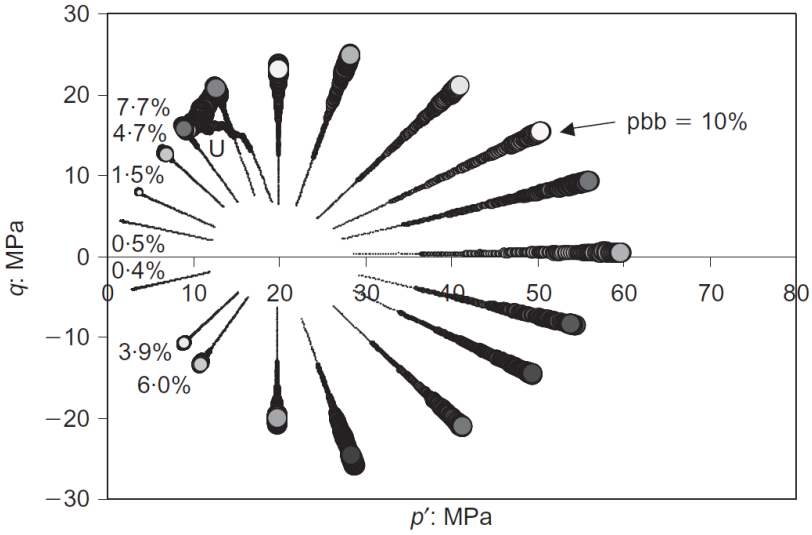

(a)

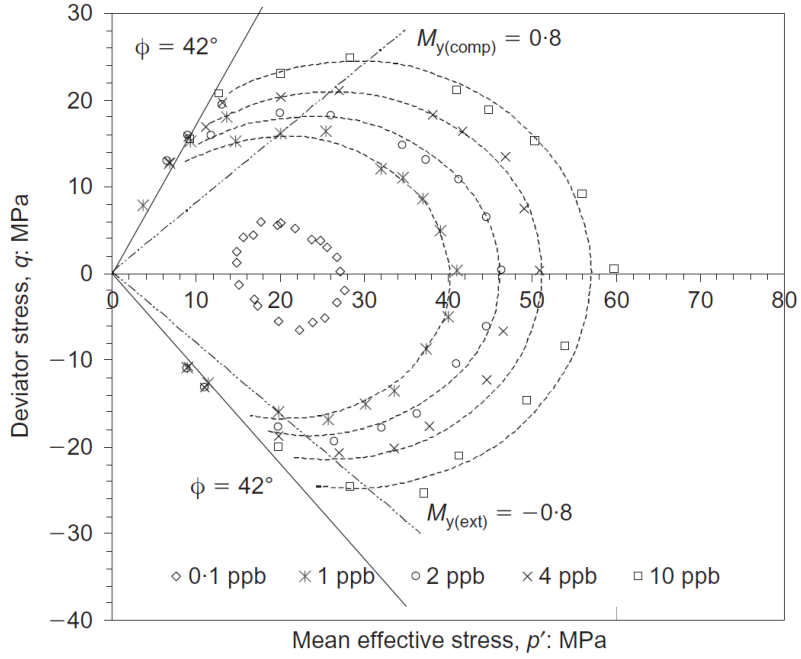

(b)

Figure 2.39 Multiple yield surfaces in relation to particle breakage: (a) continuous breakage; (b) quantity and shape of pbb surfaces (Cheng *et al.*, 2004)

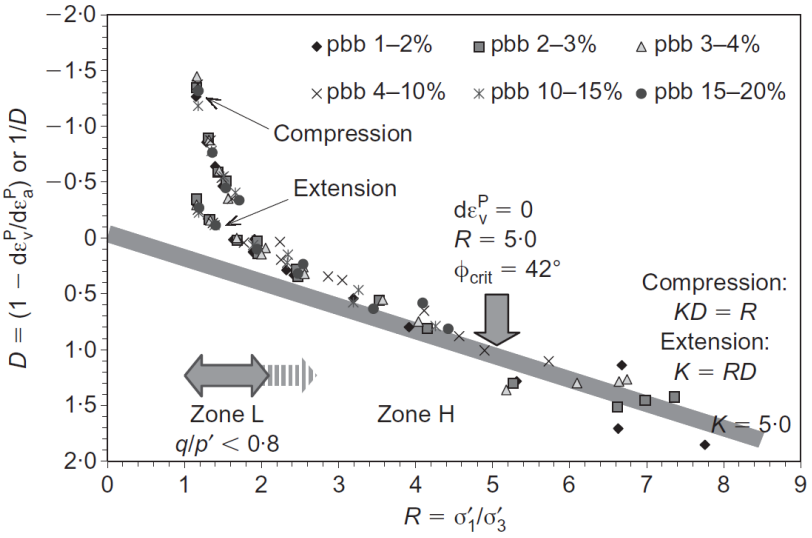

(a)

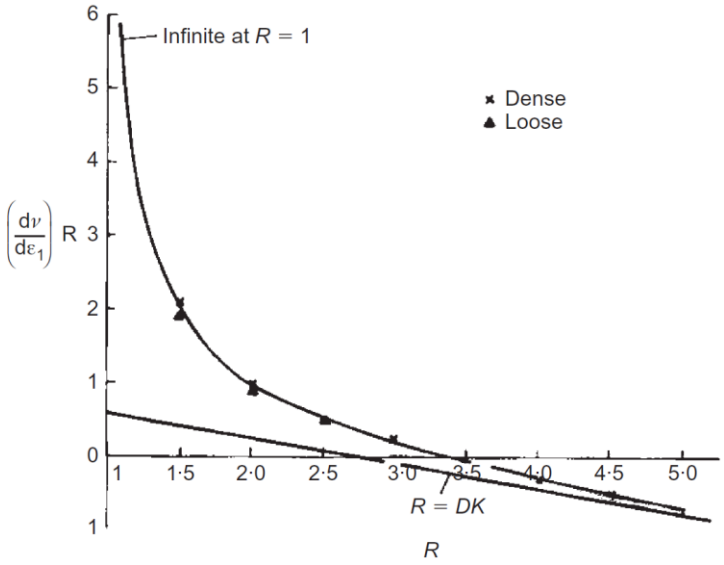

(b)

Figure 2.40 Comparison of stress-dilatancy of Zone H and Rowe's theory: stress-dilatancy in Zone H; (b) Rowe's theory (Cheng *et al.*, 2004)

Cheng and Bolton (2005) investigated the critical state of the crushable soils based on the same simulation method as Cheng *et al.* (2003) described above. Results of four series of tests, namely three series of constant p' shear tests and a series of constant volume (undrained) shear tests were compared: Series 1: constant-p' shearing tests of a set of identical DEM assemblies with same initial voids ratio of 1.73 and an isotropic

consolidation history; Series 2: constant-p' shearing tests of a set of identical DEM assemblies with same initial voids ratio of 2.08 and an isotropic consolidation history; Series 3: constant-p' shearing tests of a DEM assembly with initial voids ratio of 2.08 and an isotropic over-consolidation history with $p'_{max} = 40$ MPa and unloading to different stress levels; Series 4: constant-volume shear tests on a DEM assembly with initial voids ratio 2.08 that was isotropically consolidated to different stress levels.

The critical state lines of those tests are given in Figure 2.41. It was found that the CSL is not necessarily unique. The final, *i.e.* critical state lines of Series 1, 2 and Series 3 are different in both the location and the slope, so that the critical state line varies with stress history. The critical state lines of Series 2 and Series 4 are different, so that the critical state line varies with stress path. However, the inaccuracy of the calculation of voids ratio, due to the BPM model, may lead to the differences in the location of the CSL the in $e - \log p'$ plot. In addition, as will be discussed later, the critical state line should not be expected to be unique if the particle size distribution has changed (Wood, 1990).

The deviator stress, q, against the mean effective stress, p', at the final, *i.e.* critical state, is given in Figure 2.42. The CSL in $q - p'$ space seems to be unique but the curved line implies that the critical stress ratio changes with the stress level. For low stress levels, $M = 1.7$, while for high stress level, the stress ratio decreased to $M = 1.1$. Cheng and Bolton (2005) proposed that the critical stress ratio depends on the mean stress, but is independent of stress path. However, the phenomenon may be caused by the particle breakage model. The smallest spheres within the agglomerate are not crushable. This means that as the angularity decreased and the fragments

eventually crushes into single spheres, the ultimate angle of shearing resistance should also decrease.

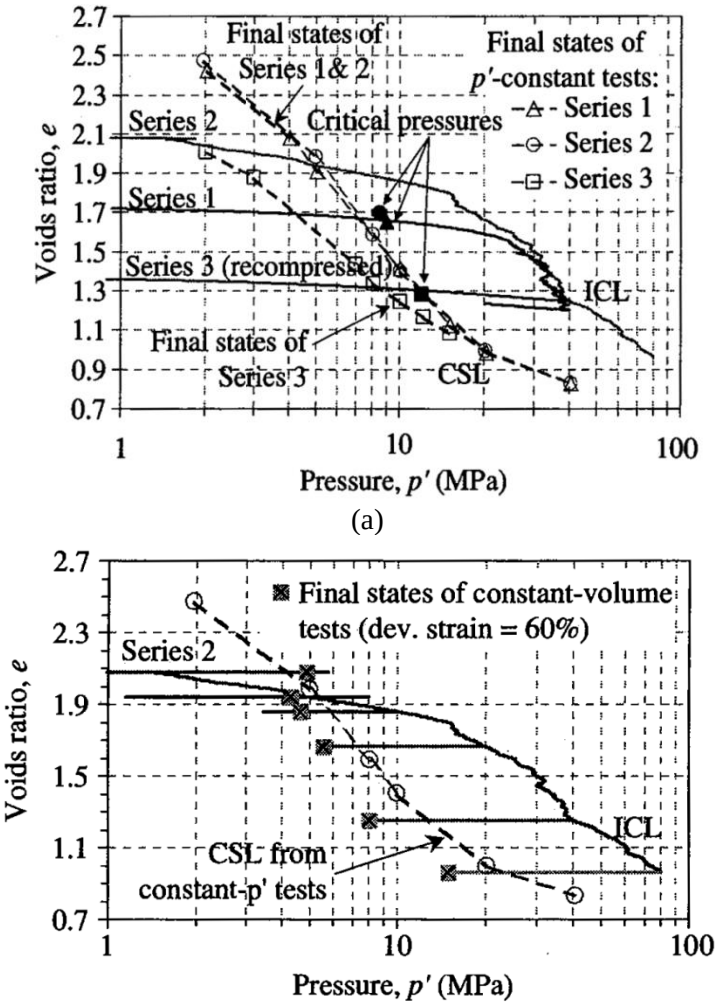

Figure 2.41 Critical state lines observed for soils: (a) different stress history; (b) different stress path(Cheng and Bolton, 2005).

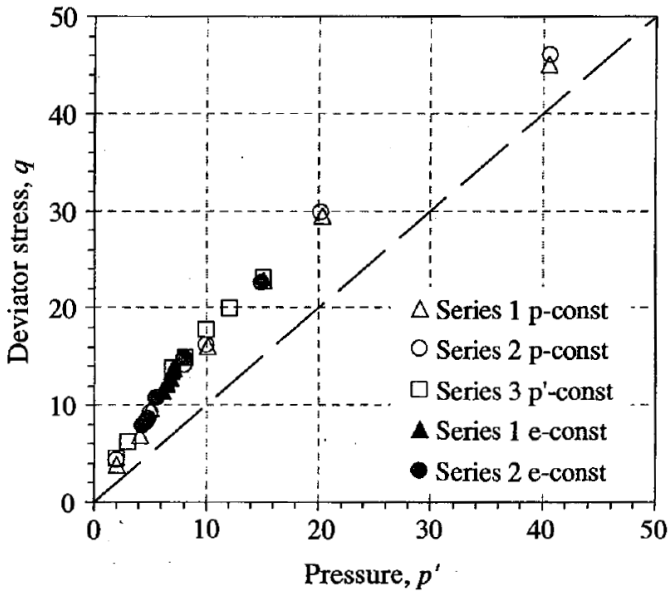

Figure 2.42 Deviator stress against pressure at final states, *i.e.* 60% deviator strain (Cheng and Bolton, 2005).

Sitharam and Vinod (2008) also investigated the Critical state behaviour of granular materials with an isotropic consolidation and unloading history. The study involved DEM and the use of a Java programme named TRUBAL, which is based on the model developed by Cundall (1978) and Cundall (1979). The shear tests with isotropic consolidation and unloading histories were carried on a sand assembly with a distribution of particle sizes and within a periodic space boundary, which is a unit cell within a large (infinite) space. In their preliminary simulation, the isotropic rebound path was found to coincide with the isotropic compression path. Hence, the properties of particles were modified in order to generate a rebound line with a reasonable slope. The shear stiffness of spheres was doubled during the unloading-reloading process. In other words, without crushing, the assembly behaviour is approximately elastic such that the unloading line coincides with the loading curve, and the apparent normal compression line in e-log p' space is simply a symptom of using the p' logarithmic scale. However, if the elastic stiffness is increased on unloading, the loading curve is

no longer followed and 'apparent' plastic behaviour is observed. Drained and undrained shear tests were carried out on the samples once they were isotropically consolidated and unloaded to target stress levels. The stress paths are given in Figure 2.43 and the achieved CSL is given in Figure 2.44. Sitharam and Vinod (2008) found that the critical state line is a unique curved line in *e*-log *p'* space, which contrasts with what Cheng *et al.* (2005) proposed.

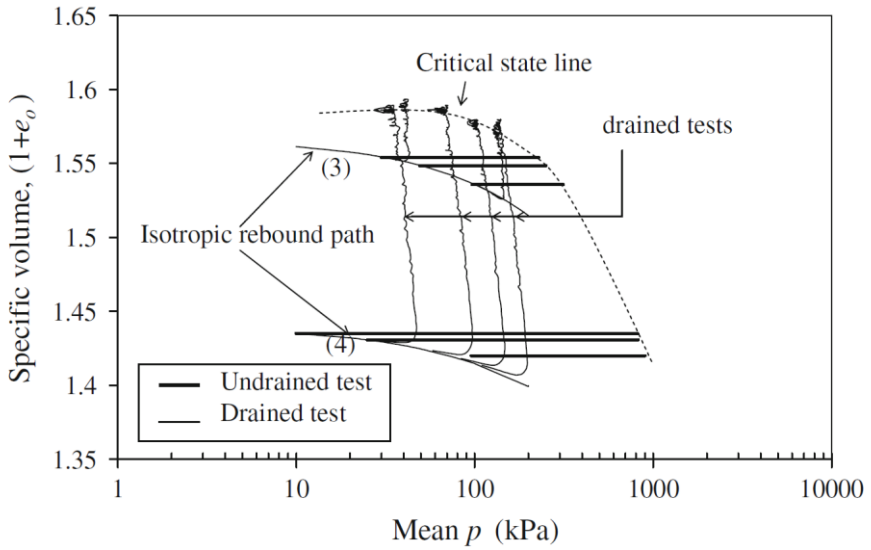

Figure 2.43 Variation of specific volume with mean stress under different stress paths for isotropically rebounded assembly of granular materials for different initial conditions (Sithram and Vinod, 2008).

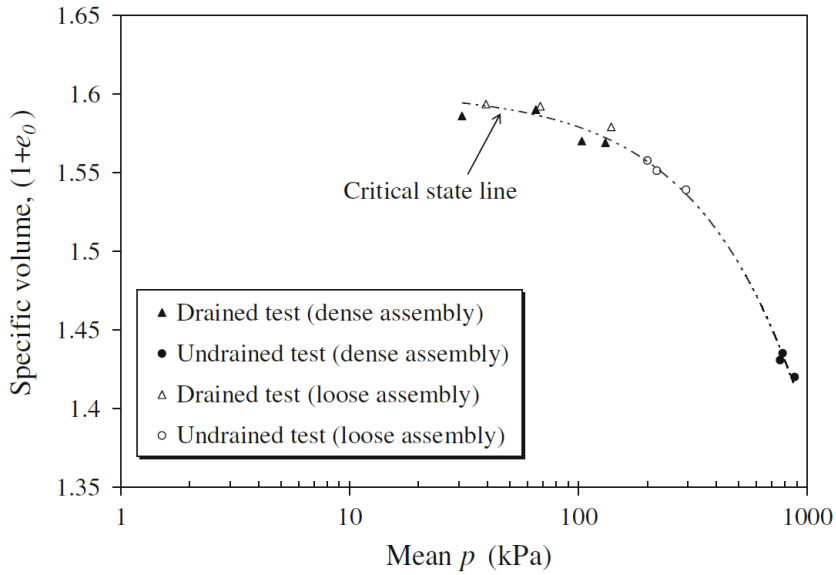

Figure 2.44 Critical state line for samples with different stress path (Sitharam and Vinod, 2008)

McDowell and de Bono (2013) applied the PBM described in Section 2.5.1 to link normal compression to the evolution of a fractal distribution of particles. The slope of the normal compression line is justified according to the mechanics of particle fracture. A sand sample with uniform particle size distribution was generated initially. Particle breakage continues as the compression stress increases. A normal compression line and an evolved grading were generated, at the end of the test. Figure 2.45 shows the change of the sample before and after compression. Many progeny particles are generated due to particle breakage. Figure 2.46 gives the evolution of the PSD as a function of applied stress. A well evolved PSD can be achieved using the PBM. Normal compression and unloading lines can be generated, as is shown in Figure 2.47. It can be seen that the existence of the normal compression line mainly results from plastic deformation, because the slope of unloading line is small and the elastic deformation makes up only a small amount of the total deformation.

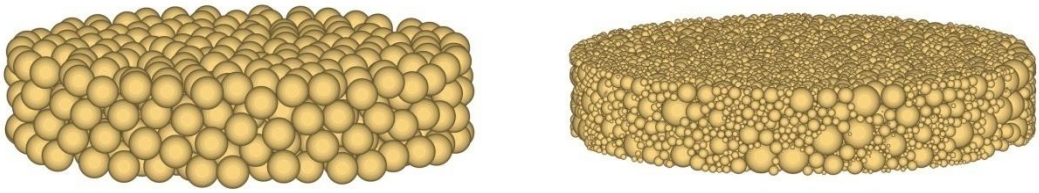

Figure 2.45 Numerical sample: (a) before compression; (b) after 100 MPa (McDowell and de Bono, 2013)

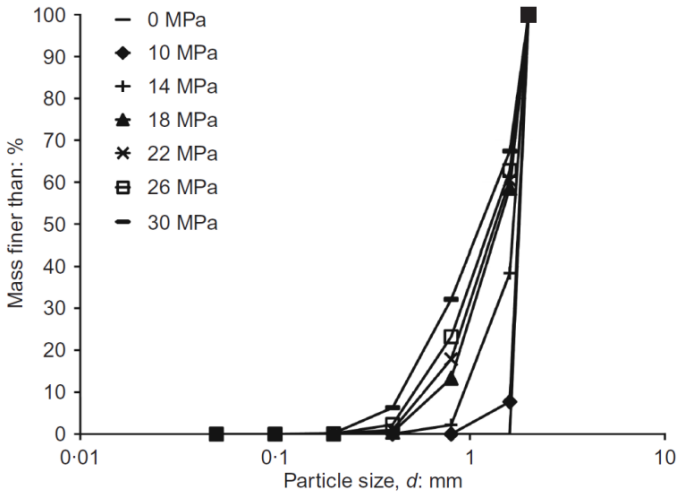

Figure 2.46 Evolving particle size distribution for simulation of silica sand (McDowell and de Bono, 2013)

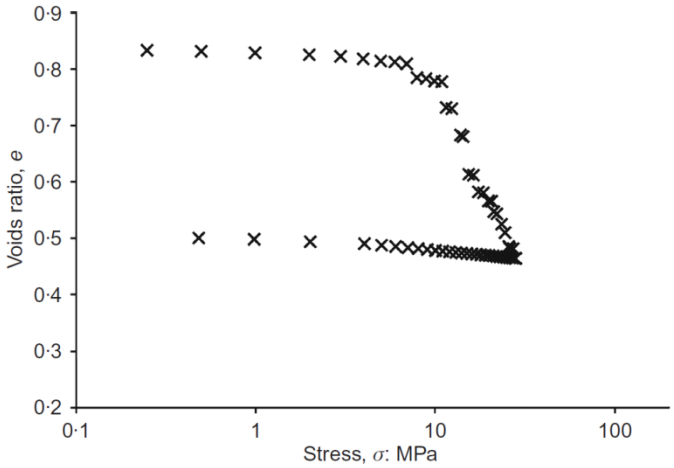

Figure 2.47 One-dimensional compression plot for simulation of silica sand (McDowell and de Bono, 2013)

McDowell and de Bono (2013) investigated the influence on normal compression behaviour of: (1) particle strength q_0, by assigning different q_0 values to the initial particles with a uniform size distribution; (2) a comminution limit, by setting a smallest size beyond which particles are no longer crushable; (3) the initial grading, by generating a new sample with a different PSD whilst maintaining the hardening law and initial q_0 unchanged; (4) the Weibull modulus *m*, by giving a different *m* value, so that both the variability of the distribution of strength and the hardening law are changed at the same time; and (5) the breakage mechanism, by applying trilateral and quadrilateral breakage mechanism, as has been shown in Figure 2.30 (b) and (c).

Figure 2.48 shows the normal compression lines for different initial strength, q_0, and the normalized stress-strain curve. The 'average' or 37% particle strengths, q_0, of each sample which follow the Weibull distribution are listed on the figure. It can be seen from Figure 2.48 (a) that the yield stress increases with increasing average particle strength. The coincident normalized curves in Figure 2.48 (b) further show that the yield stress is proportional to individual particle strength.

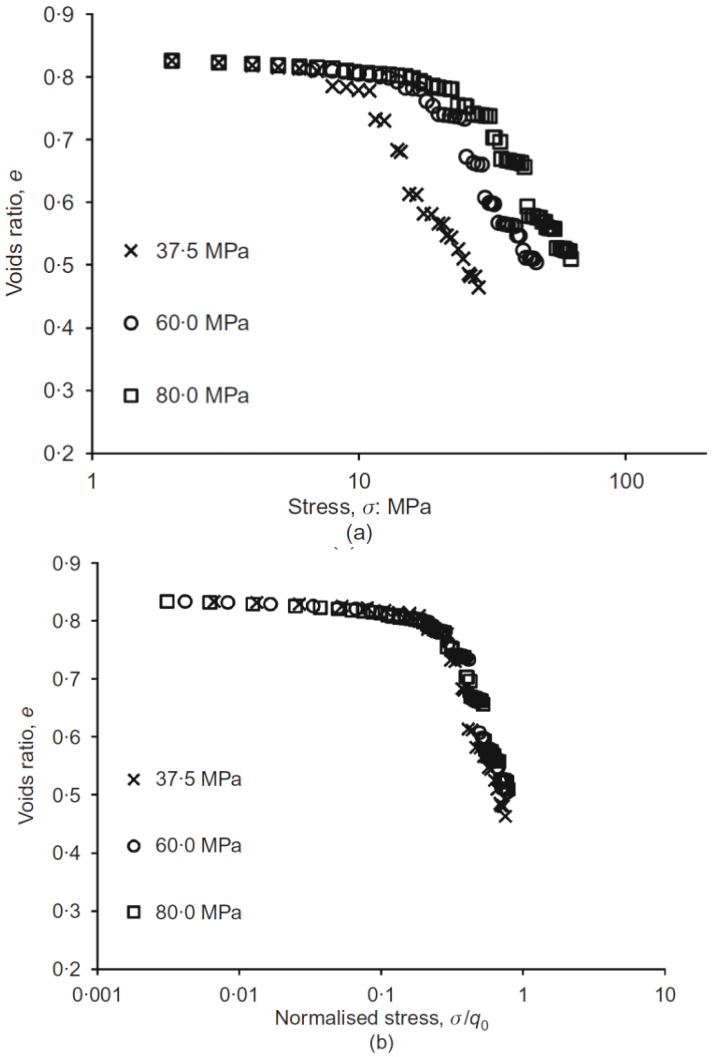

Figure 2.48 One-dimensional compression plots for: (a) various particle strengths q_0; (b) vertical stress σ normalised by particle strength q_0 (McDowell and de Bono, 2013)

Figure 2.49 compares the original normal compression curve and the curve for a sample with a comminution limit. An obvious turning can be seen when the applied

stress exceeds a certain level. The increasing quantity of uncrushable small particles leads to the failure of large particles, which is also the case for Cheng *et al.*'s (2003, 2004, 2005) work, leading to inaccurate interpretation of soil behaviour.

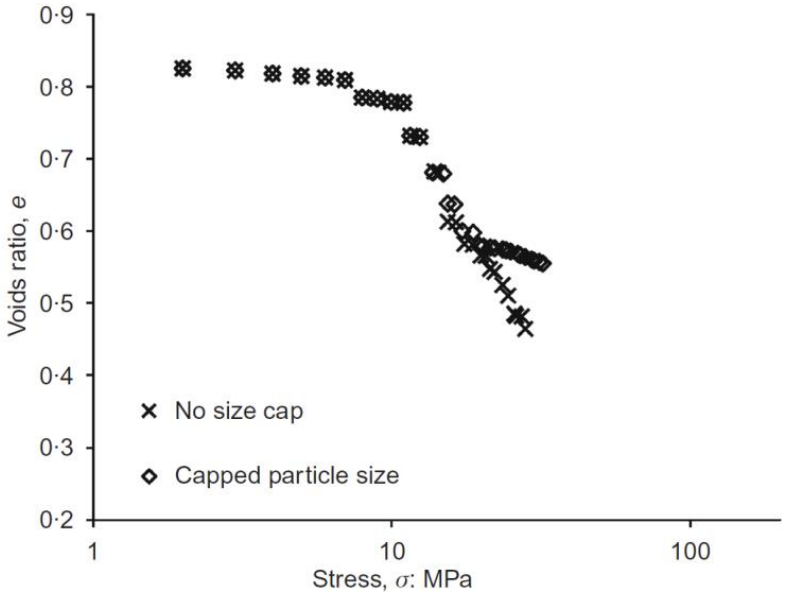

Figure 2.49 Effect of comminution limit on compression plot (McDowell and de Bono, 2013)

Figure 2.50 shows the normal compression plots for mono-disperse and graded samples. Despite the difference in initial voids ratio and grading, the two compression lines converge, which means that the plastic compressibility index is a material constant independent of initial grading in McDowell and de Bono's (2013) simulation.

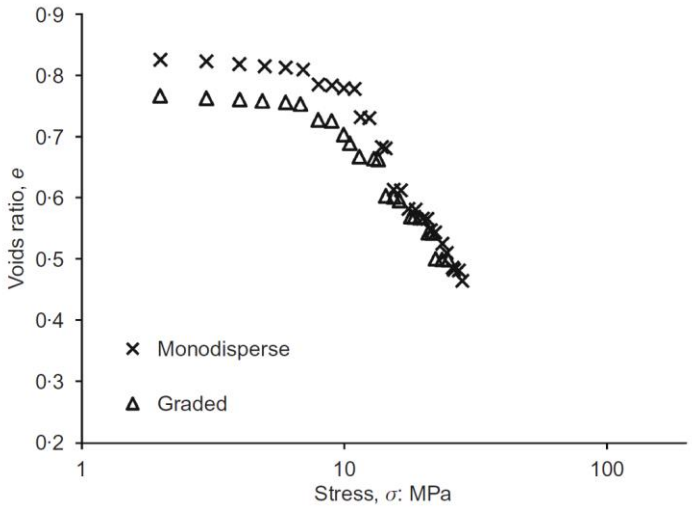

Figure 2.50 Effects of different grading on compression plot (McDowell and de Bono, 2013)

Figure 2.51 shows the normal compression plots for assemblies with different Weibull moduli while sharing the same initial PSD and average q_0. It can be seen that assemblies shows more obvious yielding with increasing Weibull modulus and the slope of normal compression line increases with increasing Weibull modulus.

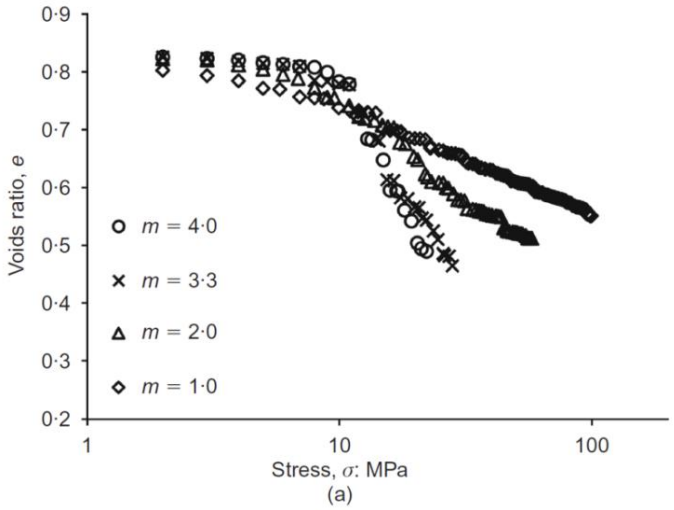

Figure 2.51 Effects of Weibull modulus on one-dimensional compression plots (McDowell and de Bono, 2013)

Figure 2.52 shows the normal compression plots and PSDs for assemblies following different breakage mechanisms. Not much difference can be observed. However the computational time can be reduced by applying a simple bilateral breakage mechanism.

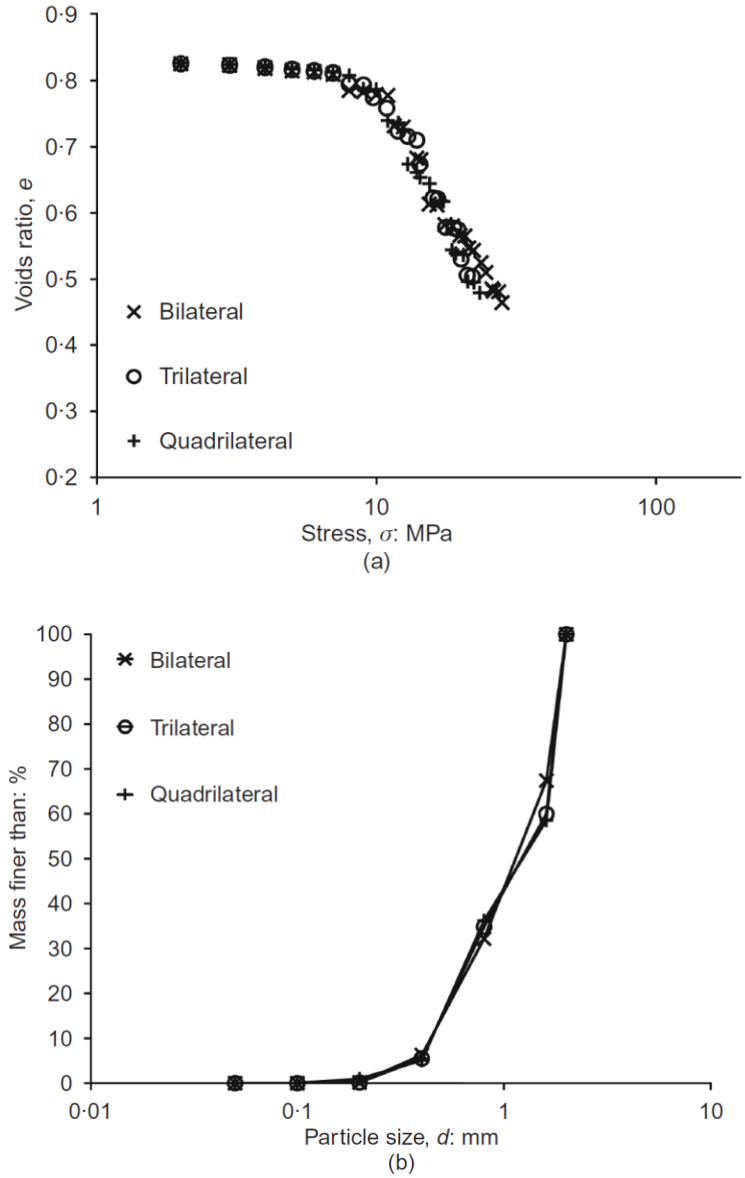

Figure 2.52 Effects of breakage mechanisms on (a) one-dimensional compression plots ; (b) final particle size distribution (McDowell and de Bono, 2013)

McDowell and de Bono (2013) also measured the fractal distribution as the slope of PSD, according to $N(L > d) \propto d^{-D}$, when plotted with two logarithmic axes, as has already been introduced at the beginning of Section 2.3.4. Figure 2.53 shows the evolving PSD with increasing stress. The slope of the PSD curves were then taken to plot the fractal dimension as a function of stress, see Figure 2.54. They showed that the fractal dimension evolved towards a final value of 2.5, which is consistent with

other researchers' observations (Turcotte, 1986; Sammis *et al.*, 1987; Palmer and Sanderson, 1991; Steacy and Sammis, 1991; McDowell and Daniell, 2001).

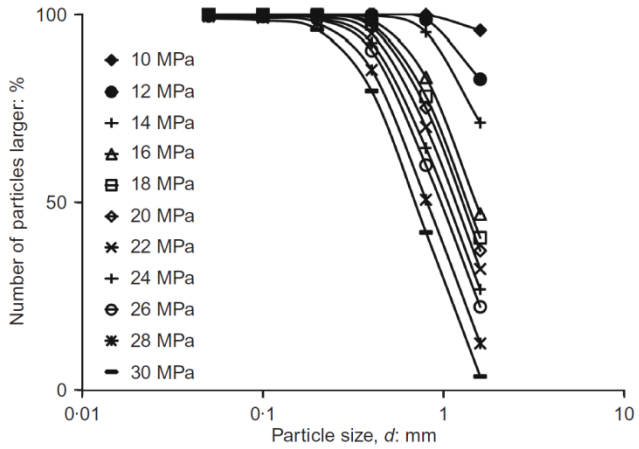

Figure 2.53 Evolving particle size distribution from simulation of silica sand plotted on double logarithmic axes (McDowell and de Bono, 2013)

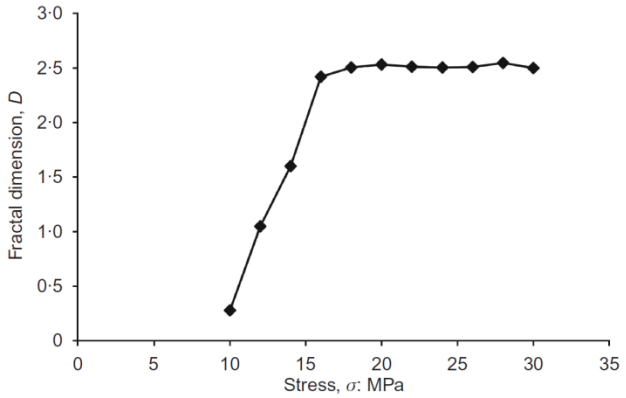

Figure 2.54 Fractal dimension as a function of stress (McDowell and de Bono, 2013)

Their simulation results show similarity with widely reported soil behaviour observed in field work and lab tests. The simple bilateral splitting breakage mechanism developed by McDowell and de Bono (2013) will be applied in this project, because it has been shown to capture the essential features of 1-D normal compression very nicely and gives the correct slope of the compression line because the problem of

having agglomerates with internal voids that become external voids when fracture occurs, has been avoided.

2.6 Summary

This chapter reviewed the development of critical state soil mechanics; the important role that particle crushing plays within the CSSM framework; the discrete element method (DEM) that can be applied to investigate granular materials and studies employing DEM to interpret critical state soil behaviour.

It is widely agreed that soil will achieve a critical state whereby under drained conditions deformation continues at constant volume and constant effective stresses to large shear strains. The critical state framework was first proposed independently by Parry (1956) and Roscoe *et al.* (1958).Various constitutive models have been proposed to explain critical state behaviour: the "Original" Cam-clay model (Roscoe *et al.*, 1958), MCC (Roscoe and Burland, 1968), CASM (Yu, 1998) and a similar model by McDowell (2002). McDowell's (2002) model tried to incorporate some micro mechanics by using McDowell and Bolton (1998) work equation incorporating particle fracture and this idea of using micro mechanics, and in particular, particle crushing, to explain soil plasticity is at the heart of this thesis. Therefore the role of particle crushing in one dimensional compression, isotropic compression, unloading and shearing to critical states has been examined by studying the existing literature to establish what further research is required - which is the subject of this dissertation.

The literature review has shown that although the agglomerate/BPM method has been able to explain qualitatively yielding and critical states, there are deficiencies such as $q \neq Mp'$ at critical state (that is to say M is not a constant as the mean effective stress

at failure increases) and voids ratio cannot be correctly quantified. The PBM model (McDowell and de Bono, 2013) shows promise and has produced good results in 1-D compression. This thesis therefore aims to extend the application of this model to the isotropic normal compression of soil, unloading and shearing to critical states, peak strength and dilation and the existence of a yield surface. None of the research reviewed in this chapter has been able to quantitatively explain these phenomena using micro mechanics. This is now what this thesis will attempt to shed light on.

Chapter 3 Methodology

3.1 Introduction

The investigations of this project are based on the discrete element modelling of fundamental geotechnical tests on crushable silica sand. The aim of the project is to link the macro mechanical behaviour of sand with the micro crushability of a single sand particle. The simulations of this project were performed using *PFC*^{3D}, the commercial software developed by ITASCA (1994). Following this introduction, Section 3.2 describes the logic of how the critical state behaviour of silica sand was investigated using discrete element simulations. Particle fracture was simulated by applying the specific population balance model (PBM) that was developed by McDowell and de Bono (2013). Section 3.3 provides an introduction to PBM in detail. The sample generation method is introduced in Section 3.4. The oedometer test and isotropic test were simulated to justify the hardening law which can be seen as a size effect on average particle strength. The triaxial shear tests, following different stress paths, were conducted on isotropically over-consolidated samples to investigate the critical state mechanical behaviour of crushable sand in the simulations. The loading procedures of normal compression and triaxial tests are described in Section 3.5. Section 3.6 explains how the simulated stresses and displacements of walls were converted into the conventional stress and strain measurements.

3.2 General descriptions

As has been described in Chapter 2, there are four basic ingredients in an elasto-plastic constitutive model within the classic critical state soil mechanics framework: the

hardening law; the elasticity law; the yield criterion; and the flow rule. The normal compression lines, which can be plotted from 1-D and isotropic normal compression tests, provide the volumetric hardening law; the unload-reloading line, which can be achieved from unloading of consolidated samples, gives the elastic law; the shape of the yield surface defines a region in stress space enclosing elastic states; the flow rule gives the ratio of plastic volumetric to plastic shear strain as a function of stress ratio and the plastic potential is given by the normal to this strain increment vector in stress space when the plastic strain increments, ε_v^p and ε_q^p, are plotted along the associated q and p' axes respectively.

In order to investigate the critical state behaviour of crushable soils, such as silica sand, a 1-D normal compression test, an isotropic normal compression test, an unloading test and a triaxial shear test were simulated. As the triaxial shear tests are usually conducted on isotropically consolidated samples, the isotropic normal compression simulation should be conducted first, followed by unloading and finally the triaxial shearing. The logical progression of the simulation sequence is shown in Figure 3.1.

The importance of particle fracture in fundamental soil tests has been reviewed in Chapter 2. Crushing has generally been modelled using the discrete element method (DEM) via two alternative methods: the population balance model (PBM), *i.e.* replacing 'breaking' grains with new, smaller fragments; and the bonding particle model (BPM), *i.e.* using agglomerate by bonding small spheres together. As is noted in Chapter 2, the BPM has the problem of giving inaccurate voids ratios hence making it unsuitable for solving boundary value problems; while PBM ensures the infinite breaking of particles into small fragments and quantitatively accurate prediction of the

voids ratio, hence is more suitable for solving boundary value problems. Hence the McDowell and de Bono (2013) method is used whereby the new fragments overlapping each other are contained within the parent sphere.

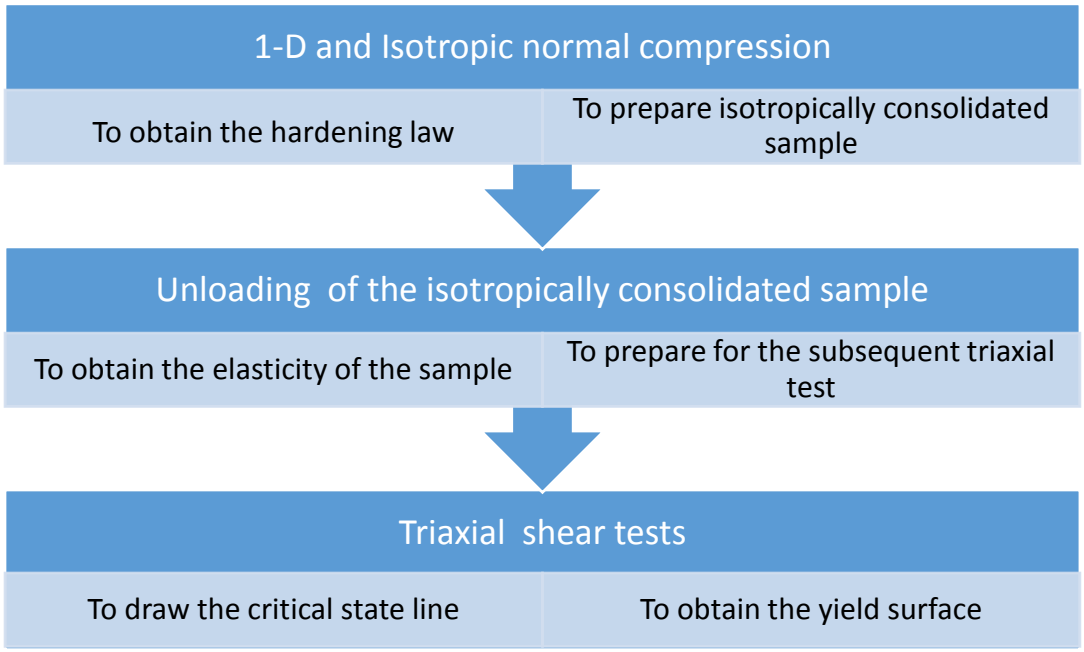

Figure 3.1 Logic of simulation of fundamental tests in this investigation

However PBM poses the problem of how to conserve mass （*i.e.* volume）when a particle splits: the fragments used to either overlap with each other or the immediate neighbours, which will cause the release of large forces because of the induced elastic energy required to push the overlapping fragments away from each other. The energy dissipation interval is hence introduced to release the induced large forces from overlapping.

3.3 Simulation of a single crushable silica sand particle

The particle forces act on each other and the boundaries through contact points in PFC. As has been described in Chapter 2: Hertz-Mindlin model produces a more realistic simulation than the simple linear model, hence the contacts between particles in this

project were defined by the Hertz-Mindlin model. The physical parameters of the simulated silica sand are given in Table 3-1, which were validated by McDowell and de Bono (2013).

Table 3-1 Physical parameters of a simulated sand particle

Input Parameter	Value
Particle Density	2650kg/m^3
Contact Model	Hertz-Mindlin
Shear Modulus, *G*	28GPa
Poisson's Ratio, υ	0.25
Particle Friction Coefficient	0.5

It should be noted that the influence of gravity was not considered in this project. Without the effect of gravity, floating particles would occur, contributing to the inaccuracy of mechanical reactions between particles in the simulation. However, the computational time would be dramatically increased when taking gravity into consideration. The influence of gravity was hence ignored in this study.

The stresses induced within particles by multiple contacts were calculated in PFC^{3D} using the octahedral shear stress which was calculated from the principle stresses, which are obtained from the stress tensor retrieved for each particle by PFC^{3D}, given by Eq. 2-79. The tensile strength, σ, and the induced octahedral stress, q, of a particle are proportional:

$$q = 0.9\sigma \tag{2-82}$$

where σ is the tensile strength calculated following Eq. 2-31 for a sphere under diametral compression. As has been described in Section 2.3.4, the clastic hardening law is the size effect on average tensile strength for crushable particles. Fracture of a

particle occurs when the calculated octahedral stress, q, is greater than the assigned value of q, using a Weibull distribution of strengths and size effect on average strengths. The initial particle size, d_0, is 2 mm for all the tests in this project with the corresponding octahedral stress, q_0, of 37.5 MPa. McDowell and de Bono (2013) compared three kinds of fracture mechanism (two, three and four equal-sized fragments) of particles and found that the mechanical behaviour is independent of the breakage mechanism. Hence the simple equal splitting (two fragments) mechanism is adopted here to reduce the computational time. Figure 3.2 shows the simple mechanism of replacing the parental large particle with two newly generated equal progeny particles. The total mass and volume of the progeny particles are equal to the parental particle. Axis 1 in Figure 3.2 stands for the direction of major principle stress; axis 3 stands for the direction of minor principle stress. The two progeny spheres lie within the parental sphere's boundary and the centres of the progeny spheres lie along axis 3, so that the progeny spheres will move apart along the minor principle stress direction due to the overlap, which is similar to what can be seen in the Brazilian test (plane strain test), where fragments move apart perpendicular to the compression direction, shown in Figure 2.15. Furthermore, no artificial size limit was set in particle breaking process, i.e. large parental particles could break into infinitely small particles as long as the crushing functions were met, as was in reality.

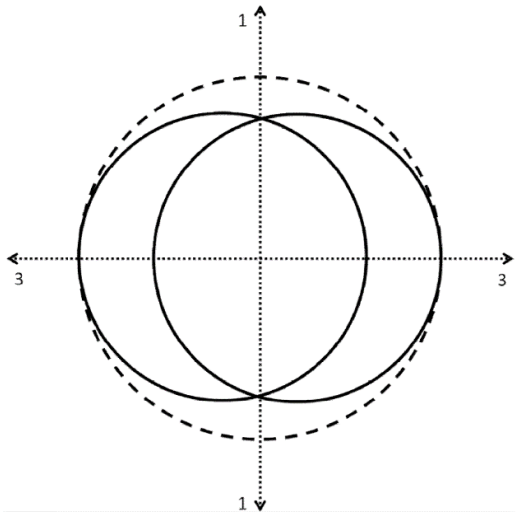

Figure 3.2 Simple particle splitting mechanism (McDowell and de Bono, 2013)

When a particle breaks in reality, internal elastic stored energy is released as new surface area is created. The fracture is a catastrophic event. This process is accounted for here by the overlapping spheres: the huge overlap causes a sudden release of elastic energy as the fragments move apart. As has been noted above, energy dissipation should be involved in the PBM to reduce the disturbance from the large overlap. The energy dissipation is realized by giving a certain number of cycles to the whole sample that are equivalent to a period of time in reality once new progeny particles are generated. The number of cycles, N_{cy}, in PFC^{3D} is calculated by

$$N_{cy} = T/tdel \tag{3-1}$$

where T stands for the real period of time and $tdel$ is the critical time step in PFC^{3D}, which increases with the increasing mass and decreases with the increasing stiffness of a particle. The period of time, T, to allow for energy dissipation is modified for different tests, for example, when there are more particles crushing more overlapping progeny particles are generated and a longer energy dissipation time is demanded to reduce the disturbance of the whole system.

Although the energy dissipation process was applied in the simulation, there still existed small amount of particle overlap, because the contact forces between particles were generated from overlapping area in PFC, resulted in volume reduction of solids, contributing to the inaccuracy in calculation of voids ratio. The overlapping effect was minimised, although could not be avoided, by applying Hertz contact model instead of Linear contact model, as has been explained in Chapter 2. The influence of the two contact models were also examined in Section 5.4.2.

3.4 Sample generation

As has been introduced in Chapter 2, the oedometer test is usually used for 1-D normal compression and the triaxial test can be used to measure K_0 or to perform different stress paths on a sample with a 'natural' (one-dimensional) history. The low aspect ratio of the oedometer sample reduces the length of the edge boundaries. This is necessary to minimise the effect of boundary shear stresses which would otherwise result in a difference between upper and lower normal stresses (McDowell *et al.*, 2003). McDowell and de Bono (2013) used a scaled down oedometer sample in their 1-D compression test to reduce the number of particles to an acceptable number and give a practical computational time. To compare with their 1-D result, isotropic normal compression was conducted on an identical oedometer sample. In the lab, isotropic compression is usually conducted in the triaxial apparatus. The height of the cylindrical sample is usually two times the diameter in the apparatus to reduce end effects, *i.e.* the friction between the top and bottom pedestal and the sample, and to ensure that it is kinematically admissible for a rupture to propagate through the sample if it's sheared from a dense overconsolidated state. The confining pressure in the

triaxial apparatus is applied by a cell pressure acting on a confining rubber membrane. This provides a constant stress boundary condition with free lateral movement. However, by applying the servo-control introduced in Section 2.4.3, a rigid confining boundary can provide control of the confining stress in the *PFC*^{3D} simulation. This boundary in *PFC*^{3D} does however prevent differential radial strain along the height of the sample with the consequence of not being able to observe any kind of shear rupture of the sample, because such a rupture would be kinematically inadmissible. At the same time, the end and side effects caused by friction can be avoided in the simulation by setting the friction coefficient of the confining wall and the upper and lower plates to zero. In addition to the oedometer sample, an alternative triaxial sample was also generated in this investigation. Isotropic compression on the triaxial sample is also simulated to prepare for later triaxial shear tests.

The sample generation started with generating the boundaries, *i.e.* walls in *PFC*^{3D}, at the target locations. The wall stiffness was the same for top, bottom and cylindrical confining walls and was set to be large enough, $10^7\ \mathrm{N/mm^2}$, to avoid particle escaping or large overlap with contacted particles. It is possible for particles to 'escape' because the DEM 'soft contact' approach permits overlap when the contact stiffnesses are not sufficiently high.

The radii expansion method (Itasca, 2005) was then applied to generate a dense random packing of the sample without large overlap between particles:

• For the chosen volume of cylinder, and the target voids ratio of the sample, calculate the total volume of particles; given the volume of each particle and the total volume, calculate the total number of particles

• Generate walls at chosen positions, *i.e.* flat walls at top and bottom and a cylindrical confining wall, with chosen stiffnesses, *i.e.* 10^7 N/mm^2.

• Generate particles with half target diameter at random locations within cylinder

• Gradually expand balls to achieve final diameter.

• Make adjustments to walls to avoid particle overlap and excessive internal forces before the sample is ever loaded.

The parameters for the oedometer sample and the triaxial sample are listed in Table 3-2. Figure 3.3 shows the initial generated oedometer and triaxial samples.

Table 3-2 Initial parameters of oedometer and triaxial samples

	Number of particles	Cylinder height, h_r,mm	Cylinder diameter, D_r,mm	Voids ratio, e	Aspect ratio,l_r=h_r/ D_r	Wall stiffness, N/mm^2	Wall friction coefficient
Oedometer	620	7	30	0.90	0.233	10^7	0
Triaxial	390	18	15	0.94	1.2	10^7	0

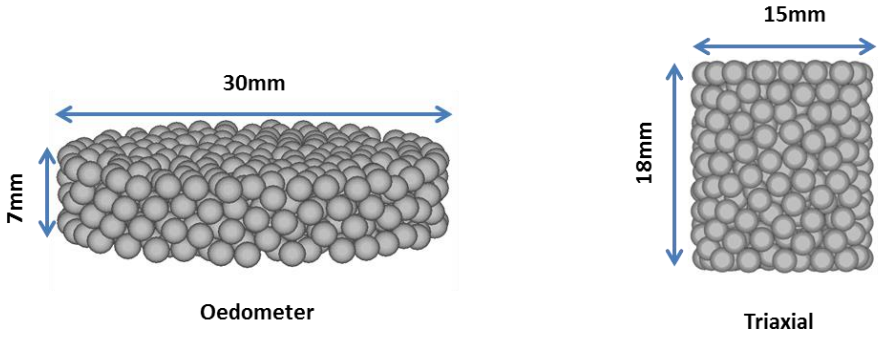

Figure 3.3 The initial monodisperse oedometer and triaxial samples

3.5 Loading procedure

3.5.1 Loading method: stress control & strain control

As has been introduced in Chapter 2, the calculation in *PFC*^{3D} is based on the iteration of the law of motion and the force displacement law. The servo-control, which relates

the target stress applied by the wall to the velocity of the wall, was employed for stress control simulations. The velocity of the wall was modified after each small time increment to control the applied stress. The key factor in servo-control was the gain parameter, G_a. The calculation of the gain parameter, G_a, has been described in Section 2.4.3 Eq. 2-77. The safety factor, α, which maintains the deviation of stress within a target limit to control the stress path, was set to be 0.1 in this project. The gain parameter was updated every 100 cycles to reduce the calculation time. For strain control simulations, a constant velocity was assigned to the wall and the induced stress, the sum of contact forces acting on the wall divided by the area of the wall, is calculated after each small strain increment. The internal stresses (as opposed to boundary stresses) was calculated using a 'measurement sphere' within PFC^{3D}.

3.5.2 1-D and isotropic compressions

The servo-control of the top wall was employed when simulating the 1-D compression test. The vertical load was applied in 0.5 MPa increments, and the octahedral stress of each sphere was calculated for every sphere. The loading procedure can be regarded as the iteration of two basic loops: a loop of particle breakage; and a loop of applying target stress. The particle breakage loop is the iteration of two steps:

- Search for 'qualifying' spheres and replace the parent sphere with two new progeny spheres according to the splitting mechanism: A particle, with diameter d_i, will crush according to the splitting mechanism described previously, when the calculated octahedral stress is larger than the predetermined q_i according to a Weibull distribution with a size effect on average strength, according to Eq. 2-84.

- Energy dissipation interval: After every ‘qualifying’ crushable sphere was replaced with two new progeny spheres, a number of cycles that equals to 0.003s were applied to the whole sample, following McDowell and de Bono (2013). The time should be large enough that the breakage of particles will not change when increasing the interval, allowing for the energy from the large particle overlaps to dissipate, *i.e.* particles with large overlaps moving apart to reduce the large induced contact forces. The time for energy dissipation may be increased when there are too many particles breaking.

When the system became stable, the octahedral stresses for all the spheres were calculated again and the ‘qualifying’ spheres crush. Another 0.003s was then required for energy dissipation. The loop continues until there was no particle breakage. The stress on the top wall may reduce, sometimes significantly, after particle crushing. Then the loop of applying the target stress was re-started:

- Adjusting the applied stress back to the target value: The servo-control of the wall is applied to modify the speed of the wall until the target stress is achieved.
- Applying the loop of particle breakage: The increased stress may result in more breakages according to the same sequence and the loop of particle breakage is applied until no more breakage occurs.

The same procedure iterated until the target stress was achieved after all the ‘qualifying’ spheres were crushed. The next stress increment was then applied. The logic of the loading procedure is shown in Figure 3.4.

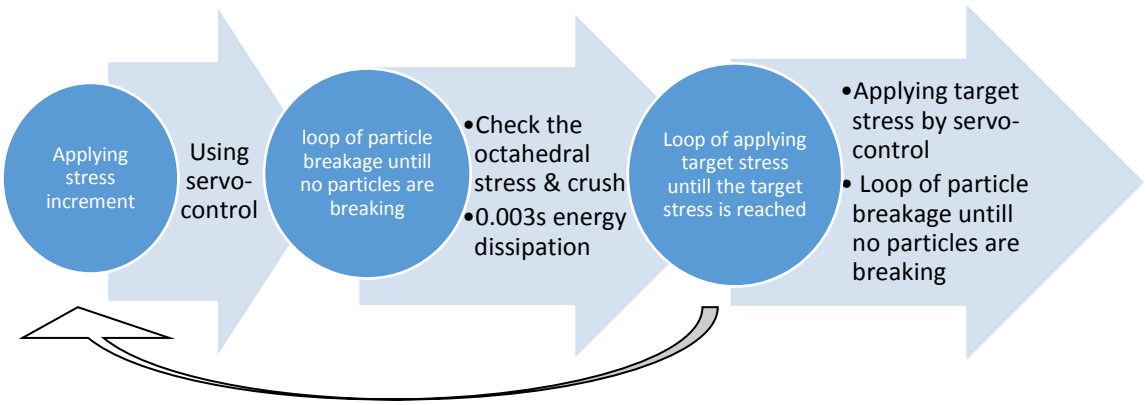

Figure 3.4 Logic of loading procedure for normal compression

The same logic of loading procedures, shown in Figure 3.4, as applied to the 1-D compression, was applied in the isotropic compression simulations. The servo-control was applied to both the top and the lateral confining walls in the isotropic simulation, while the bottom wall stays static during the loading procedure. The same target stress was assigned to both the top and the confining walls to achieve the isotropic stress state. A smaller stress increment, 0.25 MPa, was applied for the isotropic test than the 1MPa used for the oedometer test. This is because both the top and lateral confining walls are moving in the isotropic test and more rearrangement of particles may occur, so a lower stress increment is required.

3.5.3 Triaxial shear test

The loading procedure in the triaxial test involves the strain control of the top wall and stress control of the confining wall. Two kinds of triaxial test were simulated in this project: conventional triaxial test and constant mean effective stress (p') triaxial test. The strain increment and the velocity of the top wall was smaller for a constant-p' test than for a conventional test. This is because in a constant-p' test the change in axial stress, $\Delta\sigma_a$, is related to the change in confining stress, $\Delta\sigma_r$, by

$$\Delta\sigma_a = -2\Delta\sigma_r \quad (3\text{-}2)$$

Since the lateral confining wall is being unloaded, the change in axial stress has to be applied more slowly than the conventional test.

The servo-control was employed to control the pressure of the lateral confining wall: to maintain the constant confining pressure for the conventional test; and to maintain the constant mean effective stress for the constant p' test. The energy dissipation interval for the conventional test is larger than for the constant p' test, because, for samples starting from the same initial stress state, the one undergoing a conventional test is under a higher mean effective stress than the one in the constant p' test; the higher stress may lead to more particle crushing so a longer energy dissipation time is required. Table 3-3 gives the loading parameters involved in the triaxial tests.

Table 3-3 Loading parameters for triaxial shear tests

	Velocity of the top wall, m/s	Strain increment, %	Energy dissipation time, s	Servo-control target
Conventional	0.01	0.1	0.005	constant σ_r
Constant *p'*	0.001	0.005	0.003	constant *p'*

The logic of the loading procedures is the same for both the conventional and constant p' tests. The strain increment was applied to the top wall and the servo-control was applied to the confining wall at the same time. Once the target strain increment was achieved, the particle breakage loop, the same as applied in normal compression simulations, is applied: the octahedral stress of each sphere was calculated; the 'qualified' particles were replaced with two progeny particles; then the energy dissipation interval was applied. The particle breakage loop continued until no further particles are breaking. Then another strain increment was applied followed by the

particle breakage loop. The logic of the loading procedures in triaxial tests is shown in Figure 3.5

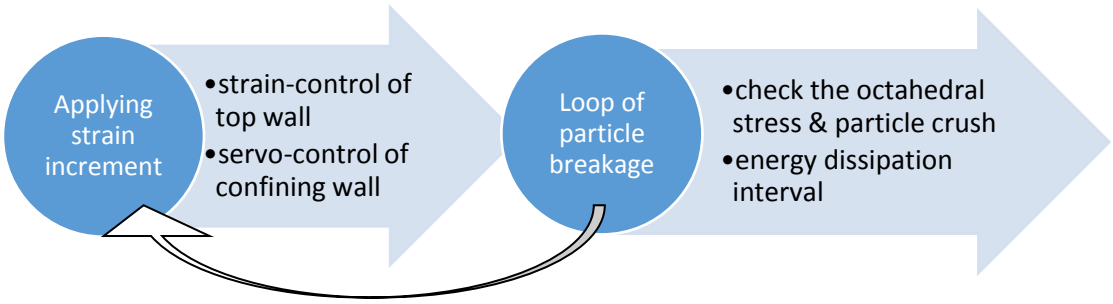

Figure 3.5 Logic of loading procedure in triaxial test

3.6 Measurement

3.6.1 Stress measurement

The stress measured on a wall in PFC^{3D} is given as the sum of all the contact forces acting on the wall divided by the area of the wall:

$$\sigma_{wall} = \frac{\sum F_i}{A_{wall}} \tag{3-3}$$

where F_i is the contact force at each contact of the wall; A_{wall} is the area of the wall. The stress on the top wall, σ_{top}, bottom wall, σ_{bottom}, and side wall, σ_r, are calculated using Eq. 3-3.

In order to accurately measure the stresses on walls, the vertical stress, σ_1, was calculated as the average value of the stress measured on the top wall, and the stress measured on the bottom wall, although the stress on the two walls were approximately the same.

$$\sigma_1 = \frac{\sigma_{top} + \sigma_{bottom}}{2} \tag{3-4}$$

3.6.2 Strain measurement

The voids ratio, e, is calculated as the volume of voids over the volume of solids. In this simulation, the volume of solids is taken as the total volume of spheres, V_{balls}, which is constant through all the tests; and the volume of box, V, is updated during the loading procedure. Hence the voids ratio is

$$e = \frac{V - V_{balls}}{V_{balls}} \tag{3-5}$$

The axial strain,ε_1, is calculated as:

$$\varepsilon_1 = \frac{\Delta h}{h} \tag{3-6}$$

where h denotes the height of the cylinder at the beginning of the test and Δh denotes the change in the height of the cylinder at the current time.

The radial strain, ε_r, is calculated as

$$\varepsilon_r = \frac{\Delta R}{R} \tag{3-7}$$

where R denotes the radius of the cylinder at the beginning of the test andΔR denotes the change in the radius of the cylinder at the moment.

The volume strain, ε_v, is conventionally taken as

$$\varepsilon_v = \varepsilon_1 + \varepsilon_2 + \varepsilon_3 \tag{3-8}$$

where ε_1, ε_2, ε_3 are strains on different stress directions.

However Eq. 3-8 is accurate only at small strains, while for large strain tests such as the triaxial shear test in this project, the volume strain cannot be calculated by simply adding ε_1, ε_2, ε_3 together. For triaxial tests in this project, the volume strain is

$$\varepsilon_v = \frac{\pi(R+\Delta R)^2 - \pi R^2}{\pi R^2} = 2\varepsilon_r + \varepsilon_1 + {\varepsilon_r}^2 + 2\varepsilon_1\varepsilon_r + {\varepsilon_r}^2\varepsilon_1 \tag{3-9}$$

At the end of the triaxial test, the axial strain could be as large as 20% to 30%; the same is true for the radial strain, so the last three components in Eq. 3-9 cannot be neglected. Hence the volume strain in this simulation is calculated as the change of volume of the cylinder box, ΔV, divided by the volume at the beginning, V:

$$\varepsilon_v = \frac{\Delta V}{V} \tag{3-10}$$

3.7 Conclusions

The logic has been introduced on how to design the fundamental tests in this project to investigate critical state behaviour of sand. The simulation method using *PFC*^{3D} has been described. The simple splitting PBM applied in this project has been introduced to model crushable silica sand. All the normal compression and triaxial tests are conducted in cylinders made with stiff walls. The initial generation method, involving radius expansion, in an oedometer sample and triaxial sample has been described. The loading procedures of different tests have been described. The applied stresses in normal compression tests are servo-controlled. The particle crushing loop in normal compression involves the calculation of the octahedral stress of each particle and the energy dissipation time after each particle crushing cycle. The loading procedure in the triaxial test involves the strain control of the top wall and servo-control of the lateral confining wall, and the particle crushing loop is the same as that for the normal

compression test except that the time for energy dissipation is modified for the conventional test. The measurement of basic stress and strain parameters from the simulations has also been introduced.

Chapter 4 Discrete Element Modelling of 1-D and Isotropic Normal Compression

4.1 Introduction

McDowell and de Bono (2013) successfully modelled one-dimensional normal compression of an oedometer sample considering particle fracture. The crushable particles are simulated by applying the population balance model (PBM) and considering the stresses induced in a particle due to multiple contacts. The normal compression line was found to be due to the evolution of a fractal distribution of particles, *i.e.* the crushing of particles at a constant fractal dimension, as has been described in Chapter 2. The slope of the one-dimensional (1-D) normal compression line (NCL)was found to be governed by the clastic hardening law, as is discussed in detail later (Section 4.3), and should be linear in $\log e - \log p'$ space.

The isotropic normal compression line is of fundamental importance as it is a pre-requisite for the study of overconsolidated materials and the development of constitutive models. In order to investigate the difference between the 1-D and isotropic normal compression, the isotropic normal compression test on an identical sample to that used by McDowell and de Bono (2013) with the same initial parameters, is modelled. The same PBM as used by McDowell and de Bono (2013) has been adopted for this investigation. The isotropic compression of the oedometer sample was simulated to check how the anisotropic distribution of local stresses causes particle crushing; whether the clastic compression would generate an isotropic normal compression line; whether the isotropic normal compression line might be parallel to

the one-dimensional normal compression line when the logarithm of voids ratio is plotted against the logarithm of mean effective stress; and whether the hardening law, described in Section 2.3.4, also governs the existence of the isotropic normal compression line for a crushable material. The above issues have been presented in McDowell *et al.* (2013), as shown in Appendix D.

In order to investigate the critical state behaviour of crushable soil, triaxial tests are involved later in this project. In order to simulate triaxial tests, isotropically consolidated samples should be prepared. However, the shape of the oedometer sample which suits the one-dimensional test, due to its low aspect ratio which reduces wall friction developing on the outer edges, is generally of the wrong aspect ratio for triaxial tests, which needs to have a larger value to reduce end effects and to allow enough space for a shear plane to develop; therefore another sample with a different geometry (aspect ratio) is required. The new sample, with a higher aspect ratio, will be referred to as the 'triaxial sample'. In this chapter a one-dimensional normal compression test is conducted on the triaxial sample, and the influence of aspect ratio is investigated by comparing the results of the one-dimensional compression on the two different samples, *i.e.* oedometer and triaxial samples. For the DEM simulations, wall friction can be eliminated completely, so such aspect ratios are unnecessary. However, for a small number of particles, both large and small aspect ratios would give a large proportion of boundary particles, which this study will address, by examining an intermediate aspect ratio with a lower proportion of boundary particles.

Isotropic normal compression is then conducted on the triaxial sample in preparation for the subsequent triaxial tests as discussed in Chapter 5. Comparisons between the

one-dimensional and isotropic normal compressions on the triaxial sample are presented.

4.2 Comparison between isotropic and 1-D normal compression

The initial parameters for the oedometer sample are given in Section 3.4, and are identical to that used by McDowell and de Bono (2013).The same crushing criterion is applied here as was employed by McDowell and de Bono (2013) and described in Chapter 3.

Figure 4.1 shows the NCL generated for the simulation of the isotropic (ISO) compression test on the oedometer sample. The NCL for the McDowell and de Bono (2013) one-dimensional (1-D) simulation is also shown in the same figure. It is clear that the isotropic normal compression line generated using the octahedral shear stress crushing criterion is parallel to the 1-D normal compression line in $\log e - \log p'$ space, and both lines have a slope of approximately 0.5. This is very reassuring, because McDowell and de Bono (2013) proposed that the slope should be given by the hardening law for the size effect on particle strength, *i.e.* clastic hardening law (Section 2.3.4), and this should be independent of the loading conditions. The theoretical value, according to clastic hardening law, of the slope of the normal compression line in $\log e - \log p'$ space should be determined only by the fractal dimension, D, and Weibull modulus,m, as has been shown in Eq. 2-48. According to Eq. 2-48, the theoretical value of the slope of the normal compression line, $\frac{m(D-3)}{3}$, is 0.5, using $m = 3.3$ (as has been described in Section 3.2) and $D = 2.5$ (as has been observed in lab tests as described in Section 2.3.4). The yield stress (in terms of p') for the isotropic test is about 11 MPa, compared to about 8 MPa for the one-

dimensionally compressed sample. Due to the isotropic stress condition, more evenly distributed contact forces will result in relatively smaller octahedral stresses for particles, hence the particles under isotropic stress state are statistically 'less vulnerable' than under 1-D stress state and the sample under isotropic compression shows higher yield stress than under one-dimensional stress conditions.

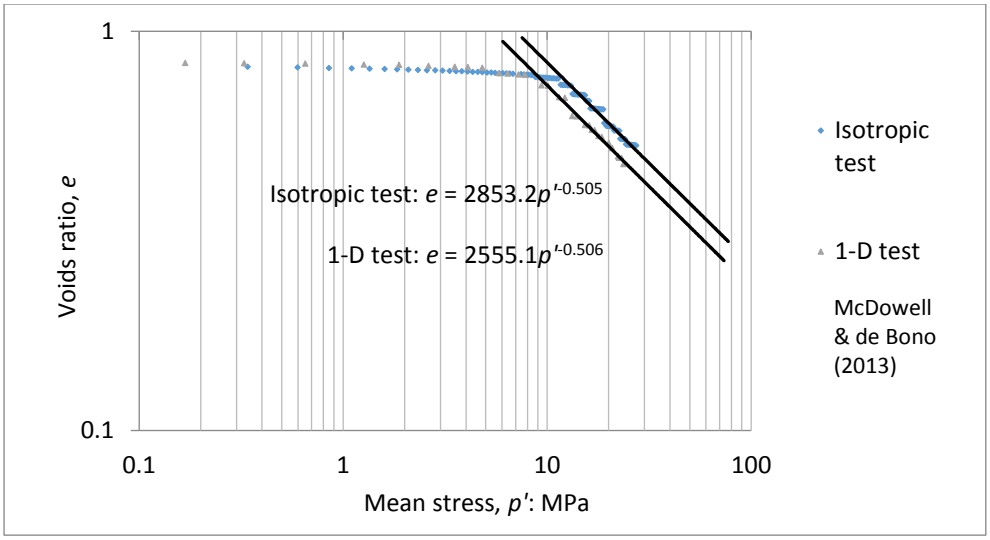

Figure 4.1 Normal compression plots for oedometer sample

The evolution of the particle size distribution for the oedometer sample under isotropic compression was measured in terms of the percentage of mass of particles smaller than a given size plotted against the logarithm of that size, in the traditional way (shown in Figure 4.2 (a)) and also by the alternative way, that is the percentage of number of particles larger than a given size (given in Figure 4.2 (b)), as described previously in Section 2.3.4. The equations depicted are for the linear parts of the curves in Figure 4.2 (b), *i.e.* the last two data points, and the exponent gives the fractal dimension assuming that the last two data points correspond to a fractal distribution, such that:

$$N(\mathrm{L} > d) \propto d^{-D} \qquad (2\text{-}40)$$

as has already been explained in Section 2.3.4. It can be seen that the fractal dimension is increasing to an ultimate value of 2.5, which is further shown by Figure 4.3 which

gives the evolving fractal dimension as a function of stress level. This is consistent with the findings of McDowell and de Bono (2013) for one-dimensional conditions.

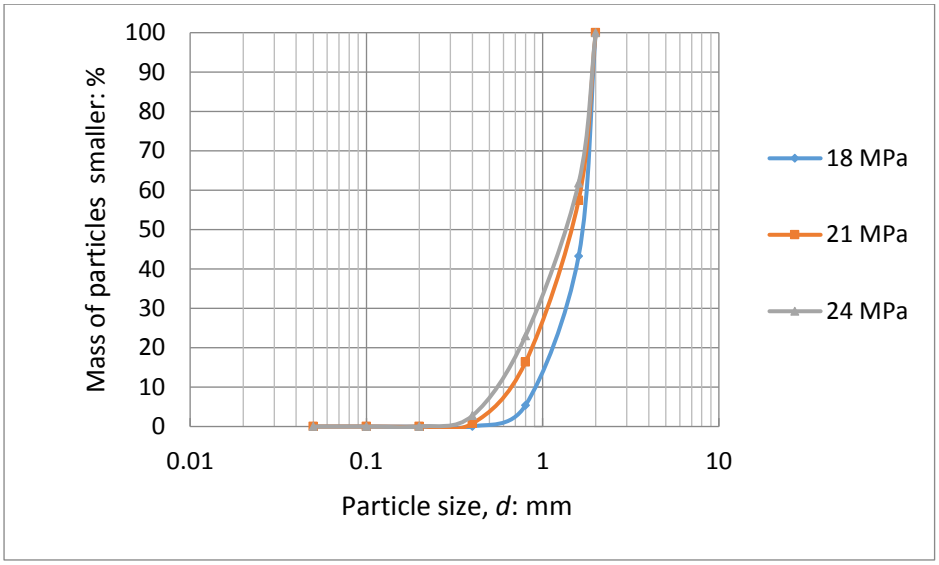

(a)

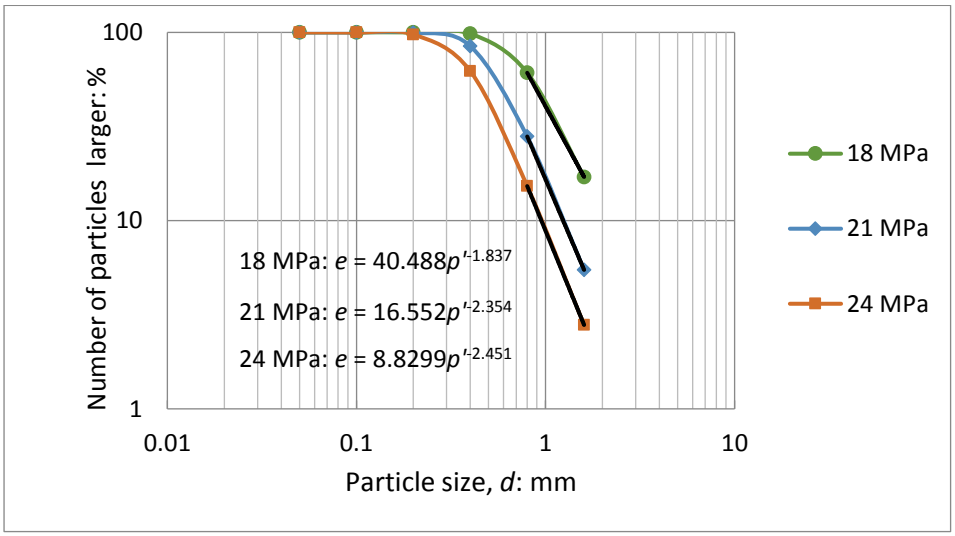

(b)

Figure 4.2 Evolving particle size distribution of oedometer sample: (a) traditional plot by mass grading curve and (b) fractal plot of number of particles on a log scale.

It is shown that particles continue to crush when the fractal dimension is reached and that the fractal dimension of 2.5 corresponds to the normal compression line with the slope of -0.5 in $\log e - \log p'$ space, following the clastic hardening law. The reason why this is important is that it has now been shown that the evolution of a fractal

dimension of 2.5 and the consequent normal compression line with a slope of 0.5 are not unique to one-dimensional conditions.

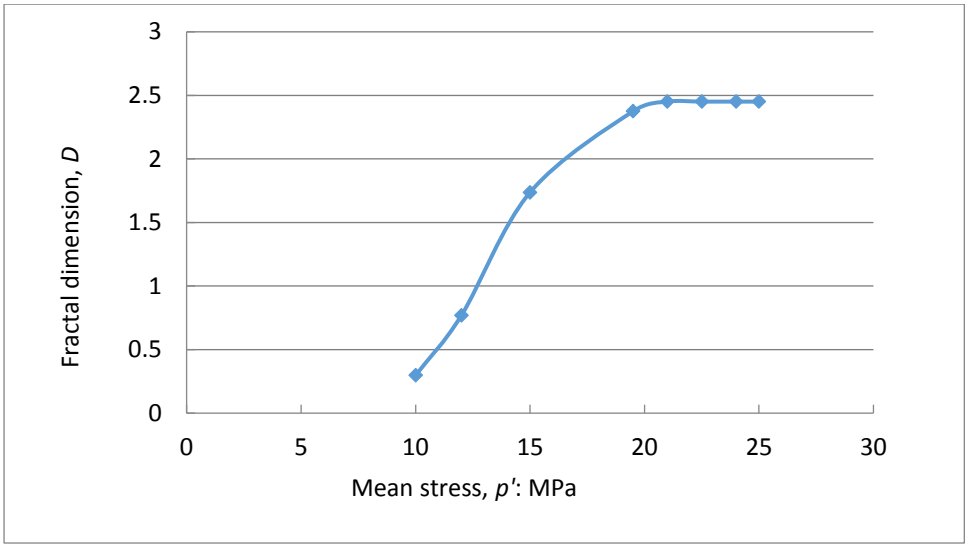

Figure 4.3 Evolving fractal dimension of oedometer sample under isotropic normal compression

To gain further insight into the micro mechanics of isotropic compression, and how it relates to the micro mechanics of one-dimensional normal compression, the particle size distributions of different points on the normal compression lines are then compared for the oedometer sample under 1-D and isotropic conditions (McDowell *et al.*, 2013). The data of the 1-D test of the oedometer sample are taken according to McDowell and de Bono (2013). Two groups of points are chosen, shown schematically in Figure 4.4.

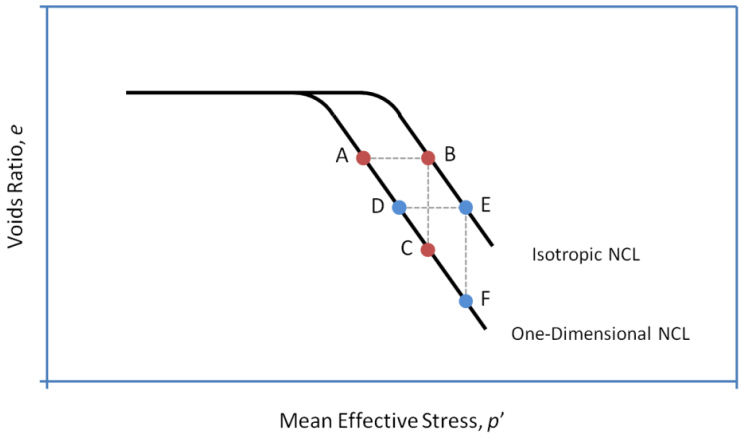

Figure 4.4 Schematic diagram on log-log axes, showing the two set of data points (ABC and DEF) at which the particle size distributions are compared

Group 1 contains three points: a point (A) on the one-dimensional NCL and a point (B) on the isotropic NCL at the same voids ratio; a point (C) on the one-dimensional NCL at the same mean effective stress as at point B. This procedure was repeated for a further set of points: D, E and F (Group 2), and all 6 data points are given in Table 4-1.

Table 4-1 Details of two groups of points chosen to compare the particle size distribution

	Group 1			**Group 2**		
Point	A	B	C	D	E	F
NCL	1-D	ISO	1-D	1-D	ISO	1-D
Voids ratio: *e*	0.565	0.565	0.485	0.525	0.521	0.464
Mean Stress: *p'*, MPa	17	21.3	21.3	20	24.3	24.3

Figure 4.5 shows the particle size distributions for the first set of data points A, B and C (Group 1) and the particle size distributions for D, E, F (Group 2) are shown in Figure 4.6. Both figures illustrate that the points at the same voids ratio on the one-dimensional and isotropic normal compression lines (*i.e.* points A and B from Group 1; points D and E from Group 2, respectively) have particle size distributions which

coincide. It is implied that the particle size distribution governs the volume change of the sample. The results appear to show that voids ratio correlates with the particle size distribution under these two different stress paths, even though the final samples are 'different' to each other when the initial samples are identical. This is perhaps not so surprising when it is considered that a strong correlation exists between average coordination number and voids ratio (Oda and Konishi, 1977). Additional comparisons of the local deviator stresses, *i.e.* the induced octahedral stress from multiple contacts, of pair A, B and pair D, E are given in Figure 4.7. The shape of the distributions of octahedral shear stress for points A and B are similar, although the values can't be exactly the same because a different local packing of particles will result in a different distribution of contact forces, which governs the octahedral stress using Eq. 3-1. The same can be observed for points D and E. Similar distributions of octahedral shear stress are observed for samples subjected to 1-D and isotropic normal compressions. Figure 4.7 also shows large induced octahedral stresses under isotropic stress conditions, which means that local anisotropy exists under macroscopic isotropic stress conditions and the induced octahedral stresses give rise to particle breakage, according to the applied breakage criterion. The aim of comparing the distribution of octahedral stress is to establish whether an isotropic stress state could give rise to a normal compression line through internal local anisotropy throughout the sample. The results have shown that at a given voids ratio, the particle size distributions are similar and given that the parallel normal compression lines have evolved through a particle size effect on average strength using the octahedral shear stress, q, then one might conjecture that at a given voids ratio, the distribution of q might be similar under both 1-D and isotropic conditions. Although there are localised

differences between the two distributions in Figure 4.7 at the two different voids ratios, they are indeed broadly similar, and so the perhaps surprising result is that isotropic compression, at least in these simulations, gives rise to similar anisotropic stresses as 1-D conditions.

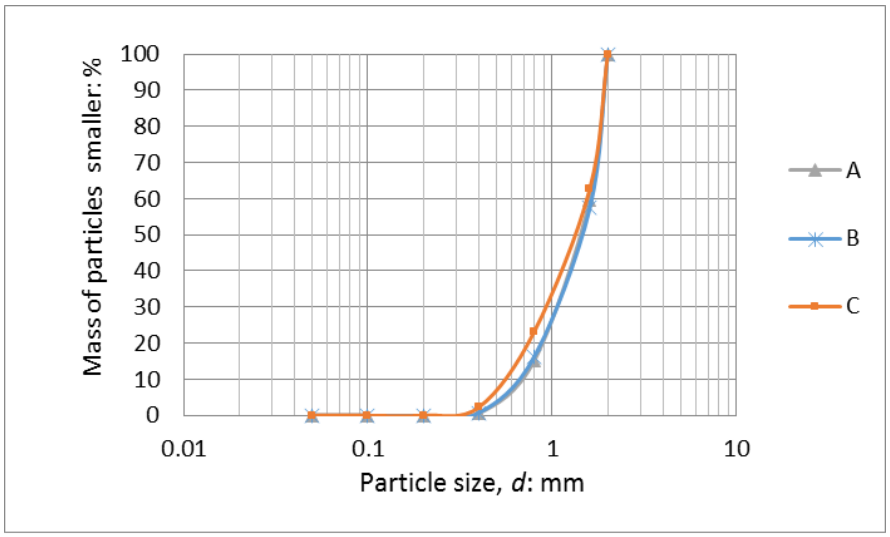

(a)

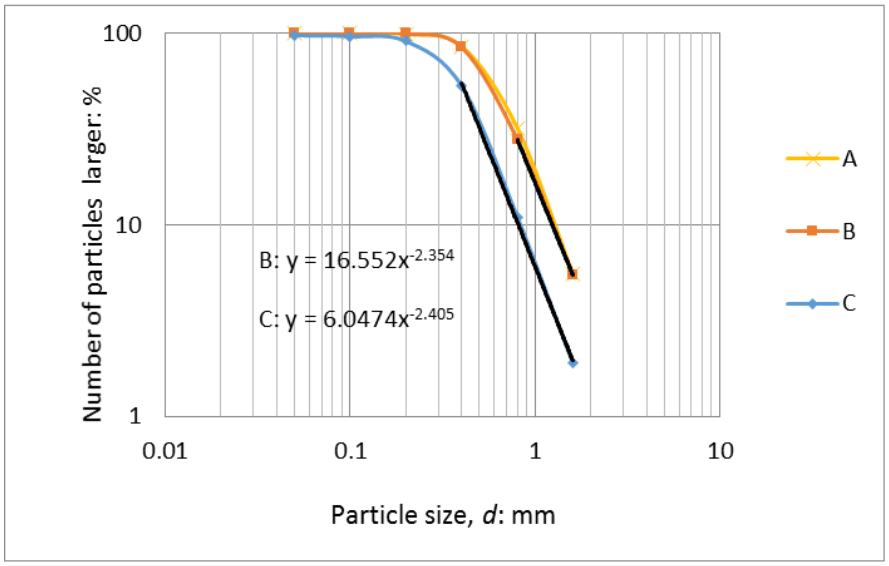

(b)

Figure 4.5 Evolving particle size distributions for points A, B and C: (a) percentage by mass of particles finer than size d against size d on the traditional linear-log scale and (b) percentage by number of particles greater than size d against size d on log-log axes.

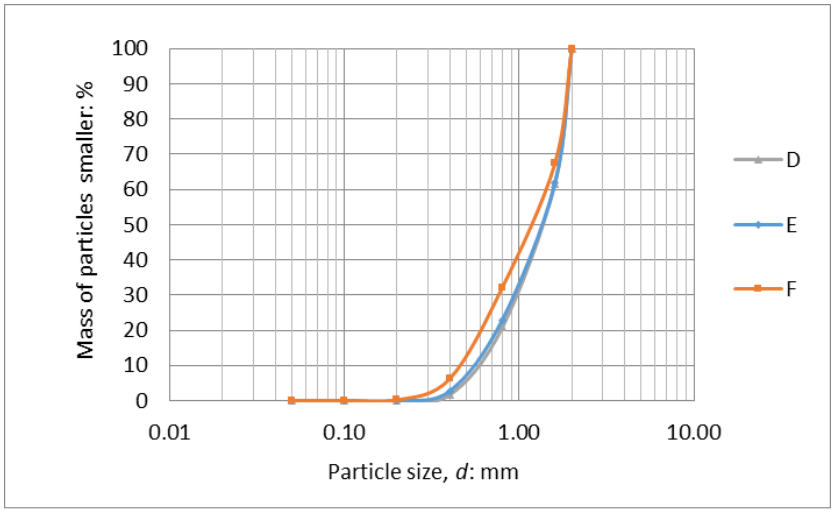

(a)

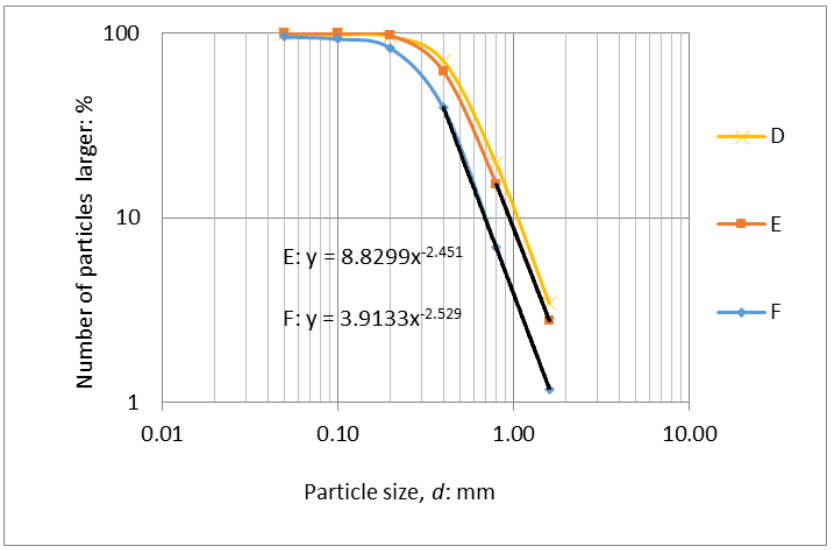

(b)

Figure 4.6 Evolving particle size distributions for points D, E and F: (a) percentage by mass of particles finer than size *d* against size *d* on the traditional linear-log scale and (b) percentage by number of particles greater than size *d* against size *d* on log–log axes

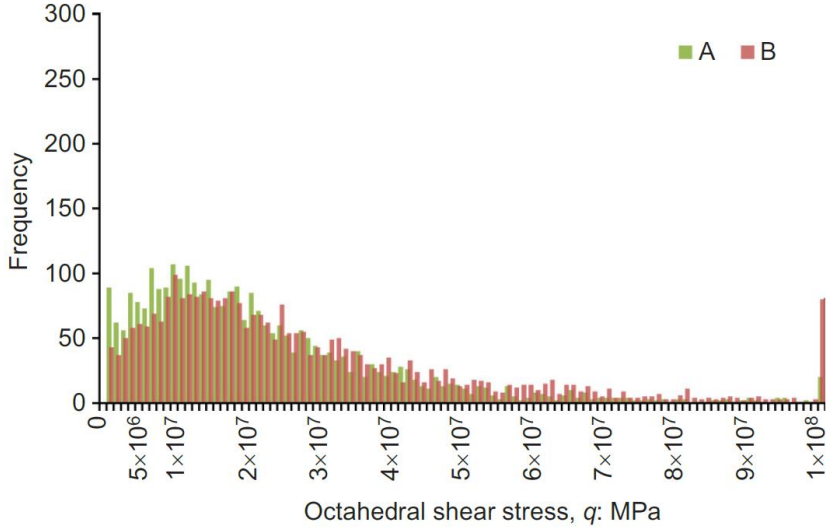

(a)

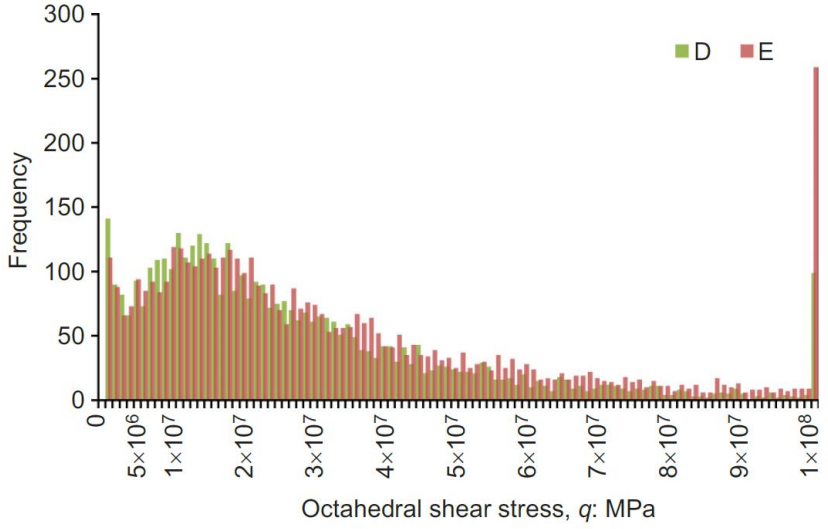

(b)

Figure 4.7 Distribution of octahedral shear stress q for the particles: (a) at points A and B; (b) at points D and E

4.3 Comparison of the influence of aspect ratio

The applied breakage criterion has been proven to give rise to an isotropic normal compression line with the slope agreeing with the theoretical prediction, as has been described in Section 4.2.The crushable sample will produce a lot of fragments during triaxial shearing, so the calculation in PFC^{3D} will be very time demanding. The problem hence is that, if the oedometer sample aspect ratio is maintained and the number of particles reduced, then the proportion of boundary particles increases

significantly. To investigate the influence of the aspect ratio, a small 'triaxial' sample with higher aspect ratio, 1.2, compared to the oedometer sample, 0.233, is subjected to 1-D compression. Geometry details of the triaxial sample were shown in Section 3.4. It is informative to make comparisons between the1-D compression of the triaxial sample and the oedometer sample (McDowell and de Bono, 2013).

Figure 4.8 shows the 1-D NCL of triaxial sample against the oedometer sample data by McDowell and de Bono (2013). The slope of the 1-D NCL for the triaxial sample is approximately -0.5, consistent with previous work, and in agreement with both experimental data (McDowell, 2002) and the theoretical value. The yield stress for the triaxial sample is slightly higher than that of the oedometer sample. Although the triaxial sample is much smaller than the oedometer sample, the triaxial sample has a more gradually evolved yield region compared with McDowell and de Bono's (2013) 1-D sample. The reason behind these observations must relate to the boundary effects alluded to previously: that is particles in contact with rigid walls have relatively smaller coordination numbers and hence are more susceptible to crushing. The influence of boundary particles will be greatest when the sample contains fewest particles- *i.e.* at the beginning when the number of particles has not increased due to particle crushing. These boundary particles with generally lower coordination numbers, leading to higher induced octahedral shear stresses and a resulting lower yield stress corresponding to the onset of fracture. Thus the proportion of boundary particles is examined for the two different aspect ratios. Assuming the probability of the appearance of a sand particle per unit surface area is P_r, then the total number, N_s, of particles distributed on the surface of the sample can be calculated, given the diameter, D_r, and the height, $h_r$of the sample:

$$N_s = P_r \times (0.5\pi D_r^2 + \pi D_r h_r) \quad (4\text{-}1)$$

The total number of particles,N_v, contained in the cylinder can be calculated, taking d_0 as the initial dimension of the sand particle:

$$N_v = P_r \times 0.25\pi D_r^2 \times h_r/d_0 \quad (4\text{-}2)$$

So that, the proportion of particles on the surface, S_p, can be calculated:

$$S_p = \frac{N_s}{N_v} == \frac{2d_0}{h_r} + \frac{4d_0}{D_r} \quad (4\text{-}3)$$

The proportion of surface particles, S_p, for oedometer sample is 0.84 according to Eq. 4-3, using the geometry parameters provided in Table 3-2, while the S_p for triaxial sample is 0.75. Hence, the gradually evolved yield region for the triaxial sample and the sudden yield of the oedometer sample can be explained. Figure 4.9 shows the contact force distribution of the two samples at the same stress level, *i.e.* $p' = 8$ MPa. The influence of boundary conditions (aspect ratio) can be seen in the contact force diagrams (forces drawn to same scale) in Figure 4.9, where many more strong force columns are observed for the oedometer sample - leading to higher octahedral shear stresses. Hence the triaxial sample has a higher yield stress and more gradual yielding compared to the oedometer sample.

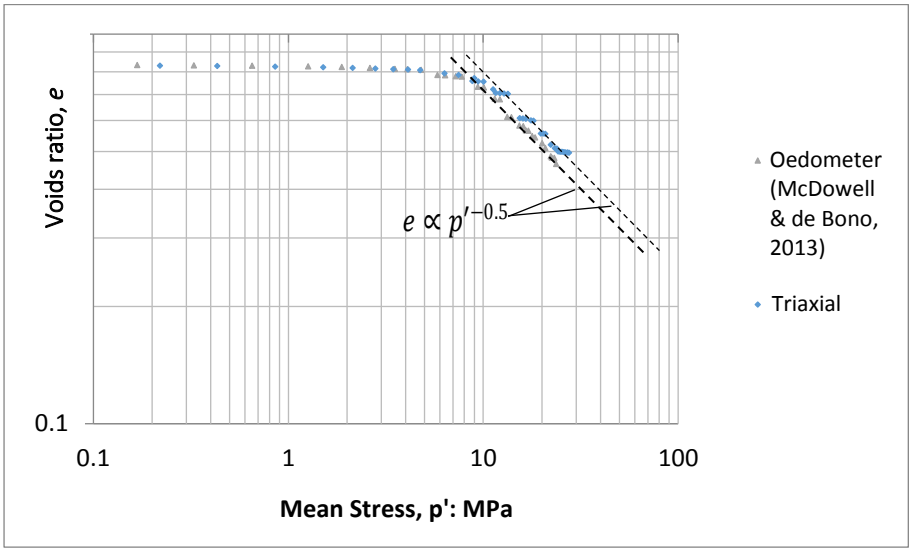

Figure 4.8 One-dimensional normal compression plots for samples with different aspect ratio

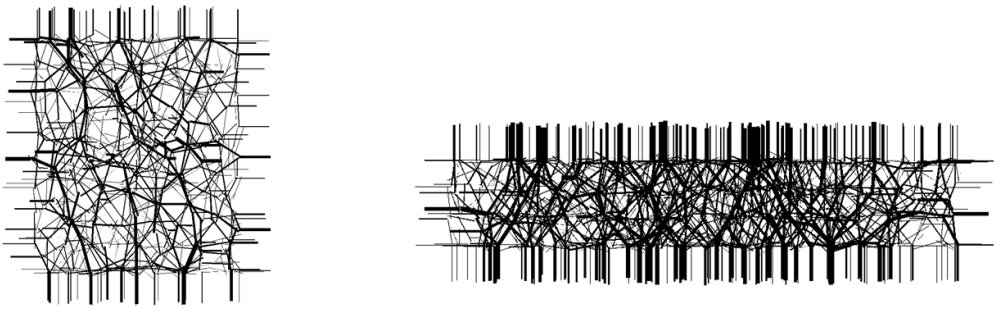

(a) (b)

Figure 4.9 Contact force distribution of one-dimensional compression at p'=8 MPa: (a) triaxial sample, maximum contact force 1.916×10^2N; (b) oedometer sample, maximum contact force 2.239×10^2N.

4.4 1-D and isotropic normal compression results for triaxial sample

Since the change of aspect ratio doesn't significantly influence the clastic compression behaviour of the simulated crushable material, isotropic normal compression is conducted on the triaxial sample in preparation for the triaxial shearing that follows unloading, which will be described and used in Chapter 5. Comparisons of the 1-D and isotropic normal compressions on the triaxial sample are described below.

Figure 4.10 shows the evolution of the lateral earth pressure coefficient, K_0, for the 1-D compression test of the triaxial sample, and a value of approximately 0.68 appears to develop after fractal crushing, although fluctuations can be observed due to particle crushing. According to the Jâky (1944) equation:

$$K_0 = 1 - \sin\phi \tag{4-4}$$

and assuming that the angle, ϕ, in this equation is the critical state angle of friction, then a value of 19° is achieved.

However in lab tests, the friction angle, ϕ, for uniform rounded sands is around 28°, corresponding to a lateral earth pressure coefficient, K_0, of 0.53, which is much lower than the simulation value. This difference is due to the simplified perfect spheres used to simulate the sand particles which are in reality angular and not spherical. Thus the simplified model can't simulate the interlock between the sand particles, which would induce larger lateral resistanceand a lower lateral earth pressure coefficient in the real sand. The high K_0 value subsequently gives rise to a low value for the critical state constant, M, discussed later in Chapter 5.

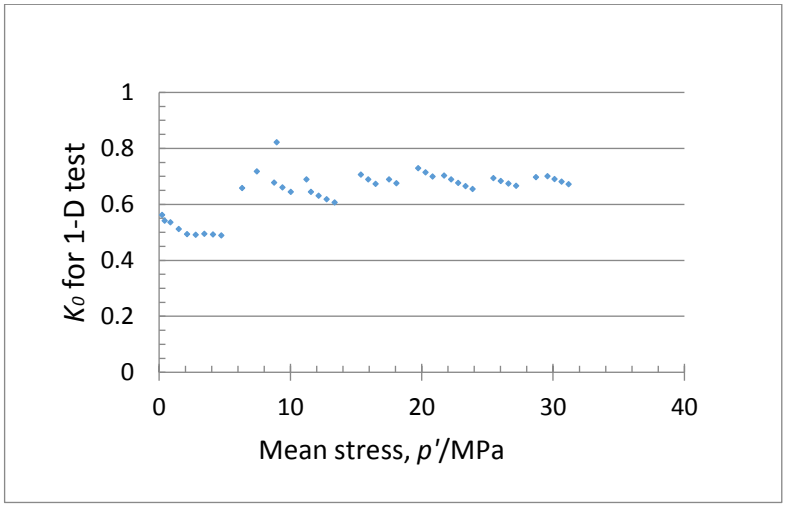

Figure 4.10 Evolving K_0 for triaxial sample during 1-D normal compression

The isotropic NCL for the triaxial sample is compared with the 1-D NCL for the same sample in Figure 4.11. It can be seen that the isotropic NCL is parallel to 1-D NCL. The two lines share approximately the same slope of -0.5, which is consistent with the findings from previous tests and from McDowell and de Bono (2013). The sample shows a higher yield stress under isotropic normal compression (12 MPa) than 1-D normal compression (10 MPa), taking the point of maximum curvature on the NCL as the yield point. The 1-D NCL and the isotropic NCL for the triaxial sample are closer than those for the oedometer aspect ratio sample, owing to the difference in the way that forces are transmitted in the sample.

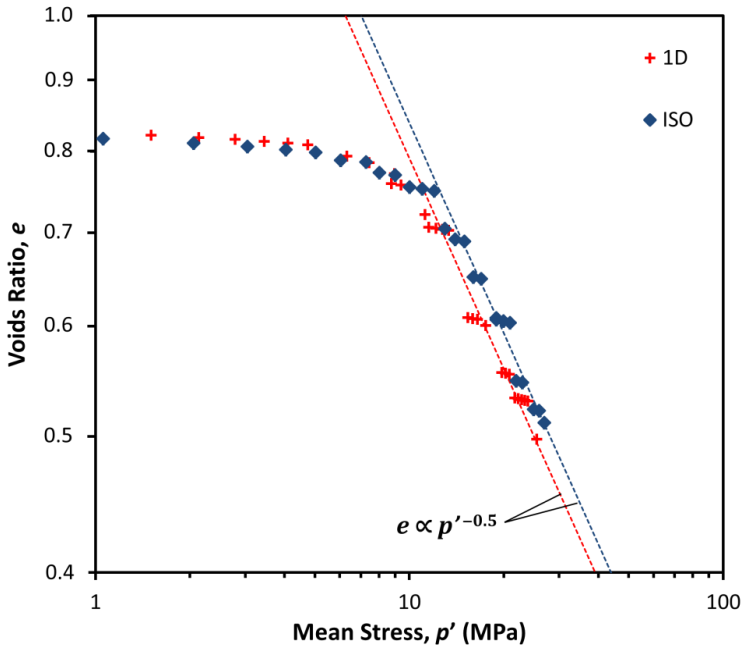

Figure 4.11 One-dimensional and isotropic compression behaviour of the triaxial sample

As has been described previously, the contact force distributions are different for the two samples. The contact force distribution for the two samples at the same stress level under different stress paths is also compared here in Figure 4.12. The value of maximum contact force for each simulation is shown in each figure. It can be seen that the maximum contact force for samples following the 1-D stress path is larger than following the isotropic stress path and the difference between the maximum contact

forces between the two paths for the oedometer sample is larger than that of the triaxial sample, which explains the larger distance between the 1-D and isotropic normal compression lines for the oedometer sample compared to the triaxial sample. With a large number of strong vertical force chains, the way forces are transmitted in the oedometer sample makes it unsuitable for isotropic tests.

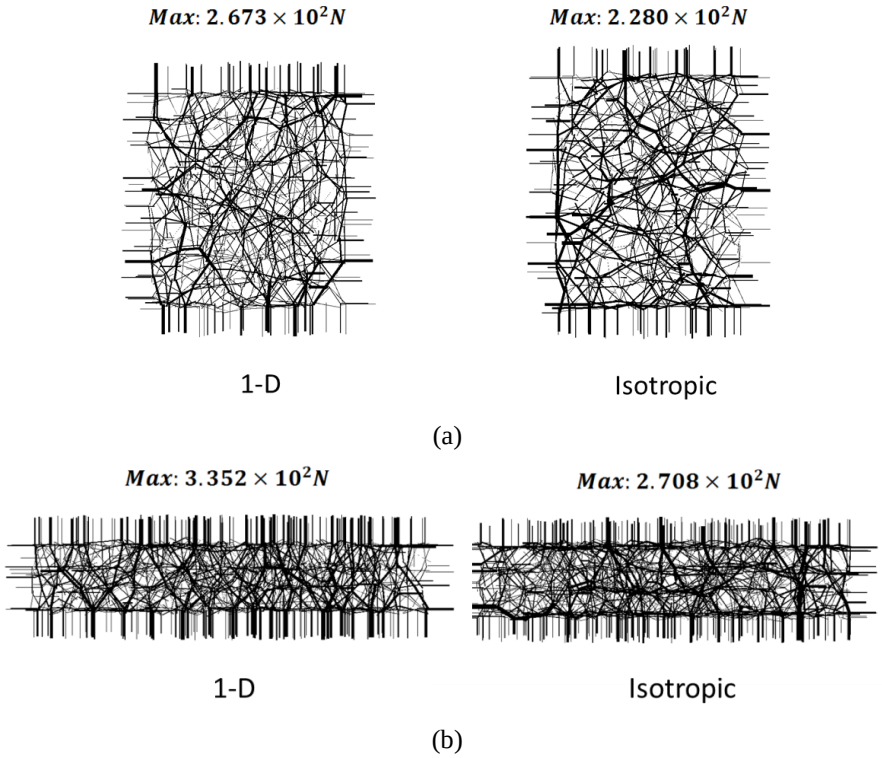

Figure 4.12 Comparison of contact force distribution under 1-D and isotropic compressions at the same stress level, p'=11 MPa: (a) triaxial sample; (b) oedometer sample.

The evolving particle size distribution is plotted in both conventional, *i.e.* percentage of mass of particles smaller than a certain size (Figure 4.13 (a)) and the alternative way of percentage of number of particles larger than a certain size (Figure 4.13 (b)).The equations depicted are for the linear parts of the curves in Figure 4.13 (b) and the exponent gives the fractal dimension. It can be seen that the fractal dimension evolves towards an ultimate value of 2.5, consistent with the oedometer sample and also with other experimental observations (Turcotte, 1986; Sammis *et al*. 1987; Palmer

and Sanderson, 1991; Steacy and Sammis, 1991; McDowell and Daniell, 2001; McDowell and de Bono, 2013).

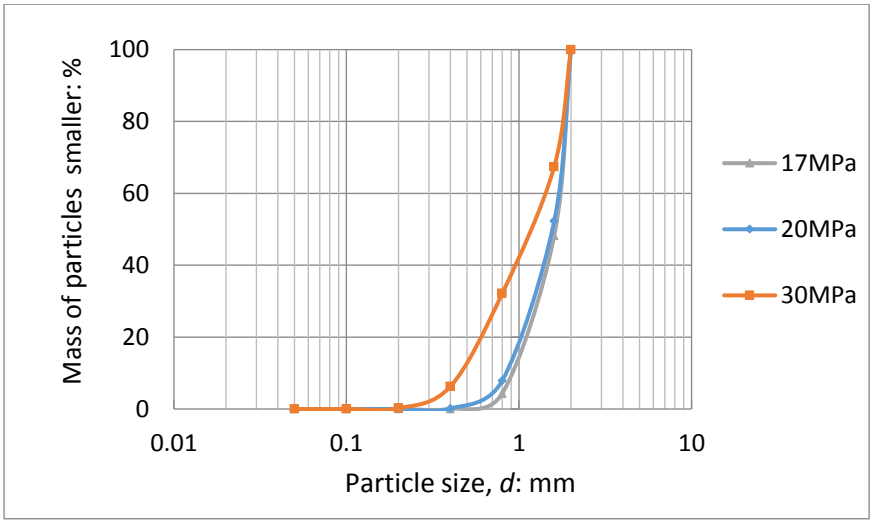

(a)

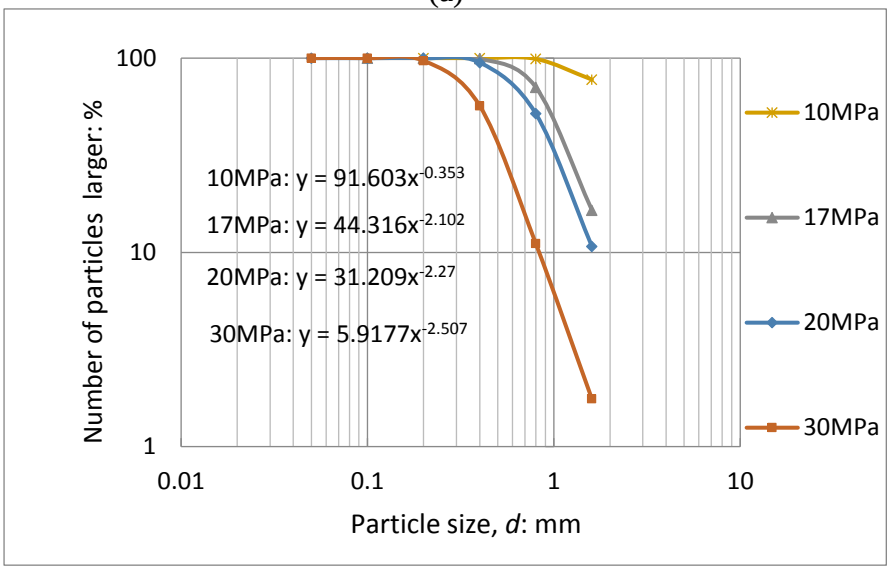

(b)

Figure 4.13 Evolving particle size distribution for triaxial sample: (a) by mass of particles smaller; (b) by number of particles larger.

4.5 Conclusions

In this chapter the isotropic normal compression of an oedometer sample has been presented and the difference between the isotropic and 1-D normal compression of

this sample has been reported; the influence of aspect ratio was also examined using an alternative triaxial sample and the evolution of the particle size distribution (PSD) during isotropic normal compression has been presented for both sample geometries. For the oedometer sample, the octahedral shear stresses, due to local anisotropic stresses within a sample with isotropic boundary stresses, have been shown to give rise to an isotropic normal compression line and the evolution of a distribution of particle sizes. The fractal dimension of the simulated silica sand under isotropic compression was shown to have an ultimate limit value of 2.5, which is not therefore unique to a 1-D stress path. The isotropic NCL has been shown to be parallel to the 1-D NCL in $\log e - \log p'$ space for the oedometer sample and agrees with traditional critical state soil mechanics. The slope of the normal compression line is proved to be -0.5 for the simulated silica sand, in agreement with the theoretical value according to the clastic hardening law, when the Weibull modulus of 3.3 has been assumed to apply (for silica sand) and the fractal dimension of 2.5 has been shown to evolve. This also reinforces the proposition by McDowell and de Bono (2013) that the slope of the compression line should be solely determined by the hardening law for the average particle strength as a function of size, and this should be independent of the loading configurations of the particles for different macroscopic stress ratios. The particle size distribution (PSD) has been checked for the same sample at the same voids ratio while under different stress conditions. The voids ratio in compression tests has been shown to be uniquely related to the particle size distribution.

The 1-D normal compression of the alternative triaxial sample has been simulated. The influence of aspect ratio has been investigated by comparing the difference of the

1-D compression curves of the triaxial and oedometer samples. The aspect ratio is found to influence the behaviour of the sample through the changing of the proportion of boundary particles within the sample. It was found that a lower aspect ratio for the oedometer sample than the triaxial sample leads to an earlier and more sudden yielding of the simulated silica sand than the triaxial sample, due to a larger proportion of balls in contact with the boundary and a lower induced coordination number. Stronger force chains are observed for the oedometer sample than for the triaxial sample, which also explains the more sudden and earlier yielding of the oedometer sample. Although the geometry of the triaxial sample is different to the oedometer sample, the triaxial sample is proved to generate a similar 1-D NCL to that of the oedometer sample. Thus the "new" triaxial sample has been isotropically consolidated in preparation for subsequent shearing because it contains fewer particles (and hence gives a more acceptable computational time) and a lower proportion of boundary particles. The triaxial sample contains 390 particles whereas the oedometer test containes 620 particles.

The NCL for 1-D and isotropic tests have been shown using the new triaxial sample to be parallel and have the same slope of -0.5, which further provides credence to proposition that the hardening law governs the slope of the normal compression line. The evolution of the PSD has been checked for the triaxial sample under isotropic compression. The fractal dimension is shown to evolve towards an ultimate value of 2.5, in agreement with previous tests. Since the friction between balls and boundaries is avoided and the shear plane does not appear in the simulations, the triaxial sample

with the aspect ratio of 1.2, instead of the conventional value of 2, is deemed acceptable for subsequent triaxial simulations.

Chapter 5 Triaxial Shear and Critical States

5.1 Introduction

In Chapter 4 the 1-D and isotropic normal compression lines have been shown to be parallel to each other, details have also been presented in McDowell *et al.* (2013) as shown in Appendix D. This is consistent with the conventional critical state soil mechanics framework (Schofield and Wroth, 1968). According to the framework, the critical state line should be unique and also parallel to both normal compression lines. This is true for clays (Schofield and Wroth, 1968) but what about sands? At high stress levels, according to Wood (1990), they may be parallel, as is shown in Figure 5.1. However, more work is required to establish the extent to which this is the case. This chapter will use the DEM PBM method to establish a critical state line and to ascertain whether it is parallel to the normal compression lines established in the previous chapters.

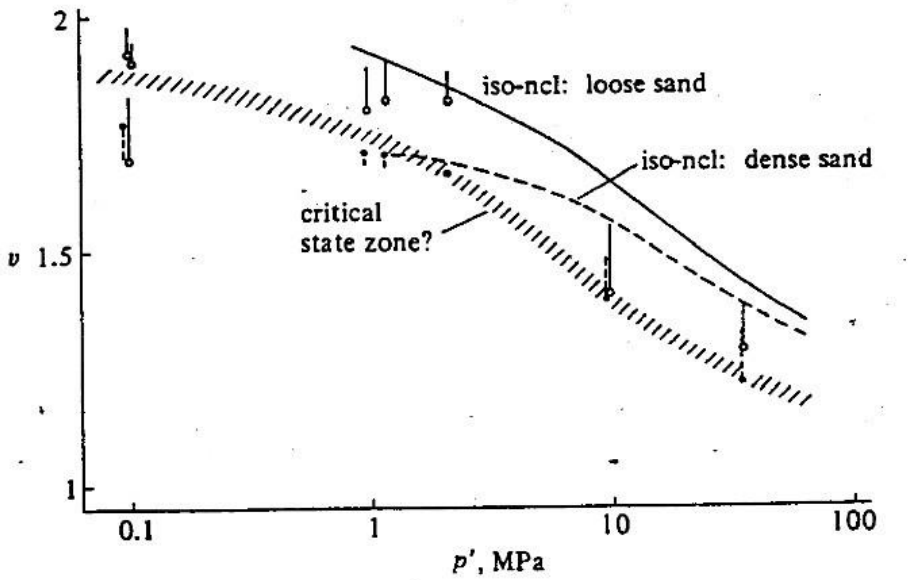

Figure 5.1 Normal compression lines and critical state line (Wood, 1990)

Much laboratory and computational work has been carried out to investigate the critical state behaviour of soils. However, due to the limitation of testing equipment and methodology the critical state of sand is hard to obtain in lab tests. For example: strains greater than about 20% are difficult to achieve in the lab; the initial states of different samples are hard to control to be exactly the same and different samples may have different micro-structures which may lead to different mechanical behaviour, even at the same voids ratio. There still exists a question of whether the CSL for sand is necessarily unique as for clay, and what shape it should be when voids ratio (or its logarithm) is plotted against the logarithm of effective stress.

This chapter presents an investigation of the behaviour of isotropically over-consolidated sands under triaxial shearing. One of the key aims in this chapter is to take the next step towards achieving a realistic critical state line in DEM, using a crushable sand with realistic characteristics—*i.e.* experimentally obtained strengths and hardening law, and the ability for particles to fragment repeatedly over a wide range of scales (a feat not possible using agglomerates). Another objective is to clarify whether the critical state line obtained from triaxial shear tests on the over-consolidated sand is parallel to the normal compression line defined by the hardening law. The discrete element method has been used to investigate the micro mechanics of shearing to a critical state on the loose and dense sides of critical. As has been presented in Chapter 4, isotropic compression of crushable silica sand has previously been modelled in 3D using a number of particles and without the use of agglomerates. The same procedure is used here. Particle fracture is governed by the octahedral shear stress within the particle due to the multiple contacts and a Weibull distribution of strengths. In the work presented here, a triaxial sample, as described in Chapter 4, is

compressed isotropically to 20 MPa, then unloaded to various stresses, resulting in samples with a range of over-consolidation ratios. These samples are then sheared (via conventional, *i.e.* constant confining stress, and constant-p' triaxial simulations) to critical states to reveal the critical state line in $\log e - \log p'$ space. The lateral earth pressure coefficient, K_0, obtained from one-dimensional compression is used to predict a critical state angle of friction for the soil, which is then used to predict the critical state friction constant M and compared to the data from the simulations. McDowell et al. (2015) has presented the research regarding the above considerations, as is attached in Appendix E. In addition, another series of shear tests are simulated on the triaxial sample with 17 MPa isotropic over-consolidation history and different over-consolidation ratios. The influence of p_0' is examined and the uniqueness of the CSL is discussed.

5.2 Preparation of over-consolidated samples

The isotropically consolidated triaxial sample has been simulated and presented in Chapter 4. In order to prepare overconsolidated samples for subsequent shearing, isotropic unloading is carried out for samples from alternative stresses of 17 MPa and 20 MPa on the isotropic normal compression line. The isotropic unloading in this simulation involves the application of servo-control to both the top and lateral confining walls as in isotropic compression. The unloading logic is the same as the isotropic loading described in Chapter 3, except that the directions of the movements of the walls are opposite to the loading procedure. The same target pressure is assigned to the top and lateral walls during each time-step and the servo-control of the walls helps to maintain the stress path and avoid a sudden change in induced stress as the target stress is approached. The velocity of walls is then set to zero and the loop of

particle breakage is then applied to allow the 'qualified' particles to break and to permit the induced energy from the particle overlap created by the chosen particle splitting model, to dissipate after particle breakage. The iteration of unloading to target pressure and the loop of particle breakage, as shown in Figure 3.4, continues until the mean effective stress, p', reaches the target unloading stress. Several different target stresses were chosen, the lowest of which was 0.5 MPa.

Figure 5.2 shows the two unloading curves from isotropic stresses of 17 MPa and 20 MPa together with the normal compression line for the isotropic simulation. Very small amounts of volumetric expansion are observed during unloading, which means the volume change during normal compression mainly comes from plastic deformation while the elastic deformation is relatively small. If the particles cannot break, there will be no clear transition from elastic to plastic behaviour, and no distinct unloading line would be observed, as is the case for example in Sitharam and Vinod (2008), Minh and Cheng (2013) and Wang (2014).

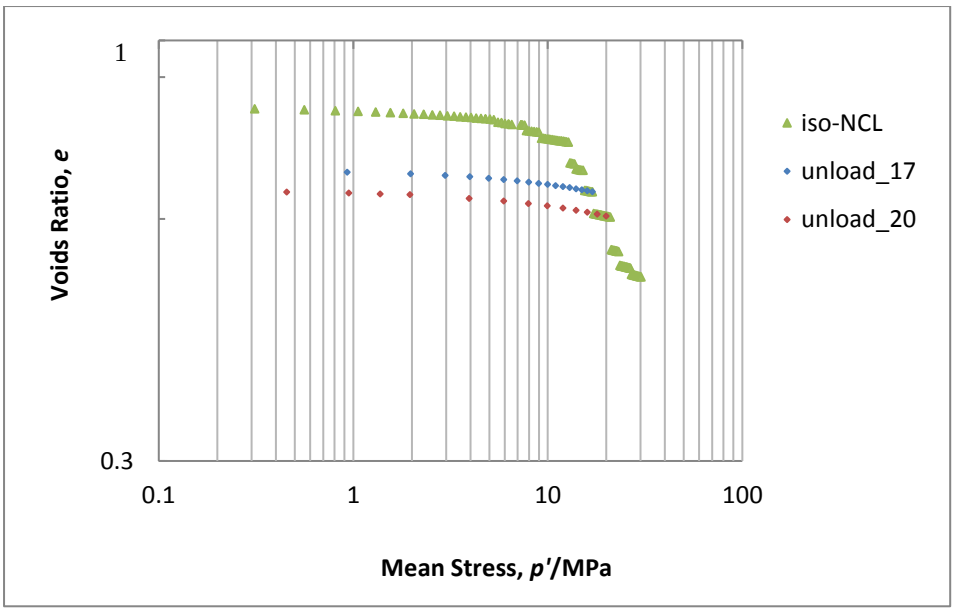

Figure 5.2 Unloading line of samples with 17 MPa and 20 MPa isotropic consolidation history respectively

5.3 Macro observations during shearing to critical state

5.3.1 Stress path effects

The conventional and constant p' shearing of the isotropically over-consolidated samples are conducted on the series of samples with 20 MPa pre-consolidation pressure to investigate the influence of stress path. Points at 1 MPa, 2 MPa, 4 MPa, 6 MPa, 8 MPa, 10 MPa and 12 MPa on the unloading line in Figure 5.2 were chosen to carry out the 'conventional' triaxial shear tests, *i.e.* keeping the confining pressure constant and slowly increasing the displacement of the top wall. Points at 2 MPa, 4 MPa, 6 MPa, 8 MPa, 10 MPa and 12 MPa were also chosen to carry out the constant mean effective stress, p', triaxial shear, *i.e.* by slowly increasing the displacement of the top wall and adjusting the movement of the lateral confining walls using servo-control to keep the mean effective stress, p', constant, as has been described in Chapter 3. The iteration of the application of applying a target strain and the loop of particle breakage involved during shearing, is described in Chapter 3. The test results for the 12 MPa sample are not shown in this chapter, because of the impractical computational time, i.e. running for 6 months without reaching the critical state, which makes it not suitable for analysing the critical behaviour of the simulated silica sand. The results of both the conventional and constant-p' shear tests of the 12 MPa sample are shown in the next chapter to analyse the yielding behaviour of the simulated sand sample.

Conventional triaxial shear

Figure 5.3 shows the stress-strain and volumetric-axial strain plots for the conventional tests on samples under different confining stresses ($p'_0 = 20\ MPa$). The

axial strain is conducted to 30% to make sure that the sample has reached the critical state.

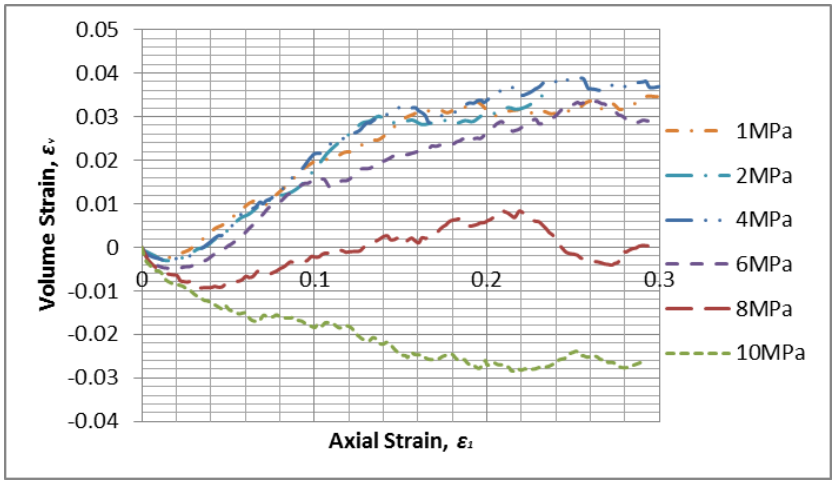

(a)

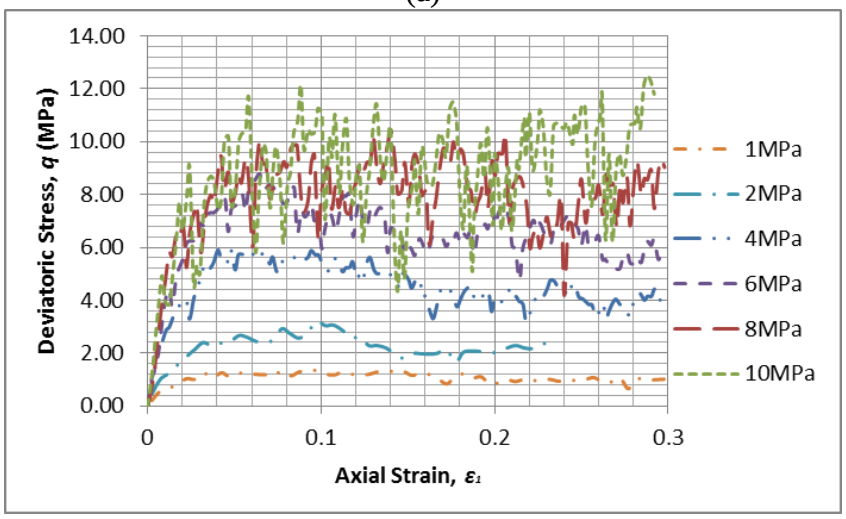

(b)

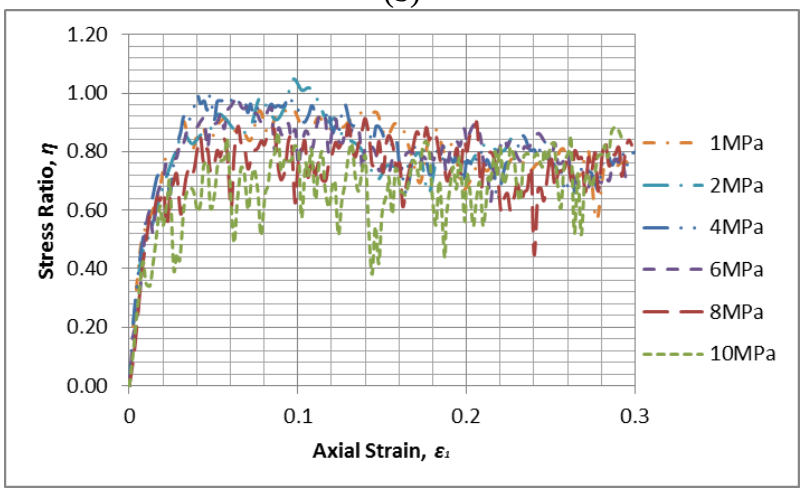

(c)

Figure 5.3 Stress-strain and volume plots for samples under conventional shearing with p_0'=20 MPa and different confining pressures

It can be seen from the volumetric plots in Figure 5.3 (a) that the samples under low confining stresses, *i.e.* below 8 MPa, tend to dilate after the initial contraction under shearing, implying that the initial states of these samples lie on the dense/dry side of the critical state line. The volumetric strain of the sample with 8 MPa confining stress shows slight contraction followed by dilation and finally tends to approximately 0, even though it is a drained test – and therefore it must have started off near or on the critical state line. The sample with large confining stress, 10 MPa, shows contraction throughout the shearing, which indicates the initial state of the sample lies on the loose/wet side of the critical state line.

Figure 5.3 (b) shows the evolution of deviatoric stress against axial strain. A clearer view of the $q - \varepsilon_a$ plot, which has large fluctuation but is crucial when describing the behaviour of the sample, is shown in Figure 5.4 with a fitted smooth curve. The method of smoothing the discrete data points, a fit of an equation which follows the expected form, will be presented in Chapter 6. The term 'conr' in Figure 5.4 denotes the stress path with constant confining stress. Peak deviator stresses can be observed for 2 MPa, 4 MPa, 6 MPa and 8 MPa samples, as expected for dense/dry side behaviour. The deviator stress for the sample subjected to conventional shearing at 10 MPa contracts to a critical state and exhibits no obvious peak strength. Considering the fitting method of the data points, the slight peak observed is due to the significant scatter of the data points and not perfectly matched fitting curve. However, for data points with such scale of scatter, it is very difficult to deliver a perfectly matched fitting curve. The curve shown in Figure 5.4 is already the best at the moment.

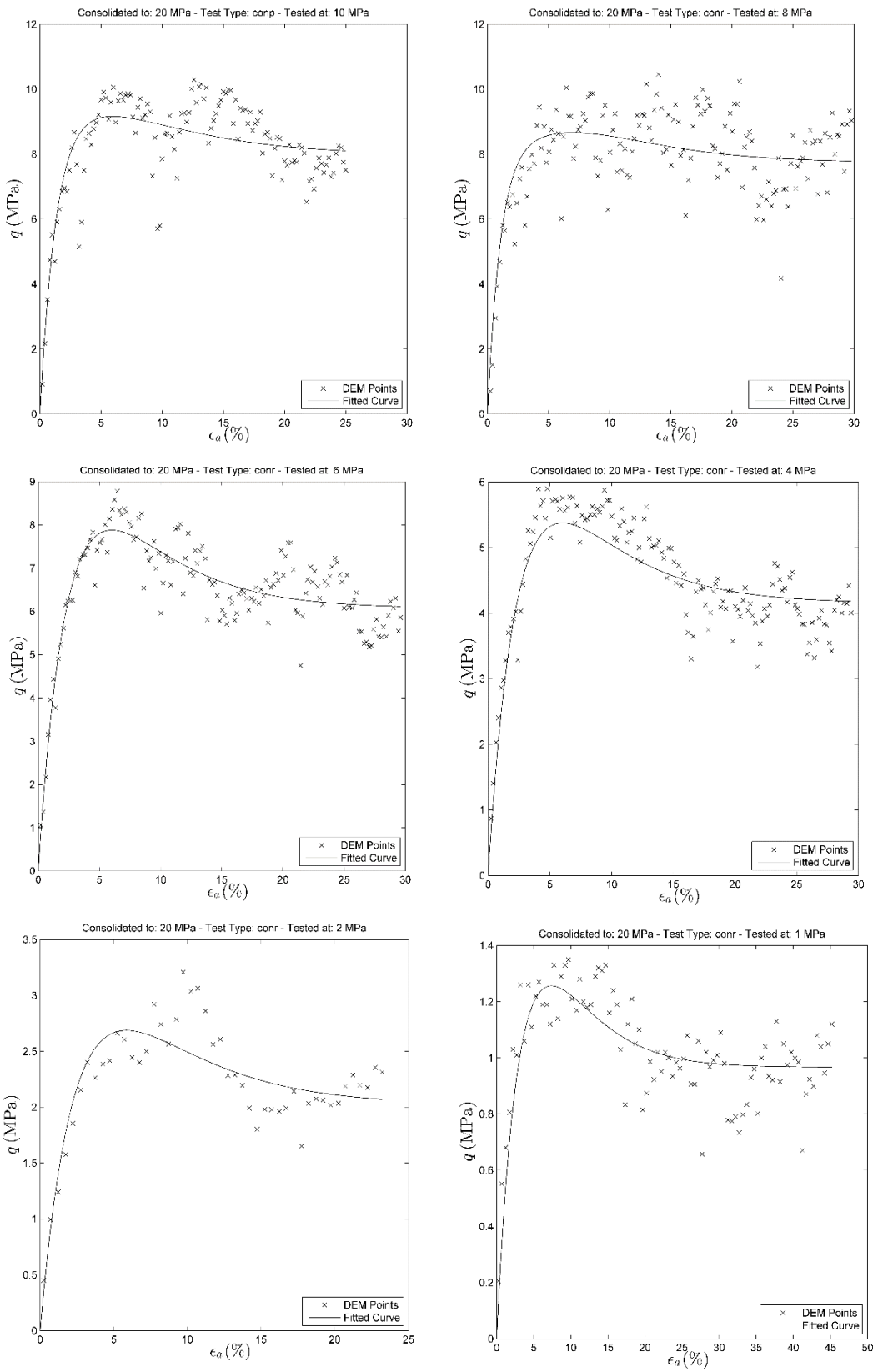

Figure 5.4 Stress-strain plots with fitted curve for triaxial shear at constant confining stress and a preconsolidation stress of 20 MPa

Significant scatter can be observed for the 10 MPa sample because of the significant breakage occurring and the relatively small sample with a small number of particles. In fact for all samples up to and including an initial stress of 6 MPa, the peak stress ratio and dilation show little variation (Figure 5.3). This has implications for the shape of the critical state line in log e –log p' space, which will be discussed shortly. As the confining stress increases beyond 6 MPa, the peak stress ratio and dilation reduce.

Figure 5.3 (c) presents the evolution of stress ratio, η, as a function of axial strain. Peak stress ratios can be observed for samples on the dense/dry side of critical state, *i.e.* samples with confining pressure up to 8 MPa. The stress ratio for the 10 MPa sample keeps increasing to a final stable value, although significant scatter due to particle crushing can be observed. Most importantly, all the stress ratios for different samples finally evolve towards approximately 0.75, implying that the critical stress ratio, M, is a constant and equal to 0.75. It has been discussed in Chapter 4 that the Jâky (1944) equation relates the lateral earth pressure coefficient, K_0, to an angle of shearing resistance, as shown in Eq. 4-4. The friction angle for this triaxial sample is calculated to be 19° according to Jâky's equation. Wood (1990) presents an interesting discussion regarding the angle in this equation. For normally consolidated clay it is widely accepted that the angle of friction in Eq. 4-4 should be φ_{crit}. However, for sand, Wood (1990) suggests that K_0 depends on the in-situ structure of the sand and so should be expected to correlate with the peak angle of shearing resistance, *i.e.* φ_{max} which is a function of the initial relative density and structure (influenced by particle shape) of the sand at low stress levels. Adding to this conjecture, if one considers a dry stone wall, in which angular pieces of stone are placed together forming a vertical wall, the angle of repose is 90°, giving K_0=0. The wall supports its own weight

perfectly with no horizontal stress because of the extreme particle interlock. However, beyond yield on the normal compression line, as particles crush and a fractal PSD emerges, φ_{max}would not be the appropriate parameter to use in Eq. 4-4. It is well known that both clay and sand form very similar normal compression lines beyond yield, albeit at different stress levels. It seems unlikely that these would arise from completely different processes. It is therefore proposed that for normally compressed sand, φ_{crit} is the correct parameter to use in Jâky's equation, as is the case for normally consolidated clays (note that for a clay sedimenting out from a slurry before yield and normal compression, as for the sand at low stress levels, ϕ_{crit}would not be appropriate in this case) as proposed by de Bono and McDowell (2016). The critical state stress ratio, φ_{crit}, also known as the critical state dissipation constant in Eq. 2-9, is usually calculated using:

$$M = \frac{6\sin\phi}{3-\sin\phi} \tag{5-1}$$

If the critical state friction angle,ϕ_{crit}, is the appropriate angle of friction in Eq. 4-4 for a normally compressed sand, then the critical state stress ratio, *M*, is calculated to be 0.73, according to Eq. (5-1), giving ϕ_{crit}=19°—which has been calculated in Chapter 4 . The predicted *M* value agrees with the simulation results that the value of *M* is approximately 0.75. Hence it is proved that for the clastic normal compression of a sand, the friction angle for sand in Jâky's equation is the critical state friction angle, as for clay.

The constant *M* value at a critical state observed in this simulation is different from the findings of Cheng and Bolton (2005) that the critical stress ratio changes with the confining stress level. The critical stress ratios in their simulations varied from *M*=1.7

at low stress levels to M=1.1 at high stress levels. However the critical stress ratio is usually considered to be a material constant and independent of the stress level (Wood, 1990). One might argue that if the particle size distribution is evolved and fractal, the critical state angle of friction would be constant with confining stress level. For the agglomerates used by Cheng and Bolton (2005), this would certainly not have been the case. To further illustrate the point, a vertical mid-plane section has been taken through the sample at an axial strain of 23.2% (*i.e.* at critical state), at two different stress levels - one at a constant confining stress of 2 MPa stress and the other at a confining stress of 10 MPa (Figure 5.5). It can be seen that the one under higher stress produces a lot of fines, i.e. particles whose dimension is smaller than 0.1mm in this project, which seem to have no contacts with surrounding spheres and the local particle arrangements of the two samples are hard to compare. If the spheres with no contacts with neighbours are then deleted, 724 in total for the 2 MPa sample and 1858 in total for the 10 MPa sample, and the sectional view redrawn for the two samples without the 'inactive' spheres (Figure 5.6), they are easier to compare, and show a higher degree of similarity. That is to say that the distribution of particle sizes carrying the stress at a critical state, appear to be similar at both stress levels and would support the hypothesis proposed above. It should be clarified that the floating fines would not appear if the influence of gravity is considered. However the computational time would become inapplicable to consider gravity in the simulation, as has been described in Chapter 3.

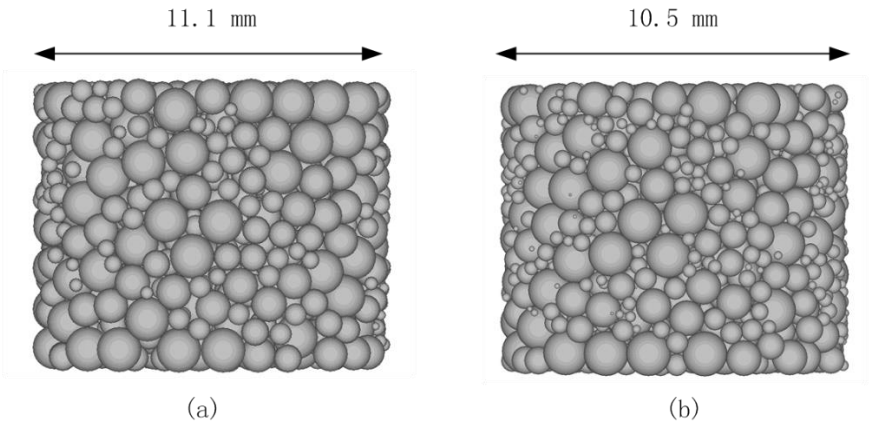

Figure 5.5 Samples at critical state at same axial strain of 20%: (a) constant confining stress of 2 MPa; (b) constant confining stress of 10 MPa.

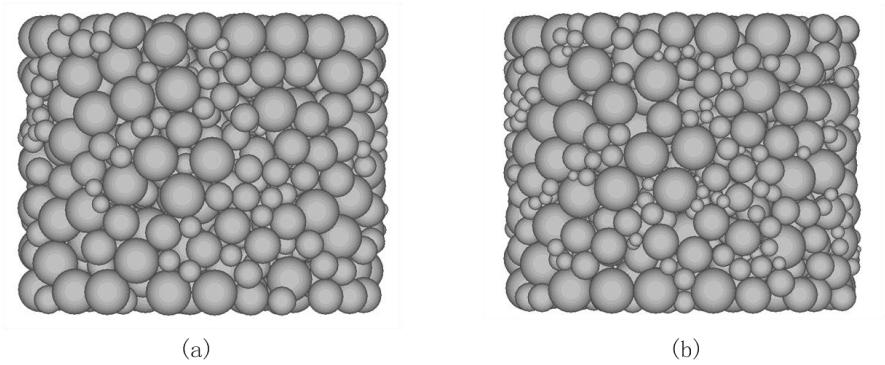

Figure 5.6 Samples at critical state after deleting inactive spheres: (a) constant confining stress of 2 MPa; (b) constant confining stress of 10 MPa.

With the use of the Cheng *et al.* (2003) agglomerate model, an artificial limit on the smallest crushable diameter of a particle was set, since the spheres themselves are not crushable. This means that as agglomerates crush, the particles comprise fewer and fewer spheres, which permits less interlock, giving a reduced angle of shearing resistance and hence a lower critical state M. One can expect an increasing K_0 value with the increase of mean effective stress during a one-dimensional test with the application of the bonded particle model (BPM).

Constant p' triaxial shear

Figure 5.7 shows the stress-strain and volumetric plots for the series of constant-*p'* shearing on samples from 2 MPa, 4 MPa, 6 MPa, 8 MPa and 10 MPa. All the simulations in this case demonstrate dilation and peak strengths, *i.e.* behaviour on the dense side of the CSL. It can be observed from Figure 5.7 (a) that the dilations of samples up to 8 MPa mean effective stress show little variation. However, the dilation of sample with 10 MPa mean effective stress is much smaller than the other four tests, implying that the initial state of the sample lies on the dense/dry side of the CSL and near the point of intersection of the CSL and the unloading line.

Figure 5.7 (b) shows that peak strength increases with the increase of mean effective stress, while the scatter for the 10 MPa sample under constant *p'* shearing is not as significant as under conventional shearing. This can be explained by noting that conventional shearing leads to a higher mean effective stress than constant *p'* shearing and hence results in more particles crushing which causes the larger fluctuations in deviatoric stress. The stress ratio evolves towards the final value of 0.75 for all the samples, the same as that for samples subjected to conventional shearing. For convenience, Figure 5.8 shows a clearer stress strain plot with fitted curve of Figure 5.7 (b). The term 'conp' in Figure 5.8 denotes the constant-*p'* stress path.

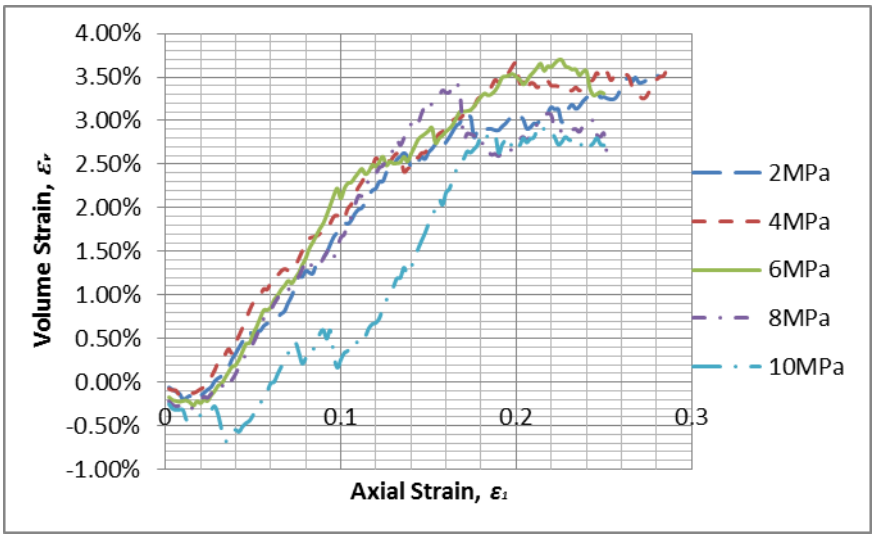

(a)

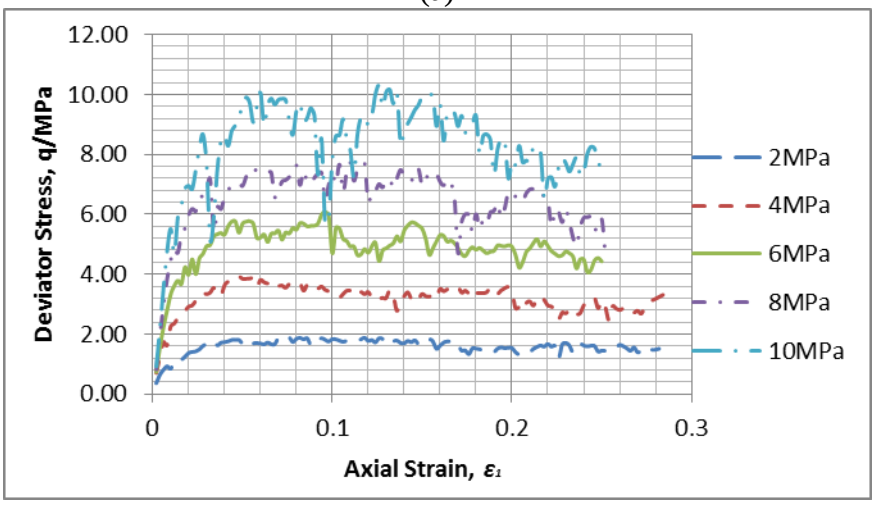

(b)

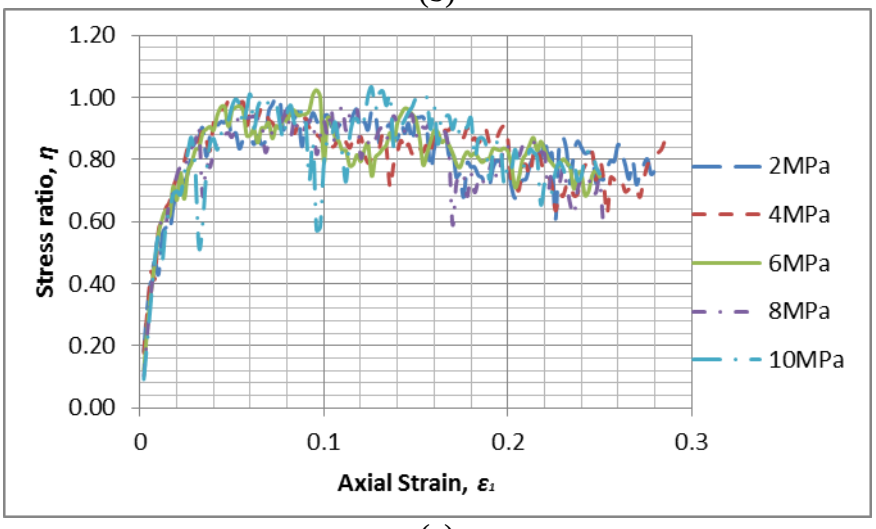

(c)

Figure 5.7 Stress-strain and volume plots for samples under constant *p'* shearing with p_0'=20 MPa and different mean effective stresses

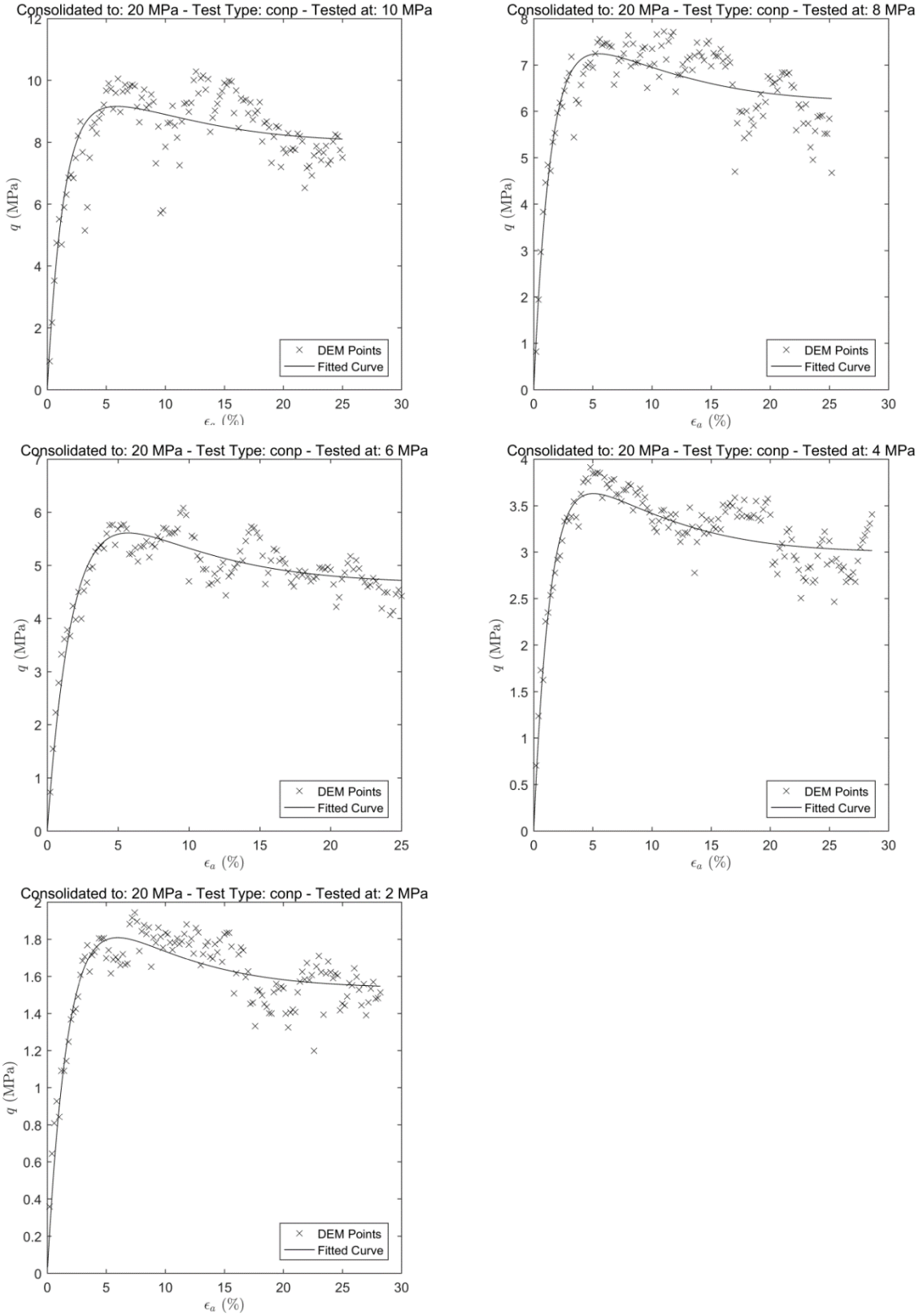

Figure 5.8 Stress-strain plots for triaxial shear with fitted curve at constant p' and a preconsolidation stress of 20 MPa.

Critical state line for samples with 20 MPa preconsolidation stress

The critical states of samples in this simulation are taken to occur when the volumetric strain, deviator stress and stress ratio are stable or fluctuate around a stable value, *i.e.* when the axial strain is larger than about 20%. The critical state line (CSL) of the sample with 20 MPa isotropic over-consolidation history is shown in Figure 5.9. The red dots resemble the critical states for samples subjected to conventional shearing while the green dots resemble critical states for samples subjected to constant-*p'* shearing. The red and green arrows indicate the two state paths respectively.

The critical state line can be seen to be curved in log *e*-log *p'* space, and appears to become approximately parallel to the isotropic normal compression line at high stresses, in agreement with the conventional Critical State Soil Mechanics framework. The observation that at low stresses, the CSL is not parallel with the NCL has been observed experimentally, Wood (1990) for example – see Figure 5.1. The parallel CSL at high stresses therefore also agrees with the compression law proposed by McDowell and de Bono (2013), which predicts a slope of -0.5 for this sand.

It is reassuring to see that the critical states obtained from both sets of shear tests lie on the same critical state line. Moreover, it is interesting to observe the difference in behaviour of the two different shear tests conducted from initial states of *p'*=8 and 10 MPa. The sample subjected to conventional shearing from 8 MPa, which exhibited approximately 0% volumetric strain, was indeed close to critical, as predicted previously. The sample subjected to constant-*p'* shearing from 8 MPa however, dilated to a critical state, as can be seen in Figure 5.9. An even starker contrast can be observed between the two samples sheared from *p'*=10 MPa, in which the conventionally

sheared sample (in which the mean stress increases), undergoes significant contraction to reach the CSL, whereas the constant-*p'* sample dilates to reach a critical state.

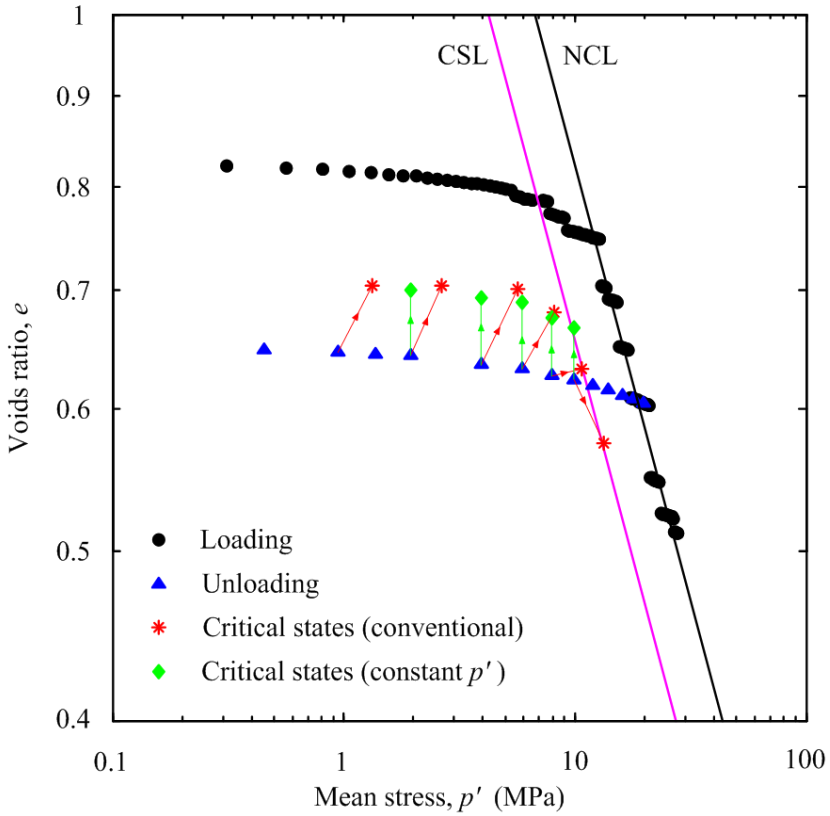

Figure 5.9 Critical states for samples with p_0'=20 MPa

5.3.2 The influence of p_0'

Shearing of samples with 20 MPa overconsolidation history has given a critical state line which is parallel to the normal compression line. However, only three data points lie on the linear part of the CSL. To obtain more data points and to investigate the uniqueness of the CSL, shearing of samples with another pre-consolidation pressure were carried out. The impact of the difference in pre-consolidation pressure is also investigated. Samples were therefore unloaded from an alternative isotropic pre-consolidation pressure of 17 MPa. Because the sample contains many more particles when compressed to a stress larger than 20 MPa, the computational time will be too

large to be practical, and because the samples compressed to *p'* smaller than 17 MPa give a particle size distribution which has not evolved to be fully fractal, as is shown in Figure 4.14, 17 MPa was chosen to compromise on both these issues. Samples at mean effective stresses of 2 MPa, 4 MPa, 6 MPa, 8 MPa, 10 MPa and 12 MPa on the unloading line were chosen to simulate the conventional and constant-*p'* triaxial shear tests.

The behaviour of samples with 17 MPa pre-consolidation pressure is observed to be similar to the behaviour of samples with 20 MPa pre-consolidation pressure. Figure 5.10 and Figure 5.11 present the volumetric and stress-strain behaviours of samples with 17 MPa pre-consolidation pressure and subjected to conventional shearing and constant-*p'* shearing respectively. For convenience of the observation of the behaviour of samples, Figure 5.12 and Figure 5.13 shows the smoothed curve of the $q - \varepsilon_a$ plots for 17 MPa samples under conventional triaxial shearing and constant-*p'* shearing respectively. The stress ratios for all the samples evolve towards a final critical value of approximately 0.75, in agreement with the predicted *M* value.

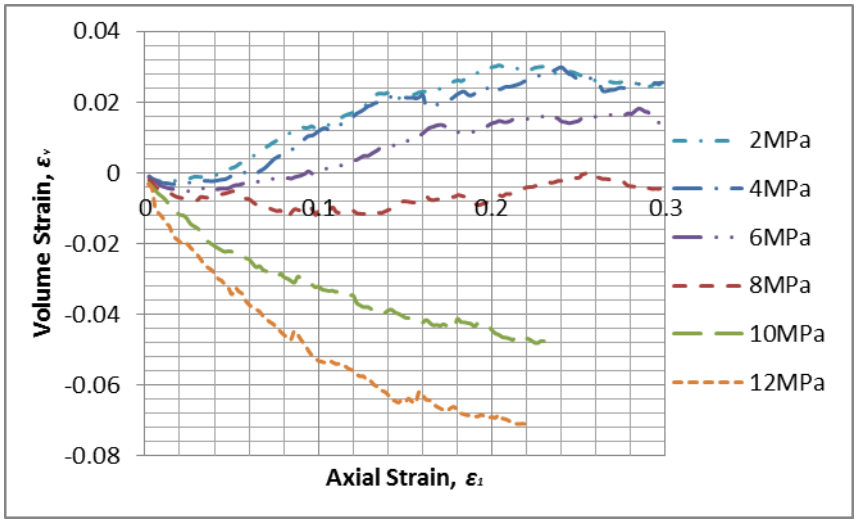

(a)

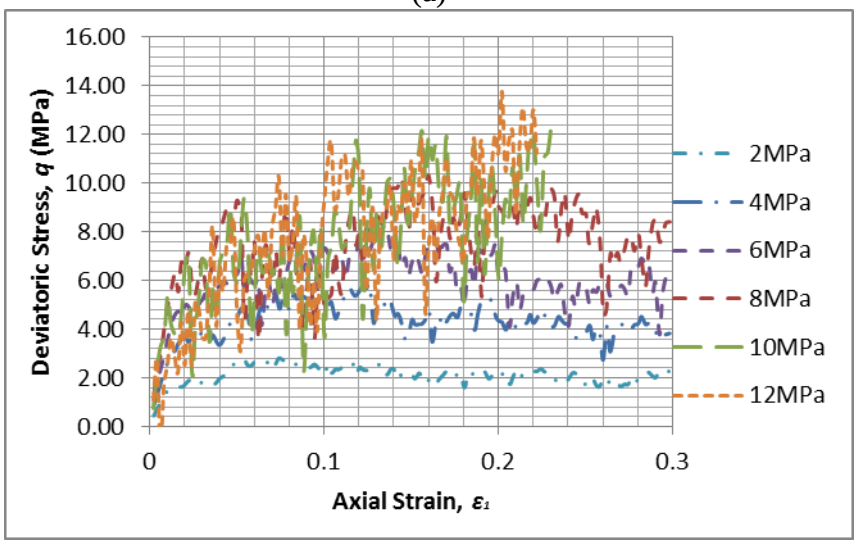

(b)

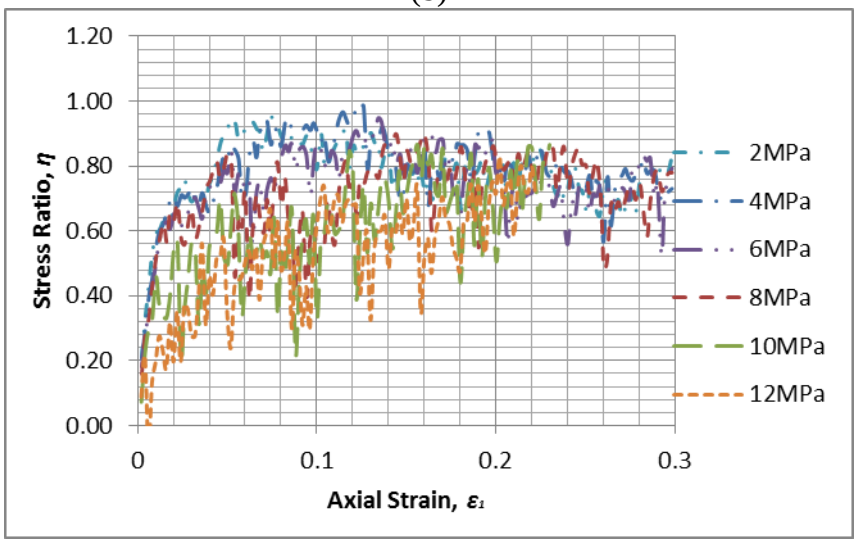

(c)

Figure 5.10 Stress-strain and volume plots for samples under conventional shearing with p_0'=17 MPa and different confining pressures

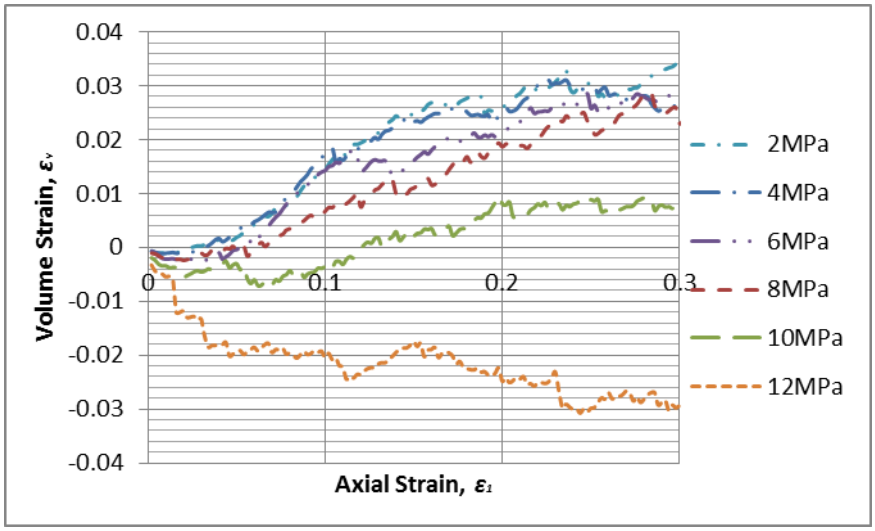

(a)

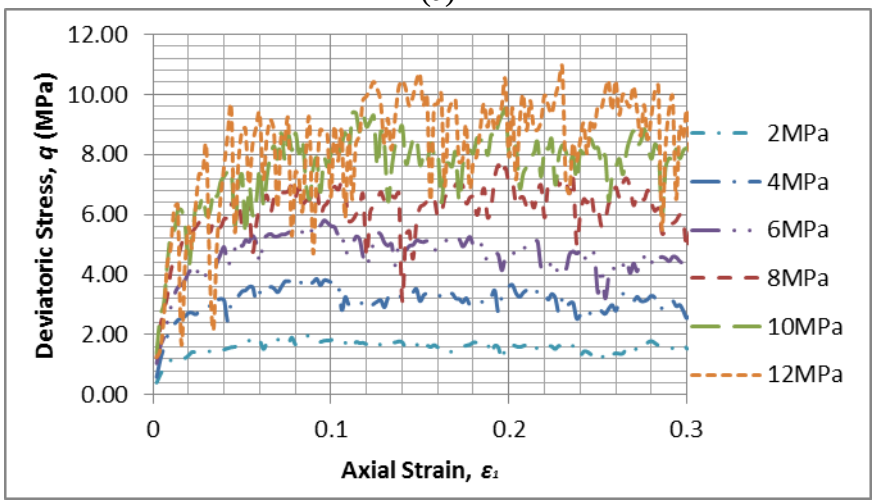

(b)

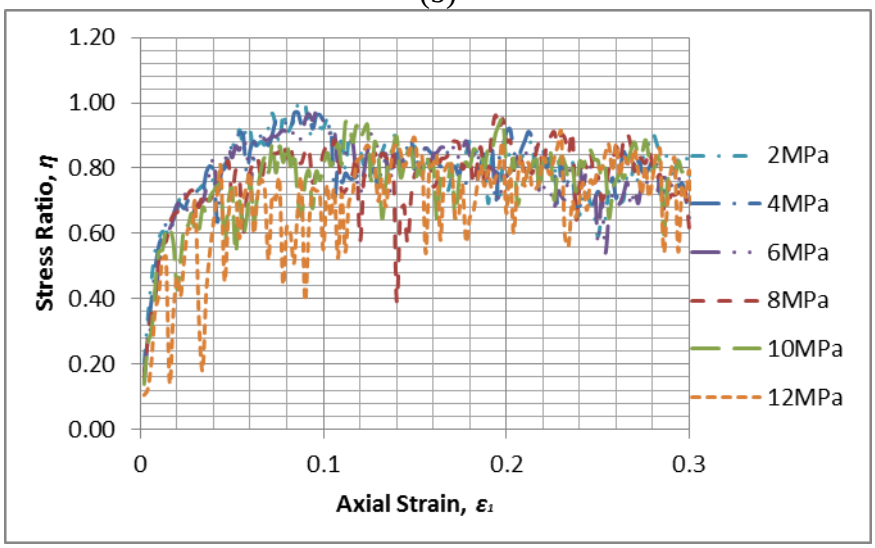

(c)

Figure 5.11 Stress-strain and volume plots for samples under constant-p' shearing with p_0'=17 MPa and different mean effective stresses

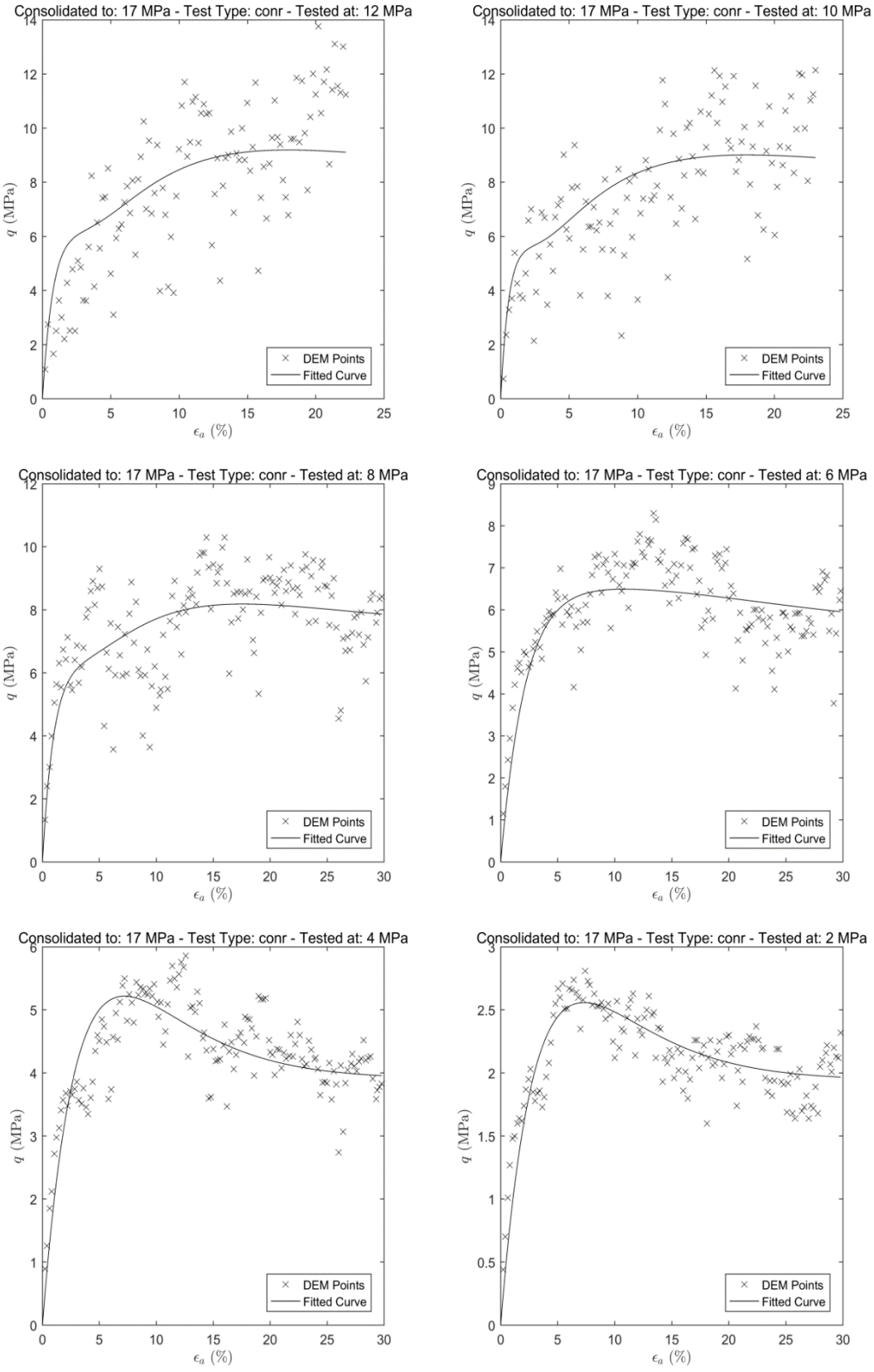

Figure 5.12 Stress-strain plots with fitted curve for triaxial shear at constant confining stress and a preconsolidation stress of 17 MPa.

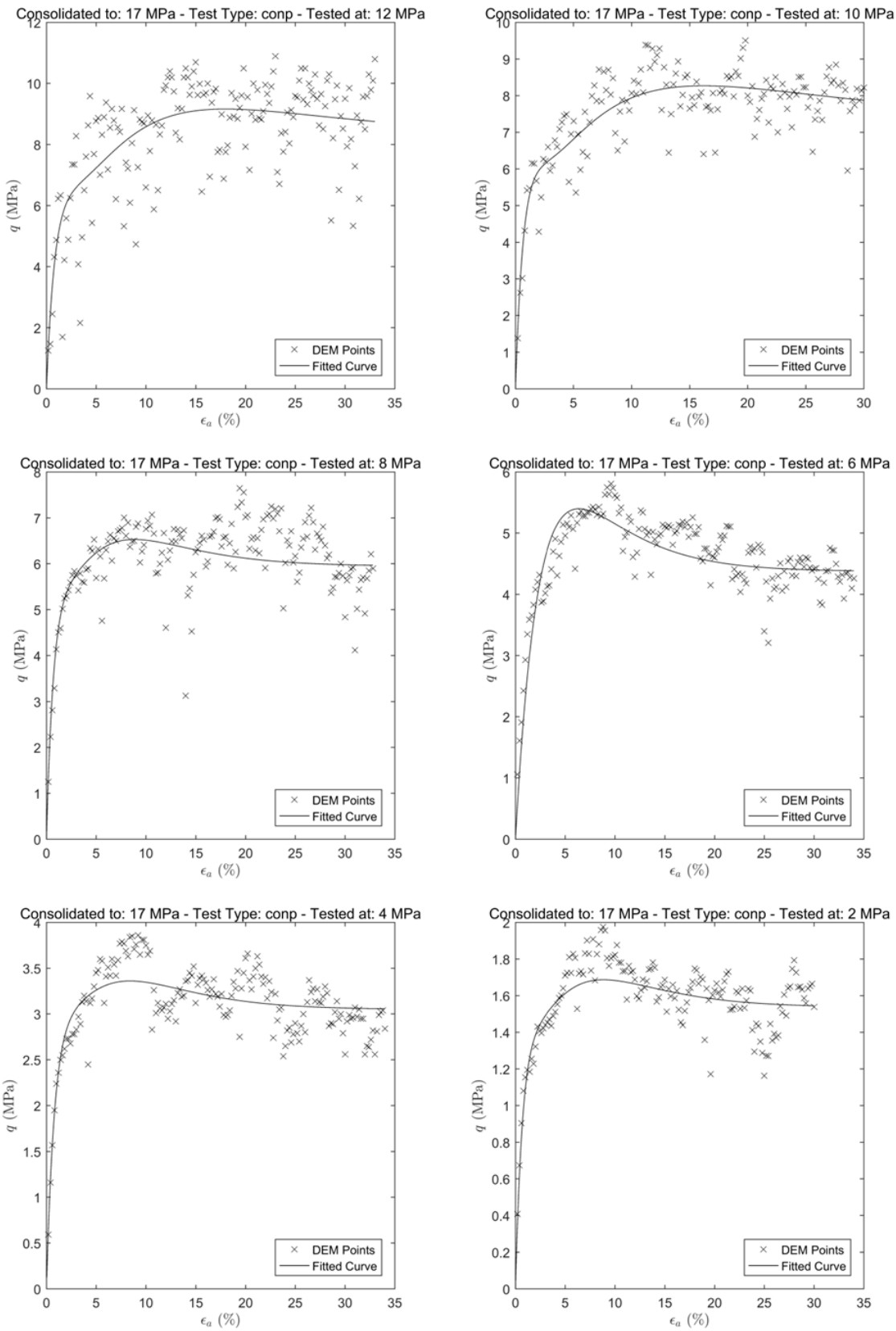

Figure 5.13 Stress-strain plots with fitted curve for triaxial shear at constant-*p'* and a preconsolidation stress of 17 MPa.

For samples at low initial mean effective stress levels, *i.e.* up to and including 6 MPa, peak strength, peak stress ratio and dilation after the initial contraction can be seen, implying that the initial states of the samples lie on the dense side of the CSL. The sample with 8 MPa confining stress shows almost no volumetric strain during conventional shearing, as shown in Figure 5.10 (a), implying that the initial state of the sample lies close to the point of intersection of the CSL and the unloading line. However the 8 MPa sample shows obvious dense behaviour when the constant *p'* stress path is followed. Samples under higher stress levels, *i.e.* larger than 10 MPa mean effective stress, contract during shearing and no peak strength or stress ratio can be observed. Large fluctuations can be seen for the samples during high stress shearing because of the large amounts of particle crushing, as is the case for the sample with 10 MPa confining stress and a 20 MPa over-consolidation history.

Effects of pre-consolidation stress on the behaviour of simulated sand

Comparisons can be made between the behaviour of the two most interesting samples starting near critical, with different pre-consolidation pressures and which follow the same stress path during shearing.

Figure 5.14 presents the stress-strain and volumetric plots of samples with 17 MPa and 20 MPa pre-consolidation pressures and a constant *p'*=10 MPa stress path. Much more obvious dilation and peak strength can be observed for the 20 MPa sample than for 17 MPa sample. Since the initial states of the two samples lie close to the CSL and the final states of the two samples lie on the curved portion of the CSL, the overconsolidation ratio (OCR) affects the behaviour of the two samples considerably. The initial state of the 20 MPa sample lies further away from the CSL than the 17 MPa

sample at the same initial stress level. For samples, the initial states of which lie on the dense side of the CSL and the final stress states of which lie on the curved region of CSL, the higher the over-consolidation ratio is, the more obvious the dense behaviour, *i.e.* dilation and peak strength, that can be observed. In other words, the behaviour of the sample when subjected to shearing is quite sensitive to the OCR when the initial state is near the curved region of the CSL.

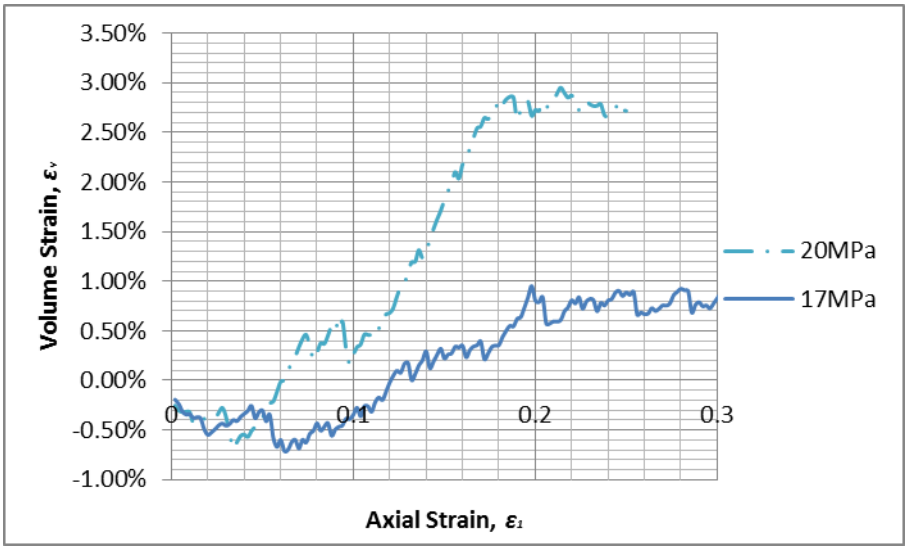

(a)

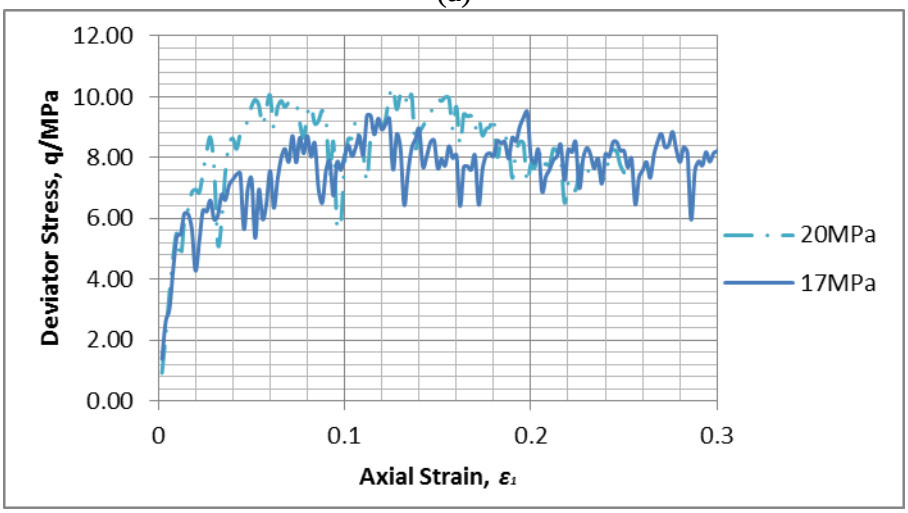

(b)

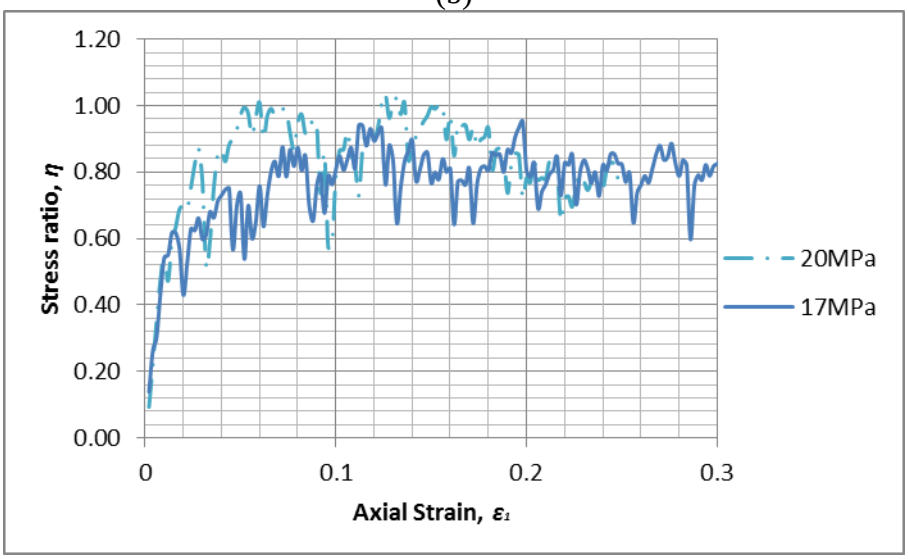

(c)

Figure 5.14 Comparisons of constant-*p*' tests for two different samples at mean effective stress equal to 10 MPa.

Effect of pre-consolidation on the uniqueness of CSL

The critical states for samples with 17 MPa pre-consolidation stress are taken using the same method as for samples with 20 MPa pre-consolidation stresses, *i.e.* the average value of the volumetric strains and deviator stresses when the sample reaches a stable state, typically after 20% axial strain. The critical state line and unloading line for 17 MPa samples are presented in Figure 5.15 together with the CSL and the unloading line for 20 MPa samples already presented in Figure 5.9, as well as the initial isotropic normal compression line.

A curved CSL for 17 MPa samples can be observed. The high stress linear part of the CSL for the 17 MPa samples coincides with that of the 20 MPa samples. With the data points obtained from the shearing of 17 MPa preconsolidated samples, the high stress linear part of the CSL containing 8 points can then be drawn and the slope of the CSL is indeed -0.5 in log e-log p' space, and is therefore parallel to the normal compression lines as is predicted by the CSSM framework and in agreement with the hardening law proposed by McDowell and de Bono (2013). The low stress part of the CSL for 17 MPa samples lies above that for 20MPa samples. Since the high stress part, *i.e.* linear part, of the CSL has been shown to be related to the clastic hardening law- the average strength of a particle as a function of the particle size—the differences in the low stress part of the CSL for the two series of samples can also be explained by the particle size distribution (PSD). As presented in Figure 4.14, the fractal dimension of the triaxial sample at p'=17 MPa is 2.17 and at p'=20 MPa is 2.27. A fully evolved PSD would associate with the fractal dimension of 2.5 in this case (McDowell and de Bono, 2013); hence the PSDs for the two series of samples are not fully evolved. Without a fully

evolved PSD, the critical state line cannot be expected to be unique. It can be observed from Figure 5.15 that the dilation of 20 MPa sample, i.e. the distance between the unloading line and the CSL at low stresses, is larger than that of 17 MPa sample.

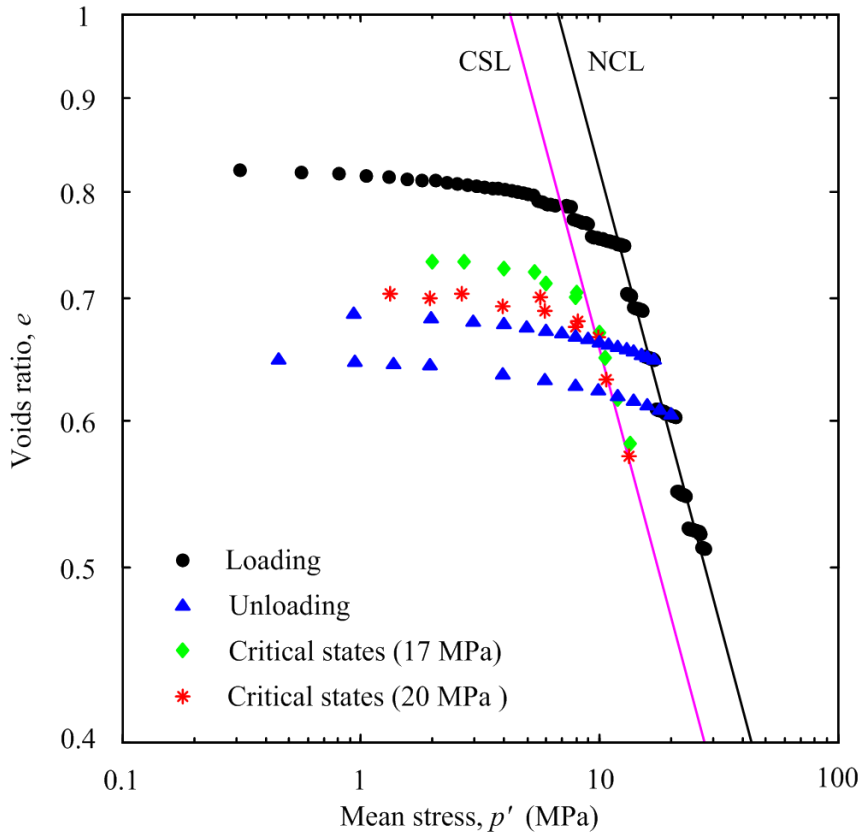

Figure 5.15 Critical state line for samples with different pre-consolidation pressures.

From these results, particularly the conventional triaxial tests, which exhibited ductile behaviour and contraction at the highest stresses, it can therefore be seen that fractal distribution of particles which resulted from crushing during normal compression (in this case of 17 MPa and 20 MPa) is the key to explaining the behaviour of overconsolidated sands on the dense and loose sides of critical. However, although Figure 5.15 suggests a unique critical state line, if the same sample was unloaded, 'reconstituted' to a looser state, then re-compressed and again unloaded to various over-consolidation ratios, one would expect a different critical state line to be observed upon shearing, particularly at low stresses (Wood and Maeda, 2008; Bandini and Coop,

2011). That is to say that the critical state line observed in Figure 5.15 is not fixed, but rather is a function of the crushing that has occurred, *i.e.* the particle size distribution achieved from isotropic compression to 17 MPa and 20 MPa. It is also important to note that although Coop *et al.* (2004) showed that crushing and volume change can occur in ring shear tests to shear strains over the order of 1000%, what we are examining here is the conventional notion of a critical state (Schofield and Wroth, 1968) at around 15 – 20% strain at which the volume and effective stresses are approximately constant. One might anticipate then that for very large stresses on the isotropic NCL, unloading and shearing would give rise to a CSL which is unique and independent of preconsolidation pressure because the particle size distribution has already fully evolved to D=2.5.

5.4 Micro behaviour of sample during shearing

The macro behaviour of the sample, as a result of the micro breakage mechanism of a single particle and the average strength of a particle as a function of particle size, has been proven to be in agreement with the mechanical predictions (e.g. Wood, 1990; McDowell and Bolton, 1998; McDowell and de Bono, 2013) and laboratory observations (Wood, 1990; Pestana, 1994). A micro mechanical analysis of the simulated sample during shearing to critical state is presented in this section.

5.4.1 The evolution of the total number of spheres when shearing to critical state

It is usually acknowledged that the energy dissipation at a critical state is by frictional sliding and rolling between particles and that particle breakage which is widely observed during shearing should cease at a critical state. At least, this is consistent

with the notion of volumetric hardening in which the plastic hardening is due to the creation of new particle surface area and that plastic hardening ceases at a critical state. Coop *et al.*(2004) performed ring shear tests on sands and found that sand particle breakages occur even at hundreds of percent strain. However, for conventional triaxial shearing or constant-*p'* shearing, it is still believed that particle breakage should not be a dominant feature of the mechanical behaviour at a critical state. The evolution of the total number of particles was therefore examined for all the samples subjected to conventional or constant-*p'* shearing and pre-consolidation pressures of 17 MP or 20 MPa. Figure 5.16 and Figure 5.17 show the evolution of the total number of spheres against the axial strain for samples with pre-consolidation pressures of 20 MPa and 17 MPa respectively. For all the simulations, the total number of spheres continues to increase while shearing at a critical state, which means that particle breakage still contributes to the energy dissipation at a critical state, albeit by a very small amount. The crushing particles at critical state are 'fines' with the smallest dimensions, so that the total volume of crushing particles is small. The higher the mean effective stress is, the higher the rate of increase of the number of spheres with strain.

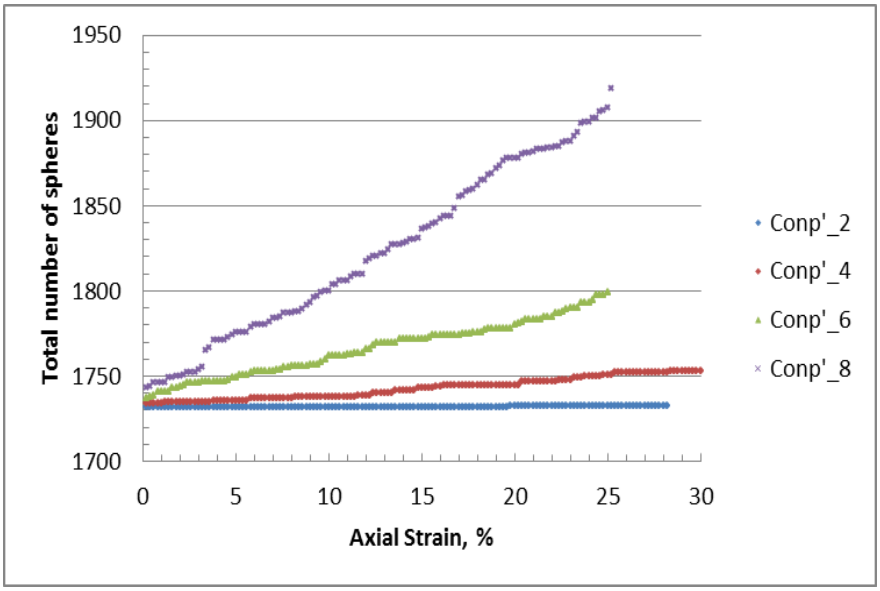

(a)

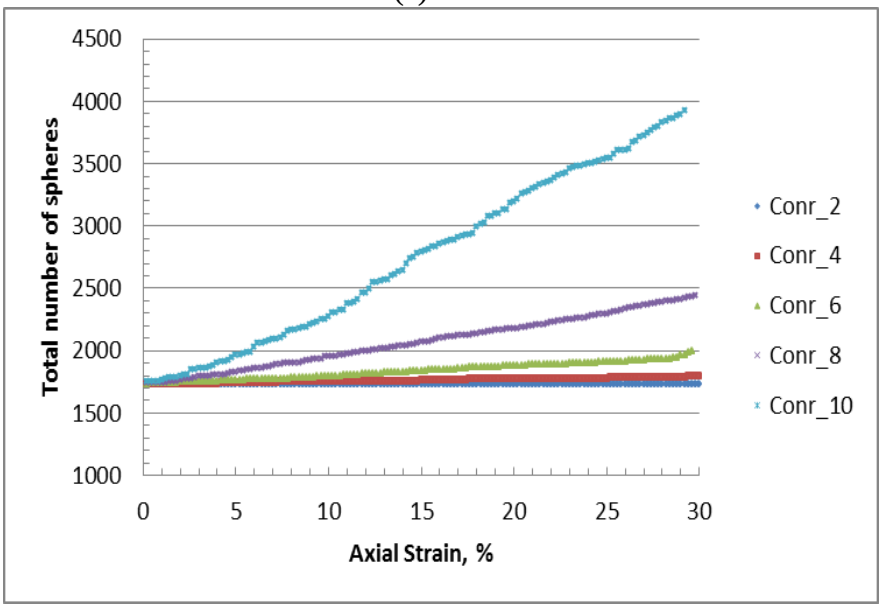

(b)

Figure 5.16 The evolution of total number of spheres as the axial strain increases for samples with p_0'=20 MPa : (a) constant-p' stress path; (b) conventional constant confining pressure stress path

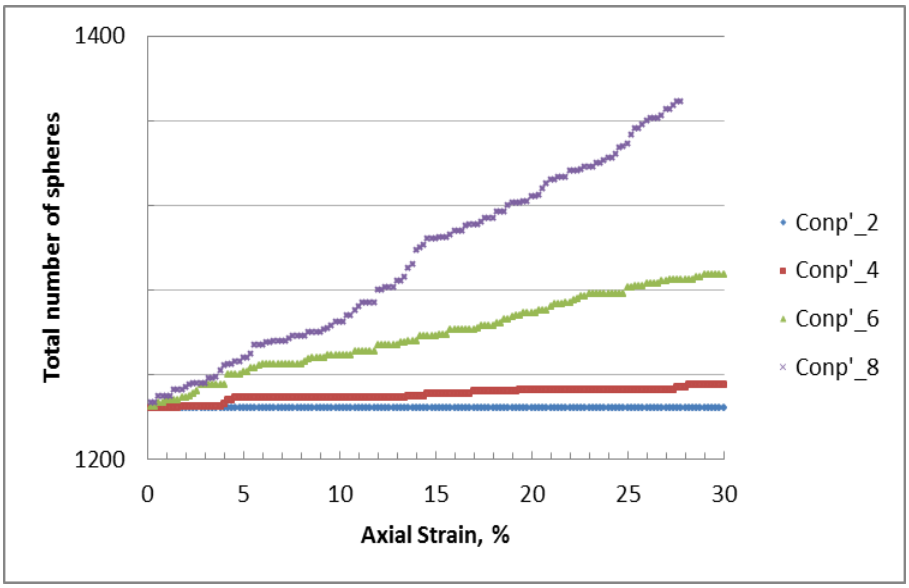

(a)

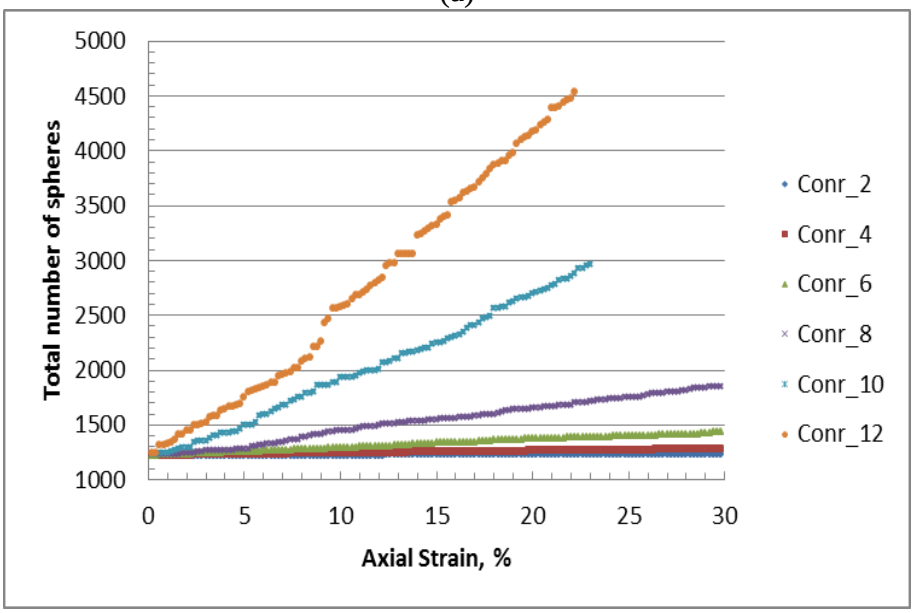

(b)

Figure 5.17 The evolution of total number of spheres as the axial strain increases for samples with p_0'=17 MPa: (a) constant-p' stress path; (b) conventional constant confining pressure stress path.

The evolution of the total number of spheres for the two samples sheared at 8 MPa with alternative pre-consolidation pressures is shown in Figure 5.18. The two lines are parallel; however the sample with 20 MPa preconsolidation pressure has a much larger number of spheres to begin with which means the proportion of crushing particles is

smaller for the 20 MPa sample than for the sample with a preconsolidation pressure of 17 MPa. Hence the scatter in the strength data, for example Figure 5.3, 5.7, 5.10 and 5.11, can be minimised by using samples with a much larger number of spheres. The particle size distributions of the two samples at critical state are examined. Due to the existence of a large amount of 'fines', which makes no contribution to the system mechanically for a lack of contacts with surrounding particles due to the small size, the mechanical particle size distribution is also examined, considering only particles with contacts. Particles with no contacts are considered mechanically inactive and are ignored when measuring the mechanical PSD. Figure 5.19 shows the particle size distribution of the two samples at critical state, *i.e.* 20% axial strain, measured in both ways. The term '_M' means the mechanical measuring method. It can be seen that the 20 MPa sample has larger proportion of small particles (d<0.5 mm) than the 17 MPa sample, when all the particles are considered. However, the mechanically active particles are mostly (more than 95%) larger than 0.5 mm, which means that coarse particles contribute more to the system mechanically than 'fines'.

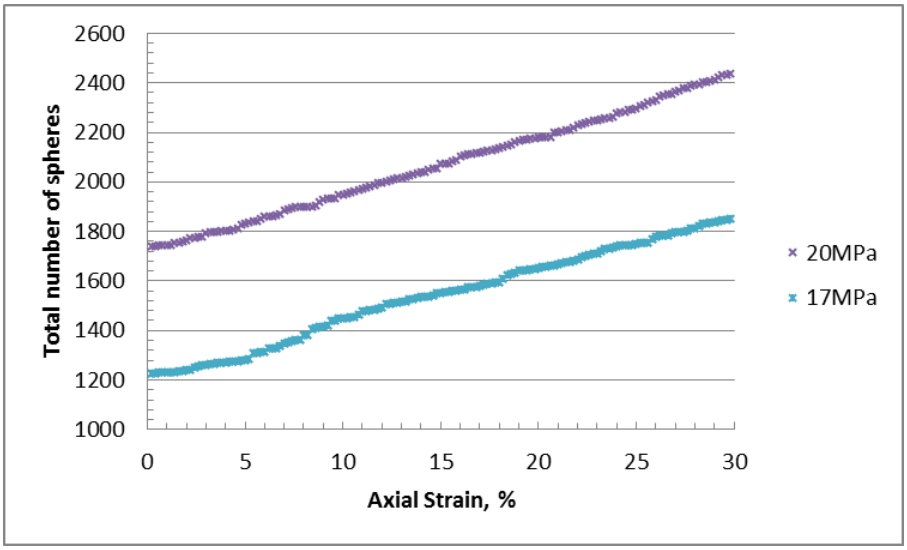

Figure 5.18 The evolution of the total number of spheres during conventional shear with the confining pressure of 8 MPa

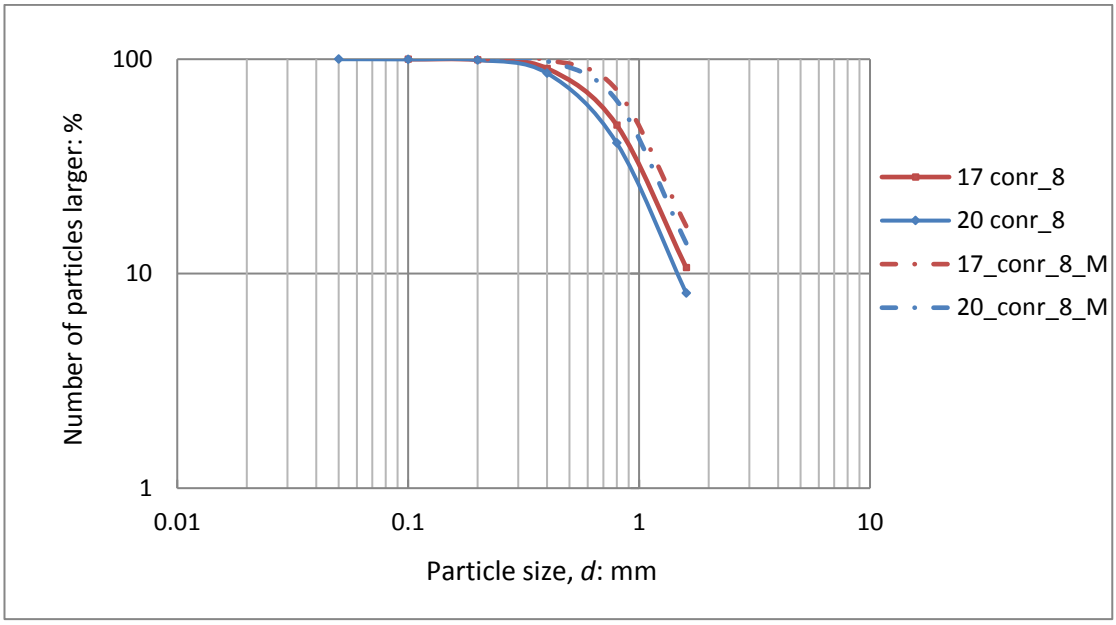

Figure 5.19 PSD and mechanical PSD at critical state.

5.4.2 The evolution of average coordination number during shearing

The average coordination number, *Z*, is an important micro mechanical parameter that helps define the crushability of a sample. The conventional method to calculate Z is:

$$Z = \frac{2C}{N} \tag{5-2}$$

where

- C is the total number of contacts;
- N is the total number of particles.

Thornton (2000) pointed out that there is possibility of the existence of particles with 0 or only one contact which won't contribute to the stable state mechanically. A mechanical average coordination number, Z_m, was therefore proposed by Thornton (2000):

$$Z_m = \frac{2C - N_1}{N - N_0 - N_1} \tag{5-3}$$

where N_0 and N_1 are the number of agglomerates with zero and one contacts respectively. However, in a stable state, every particle should be surrounded by balanced contact forces otherwise the particle will move under the unbalanced force, so N_1 is always zero.

In this simulation, the average coordination number is calculated in the most direct way: count the coordination numbers for each particle, add them together and divide the total coordination number by the total number of particles. The mechanical coordination number, Z_m, is calculated in the same way: count the coordination numbers for each mechanically active particle and add them together and divide the total mechanical active coordination number by the total number of mechanically active particles. This is better than using the alternative method of counting 'mutual' contacts between spheres as this causes problems at the sample boundaries.

Figure 5.20 and Figure 5.21 present the evolution of the average coordination numbers of samples with pre-consolidation pressures of 20 MPa and 17 MPa respectively when shearing to a critical state. The average coordination numbers for all the samples decrease throughout the test. The higher the mean effective stress is, the greater the rate at which the average coordination number decreases as strain increases. The initial average coordination number for a sample increases with the increase of initial mean effective stress, since the sample under a high stress level has a relatively denser packing and a smaller voids ratio.

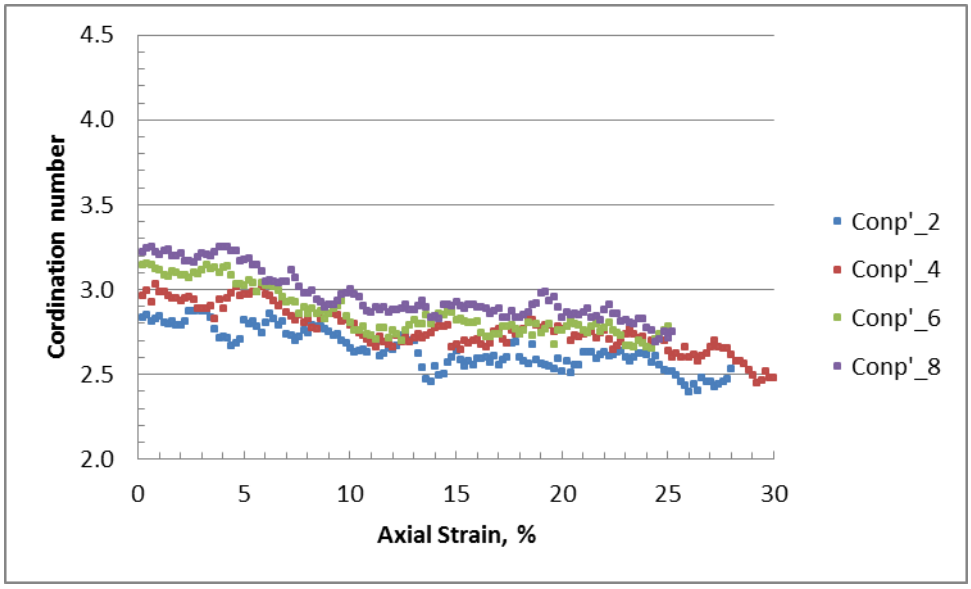

(a)

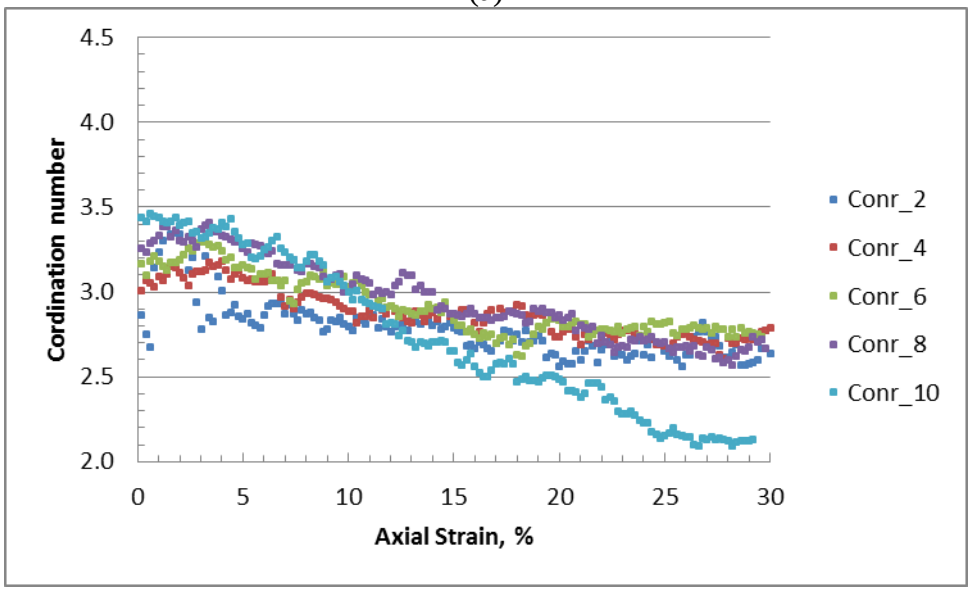

(b)

Figure 5.20 Evolution of average coordination number of samples with p_0'=20 MPa: (a) constant-p' stress path; (b) conventional constant confining pressure stress path

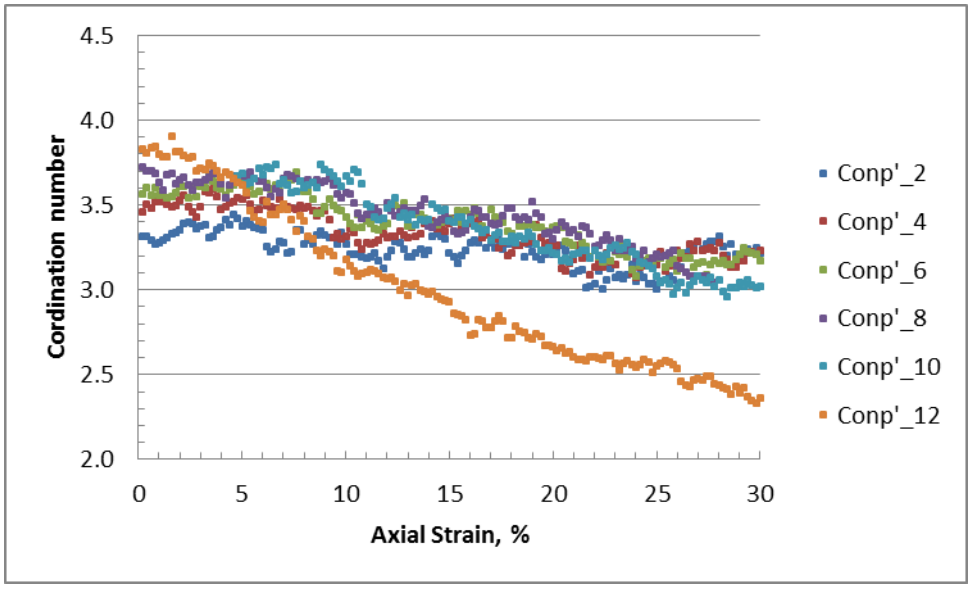

(a)

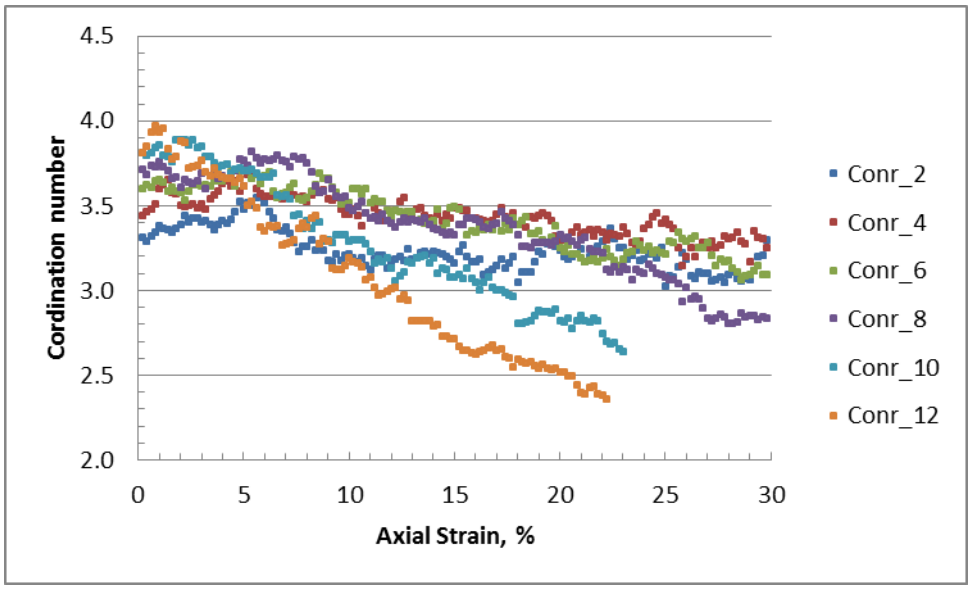

(b)

Figure 5.21 Evolution of average coordination number of samples with p_0'=17 MPa: (a) constant-p' stress path; (b) conventional constant confining pressure stress path

The evolution of average mechanical coordination numbers for samples with pre-consolidation pressures of 20 and 17 MPa are shown in Figure 5.22 and Figure 5.23 respectively. The average mechanical coordination numbers for the samples at low stress levels, *i.e.* samples with initial mean effective stresses up to 6 MPa for both pre-consolidation pressures of 17 MPa and 20 MPa, show almost no change during shearing.

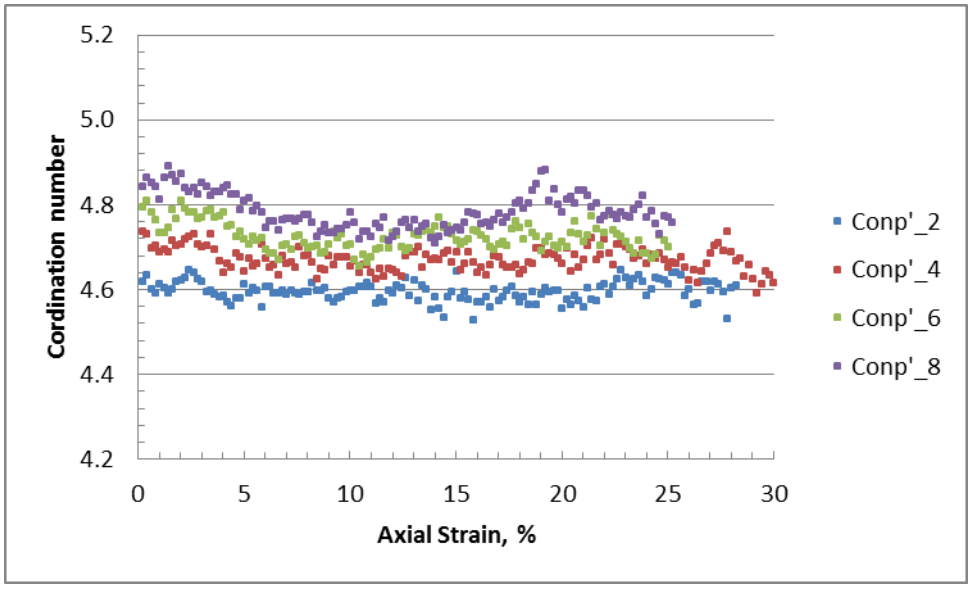

(a)

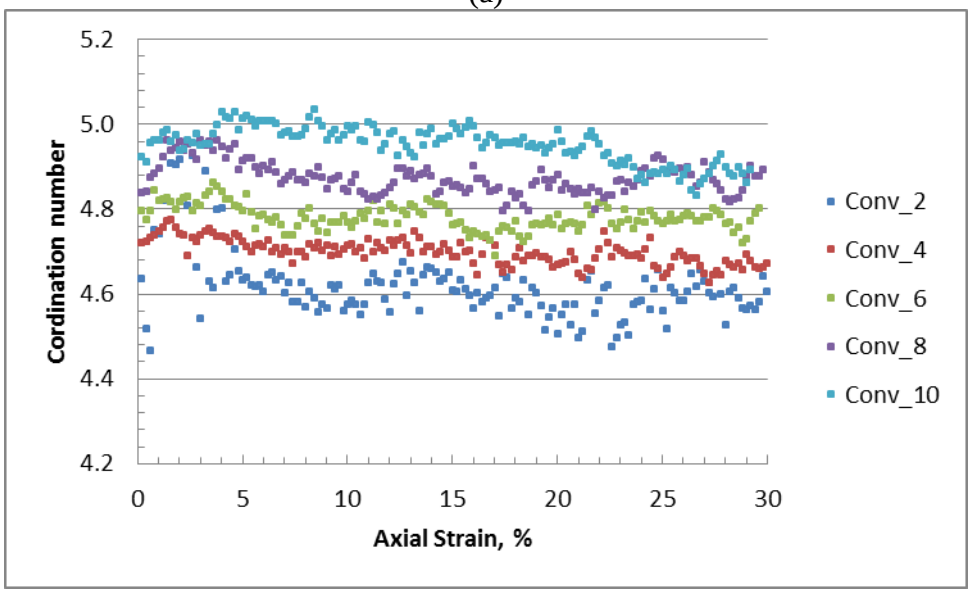

(b)

Figure 5.22 Evolution of average mechanical coordination number of samples with p_0'=20 MPa: (a) constant-p' stress path; (b) conventional constant confining pressure stress path

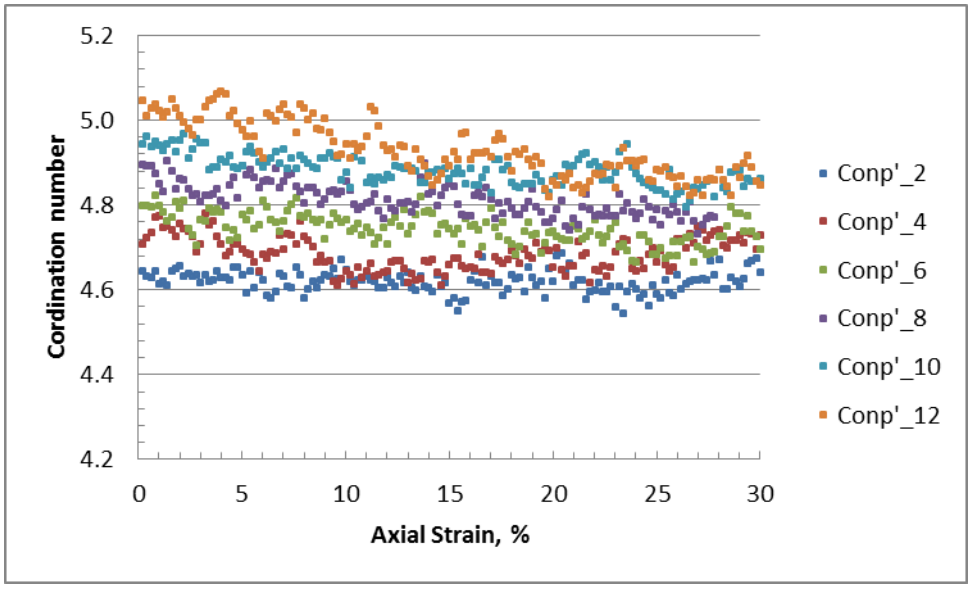

(a)

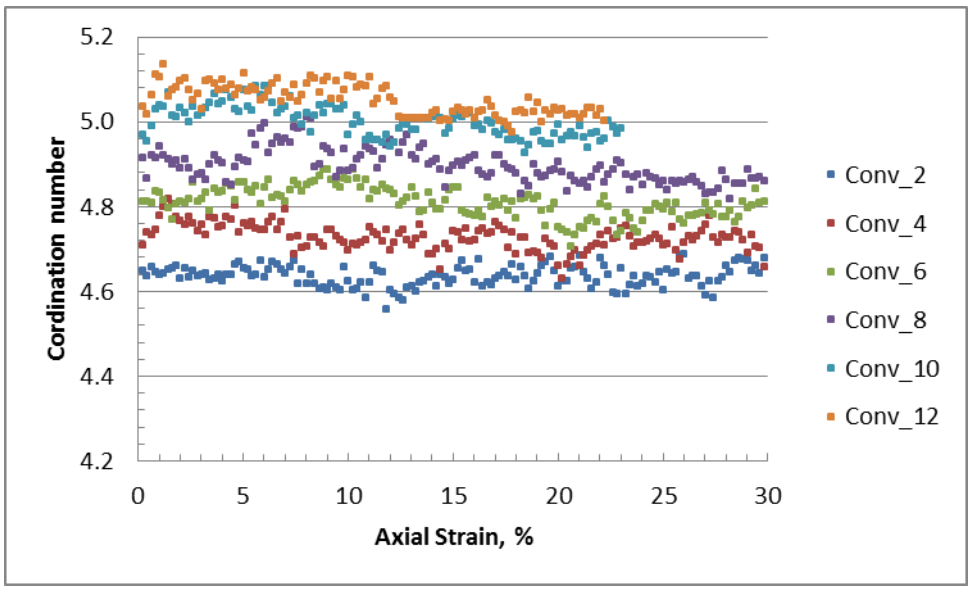

(b)

Figure 5.23 Evolution of averagemechanical coordination number of samples with p_0'=17 MPa: (a) constant-p' stress path; (b) conventional constant confining pressure stress path

A slight decrease in the average mechanical coordination number can be observed for samples at high stresses, which is under contraction, which is different from Bolton *et.al* (2008), who used agglomerates when simulating the crushable particles (Figure 5.24). Their linear contact model together with the constant stiffness applied to

'internal' spheres under all stress states leads to large overlap between particles under compression, as was proved by Wang (2014). After the breakage of an agglomerate, the fragments are under relatively lower stress states than before, and relatively smaller overlaps between spheres within the fragments will be generated as the interiors of the agglomerates expand after fracture. This means that extra contacts will be generated as the expanding agglomerates fill the void space, increasing the co-ordination number.

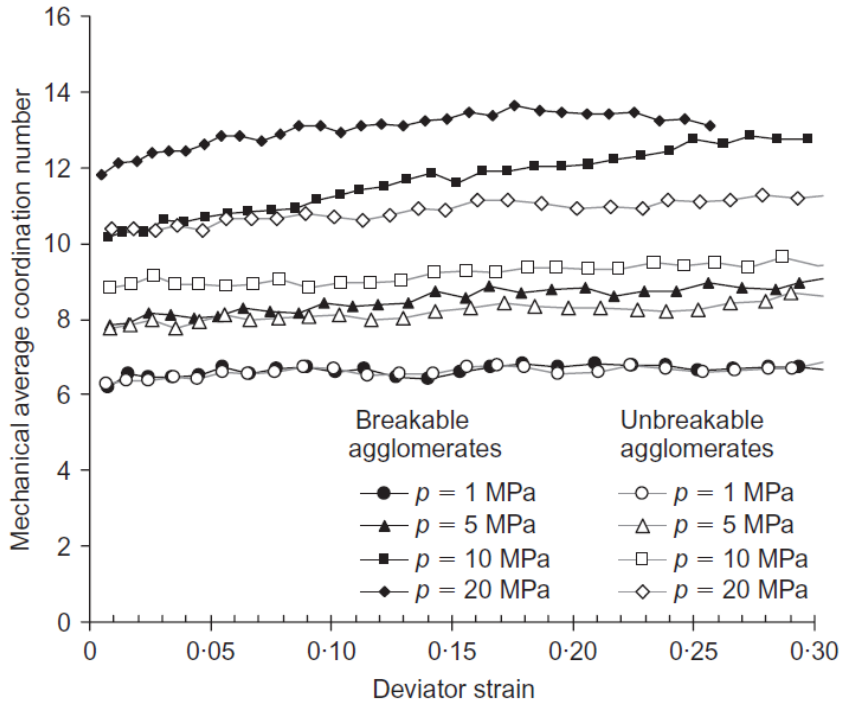

Figure 5.24 Evolution of mechanical average coordination number during triaxial shearing (Bolton et al. 2008)

Fonseca *et al.* (2013) examined the relation between the coordination number and the void ratio in lab triaxial tests using CT scanning to obtain the evolution of the average coordination number during shearing (Figure 5.25). They proposed that the average coordination number decreases with increasing axial strain, in agreement with the DEM results presented previously (Figure 5.22 and Figure 5.23). However, their average coordination number is much higher than the number obtained in this research. It can be explained that real sands show angularity and have higher chance to build

interlock and contacts with surrounding aggregates than spheres, so that the perfectly rounded spheres will lead to much lower coordination number than real sand.

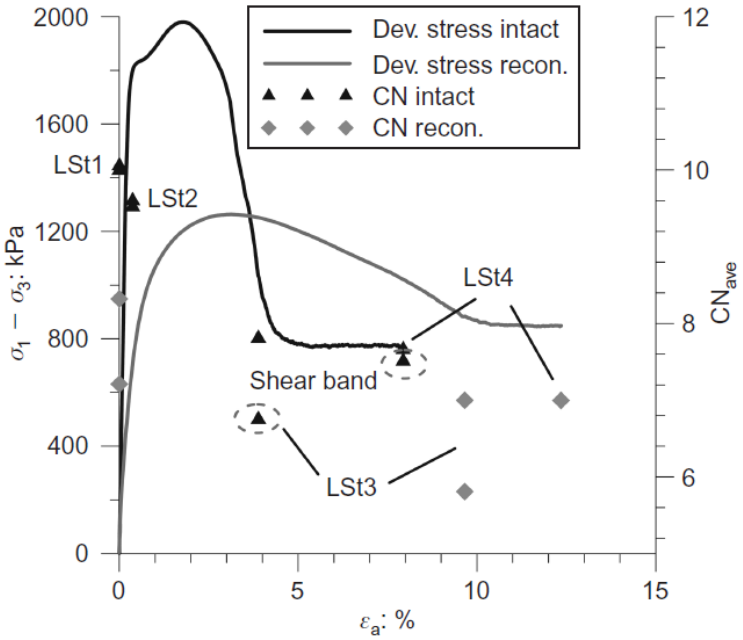

Figure 5.25 Evolution of coordination number with deviatoric stress response during shearing (Fonseca et al. 2013)

Given the linear increase in the total number of particles with strain throughout the test and the slight fluctuation of the average mechanical coordination number around a constant value, it can be assumed that the reduction of the average coordination numbers in Figure 5.20 and Figure 5.21 come from newly generated fragments which have no effective contacts and flow freely within the voids between larger particles. So, particles continue to crush at a critical state, while some of the 'fines' (newly generated small fragments) does not mechanically influence the macro behaviour of the sample at critical state. It also explains why the particle crushing at critical state cannot be measured in lab: the particle crushing comes mainly from the smallest particles for which the size is too small to be accurately measured. That is to say, the crushing at a critical state would not be measured by a sieving analysis.

The vertical sectional views of different samples at critical states are presented in Figure 5.26. It can be seen that at low stress levels, at 2 MPa mean effective stress for example, most of the particles have contacts with surrounding spheres at a critical state; while at high stress level, 10 MPa mean effective stress for example, a lot of tiny fragments without any contacts can be observed. The tiny fragments are also susceptible to breakage since the size is too small to obtain large number of contacts and hence a large tensile stress is easily induced if the particle should become loaded at a later stage. However what is apparent is that at a critical state, the crushed 'fines' does not contribute much to the mechanical response of the material. In this sense plastic hardening can be deemed to have ceased at a critical state.

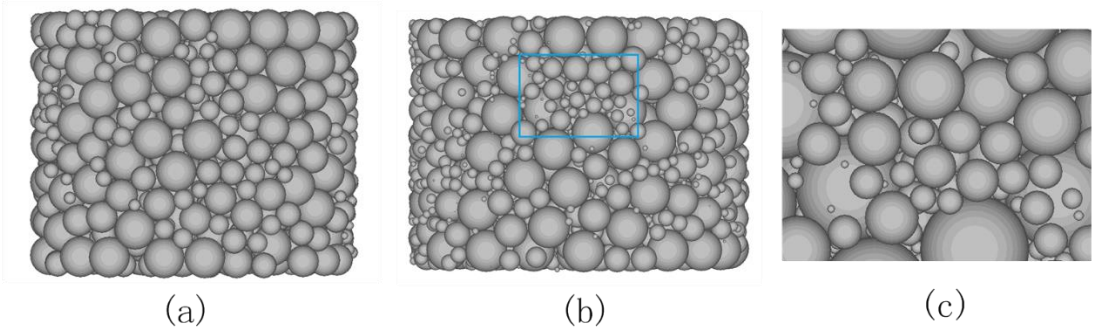

Figure 5.26 Vertical section of different samples at critical state: (a) constant confining stress of 2 MPa; (b) constant confining stress of 10 MPa; (c) enlarged view of the blue area in (b).

5.5 Conclusions

A previously used particle splitting model has been used to investigate the evolution of critical states. The triaxial sample of spheres has been isotropically compressed to alternative stresses of 17 and 20 MPa, well beyond yield and such that a fractal distribution of particles has largely evolved. The 17 MPa and 20 MPa isotropically consolidated samples have been isotropically unloaded to various stress levels and then conventional and constant-*p'* triaxial shear tests have been performed.

All samples reach a critical state with a critical state constant, *M*, which is consistent with the predicted value using the measured value of K_0 under one-dimensional normal compression, suggesting that for sand that is normally compressed beyond yield, the friction angle in Jâky's (1944) equation is the critical state friction angle, as for clay. The application of the PBM, avoiding the artificial limit of crushable particle size, contributes to the accurate calculation of *M*, which is not constant with increasing stress level for simulations applying the BPM.

At low stress levels the samples exhibit a peak strength and dilation, which both reduce as the initial isotropic stress increases. The conventional triaxial tests of samples from 8MPa with the pre-consolidation pressures of 17and 20MPa, exhibit little volume change even though drained and thus the initial state of the sample has been established to be close to critical, while that sheared from 10 MPa, with 17 and 20 MPa preconsolidation stresses, exhibit ductile behaviour and contraction to a critical state. The stress path greatly influences the behaviour of samples. The 10 MPa sample with 20 MPa preconsolidation stress dilates to critical state following a constant p' stress path and contracts to critical state following a constant confining stress (conventional) stress path. Samples following the conventional stress path are at higher mean effective stress level than samples following the constant-*p'* stress path, resulting in more fragments and smaller amounts of dilation than samples under constant p' shearing from the same initial mean effective stress. The pre-consolidation pressure also influences the behaviour. For samples following the same stress path, the one with the higher over-consolidation ratio produces a smaller proportion of fragments than the one with the low over-consolidation ratio.

At high stress levels, the CSL has been shown to be unique for the sample, independent of the stress path, mean effective stress and the pre-consolidation pressure. At high stresses, the CSL is parallel to the one-dimensional and isotropic normal compression lines in log e – log p' space, in agreement with conventional CSSM. At low stresses and high over-consolidation ratios, the CSL is not parallel to the NCL and its exact location depends on the pre-consolidation pressure. In this sense the CSL is not unique at low values of OCR. One would assume that as the preconsolidaton pressure increases, this portion of the CSL at large values of OCR also becomes unique, when the isotropically clastically compressed sample has fully evolved to a fractal dimension of 2.5.The particle splitting model has therefore been able to capture the essential behaviour of overconsolidated sands sheared to critical states.

The simulations have also shown that crushing continues at a critical state, although this involves the production of ‘fines’ only. This has the effect of reducing the average co-ordination number but the average mechanical co-ordination number is relatively unaffected. It is important that the simulations have shown the production of only fine particles at a critical state, since we would still wish to retain the notion of a critical state as a state where plastic hardening has ceased, *i.e.* no crushing.

Chapter 6 CSL and Yield Surface

6.1 Introduction

In previous chapters, the particle splitting model (McDowell and de Bono, 2013) has been used to investigate the behaviour of simulated silica sand under 1-D compression, isotropic compression, unloading and shearing. The 1-D and isotropic normal compression lines and the critical state line have been shown to be parallel to each other in log *e*- log *p'* space at high stress, consistent with the conventional critical state soil mechanics framework. The question is then raised whether the splitting model will also produce reasonable behaviour of simulated sand in stress space: that is, whether it is possible to establish a 'Cam clay type' yield surface for overconsolidated sand using the DEM model adopted in this thesis. The yield surface in stress space, *i.e. q-p'* space, is a key element when describing the behaviour of a soil. Therefore yielding of the simulated sand in states looser and denser than critical will be investigated in this chapter.

Different definitions of yielding of soil as well as different methods of choosing yield points have been proposed during the last eight decades of research into soil behaviour. Comparisons will be made here on choosing yield points according to different methods. The stress strain plots presented in Chapter 5 will be adopted when choosing the yield points. However, the stress-strain plots show significant scatter due to particle breakage during shearing, and the small number of particles used for the test; the sample used here could hardly be described as a continuum. A smoothing method of the data will be introduced in order to produce a curve which best fits the stress-strain data.

This chapter will also give a brief discussion of the flow rule of the simulated sand by comparing the location of the CSL and the shape of yield surface in stress space.

6.2 Definition of yielding and yield point

6.2.1 Definition of yielding

Most conventionally, yielding of a material is defined as the stress at which a material begins to deform plastically. The yielding generally corresponds to the change of stiffness of the material. The material shows only elastic deformation prior to yield. The concept of yield helps determine the safety limits of performance of soils. However, soils and sands usually show a soft failure mode with a more gradual yielding region which does not cause catastrophic failure immediately, and which makes it difficult to determine a yield start point. In addition, whilst yield for a clay is relatively easy to determine, for sand, by the time the experimentalist believes a sand has yielded, the behaviour has already moved well beyond that yield point; there is no single well defined yield point in any space.

One definition of yield involves some interpretation of the degradation of stiffness. Jardine (1992) defined three characteristic zones which sub-divide the interior region enclosed with the outer bounding surface in normalised stress-space (Figure 6.1).

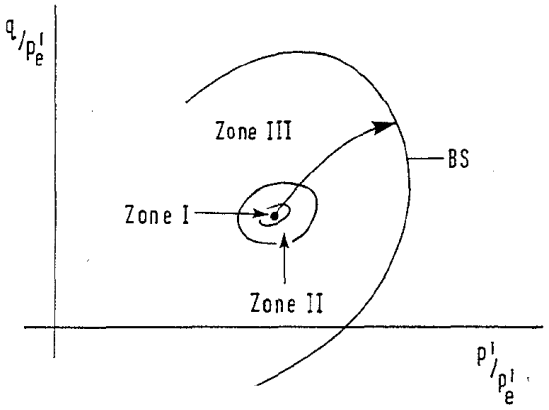

Figure 6.1 Identification of Zone I, II and III in normalised stress space (Jardine, 1992)

Within Zone I, soil shows purely linear elastic behaviour, which means the unloading line coincides with the loading line in voids ratio – mean effective stress space (or variations thereof). The strain limit of Zone I is usually smaller than 0.001% axial strain. In Zone II, soil shows non-linear elastic behaviour, which means a fully recoverable behaviour with a closed unload-reload cycle (quasi-elastic hysteretic behaviour). The strain limit of Zone II is usually smaller than 0.01%. For Zone III, soil deformation consists of both elastic and plastic parts. On the state boundary surface (also known as yield surface), soil shows only plastic deformation. It is agreed that the purely elastic deformation region of soil is very small and the gradual yielding results in a curve for the stress-strain plot which exhibits no sharp change in stiffness.

6.2.2 Methods of choosing yield point

Due to the absence of an obvious yield point, several methods have been proposed to establish what yield might be taken to be.

Intersection method

The maximum curvature on a stress strain curve plays an important role in describing the behaviour of a soil. For example, the point of maximum curvature is considered

an important point in determining the yield stress in the Cassagrande (1936) method for interpretation of oedometer tests (Craig, 1997). Yasufuku *et al.* (1991) took the maximum curvature on the stress-strain plot from a triaxial shear test as the yield point, which corresponds to the start of fully plastic deformation (Hashiguchi, 1978). Nakata *et al.* (2001) took the maximum curvature on the 1-D NCL on $e - \log \sigma_v'$ space as the yield point in 1-D normal compression tests. The logic of the method can be explained: in a 'stress-strain' plot, the slope of the tangent to any point on the curve corresponds to the stiffness at that point and the curvature of the curve relates with the changing rate of the stiffness; so that by choosing the maximum curvature on a stress-strain plot, the point corresponding to the fastest changing of the stiffness of the material is located. The yield point located using this method produces an index of the safety limit, beyond which the stiffness reduces very quickly.

However, due to the limit in computational power until very recently, the location of the maximum curvature could not be located accurately and the yield point was calculated using intersecting tangents to the stress-strain curve pre- and post-yield to obtain the yield point, as was applied by Yasufuku (1991), Figure 6.2.

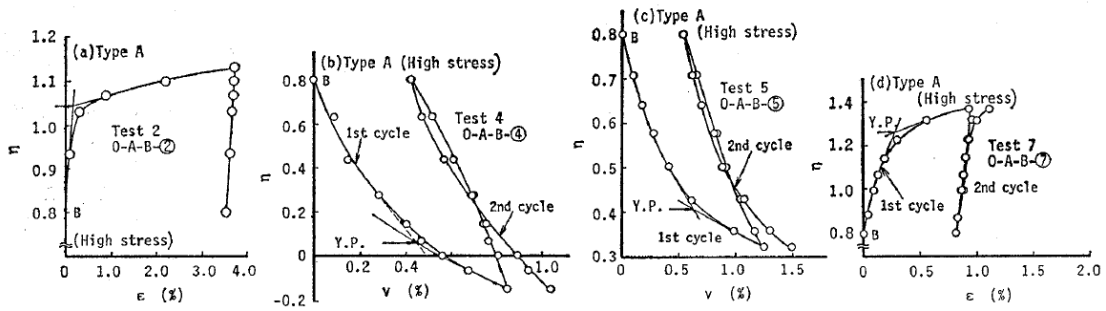

Figure 6.2 Yield points on the stress-strain plots using intersection method (Yasufuku *et al.*, 1991)

The yield points in Figure 6.2 are identified with arrows and labelled. It can be seen that the chosen yield points appear at very low strain levels and lie close to the maximum curvature of the curve but the yield stress and strain given by this method

do not actually lie on the stress-strain curve. Cheng (2004) also used the intersection method to locate the yield point of samples under triaxial shear simulations (Figure 6.3). However, the method may lead to inaccurate yield points when the pre-yielding and post-yield regions are not obvious.

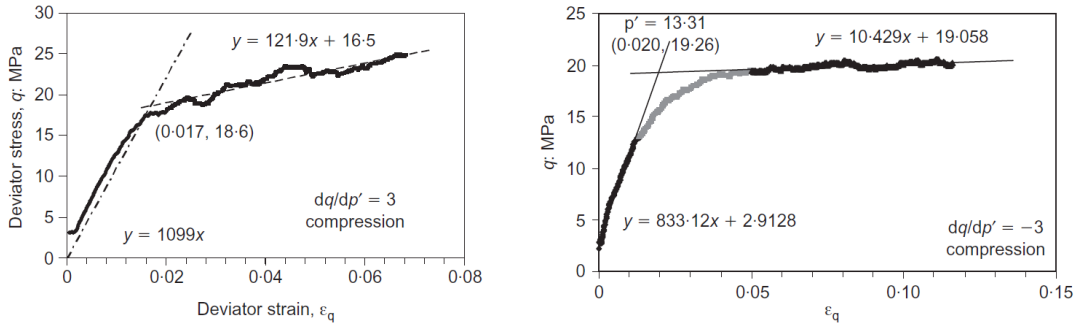

(a) (b)

Figure 6.3 Yield points according to the intersection method (Cheng, 2004)

It can be seen from Figure 6.3 (a) that the pre-yielding region is such that the deviator strain is taken to be smaller than 2% and post-yielding is chosen as corresponding to the deviator strain between 2% and 7%, while the yielding continues and deviator stress still increases with strain. It can be expected that a third region will occur at large strains as the sample tends to a critical state. The post-yielding region in Figure 6.3 (b) plot is between 5% and 12% deviator strain, which is larger than the range in Figure 6.3 (a) and the stress does not increase with increasing strain in this post-yield region. The yield strength in Figure 6.3 (b) plot is approximately the critical state deviator stress, while the yield strength in (a) is not. The conventional intersection method tends to overestimate the yield stress for a gradually developed yield. Figure 6.3 (b) is a typical case in point: the yield point lies far above the curve and cannot show the character of the maximum curvature on the curve. Different choices of pre-yield and post-yield regions also lead to different yield points with totally different physical meanings, which makes the method not that accurate in choosing yield point.

In other words, the application by eye of the tangents in Figure 6.3 is subjective and different engineers would arrive at different estimates of the yield stress.

Modified intersection method

In order to generate a yield surface with consistency, all the points lying on the surface should have a unified physical meaning. Based on the logic of the conventional intersection method, *i.e.* using tangential fitting lines of pre-yield and post-yield regions to locate the maximum curvature of the curve, a modified intersection method will be applied in this study: the yield strain is determined by the intersection of the linear fit to the pre-yielding region and the horizontal fit to the final critical state; the yielding deviator stress is the stress on the curve corresponding to the determined yield strain. In this way, the chosen yield point will lie on the curve. This is a simplified method based on the Cassagrande method for determination of preconsolidation pressure (Craig, 1997).

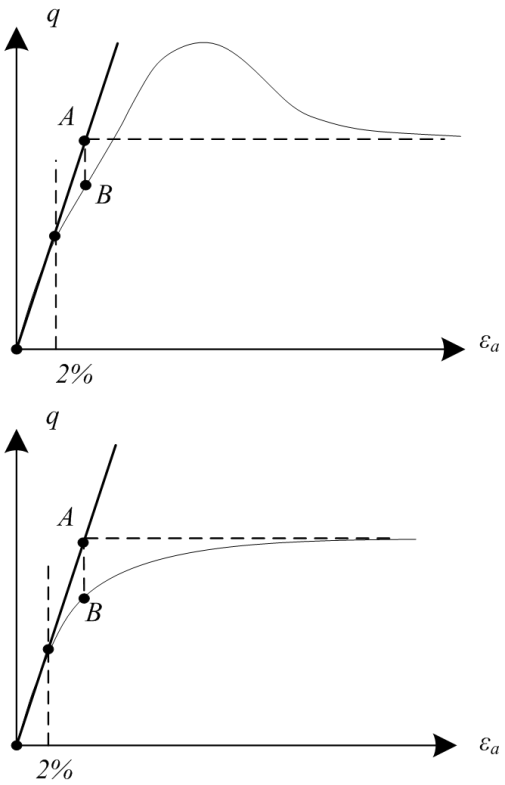

Figure 6.4 Schematic plot of the modified intersection method of choosing yield point

Figure 6.4 presents the modified intersection method of choosing the yield point on a stress-strain plot schematically for samples on both dense and loose sides of critical state. The straight solid line is the linear fit to the data points within the first 2% axial strain using the polyfit function in Matblab. Point A is the intersection of this line to the horizontal line representing the critical state, which is the average stress of points when the axial strain is larger than 20%. The yield point is point B which lies on the stress-strain curve at the same strain as point A.

Maximum curvature method

The two methods described previously, the intersection method and modified intersection method, are based on logic to locate the maximum curvature of the plot. However both the methods can only give an approximation and not accurately measure

the point of maximum curvature. With the advanced computer technology now that exists, a new method that accurately measures the maximum curvature will be presented in this chapter. The yield point is considered to be at the point of maximum curvature on a stress-strain plot of the simulated sand under triaxial shearing.

A circle fit function in MATLAB developed by Izhak Bucher (1991) is employed to fit the discrete data points on the curve into different inscribed circles. The MATLAB code of circle fit is given in Appendix C. Given that the maximum curvature means the point on a curve that has an inscribed circle with the smallest radius, the radius of different circles are then compared and the point associating with the smallest radius is taken as the yield point.

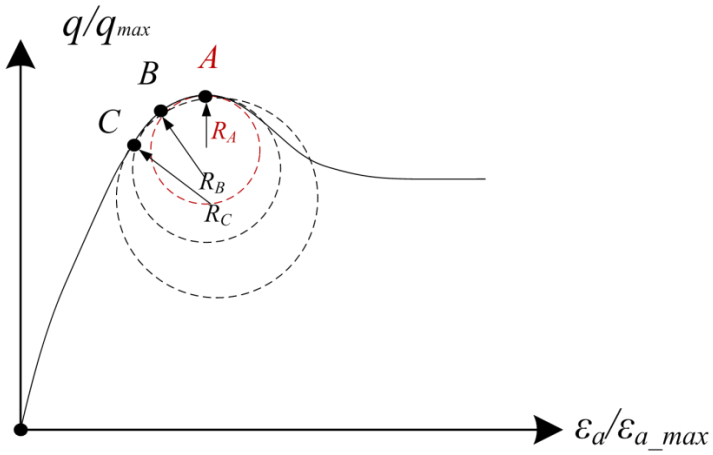

Figure 6.5 Schematic plot of the maximum curvature on a curve

Figure 6.5 presents the method of locating the maximum curvature point on a curve. An inscribed circle is drawn through each point on the curve, taking points A, B and C as typical points. For the correct determination of the maximum curvature it is necessary to assure both axes are equal in scale hence q and ε_a are normalised by their respective peak values. The circle with the smallest radius is the one drawn through point A, $R_A<R_B<R_C$. Point A is hence determined to be the point associated with the maximum curvature, *i.e.* yield point, in this plot.

Combined method

The stress-strain plot for triaxial shearing of soils on the dense side of critical state usually shows a peak, as has been pointed out by Wood (1990), Pestana (1994) and Klotz and Coop (2002). The peak strength on the stress-strain plot corresponds to the maximum dilation rate (Figure 6.6) when volumetric strain is plotted against axial strain. Beyond the peak strength, the material exhibits rupture softening and the sample dilation rate reduces to zero at a critical state. The engineer would not wish to approach the peak strength once the critical stress ratio is exceeded because this would present the danger of a catastrophic soil failure. As is shown in schematic Figure 6.6, point A is the peak stress in the $q - \varepsilon_a$ plot and point A*'* in the volume plot is the projection of point A; point B' is the lowest point in the volume plot and point B is the projection of point B' in the $q - \varepsilon_a$ plot; meanwhile the deviator stress at B is equal to the critical state deviator stress. The plastic dilation starts after B' and the maximum rate of dilation occurs at point A'. Since the peak stress or strength in the stress-strain plot is usually associated with the maximum curvature (the maximum rate of change of stiffness (approximately)), for consistency, the yield point on the loose side of critical state is taken as the maximum curvature of the stress strain plot. In this way, the maximum curvature definition of yield should give a peak strength for dense soils and a yield stress that corresponds approximately to the value given by the maximum curvature method on the loose side of critical.

The following yield criterion is adopted in this study: for the sample showing obvious peak behaviour, *i.e.* peak stress is 10% higher than the critical stress, the peak stress is

taken as the yield point; for the sample showing no obvious or no peak behaviour, the point corresponding to the maximum curvature is taken as the yield point.

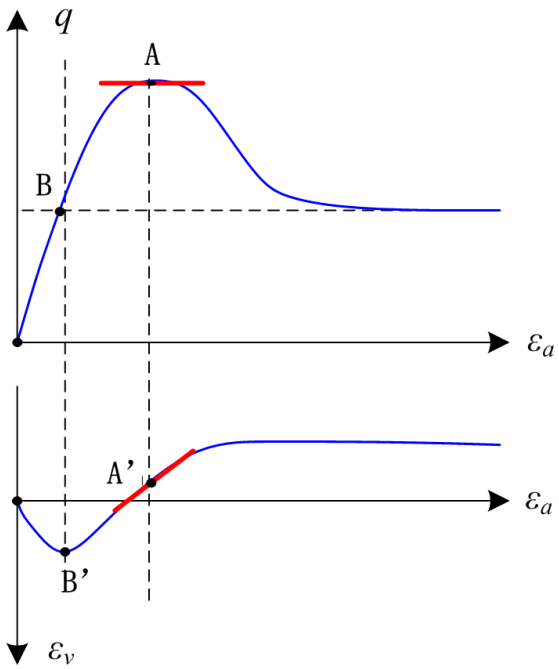

Figure 6.6 Schematic plot of peak and critical strength and associated dilation

Stiffness degradation method

Instead of taking the fastest rate of the change of stiffness, *i.e.* maximum curvature on the stress-strain plot, the threshold of the change of stiffness is also taken as a yielding criterion here in what is referred to as the stiffness degradation method. This method consists of three steps:

- Reproduce the curve with normalised deviator stress, q/q_{max}, of the data (q_{max} is the maximum q in the raw data);
- Draw the linear fit line of the curve within the first 2% axial strain;

- Determines the difference in q/q_{max} at each ε_a between the curve and the fitted line.

The yielding point is taken as the point when the difference in normalised deviator stress equals a certain threshold, *i.e.* point A in Figure 6.7. A range of values were tried and the threshold was determined to be 0.2 to give good choice of yield point.

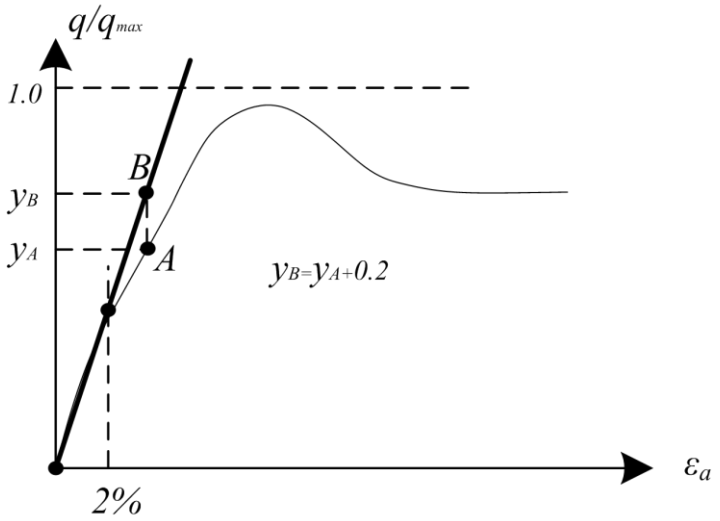

Figure 6.7 Schematic plots of the stiffness degradation method

The basic logic of the method is that the difference of the normalised stress between the fitted curve and the linear fit comes from the cumulative change of the stiffness of the material; the cumulative change shows the ongoing of yielding of the material; when the change is large enough, the material is taken as having yielded. The method takes the first 2% axial strain as the threshold beyond which the plastic deformation takes place, because the lowest point in the volumetric plot of those shear tests on dense samples appear roughly around 2% axial strain.

6.3 Data smoothing function

Since particle breakage is considered for all the simulations in this study, and due to the small number of particles, large fluctuations can be observed for all the plots. The

scatter of the data points makes it difficult to choose a yield point. Therefore, the data needs to be smoothed. Two methods are applied here when smoothing the data points: direct smoothing of data points using MATLAB; and a smoothing curve that follows an equation which is used to give good fit of the data points and which has been shown to work well in experimental direct shear tests (proposed by Hashemi). Both methods involve the data processing in MATLAB.

6.3.1 Direct smoothing

There are two steps in the direct smoothing method:

(1) directly smooth the input data points of the stress- strain plot in MATLAB;

(2) 'polyfit' the smoothed stress values with the polynomial with seven data points. Finally a curve is generated after the smoothing of data points.

The fitted smooth curves together with the raw data points of the four series of tests are presented in Figure 6.8 to 6.11 respectively. The term 'Conp' stands for the constant-*p'* test and the subscribed number shows the value of the mean effective stress through the test. The term 'Conr' stands for the constant confining stress test and the subscribed number shows the value of the confining stress through the test. It can be seen that although the curves are smooth and give good fit for low stress level tests, the curves cannot give good fit to the data points at high stress levels, because of the scatter caused mainly by crushing.

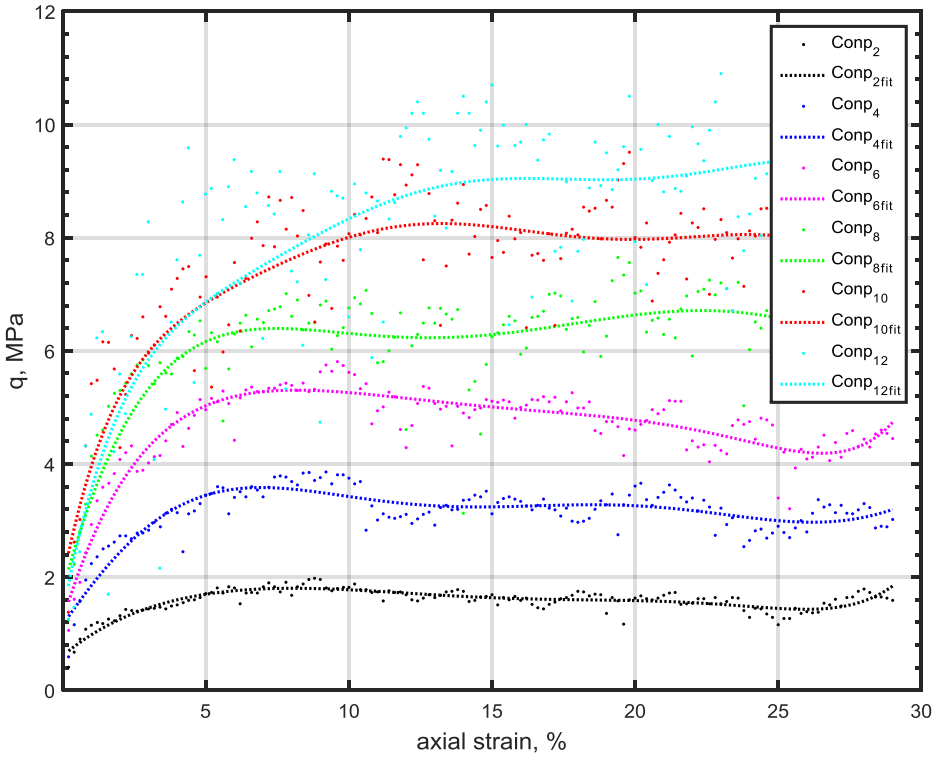

Figure 6.8 The smoothed $q - \varepsilon_a$ curves of triaxial shear test of samples at constant-p' and 17 MPa preconsolidation pressure.

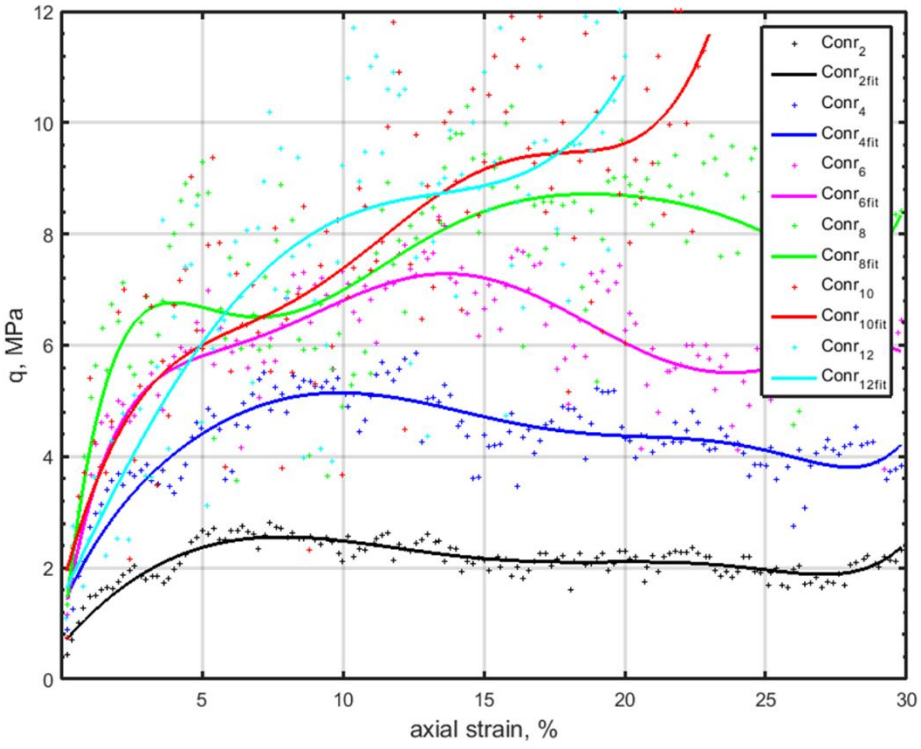

Figure 6.9 The smoothed $q - \varepsilon_a$ curves of triaxial shear tests of samples at constant confining stress and 17 MPa preconsolidation pressure.

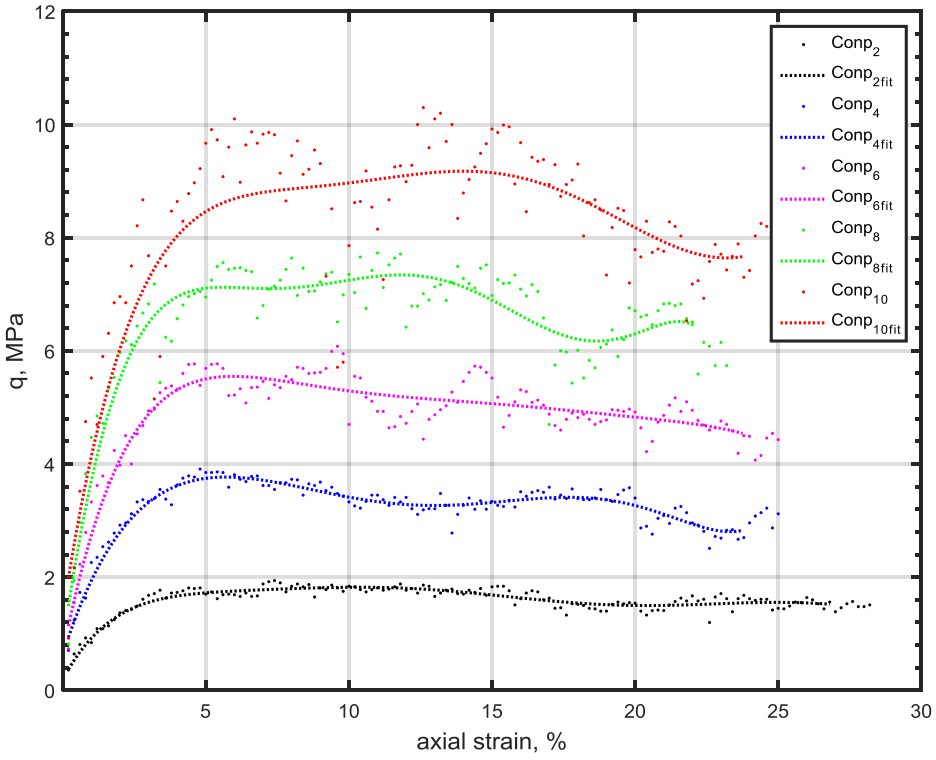

Figure 6.10 The smoothed $q - \varepsilon_a$ curves of triaxial shear tests of samples at constant-p' and 20 MPa preconsolidation pressure.

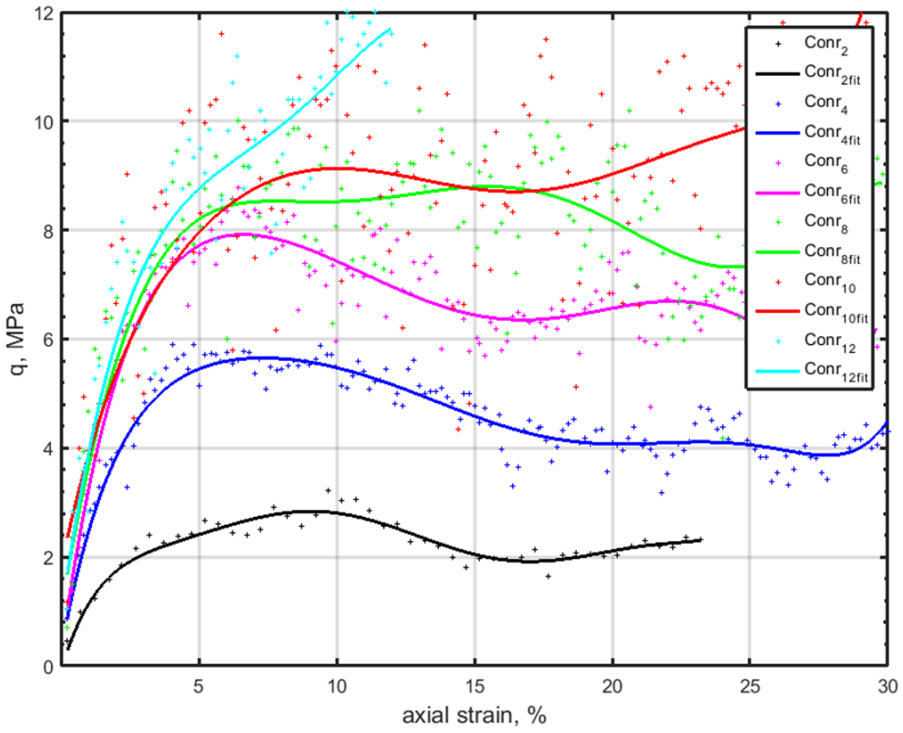

Figure 6.11 The smoothed $q - \varepsilon_a$ curves of triaxial shear tests of samples at constant confining stress and 20 MPa preconsolidation pressure.

6.3.2 Smoothing according to an exponential function

Hashemi (2016) proposed two equations to give a fit of direct shear test data,

$$u = u_r + e^{a_1 w_h}(A_1 + B_1 \cdot w_h) \tag{6-1}$$

where

- u is the vertical displacement;
- w_h is the horizontal displacement;
- u_r is a constant such that $u = 0$ when $w_h = 0$;
- A_1, B_1 and a_1 are constants to be determined in MATLAB calculation.

$$\tau = \tau_r + \sigma_n \frac{du}{dw_h} = \tau_r + \sigma_n \cdot e^{a_1 w_h}(A_1 \cdot a_1 + B_1 + B_1 \cdot a_1 \cdot w_h) \tag{6-2}$$

where

- τ is shear stress;
- τ_r is the constant such that $\tau = 0$ when $w_h = 0$.

Due to the irregular three part shape of the $q - \varepsilon_a$ plot, it was decided to introduce an extra exponential term to give a better fit to the data points. Because of the significant scatter of the stress data, σ_n in Eq. 6-2 is not used. It is only the general shape of the equation that is demanded, but not the physical meaning of each component in the equation, and the function of σ_n can be replaced by modifying the value of other constants in the equation. The smoothing code is shown in Appendix A and B. The fitted curve may not be as smooth as a single exponential one but will be closer to the raw data and hence gives more accurate representation of the behaviour of the sample. The equation for the triaxial shear data is

$$q = q_r + e^{a \cdot \varepsilon_a}(A_1 \cdot a_1 + B_1 + B_1 \cdot a_1 \cdot \varepsilon_a) + e^{a_2 \cdot \varepsilon_a}(A_2 \cdot a_2 + B_2 + B_2 \cdot a_2 \cdot \varepsilon_a) \quad (6\text{-}3)$$

where

- q is the deviator stress;
- ε_a is the axial strain;
- q_r is a constant such that the value of q equals zero when the axial strain $\varepsilon_a = 0$;
- A_1, B_1, a_1 and A_2, B_2, a_2 are factors for the two exponential parts that can be determined by the best fit of the data.

MATLAB is then used to determine the best fit curve to the raw data from the simulated triaxial shear tests. The deviator stress and the corresponding axial strain are inserted into MATLAB matrices and the values of q_r, A_1, B_1, a_1 and A_2, B_2, a_2 are calculated to give the minimum total variance between the fitting curve and the raw data points.

The fitted curves according to the double exponential equation have already been presented in Chapter 5, Figures 5.4, 5.8, 5.12 and 5.13.

Figure 5.13 shows the curve fit against the raw data from constant *p'* triaxial shear tests on samples with 17 MPa overconsolidation history. Figure 5.12 presents the curve fit against the raw data from conventional triaxial shear tests with constant confining pressure on samples with 17 MPa overconsolidation history. Figure 5.8 shows the fit against the raw data from constant *p'* triaxial shear tests on samples with 20 MPa overconsolidation history. Figure 5.4 presents the curve fit against the raw data from conventional triaxial shear tests with constant confining pressure on samples

with 20 MPa overconsolidation history. The best fit curves following Eq. 6-3 give good representation of the behaviour of samples under triaxial shearing. These fitted curves for the different tests have subsequently been adopted to choose the yield points.

6.4 Yield points and yield surface

6.4.1 Yield points

The yield points chosen according to the five different methods:

- the intersection method, which directly takes the intersection points of the two linear fits as the yield point;
- the modified intersection method, which uses the intersection of the two linear fits to locate the strain of the yield point, and the yield point is the point on the $q - \varepsilon_a$ curve that corresponds to the located strain;
- the maximum curvature method, which takes the yield point as the accurately located maximum curvature on the $q - \varepsilon_a$ plot;
- the combined method, which takes the yield stress as the peak stress on the $q - \varepsilon_a$ plot for samples on the dense side of the critical state and the maximum curvature on the $q - \varepsilon_a$ plot for samples on the loose side of the critical state;
- the stiffness degradation (change in stiffness) method, which takes the yield point as point where the stiffness degradation is beyond a certain threshold

The MATLAB code of choosing the yield points is given in Appendix A. The results are shown in Figure 6.12 to 6.15. The blue square gives the yield point according to the intersection method. The pink triangle presents the yield point according to the modified intersection method. The green dot resembles the yield point according to

the maximum curvature method. The red diamond shows the yield point taken according to the combined method: peak point on the dense side of critical state and the maximum curvature on the loose side of critical state. The light blue triangle shows the yield points following the degradation of stiffness (change in stiffness) method which takes the cumulative change in stiffness as the yielding criterion.

It can be seen that on the dense side of critical state the maximum curvature points (green dots) and peak stress points (red diamonds) lie close to each other. The modified intersection points (pink triangles) lie below the maximum curvature points and combined method points. This is because the horizontal line at $q = q_c$ and the initial straight line fit to the first 2% strain to find the intersection, gives a value of q at the target strain on the stress-strain curve which curve is always smaller than the critical state deviator stress (and hence by defining the peak or maximum curvature points), as is shown in Figure 6.4. The yield points according to the intersection method (blue squares) lie below the peak and maximum curvature points for the same reason described above. The cumulative stiffness degradation points (light blue triangles) also give relatively lower yield points than the first two methods, because the threshold of the degradation in stiffness is not large enough (approximately 0.2). However, in order to give a reasonable threshold on the loose side of critical state resulting in a yield stress smaller than the critical deviator stress, the value of the threshold cannot be too large. If the threshold is large enough to result in a peak stress on the dense side of critical state, the value of the yield stress on the loose side of the critical state will always be the critical state deviator stress.

Apart from the intersection method, all the other four methods give roughly the same yield points for samples on the loose side of critical state; that is for curves that show no peak behaviour. It is true for the intersection method that on the loose side of critical state, yield develops gradually and the yielding region is too large that the straight fit line of the post-yield region is a horizontal line at $q = q_c$, so that the yield stress taken directly from the intersection will always be equal to the critical deviator stress, q_c, and the yield point will always lie above the $q - \varepsilon_a$ curve. This means that this method will always give a yield stress ratio that is the critical state stress ratio. So that the yield point chosen by the intersection method contributes no engineering useful limit: too conservative on the dense side and cannot use the material efficiently; too dangerous on the loose side of critical state, the material will provide no more support and fail at the given limit. The method is not suitable for choosing yield point.

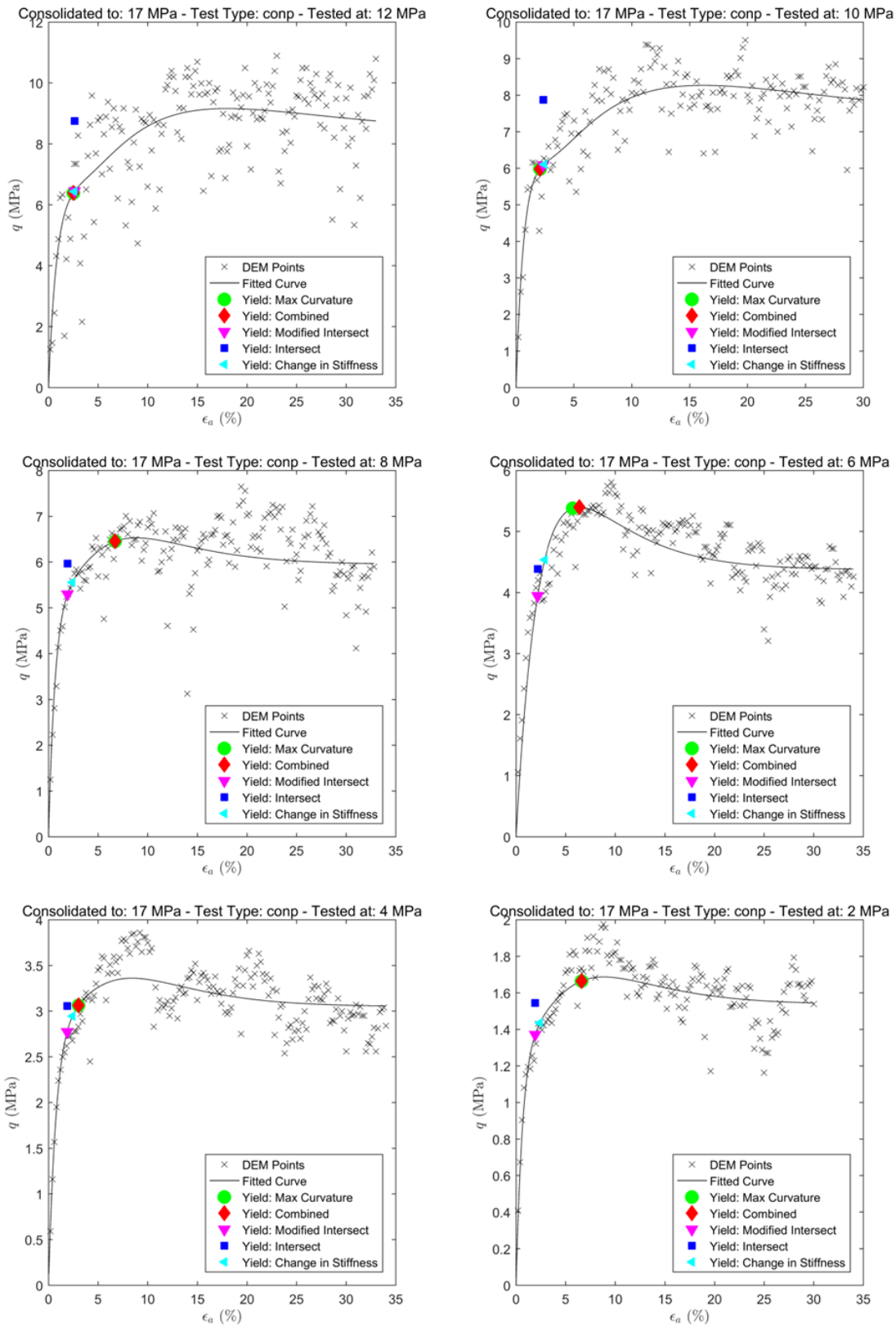

Figure 6.12 Yield points according to different methods for the 17 MPa samples under constant-p' triaxial shearing.

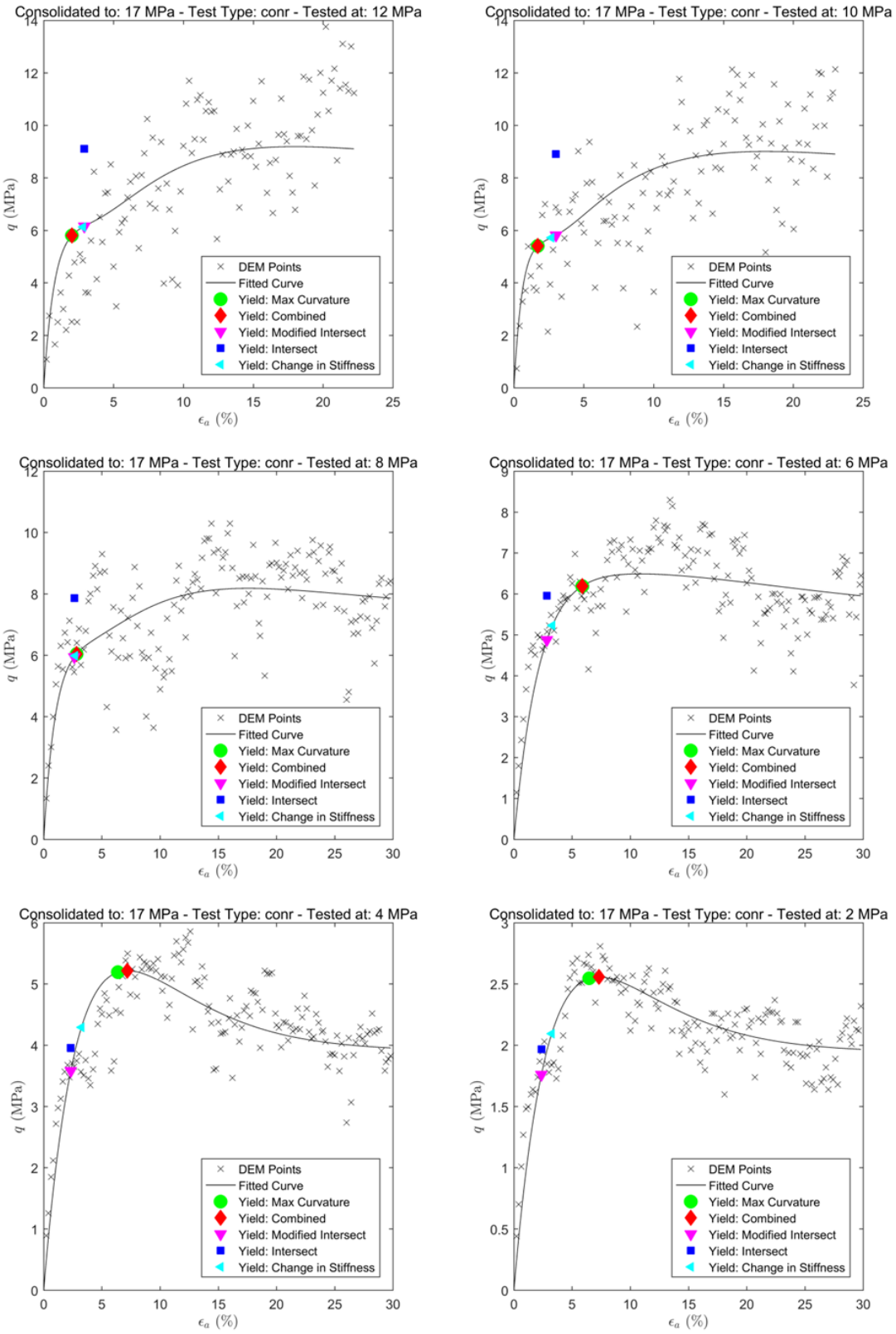

Figure 6.13 Yield points according to different methods for the 17 MPa samples under constant confining stress triaxial shearing.

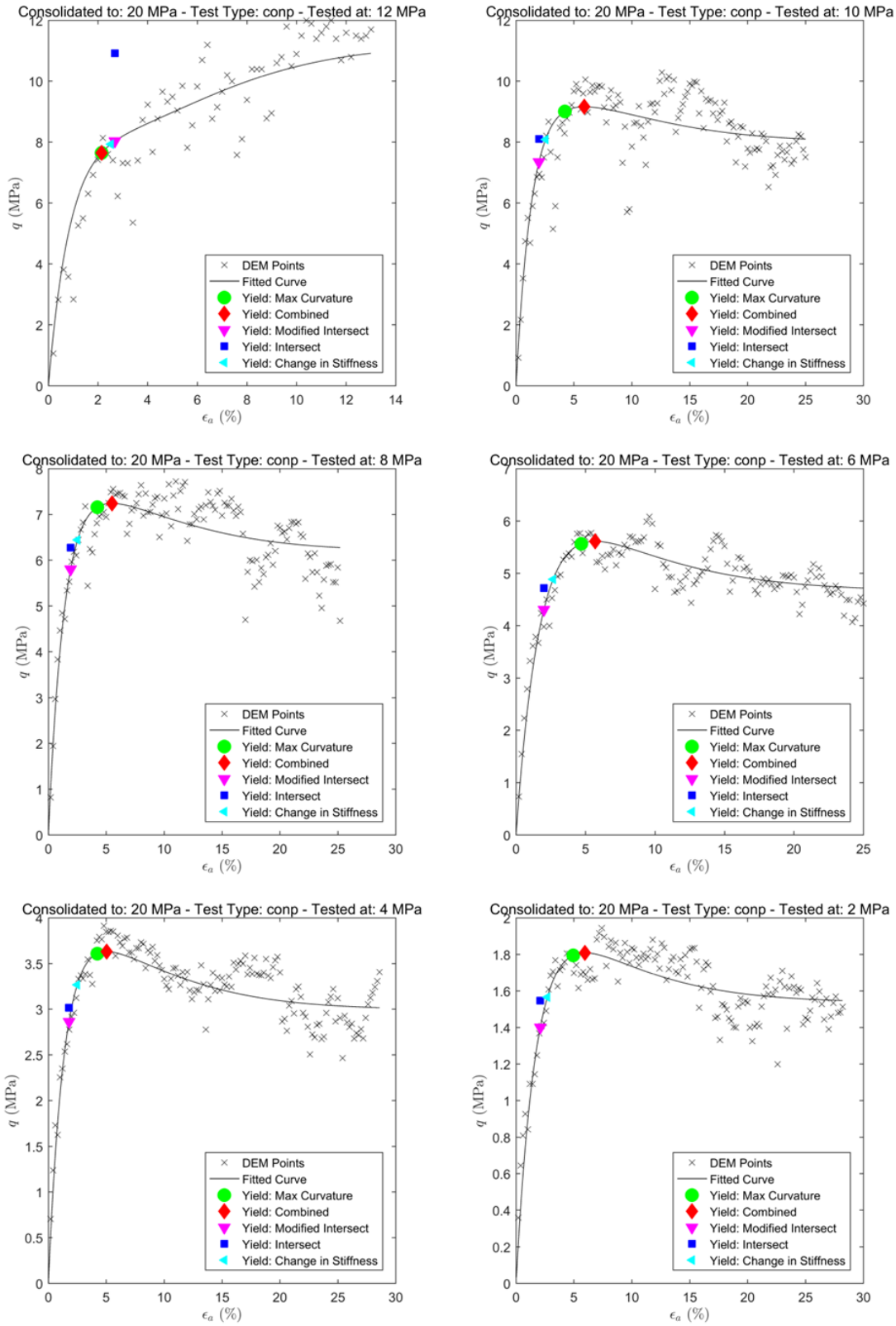

Figure 6.14 Yield points according to different methods for the 20 MPa samples under constant-*p'* triaxial shearing.

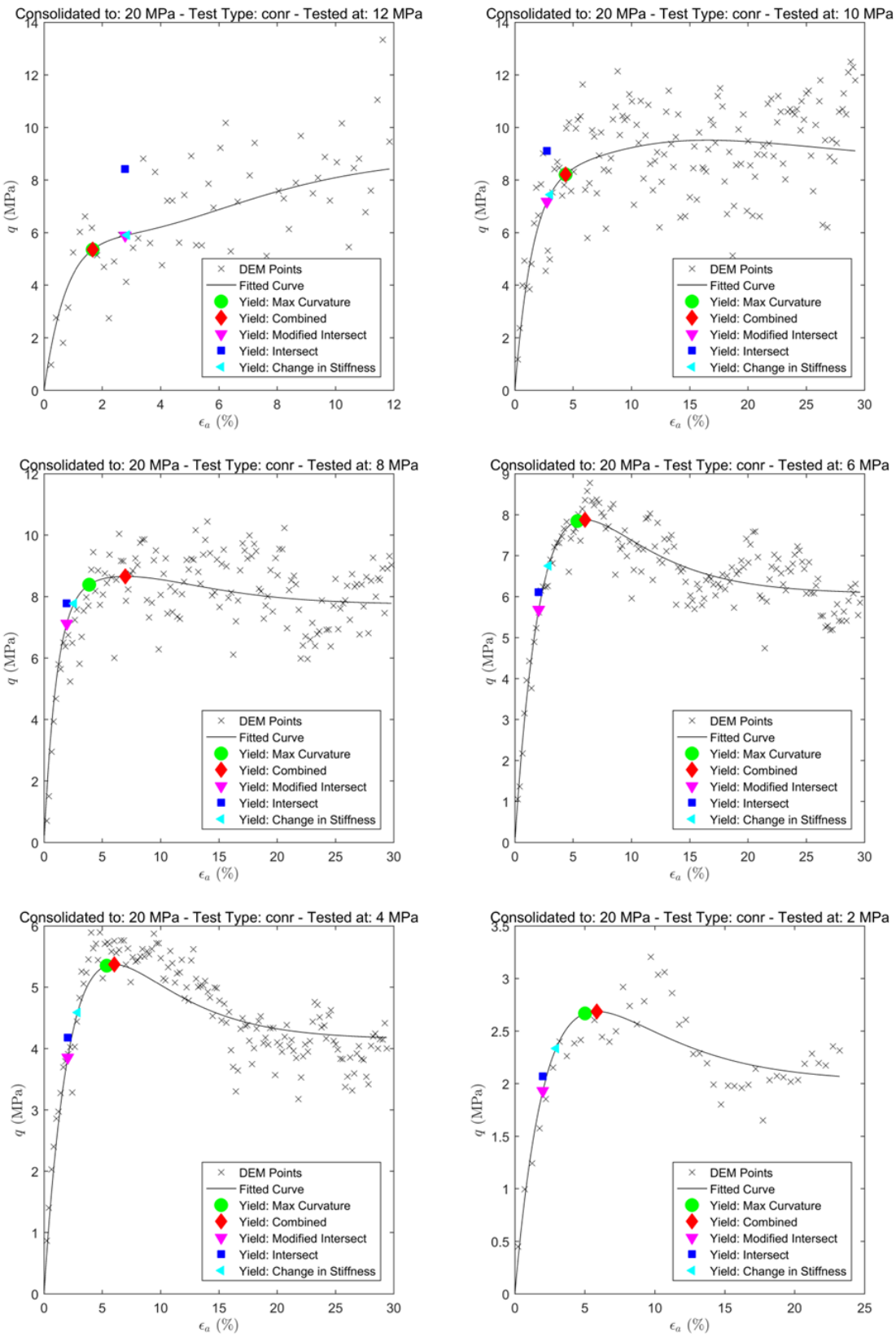

Figure 6.15 Yield points according to different methods for the 20 MPa samples under constant confining stress triaxial shearing.

6.4.2 Yield surfaces

The yield surface in stress space consisting of the yield points corresponding to the five alternative different methods, is now considered. In order to give the best fit of the discrete yielding points, an equation is required to give good prediction of the yield surface. Since the shape of yield surface depends on soil type and soil history, an equation will be used that permits a range of different shapes to be attempted, such that the one which generates the smallest variance between the discrete points and the fitted curve will be determined to be the yield surface of the simulated sand.

The CASM model (Yu, 1998), as has been introduced in Chapter 2, proposed a simple unified equation that successfully predicted a family of yield surfaces for both clay and sands:

$$\eta = M \times \left[ln\left(\frac{p_0'}{p'}\right) / \, ln\, r^* \right]^{1/n} \tag{6-4}$$

where

- η is the stress ratio;
- p_0' is the preconsolidation stress;
- r^* is the spacing ratio;
- n is the stress-state coefficient, a new material constant that determines the shape of the yield surface. The value of n usually ranges between 1.0-5.0.

The normalised form of Eq. 6-4 is:

$$y = x \times M \times \left[\ln\left(\frac{1}{x}\right) / \ln r^*\right]^{1/n} \quad (6\text{-}5)$$

where $x = p'/p'_0$; and $y = q/p'_0$.

Similarly, McDowell (2002) also proposed an equation from a mathematical derivation, which produces exactly the same family of yield surfaces as the CASM model:

$$\eta = N\left[(a+1)\ln\frac{p_0}{p}\right]^{\frac{1}{a+1}} \quad (6\text{-}6)$$

where N is the stress ratio corresponding to the peak value of q on the yield locus; and a is a material constant similar to n in the CASM equation.

The normalised form of the McDowell (2002) equation is:

$$y = x \times N \times \left[(a+1) \times ln\left(\frac{1}{x}\right)\right]^{1/(a+1)} \quad (6\text{-}7)$$

where $x = p'/p'_0$; and $y = q/p'_0$.

If the normalised CASM equation, Eq. 6-5, is adopted to fit the yield surface, only one variable, n, needs to be determined. The values of M and r^* are obtained from the triaxial shear test result: the critical stress ratio, M, is approximately 0.75, as has been presented in Chapter 5;the spacing ratio, r^*, is 20/12, because the mean effective stress of the intersection of the CSL and the unloading line from 20 MPa is approximately 12 MPa, as can be seen from Figures 5.9 and 5.15. However there are two variables in the normalised form of the McDowell equation, Eq.6-7: both the a value and the peak points stress ratio N are to be determined. With lower degree of freedom, the CASM equation is then adopted to plot the yield surface. The value of n is calculated

(within the range of 1.0-5.0) such that the variance between the fitted surface and the data points is minimized.

Since the two equations give the same yield surface, it can be derived that:

$$\frac{M}{N} = [(a+1)lnr^*]^{\frac{1}{a+1}} \tag{6-8}$$

and

$$n = a + 1 \tag{6-9}$$

So that the parameters in the McDowell equation can then be determined using Eq. 6-8 and Eq. 6-9, once the CASM equation is solved. In other words, the associated value of the peak stress ratio *N* for the McDowell (2002) yield surface can be determined if required.

Figure 6.16 presents the normalised best fitted yield surface of the simulated sand and the chosen yield point using the five different methods. The smooth black curves are the predicted yield surface according to CASM, Eq. 6-5. The small circles are the yield points for samples with 17 MPa preconsolidation pressure. The small crosses are the yield points for samples with 20 MPa preconsolidation pressure. The thick black lines are the CSL with the slope of 0.75.

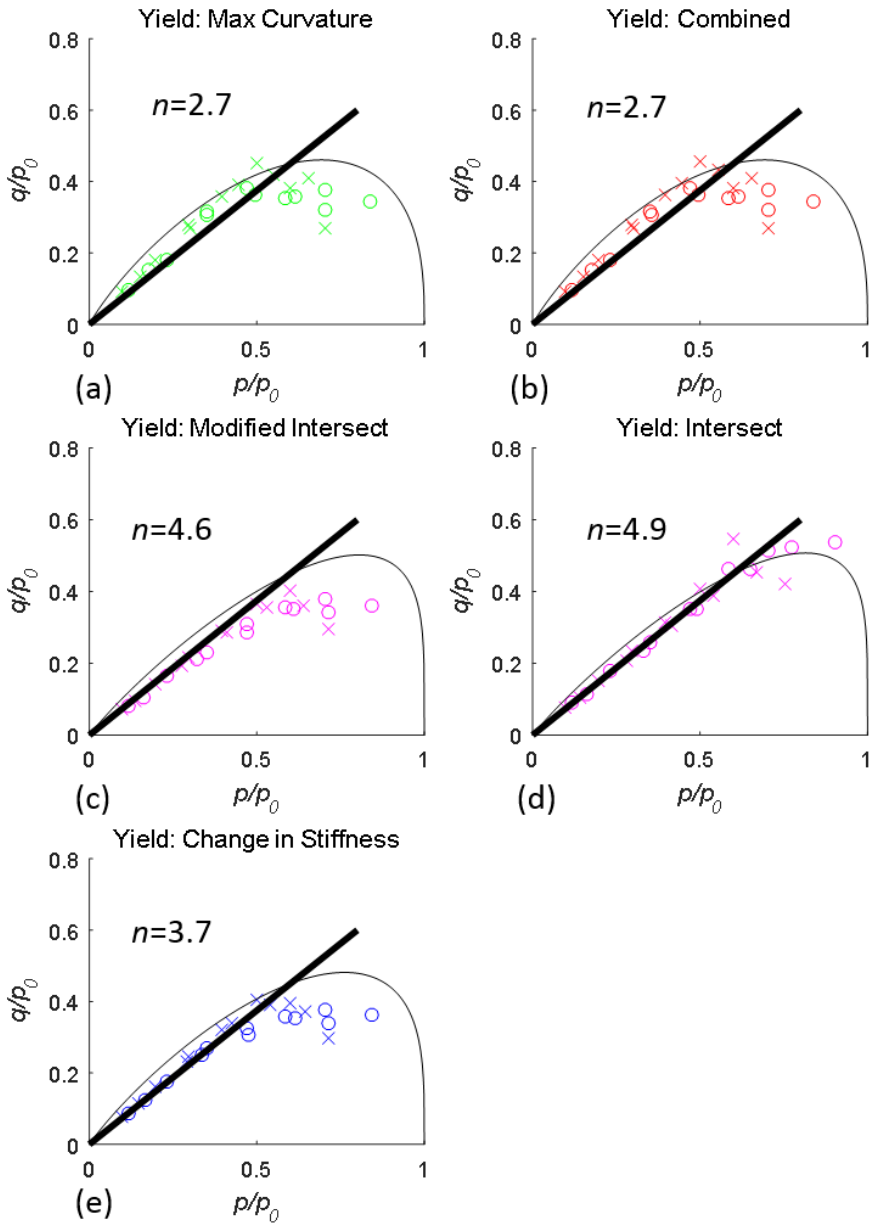

Figure 6.16 Yield surfaces according to different methods of choosing yield point: (a) maximum curvature method; (b) combined method; (c) modified intersection method; (d) intersection method; (e) change in stiffness method.

It can be seen that different curves are generated because of the variation in the methods of choosing the yield points. The stress-state parameter *n* for the first two methods, *i.e.* maximum curvature method and the combined method, has the same value of 2.7 in each case, while the value of *n* for intersection method is 4.6 and is 4.9

for the modified intersection method and 3.7 for the degradation in stiffness method. It can be seen that the yield surface according to the CASM equation fits well the data points for the maximum curvature method and the combined method (peak and maximum curvature points) except for the data points on the loose side of critical state. The underestimation of the yield points happens for all five methods. It is assumed that the smoothing method of the raw data in stress-strain plot may have resulted in the inaccurate location of the yield point. Because the high stress triaxial shear tests have large amounts of particle breakage, a sudden drop of the deviator stress tends to occur after each particle breakage. The exponential fitting of the raw data considering all the data points may generate a fitted curve at a relatively lower place than it should be. It is also noted that, for all the other three methods, the data points on the dense side of critical state lie below the fitted yield curve and lie at or below the critical state stress ratio.

The method of choosing the yield point is responsible for the gap between the data points and the yield curve on the dense side of critical state. In the intersection and modified intersection methods, the horizontal fitted straight line going through the critical state is taken to locate the intersection point, so that the yield stress is always smaller than or equal to the critical state q. In the stiffness degradation method, the threshold of the difference between the linear fit (first 2% axial strain) and the curve is defined to be approximately 20%, beyond which the sample is considered as having yielded, in order to have a yield stress smaller than the critical state q on the loose side of critical state. However for samples on the dense side of critical state, this definition of the threshold will also lead to a yield stress that is smaller than the peak stress q. Therefore the data points obtained from these three methods lie below or on

(intersection method) the CSL in stress space. Since the yield surface is taken to be convex according to conventional plasticity theory, and the CASM equation uses the intersection point of the CSL and yield surface as the datum point through which to fit the curve with the appropriate value of *n*, the yield surface on the dense side of critical state always lie above the CSL in the CASM model. That is to say, the yield surfaces in Figure 6.16 are not best fit curves but are the best fit yield surfaces constrained by a spacing ratio of 20/12 and a critical state ratio of 0.75: every yield surface passes through the normalized value of $p'/p'_0 = 12/20 = 0.6$ and stress ratio 0.75. The yield surfaces in Figure 6.16 are the best curves using the best fit n values with these constraints. The intersection, modified intersection and stiffness degradation methods therefore underestimate the yield stress given by this yield surface on the dense side of the critical state.

As has been described previously, the value of peak point stress ratio, *N*, in Eq. 6-7 can be determined according to Eq. 6-8 and Eq. 6-9 when Eq. 6-5 is solved. The calculated values of *n* in Eq. 6-5, which leads to the minimum variance between the predicted yield surface and the raw data points, are then taken to calculate *N*. The peak stress ratio for the maximum curvature and combined methods are 0.67; the value is 0.63 for the modified intersection method; 0.62 for the intersection method; 0.63 for the stiffness degradation method. The stress ratio at the peak stress on the yield surface is different from the critical state stress ratio, so that the peak stress on the yield surface and the intersection point of the CSL and the yield surface do not coincide. It is therefore acknowledged that the non-associative flow rule is followed for the simulated sand, which is consistent with experimental data for soils, as pointed out by Yu (1998) and Chandler (2000). Figure 6.17 presents schematically the relative

locations of the peak stress and the critical state point on the yield surface. The straight arrow shows the direction of plastic potential and the dashed lines show the tangential line and the normality of the yield surface at the intersection with the CSL. When the two points coincide with each other, the plastic yield surface and the plastic potential surface coincide at this point, i.e. $Q=f$, so that the associative flow rule is followed, and the plastic strain increment vector is normal to the yield surface in Figure 6.17 (a). Figure 6.17(b) shows the general case when the sand exhibits non-associative flow.

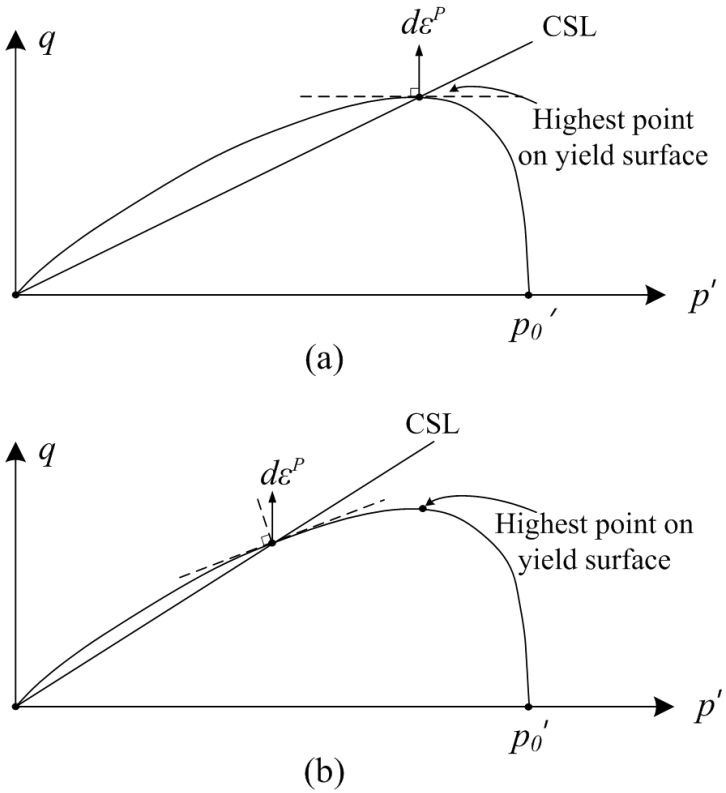

Figure 6.17 Schematic plot of the location of the highest point on yield surface and the direction of the plastic strain increment vector: (a) highest point coincides with the intersection of CSL and yield surface; (b) peak stress and critical state do not coincide.

6.5 Conclusions

Five methods of choosing the yield point have been introduced: the intersection method, modified intersection method, maximum curvature method, combined method and stiffness degradation method. The logic of the first four methods are based

on the definition of yield as the fastest rate of the change of stiffness, *i.e.* the maximum curvature on a stress-strain plot. The combined method considers the strain-softening point (peak stress) on the stress-strain plot as the yield point for heavily overconsolidated sands. The logic for the last method, the stiffness degradation method, is based on the definition of yield point as corresponding to a proportional reduction in the change of stiffness, *i.e.* approximately 20% deterioration of the secant stiffness.

Significant scatter of the data also presented much difficulty in choosing the yield point. The discrete data points were then smoothed directly in MATLAB and the smoothed curves are generated with the application of the polyfit command. The directly smoothed curve cannot show the expected shape of the stress-strain plot of the sample very well. Method was adopted using an equation which provides the capability of adopting the correct shape and which was fitted to the data. This gives good representation of the behaviour of sample and was therefore adopted to choose the yield point from.

The yield points from the maximum curvature method and the combined method are very close for samples on the dense side of critical states, while on the loose side the two methods give the same result. The other three methods tend to underestimate the yield stress on the dense side of critical states. Except for the intersection method, all four other methods produce very close yield points for samples on the loose side of critical states. The intersection method is not suitable to locate the yield point when the sample shows gradual yielding. The yield stresses for all samples have been used to establish state boundary surfaces according to each method respectively. It has been

found that the CASM model (Yu, 1998) and McDowell's (2002) model, both of which have been introduced in Chapter 2, give good prediction of the shape of the yield surface of the simulated sand.

What is important here is that the definition of yield has been rigorously and scientifically assessed, and the yield surfaces obtained for the different methods, are remarkably similar, and in engineering terms, the analysis lends confidence to the approach. It would appear that a 'Cam clay type' yield surface in stress space has indeed been determined for the DEM crushable soil using the particle splitting model and this is an important contribution of this research. In addition, the DEM splitting model has shown that the critical state is not coincident with the peak deviatoric stress on the yield surface, and such non-associative flow is normally observed for granular materials. This means that the model holds much promise for the modelling of constant volume tests on sand, for example.

Chapter 7 Conclusions and Recommendations for Future Work

7.1 Conclusions

This study used DEM simulations to investigate the micro and macro mechanics of the behaviour of crushable soil. From a micro perspective, the crushing of a single particle has been realized by considering the size effect of particle strength which follows a Weibull statistical distribution. From a macro view, the simulated sand successfully produces behaviour which compares well with real sand during 1-D normal compression, isotropic normal compression and triaxial shearing to critical states. The conclusions of this project are listed as below.

7.1.1 1-D and isotropic normal compressions

The simple breakage population balance model (PBM) developed by McDowell and de Bono (2013) has been applied to simulate crushable silica sand under 1-D and isotropic normal compression. For different sized particles, the size effect on the particle strength was considered. For same sized particles the Weibull distribution of strengths was applied. The crushing of a particle was governed by the octahedral shear stress generated from multiple contacts with surrounding particles. The 1-D and isotropic normal compression lines (NCL) were obtained and compare well with the NCL presented by McDowell and de Bono (2013). The evolution of particle size distribution was examined in both the conventional way, *i.e.* percentage of the mass of particles larger than a size, and an alternative way of measuring the number of particles greater than size *d* against size *d* on log-log axes. The initially uniform sized particles were proven to give rise to a fractal distribution of sizes with the fractal

dimension of 2.5 under both 1-D normal compression and isotropic compression; the evolution of D=2.5 for isotropic conditions is a new finding of this research. Given the obtained fractal dimension, the theoretical slope of the 1-D and isotropic NCL in log e- log p' space should have the same value of -0.5, according to the clastic hardening law (McDowell, 1996). The obtained isotropic and 1-D NCLs from the simulations agree with this prediction and with experimental data. The microscopic anisotropic stresses (octahedral stresses) were shown to give rise to macroscopic isotropic clastic behaviour. The volumetric hardening, *i.e.* during normal compression, has therefore been proven to result from the fractal crushing and the size effect on strength of single particles.

The geometry of the sample was examined to influence the behaviour of a sample through the boundary effect, *i.e.* particles in contact with the boundary are more susceptible to crushing and the proportion of boundary particles changes with aspect ratio. The boundary effect can be minimized by using a larger sample, reducing single particle size or (because of the computational restrictions that these methods impose) by choosing proper aspect ratio.

7.1.2 Triaxial shear and critical states of the simulated sand

"Conventional" constant confining stress triaxial shear and constant mean effective stress triaxial shear tests on the isotropically over-consolidated simulated sand have been performed. The samples were sheared to critical states using strain control. The influence of stress path and preconsolidation pressure have been examined.

All samples, at critical states, exhibit a critical state friction constant, M, which is approximately 0.75 and independent of the stress level or stress path. The value of M

is consistent with the predicted value using the measured value of K_0 under one-dimensional normal compression; that is to say the corresponding friction angles agree. It is therefore suggested that for sand that is normally compressed beyond yield, the friction angle in Jâky's (1944) equation is the critical state friction angle, as for clay. This agrees with the assumption that once on the NCL, the effect of the initial density and structure and hence maximum angle of friction have been eradicated. The PBM applied in this study, avoiding the artificial limit of a crushable particle size (comminution limit), contributes to the accurate calculation of M, which has been proposed to depend on the stress level for simulations applying the BPM (Cheng & Bolton, 2004).

Samples on the dense side of critical state show peak strength and dilation while samples on the loose side of critical state show ductile contraction; that is to say the simple DEM soil here appears to obey CSSM. Samples which lie close to the critical state initially deserve more attention because the stress path shows a much greater influence on the behaviour of these samples; for example the 8 MPa sample with p_0'=17 MPa and the 10 MPa sample with p_0' =20 MPa. The two samples show peak strength and dilation following the constant-p' stress path and ductile contraction following the conventional stress path with constant confining stress. The simulated soil, following fractal crushing and a size effect on average strength and a Weibull distribution of strengths for a given size, has been proven to successfully produce typical sand behaviour under triaxial shearing.

The critical state line (CSL) has been obtained and presented in $\log e - \log p'$ and $q - p'$ space. The CSL has been proven to be of similar shape and parallel to the 1-D and

isotropic NCL at high stress levels in $\log e - \log p'$ space with a slope of -0.5 and is unique for the simulated sand, independent of the stress path or preconsolidation stress. The DEM based on the micro mechanics has therefore been proven to give rise to a CSL within the CSSM framework. At low stresses, the location of the CSL in $\log e - \log p'$ space has been shown to depend on the preconsolidation pressure. The reason is that at the preconsolidation stress, the fractal distribution of particle sizes has not fully evolved. One would anticipate that for high preconsolidation pressures, the CSL would be unique even at low stress levels.

Particle crushing is observed at critical state. However, it has been proven that the newly generated fragments are mainly mechanically inactive. The crushing at critical state reduces the average coordination number considerably while the mechanical average coordination number stays approximately stable, which means the plastic hardening is essentially complete at critical state: the production of new 'fines' does not affect the mechanical behaviour.

7.1.3 Yield criterion and yield surface of the simulated sand

Given the absence of a generally accepted method to determine the yield point, five alternatives of choosing the yield point on a stress-strain plot have been compared: the intersection method, modified intersection method, maximum curvature method, peak and maximum curvature combined method and stiffness degradation method. The intersection method always gives a yield point that lies above the stress-strain curve. Taking the horizontal line through the critical deviator stress as a reference line on the deviatoric stress-axial strain plot, the intersection method always gives a yield stress equal to the critical state stress. The modified intersection method tends to

underestimate the yield stress on the dense side of critical state because it uses the same method as intersection method to locate the yielding strain, while at the same strain, the yield point is always below the point from the intersection method, so that the yield stress is always smaller than the critical state deviator stress. Yield points according to maximum curvature method and the combined method are roughly the same, because the peak stress point and maximum curvature point are very close for samples on the dense side of critical states. The stiffness degradation method also underestimates the yield stress for samples on the dense side of critical states, because the threshold cannot be set too large to result in a yield stress higher than the critical state deviator stress on the loose side of critical and, therefore, leads to an underestimated value on the dense side. However, the yield stress on the dense side of critical state is usually higher than the critical state deviator stress due to the convex shape of the yield surface. Given the above comparisons, the maximum curvature method and combined method have been shown to produce more mechanically meaningful and useful (in terms of making engineering judgements) yield points than the other three methods.

The yield surfaces consisting of the points determined following the five methods have been presented. The theoretical predicted yield surfaces according to CASM (Yu, 1998) were plotted. A 'Cam-clay' type yield surface, according to CASM, fits well the data points obtained from different methods. The best fit of the theoretical yield surface appears to be the one for yield points chosen from the maximum curvature method and the combined method. The DEM of crushable soil has therefore been shown using the particle splitting model to generate a 'Cam-clay' type behaviour in triaxial shearing. It has also been shown that the critical state is not coincident with

the peak deviatoric stress on the yield surface, and such non-associative flow is normally observed for granular materials as reported by Yu (1998), for example. This means that the model holds much promise for the modelling of constant volume tests on sand, for example, where a peak strength is obtained for undrained loose sand.

7.2 Recommendations for future work

The study based on the simplified breakage model has also raised issues worthy of further investigation:

7.2.1 Better geometry of grains

The breakage model can be improved by replacing spheres with clumps. As has been described, the geometry of sand particles has a major influence on the behaviour of sand. The interlocking and rotation of particles depends on the particle shape. The maximum and critical state friction angles are therefore influenced by the particle shape. The perfectly rounded spheres result in unrealistic friction angles and do not permit the development of a rupture surface. Clumps, with a relatively more realistic shape than spheres, will produce more realistic friction angles, so that the critical state stress ratio should be more comparable to lab test results. Moreover, a rupture surface of a few particles thickness should develop with the application of clumps, provided the sample geometry permits this and the sample comprises a sufficient number of particles.

7.2.2 Reducing boundary effect

The sample used in this study contained a very limited number of particles, *i.e.* 390 and 620 particles to start with, which lead to a large proportion of particles in contact

with the boundary and hence being more susceptible to crushing than the inner particles. The aspect ratio influences the behaviour of a sample consisting of a small number of particles. This 'boundary effect' can be reduced when the sample contains a much larger number of particles.

7.2.3 Using a flexible membrane instead of stiff confining walls

The stiff confining walls applied in this simulation leave no possibility of the development of a shear plane. By using a flexible membrane instead of stiff confining walls, shear planes would be allowed to develop under triaxial shear. The aspect ratio of the triaxial sample should be modified: the height of the sample should be long enough, considering the possible friction angle, to leave space for the rupture to evolve across the diameter of the sample and hence generate a shear plane.

7.2.4 Constant volume shearing

The macro and micro behaviour of crushable soil under drained triaxial shear has been investigated, but the undrained behaviour of crushable soil still needs clarification. By carrying out constant volume (undrained) shear tests, it will be possible to investigate the role of crushing in undrained behaviour, and whether such behaviour is consistent with the CSSM framework, in addition to explaining some of the rather unusual data in the literature for undrained sand behaviour.

7.2.5 Investigating the behaviour of crushable soil at low stress level.

The CSL in log *e*- log *p'* space has been shown to be unique and parallel to the NCL at high stresses. However, the linearity and uniqueness is lost at low stress levels and the reason has been proposed that the particle size distribution has not fully evolved. In other words, shown schematically in Figure 7.1, the behaviour in region A has been investigated while the behaviour in region B still needs to be clarified. Future work should focus on the non-uniqueness of critical states as a function of the evolved particle size distribution and whether at high enough preconsolidation stresses, the non-uniqueness can be eradicated.

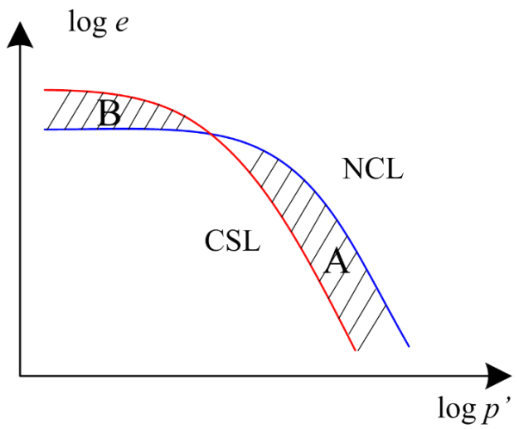

Figure 7.1 Schematic plot of the studied region A and to be studied region B.

There can be many more examples. Creep has not been investigated. Nor has the effect of principal stress rotation. The model has not been applied to boundary value problems and compared with FEM models using the DEM derived constitutive model. These are all avenues for future research that must be explored. However, it is important to finally note the important contribution that this thesis has made, which has been to use DEM to model crushable soil and to show that not only does it obey CSSM, but it obeys classic plasticity-type constitutive models for sand. The model therefore shows much promise in being able to further the micro mechanical understanding of all of the phenomena highlighted above.

References

Åström, J. a., & Herrmann, H. J. (1998). Fragmentation of grains in a two-dimensional packing. *The European Physical Journal B - Condensed Matter and Complex Systems*, **5**(3), 551-554.

Atkinson, J. (2007). The Mechanics of soils and Foundations, Taylor & Francis Group, London and New York.

Bandini, V., & Coop, M. R. (2011). The influence of particle breakage on the location of the critical state line of sands. *Soils and Foundations*, **51**(4), 591-600.

Been, K., & Jefferies, M. G. (1985). A state parameter for sands. *Géotechnique*, **35**(2), 99-112.

Been, K., & Jefferies, M. G. (2004). Stress-dilatancy in very loose sand. *Canadian Geotechnical Journal*, **41**(5), 972-989.

Been, K., Jefferies, M. G., & Hachey, J. (1991). The critical state of sands. *Géotechnique*, **41**(3), 365-381.

Bishop, A. W., & Henkel, D. J. (1962). The measurement of soil properties in the triaxial test. Edward Arnold, London, 2nd ed.

Bolton, M. D. (1986). The strength and dilatancy of sands. *Géotechnique*, **36**(1), 65-78.

Bolton, M. D., Nakata, Y., & Cheng, Y. P. (2008). Micro- and macro-mechanical behaviour of DEM crushable materials. *Géotechnique*, **58**(6), 471-480.

Casagrande, A. (1936). The determination of the pre-consolidation load and its practical significance. *Proceedings of the international conference on soil mechanics and foundation engineering*. Harvard University Cambridge. 60-64.

Chandler, R. J. & Cotecchia, F. (2000). A general framework for the mechanical behaviour of clays. *Géotechnique*, **50**, 431-447.

Cheng, Y. P., Bolton, M. D., & Nakata, Y. (2004). Crushing and plastic deformation of soils simulated using DEM. *Géotechnique,* **54**(2), 131-141.

Cheng, Y. P., Bolton, M. D., & Nakata, Y. (2005). *Grain crushing and critical states observed in DEM simulations*. Powders and Grains.

Cheng, Y. P., Nakata, Y., & Bolton, M. D. (2003). Discrete element simulation of crushable soil. *Géotechnique*, **53**(7), 633-641.

Cil, M. B., & Alshibli, K. A. (2012). 3D assessment of fracture of sand particles using discrete element method. *Géotechnique Letters*, **2**, 161-166.

Consoli, N. C., Casagrande, M. D., & Coop, M. R. (2007). Performance of a fibre-reinforced sand at large shear strains. *Géotechnique,* **57**(9), 751-756.

Coop, M. R., Sorensen, K. K., Bodas Freitas, T., & Georgoutsos, G. (2004). Particle breakage during shearing of a carbonate sand. *Géotechnique,* **54**(3), 157-163.

Coulomb, C. A. (1773). Essai sur une application des regles des maximis et minimis a quelques problems de statique relatifs a l'architecture. *Mem. Pres. Par div. savants*, **7**, 343-382.

Craig, R. F. (1997). Craig's Soil Mechanics 6th, Taylor & Francis Group, London and New York.

Cui, L., & O'Sullinvan, C. (2006). Exploring the macro- and micro-scale response of an idealised granular material in the direct shear apparatus. *Géotechnique*, **56**(7), 455-468.

Cundall, P. A. (1988). Formulation of a three-dimensional distinct element model-Part I. a scheme to detect and represent contacts in a system composed of many polyhedral blocks. *Int. J. Rock Mech. Min. Sci. & Geomech. Abstr.,* **25**(3), 107-116.

Cundall, P. A., & Strack, O. D. L. (1978). The distinct element method as a tool for research in granular media. Report to the National Science Foundation Concerning NSF Grant ENG-76-20711, Part I.

Cundall, P. A., & Strack, O. D. L. (1978). The distinct element method as a tool for research in granular media. Report to the National Science Foundation Concerning NSF Grant ENG-76-20711, Part II.

Cundall, P. A., & Strack, O. D. L. (1979). A discrete numerical model for granular assemblies. *Géotechnique*, **29**(1), 47-65.

de Bono, J. P., & McDowell, G. R. (2014). DEM of triaxial tests on crushable sand. *Granular Matter*, **16**, 551-562.

de Bono, J. P., & McDowell, G. R. (2015). An insight into the yielding and normal compression of sand with irregularly-shaped particles using DEM. *Powder Technology*, **271**, 270-277.

Drucker, D. C. & Prager, W. (1952). Soil mechanics and plastic analysis for limit design. *Quart. Appl. Math.*, **10**, 157-165.

Drucker, D. C., Gibson, R. E. & Henkel, D. J. (1957). Soil mechanics and working hardening theories of plasticity. *Trans. ASCE*, **122**, 338-346.

Einav, I. (2007). Breakage mechanics—Part I: Theory. *Journal of the Mechanics and Physics of Solids*, **55**(6), 1274-1297.

Einav, I., Houlsby, G. T., & Nguyen, G. D. (2007). Coupled damage and plasticity models derived from energy and dissipation potentials. *International Journal of Solids and Structures*, **44**(7-8), 2487-2508.

Fonseca, J., O'Sullivan, C., Coop, M. R. & Lee, P. D. (2013). Quantifying the evolution of soil fabric during shearing using directional parameters. *Géotechnique*, **63**(6), 487-499.

Fonseca, J., Sim, W. W., Shire, T. & O'Sullivan, C. (2014). Microstructural analysis of sands with varying degrees of internal stability. *Géotechnique,* **64**(5), 405-411.

Hardin, B. (1985). Crushing of Soil Particles. *Journal of Geotechnical Engineering,* **111**(10), 1177-1192.

Hashiguchi, K. (1978). Constitutive equation of soils: 7. Theories based on elasto-plsticity. *Jour. of JSSMFE,* **18**, 131-142.

Hashemi (2016). Personal communication.

Herbst, J. A., Lo, Y. C., & Flintoff, B. (2003). Size reduction and liberation. Principles of Mineral Processing, MC Fuerstenau and KN Han (eds.), Society of Mining, Metallurgy and Exploration, Littleton, CO, 61-118.

Itasca Consulting Group (2008), Inc. PFC3D (Particle Flow Code in Three Dimensions), version 3.0. Minneapolis: ICG.

Jaeger, J. C. (1967). Failure of rocks under tensile conditions. *Int. J. Rock Mech. Min. Sci. & Geomech. Abstr.,* **4**, 219-227.

Jaky, J. (1944). The coefficient of earth pressure at rest. *J. for Soc. Of Hungarian Arch. and Engrs.*, Budapest, Hugary, (OCT), 355-358.

Jardine, R. J. (1992). Some observations on the kinematic nature of soil stiffness. *Soils and Foundations*, **32**, 111-124.

Joer, H. A., Ong, S. E. & Randolph, M. F. (1999). Friction capacity of grouted interfaces using the direct shear test. *Proceedings 8th Australia New Zealand Conference on Geomechanics: Consolidating Knowledge*. Barton, ACT, 1999 405-441.

Kendall, K. (1978). The impossibility of comminuting small particles by compression. *Nature, 272*(710-711).

Lee, D. M. (1992). The angles of friction of granular fills. PhD dissertation, University of Cambridge.

Li, H., McDowell, G.R. & Lowndes, I. (2013). Discrete element modelling of rock breakage using dense random packing agglomerates. *Géotechnique Letters*, **3**, No. July-September (2013): 98-102.

Li, H., McDowell, G.R. & Lowndes, I. (2014). Discrete element modelling of a rock breakage using dense random packing agglomerates. *Powder Technology*, **263**, 151-158.

Lim, W. L., & McDowell, G. R. (2007). The importance of coordination number in using agglomerates to simulate crushable particles in the discrete element method. *Géotechnique*, **57**(8), 701-705.

Lim, W. L., McDowell, G. R., & Collop, A. C. (2004). The application of Weibull statistics to the strength of railway ballast. *Granular Matter*,**6**(4), 229-237.

Lobo-Guerrero, S., & Vallejo, L. E. (2005). Crushing a weak granular material: experimental numerical analyses. *Géotechnique*, **55**(3), 245-249.

Lobo-Guerrero, S., Vallejo, L. E., & Vesga, L. (2006). Visualization of Crushing Evolution in Granular Materials under Compression Using DEM. *International Journal of Geomechanics*, **6**(3), 195-200.

Lubachevsky, B. D., & Stillinger, F. H. (1990). Geometric properties of random disk packings. *Journal of Statistical Physics*, **60**(5-6), 561-583.

McDowell, G. R. (2002a). On the yielding and plastic compression of sand. *Soils and Foundations*, **42**(1), 139-145.

McDowell, G. R. (2002b). A simple non-associated flow model for sand. *Granular Matter*, **4**(2), 65-69.

McDowell, G. R., & Amon, A. (2000). The application of Weibull statistics to the fracture of soil particles. *Soils and Foundations*, **40**(5), 133-141.

McDowell, G. R., & Bolton, M. D. (1998). On the micromechanics of crushable aggregates. *Géotechnique*, **48**(5), 667-679.

McDowell, G. R., & de Bono, J. P. (2013). On the micro mechanics of one-dimensional normal compression. *Géotechnique,* **63**, 895-908.

McDowell, G. R., Bolton, M. D., & Robertson, D. (1996). The fractal crushing of granular materials. *Journal of the Mechanics and Physics of Solids*, **44**(12), 2079-2101.

McDowell, G. R., de Bono, J. P., Yue, P. & Yu, H-S. (2013). Micro mechanics of isotropic normal compression. *Géotechnique Letters*, **3**, 166-172.

McDowell, G.R. & Harireche, O. (2002a). Discrete element modelling of soil particle fracture.*Geotechnique*, **52**(2), 131-135.

McDowell, G.R. & Harireche, O. (2002b). Discrete element modelling of yielding and normal compression of sand. *Geotechnique*, **52**(4), 299-304.

McDowell, G.R., & Daniell, C. M. (2001). Fractal compression of soil. *Géotechnique*, **51**, 173-176.

McDowell, G.R., Yue, P. & de Bono, J. P. (2015). Micro mechanics of critical states for isotropically overconsolidated sand. *Powder Technology*, **283**, 440-446.

Mindlin, R. D., & H. Deresiewicz. (1953). Elastic Spheres in Contact under Varying Oblique Forces. *J. Appl. Mech.*, ***20***, 327-344.

Nakata, Y., Hyodo, M., & Murata, H. (1999). A probabilistic approach to sand particle crushing in the triaxial test. *Géotechnique,* **49**(5), 567-583.

Nakata, Y., Hyodo, M., Hyde, A. F. L., Kato, Y., & Murata, H. (2001). Microscopic particle crushing of sand subjected to high pressure one-demensional compression. *Soils and Foundations*, **41**(1), 69-82.

Oda, M. (1977). Co-ordination number and its relation to shear strength of granular material. *Soils and Foundations,* **17**, 29-42.

Palmer, A. C. & Sanderson, T. J. O. (1991). Fractal crushing of ice and brittle solids. *Proceedings of the Royal Society A*. **433**, 469-477.

Parry, R. H. G. (1956). Strength and Deformation of Clay. PhD thesis, University of London.

Paniagua, P., Fonseca, J., Gylland, A.S. & Nordal, S. (2015). Microstructural study of deformation zones during cone penetration in silt at variable penetration rates. *Canadian Geotechnical Journal*, **52**(12), 2088-2098.

Pestana, J. M. (1994). *A unified constitutive model for clays and sands.* (Ph.D.), Massachusetts Institute of Technology.

Pestana, J. M. & Whittle, A. J. (1995). Compression model for cohesionless soils. *Géotechnique*, **45**(4), 611-631.

Poyody, D. O. & Cundall, P. A. (2004). Abonded-particle model for rock. *International Journal for Rock Mechanics and Mining Science*, **26**, 1097-1121.

Robertson D. & Bolton M.D. (2001). DEM simulations of crushable grains and soils. Proc. *Powders and Grains 2001*. Sendai, 623-626.

Robertson, D. (2000). Numerical simulations of crushable aggregates. Ph.D. Thesis, University of Cambridge, U.K.

Roscoe, K. H. & Burland, J. B. (1968). On generalised stress strain behaviour of wet clay. *Engineering Plasticity* (Edited by Heyman and Leckie), 535–609.

Roscoe, K. H. & Schofield, A. N. (1963). Mechanical behaviour of an idealized wet clay. *Proc. European Conf. on soil Mechanics and Foundation Eng.*, Vol. **1**, 47–54.

Roscoe, K. H., Schofield, A. N. & Wroth, C. P. (1958). On the yielding of soils. *Géotechnique*,**8**(1), 22–52.

Rowe, P. W. (1962). The stress-dilatancy relation for static equilibrium of an assembly of particles in contact. *Proc. Roy. Soc.* **267**, 500–527.

Schofield, A., & Wroth, P. (1968). *Critical State Soil Mechanics*. London.

Schöpfer, M. P., Abe, S., Childs, C., & Walsh, J. J. (2009). The impact of porosity and crack density on the elasticity, strength and friction of cohesive granular materials: Insights from DEM modelling. *International Journal of Rock Mechanics and Mining Sciences*, **46**(2), 250-261.

Sitharam, T. G. & Vinod, J. S. (2008). Critical state behaviour of granular materials from isotropic and rebounded paths: DEM simulations. *Granular matters*, **11**, 33-42.

Sladen, J. A. & Oswell, J. M. (1989). The behavior of very loose sand in the triaxial compression test. *Canadian Geotechnical Journal*,**26**(1), 103–113.

Sladen, J. A., R. D. D. & Krahn, J. (1985). The liquefaction of sands, a collapse surface Approach. *Canadian Geotechnical Journal*, **22**(4), 564–578.

Steacy, S. J., & Sammis, C. G. (1991). An automaton for fractal patterns of fragmentation. *Nature,* **353**, 250-252.

Thornton, C. (1997). Force transmission in granular media. *KONA Powder and Particle Journal,* **15**, 81-90.

Thornton, C. (2000). Numerical simulations of deviatoric shear deformation of granular media. *Géotechnique,* **50**(1), 43-53.

Tresca, H. (1864). Sur l'ecoulement des corps solides soumis a de fortes pressions, *C.R. Acas. Sci.* (Paris) **59**, 754.

Tsoungui, O., Vallet, D., & Charmet, J. C. (1999). Numerical model of crushing of grains inside two-dimensional granular materials. *Powder Technology,* **105**, 190-198.

Turcotte, D. L. (1986). Fractals and fragmentation. *Journal of Geophysical Research*. **91**, 1921-1926.

Vallejo, L. E. (1979). An explanation for mudflows. *Géotechnique*, **29**(3), 351-354.

Von Mises, R. (1913). Mechanik der festen Korper im plastisch deformation, Zustand. Nachr. Ges. Wiss. Gottingen, 582.

Weibull, W. (1951). A statistical distribution function of wide applicability. *Journal of Applied Mechanics,* **18**, 292-297.

Wood, D M. & Maeda, K. (2008). Changing grading of soil: effect on critical states. *Acta Geotechnica*, **3**, 3-14.

Wood, D. M. (1991). Soil behaviour and critical state soil mechanics. Cambridge University Press.

Wroth, C. P. (1973). A brief review of the application of plasticity to soil mechanics. *Plasticity and Soil Mechanics*, 1–11.

Yang, J., & Dai, B. B. (2011). Is the quasi-steady state a real behaviour? A micromechanical perspective. *Géotechnique*, **61**(2), 175-183.

Yasufuku, N., & Hyde, A. F. L. (1995). Pile end-bearing capacity in crushable sands. *Géotechnique*, **45**(4), 663-676.

Yasufuku, N., Murata, H., & Hyodo, M. (1991). *Soils and Foundations*, **31**, 95-109.

Yu, H. S. (1998). CASM: a unified state parameter model for clay and sand. *International Journal for Numerical and Analytical Methods in Geomechanics*, **22**(8).

Yu, H.S. (2006). Plasticity and Geotechnics, Springer, New York.

Appendix A

MATLAB Code for Data Smoothing and Choosing Yield Points

```
      This function determines a range of different 'yield points'
according to different rules and saves the output.


      2016_07_09     Version 1   C.M. Heron



      function Determine_Yield_Points_EQB


      printindiv=1; %select whether to print individual plots or not


      load('Fitting_EQB.mat');


      %1. Process 17 MPa tests
      load('Conp_17MPa.mat')
      load('Conr_17MPa.mat')
      q_out_17 = zeros(length(ls17),1);
      epa_out_17 = zeros(length(ls17),1);
      p_out_17 = zeros(length(ls17),1);


      for i=1:length(ls17)


          %1.1.1. Load data and extract parameters
          eval(['data = ',ls17{i},';']);
          p = data(:,1);
```

```
            q = data(:,2);
            epa_r = data(:,3)*100;
            epv_r = data(:,4)*100;
            qr = par_out_17{i}(1,1);
            a = par_out_17{i}(1,2);
            A = par_out_17{i}(1,3);
            B = par_out_17{i}(1,4);
            b = par_out_17{i}(1,5);
            C = par_out_17{i}(1,6);
            D = par_out_17{i}(1,7);

            %1.1.2 Create a higher density epa vector
            epa = linspace(0,max(epa_r),1000);

            %1.1.3 Calcualte the q curve based on the parameters and
equation
            q_calcA = qr + exp(a*epa).*(a*A + B + a*B*epa) + ...
                exp(b*epa).*(b*C + D + b*D*epa);
            q_calcA(q_calcA<0)=NaN;

            %1.2. Determine points of maximum curvature
            [k_max_curv] = Determine_Max_Curvature(epa,q_calcA);

        %1.2.1. Extract out q, p & epa for later plotting
            q_out_17(i,1) = q_calcA(k_max_curv)*max(q);
            epa_out_17(i,1) = epa(k_max_curv);
            if i<7 %then it is a conp test
                p_out_17(i,1) = trimmean(p,75);
            else
```

```
            p_out_17(i,1) = p(1)+ q_out_17(i,1)/3;
        end;


    %1.3. Determine yield as peak if larger q than residual q
        if max(q_calcA)>1.05*q_calcA(end)
            q_out_17(i,2) = max(q_calcA)*max(q);
            epa_out_17(i,2) = epa(q_calcA==max(q_calcA));
            if i<7 %then it is a conp test
                p_out_17(i,2) = trimmean(p,75);
            else
                p_out_17(i,2) = p(1)+ q_out_17(i,2)/3;
            end;
        else
            q_out_17(i,2) = q_out_17(i,1);
            epa_out_17(i,2) = epa_out_17(i,1);
            p_out_17(i,2) = p_out_17(i,1);
        end;
    %1.4. Determine yield as q at intersect strain of initial linear
and residual parts
        [k_intersect,      epa_intersect,      q_intersect]      =
Determine_Intersect(epa,q_calcA);
        if isempty(k_intersect)
            k_intersect=1;
        end;


        %1.4.1. Extract out values for later plotting
        %1.4.1.1. For q on fitted curve at intersect strain
        q_out_17(i,3) = q_calcA(k_intersect)*max(q);
        epa_out_17(i,3) = epa(k_intersect);
        if i<7 %then it is a conp test
```

```
        p_out_17(i,3) = trimmean(p,75);
    else
        p_out_17(i,3) = p(1)+ q_out_17(i,3)/3;
    end;

    %1.4.1.2. For q at intersect point (Helen Cheung method)
    q_out_17(i,4) = q_intersect*max(q);
    epa_out_17(i,4) = epa_intersect;
    if i<7 %then it is a conp test
        p_out_17(i,4) = trimmean(p,75);
    else
        p_out_17(i,4) = p(1)+ q_out_17(i,4)/3;
    end;

  %1.5. Determine yield as when curve deviates from initial linear
section by a certain amount
    [k_deviate] = Determine_Deviate(epa,q_calcA);
    if isempty(k_deviate)
        k_deviate=1;
    end;

    %1.5.1. Extract out values for later plotting
    q_out_17(i,5) = q_calcA(k_deviate)*max(q);
    epa_out_17(i,5) = epa(k_deviate);
    if i<7 %then it is a conp test
        p_out_17(i,5) = trimmean(p,75);
    else
        p_out_17(i,5) = p(1)+ q_out_17(i,5)/3;
    end;
```

```
        %1.6. Plot data including yield points

            if printindiv == 1

                fi = figure;

                set(fi, 'units','centimeters','Position', [2 4 16 16]);

                plot(epa_r,q/1E6,'kx');

                hold all

                plot(epa,q_calcA*max(q)/1E6,'k-');


plot(epa_out_17(i,1),q_out_17(i,1)/1E6,'go','markerfacecolor','g','m
arkersize',10);


plot(epa_out_17(i,2),q_out_17(i,2)/1E6,'rd','markerfacecolor','r','m
arkersize',9);


plot(epa_out_17(i,3),q_out_17(i,3)/1E6,'mv','markerfacecolor','m','m
arkersize',8);


plot(epa_out_17(i,4),q_out_17(i,4)/1E6,'bs','markerfacecolor','b','m
arkersize',7);


plot(epa_out_17(i,5),q_out_17(i,5)/1E6,'c<','markerfacecolor','c','m
arkersize',6);

                legend('DEM Points','Fitted Curve EQA','Yield: Max
Curvature','Yield: Max Curvature or Max q','Yield: Intersect','Yield:
Modified          Intersect','Yield:          Change          in
Stiffness','location','southeast')

                xlabel('$\epsilon_a$ (\%)','interpreter','latex');

                ylabel('$q$ (MPa)','interpreter','latex');

                title(['Consolidated to: 17 MPa - Test Type:
'   ,ls17{i}(1:4),   '   -   Tested   at:   ',   ls17{i}(6:end)   ,'
MPa'],'interpreter','none');




set(fi,'PaperUnits','centimeters','PaperPositionMode','auto',...
```

```
                'PaperSize',[16 16])
            print(['Figures_EQB\17Mpa_',ls17{i}],'-dpng','-r600');
            close
        end;

    end;

    %%%%
```

```
epv_r = data(:,4)*100;

qr = par_out_20{i}(1,1);

a = par_out_20{i}(1,2);

A = par_out_20{i}(1,3);

B = par_out_20{i}(1,4);

b = par_out_20{i}(1,5);

C = par_out_20{i}(1,6);

D = par_out_20{i}(1,7);


%2.1.2 Create a higher density epa vector

epa = linspace(0,max(epa_r),1000);


%2.1.3 Calcualte the q curve based on the parameters and
equation

q_calcA = qr + exp(a*epa).*(a*A + B + a*B*epa) + ...

    exp(b*epa).*(b*C + D + b*D*epa);

q_calcA(q_calcA<0)=NaN;


%2.2. Determine points of maximum curvature

[k_max_curv] = Determine_Max_Curvature(epa,q_calcA);


%2.2.1. Extract out q, p & epa for later plotting

q_out_20(i,1) = q_calcA(k_max_curv)*max(q);

epa_out_20(i,1) = epa(k_max_curv);

if i<7 %then it is a conp test

    p_out_20(i,1) = trimmean(p,75);

else

    p_out_20(i,1) = p(1)+ q_out_20(i,1)/3;

end;
```

```
            %2.3. Determine yield as peak if larger q than residual q
            if max(q_calcA)>1.05*q_calcA(end)
                q_out_20(i,2) = max(q_calcA)*max(q);
                epa_out_20(i,2) = epa(q_calcA==max(q_calcA));
                if i<7 %then it is a conp test
                    p_out_20(i,2) = trimmean(p,75);
                else
                    p_out_20(i,2) = p(1)+ q_out_20(i,2)/3;
                end;
            else
                q_out_20(i,2) = q_out_20(i,1);
                epa_out_20(i,2) = epa_out_20(i,1);
                p_out_20(i,2) = p_out_20(i,1);
            end;

            %2.4. Determine yield as q at intersect strain of initial
linear and
            %residual parts
            [k_intersect,      epa_intersect,      q_intersect]      =
Determine_Intersect(epa,q_calcA);
            if isempty(k_intersect)
                k_intersect=1;
            end;

            %2.4.1. Extract out values for later plotting
            %2.4.1.1. For q on fitted curve at intersect strain
            q_out_20(i,3) = q_calcA(k_intersect)*max(q);
            epa_out_20(i,3) = epa(k_intersect);
            if i<7 %then it is a conp test
```

```
        p_out_20(i,3) = trimmean(p,75);
    else
        p_out_20(i,3) = p(1)+ q_out_20(i,3)/3;
    end;

    %2.4.1.2. For q at intersect point (Helen Cheung method)
    q_out_20(i,4) = q_intersect*max(q);
    epa_out_20(i,4) = epa_intersect;
    if i<7 %then it is a conp test
        p_out_20(i,4) = trimmean(p,75);
    else
        p_out_20(i,4) = p(1)+ q_out_20(i,4)/3;
    end;

    %2.5. Determine yield as when curve deviates from initial
linear
    %section by a certain amount
    [k_deviate] = Determine_Deviate(epa,q_calcA);
    if isempty(k_deviate)
        k_deviate=1;
    end;

    %2.5.1. Extract out values for later plotting
    q_out_20(i,5) = q_calcA(k_deviate)*max(q);
    epa_out_20(i,5) = epa(k_deviate);
    if i<7 %then it is a conp test
        p_out_20(i,5) = trimmean(p,75);
    else
        p_out_20(i,5) = p(1)+ q_out_20(i,5)/3;
```

```
            end;


            %2.6. Plot data including yield points

            if printindiv == 1

                fi = figure;

                set(fi, 'units','centimeters','Position', [2 4 16 16]);

                plot(epa_r,q/1E6,'kx');

                hold all

                plot(epa,q_calcA*max(q)/1E6,'k-');


plot(epa_out_20(i,1),q_out_20(i,1)/1E6,'go','markerfacecolor','g','m
arkersize',10);


plot(epa_out_20(i,2),q_out_20(i,2)/1E6,'rd','markerfacecolor','r','m
arkersize',9);


plot(epa_out_20(i,3),q_out_20(i,3)/1E6,'mv','markerfacecolor','m','m
arkersize',8);


plot(epa_out_20(i,4),q_out_20(i,4)/1E6,'bs','markerfacecolor','b','m
arkersize',7);


plot(epa_out_20(i,5),q_out_20(i,5)/1E6,'c<','markerfacecolor','c','m
arkersize',6);

                legend('DEM Points','Fitted Curve EQA','Yield: Max
Curvature','Yield: Max Curvature or Max q','Yield: Intersect','Yield:
Modified          Intersect','Yield:          Change          in
Stiffness','location','southeast')

                xlabel('$\epsilon_a$ (\%)','interpreter','latex');

                ylabel('$q$ (MPa)','interpreter','latex');

                title(['Consolidated to: 20 MPa - Test Type:
'   ,ls20{i}(1:4),   '   -   Tested   at:   ',   ls20{i}(6:end)   ,'
MPa'],'interpreter','none');




set(fi,'PaperUnits','centimeters','PaperPositionMode','auto',...
```

```
                    'PaperSize',[16 16])
                print(['Figures_EQB\20Mpa_',ls20{i}],'-dpng','-r600');
                close
            end;

        end;



        %%%%
```

```
        %4.1. Determine fitted yield surface parameters
        for j=1:5
            %4.1.1. Combine data
            temp=[p_out_17(:,j)/17E6,q_out_17(:,j)/17E6];
            temp=[temp;[p_out_20(:,j)/20E6,q_out_20(:,j)/20E6]];
            temp(isnan(temp(:,2)),:) = [];

           %4.1.2. Determine N
            AA_rng = linspace(1.1,4.9,29);

            %4.1.3. Determine errors of fitting for each N value
            errors = zeros(29,1);
            for i=1:length(AA_rng)
                qs                                                  =
temp(:,1)*0.75.*((log(1./(temp(:,1)))/log(20/12)).^(1./AA_rng(i)));
                errors(i) = sum((temp(:,2)-qs).^2);
            end;

            %4.1.3. Determine min errorn and optimal N
            [~, idx] = min(errors(:));
            [aidx] = ind2sub(size(errors), idx);
            AA(j) = AA_rng(aidx);

            %4.1.4. Create array of data
            p_fake(:,j) = linspace(0,1,1000);
            q_fake(:,j)                                             =
p_fake(:,j)*0.75.*((log(1./p_fake(:,j))/log(20/12)).^(1./AA(j)));

        end;
```

```
%save('AA.mat','AA');



fi=figure;
set(fi, 'units','centimeters','Position', [2 1 16 25]);
subplot(3,2,1)
hold all
plot(p_out_17(:,1)/17E6,q_out_17(:,1)/17E6,'go');
plot(p_out_20(:,1)/20E6,q_out_20(:,1)/20E6,'gx');
title('Yield: Max Curvature')
xlabel('p/p_0','fontangle','italic');
ylabel('q/p_0','fontangle','italic');
plot(p_fake(:,1),q_fake(:,1),'k')
line([0 0.8],[0 0.8*0.75],'linewidth',3,'color','k');

subplot(3,2,2)
hold all
plot(p_out_17(:,2)/17E6,q_out_17(:,2)/17E6,'ro');
plot(p_out_20(:,2)/20E6,q_out_20(:,2)/20E6,'rx');
title('Yield: Max Curvature or Max q')
xlabel('p/p_0','fontangle','italic');
ylabel('q/p_0','fontangle','italic');
plot(p_fake(:,2),q_fake(:,2),'k')
line([0 0.8],[0 0.8*0.75],'linewidth',3,'color','k');

subplot(3,2,3)
hold all
```

```
plot(p_out_17(:,3)/17E6,q_out_17(:,3)/17E6,'mo');
plot(p_out_20(:,3)/20E6,q_out_20(:,3)/20E6,'mx');
title('Yield: Intersect')
xlabel('p/p_0','fontangle','italic');
ylabel('q/p_0','fontangle','italic');
plot(p_fake(:,3),q_fake(:,3),'k')
line([0 0.8],[0 0.8*0.75],'linewidth',3,'color','k');

subplot(3,2,4)
hold all
plot(p_out_17(:,4)/17E6,q_out_17(:,4)/17E6,'mo');
plot(p_out_20(:,4)/20E6,q_out_20(:,4)/20E6,'mx');
title('Yield: Modified Intersect')
xlabel('p/p_0','fontangle','italic');
ylabel('q/p_0','fontangle','italic');
plot(p_fake(:,4),q_fake(:,4),'k')
line([0 0.8],[0 0.8*0.75],'linewidth',3,'color','k');

subplot(3,2,5)
hold all
plot(p_out_17(:,5)/17E6,q_out_17(:,5)/17E6,'bo');
plot(p_out_20(:,5)/20E6,q_out_20(:,5)/20E6,'bx');
title('Yield: Change in Stiffness')
xlabel('p/p_0','fontangle','italic');
ylabel('q/p_0','fontangle','italic');
plot(p_fake(:,5),q_fake(:,5),'k')
line([0 0.8],[0 0.8*0.75],'linewidth',3,'color','k');
```

```
        set(fi,'PaperUnits','centimeters','PaperPositionMode','auto',...
            'PaperSize',[16 25])
        print('Figures_EQB\Yield_Surface','-dpng','-r600');


        end




        %A. This subfunction calculates the point of maximum curvature
        function [k_max_curv] = Determine_Max_Curvature(epa,q_calcA)


        %A.1. Create an epa scale which runs from 0 to 1 to ensure equal
scale to q
        epa_fake = linspace(0,1,length(epa));


        %A.2. Determine radius of circle which would fit to n adjacent
points
        n = 2; %num of points (even only)
        R(1:length(q_calcA)) = NaN; %initalise R
        yc(1:length(q_calcA)) = NaN; %initalise yc
        for jj=1+n/2:1:length(q_calcA)-n/2
            [~,yc(jj),R(jj),~]          =          circfit(epa_fake(jj-
n/2:jj+n/2),q_calcA(jj-n/2:jj+n/2));
        end;


        %A.3. Find where mininum R occurs but ensure it doesn't occur
when
        %flattening out again by determining location of centre of
circle
        [~,k1] = findpeaks(-R,'sortstr','descend');
```

```
        k1(yc(k1)>q_calcA(k1)) = [];


        %A.4. Pass back location

        if ~isempty(k1)

            k_max_curv = k1(1);

        else

            k_max_curv = 1;

        end;


        end


        %B. This subfunction determines intersect point

        function [k_intersect, epa_intersect, q_intersect] = ...

        Determine_Intersect(epa,q_calcA)


        %B.1. Fit a straight line to first 2% of exial strain data

        P = polyfit(epa(epa<2 & ~isnan(q_calcA)),q_calcA(epa<2 &
~isnan(q_calcA)),1);


        %B.2. Determine epa at intersect

        epa_intersect = (q_calcA(end)-P(2))/(P(1));


        %B.3. Determine q at intersect

        q_intersect = epa_intersect*P(1) + P(2);


        %B.3. Determine index of epa_intersect

        k_intersect = find(abs(epa-epa_intersect)==min(abs(epa-
epa_intersect)));
```

```
end

%C. This subfunction determines deviation point

function [k_deviate] = Determine_Deviate(epa,q_calcA)

%B.1. Fit a straight line to first 2% of exial strain data

P = polyfit(epa(epa<2 & ~isnan(q_calcA)),q_calcA(epa<2 & ~isnan(q_calcA)),1);

%B.2. At each strain level determine deviation of curve from fit

%B.2.1. Determine value of straight line fit at each epa

q_linear = P(1)*epa + P(2);

%B.2.2. Determine distance (q) between linear and curve fit

q_diff = q_calcA - q_linear;

%B.2.3. Determine where q_diff exceeds threshold

k_deviate = find(q_diff<-0.2,1);

end
```

Appendix B

MATLAB Code of Fitting Curve

```
function DEM_Fitting_EQB_Mass_Process

% This function calculated all EQA optomised fit parameters
%
%2016_07_09     Version 1   C.M. Heron
%

load('Conp_17MPa.mat');
load('Conr_17MPa.mat');
ls17 = who('-file', 'Conp_17MPa.mat');
ls17 = [ls17 ; who('-file', 'Conr_17MPa.mat') ];

par_out_17 = cell(length(ls17),1);
for i=1:length(ls17)
    eval(['[parameters,~] = DEM_Fitting_EqB(',ls17{i},',1);']);
    par_out_17{i} = parameters;
end;


load('Conp_20MPa.mat')
load('Conr_20MPa.mat')
ls20 = who('-file', 'Conp_20MPa.mat');
ls20 = [ls20 ; who('-file', 'Conr_20MPa.mat') ];

par_out_20 = cell(length(ls20));
for i=1:length(ls20)

    eval(['[parameters,~] = DEM_Fitting_EqB(',ls20{i},',1);']);
    par_out_20{i} = parameters;

end;

save('Fitting_EQB.mat','ls17','par_out_17','ls20','par_out_20');

end
```

Appendix C

MATLAB Code of Circle fit function

```
function    [xc,yc,R,a] = circfit(x,y)
%
%   [xc yx R] = circfit(x,y)
%
%   fits a circle  in x,y plane in a more accurate
%   (less prone to ill condition )
%  procedure than circfit2 but using more memory
%  x,y are column vector where (x(i),y(i)) is a measured point
%
%  result is center point (yc,xc) and radius R
%  an optional output is the vector of coeficient a
% describing the circle's equation
%
%   x^2+y^2+a(1)*x+a(2)*y+a(3)=0
%
%  By:  Izhak bucher 25/oct /1991,
   x=x(:); y=y(:);
   a=[x y ones(size(x))]\[-(x.^2+y.^2)];
   xc = -.5*a(1);
   yc = -.5*a(2);
   R  =  sqrt((a(1)^2+a(2)^2)/4-a(3));
```